GABA Transporters and L-type Amino Acid Transporter 1
Molecular mechanisms and transport modulation of two solute carrier families in pathophysiology

DISSERTATION

Zur Erlangung des

DOKTORGRADES DER NATURWISSENSCHAFTEN (DR. RER. NAT.)

der Fakultät für Biologie und vorklinische Medizin

der Universität Regensburg

Vorgelegt von

Laure Gauthier-Manuel

Aus Lons-Le-Saunier (Frankreich)

Jahr 2025

Das Promotionsgesuch wurde eingereicht am:

Die Arbeit wurde angeleitet von:

Prof. Dr. Christine Ziegler

Unterschrift:

Eigenständigkeitserklärung/Declaration

Ich erkläre hiermit, dass ich die vorliegende Arbeit selbständig verfasst und keine anderen als die angegebenen Quellen und Hilfsmittel benutzt habe. Die aus anderen Quellen direkt oder indirekt übernommenen Daten und Konzepte sind unter Angabe des Literaturzitats gekennzeichnet.
Weitere Personen waren an der inhaltlich-materiellen Herstellung der vorliegenden Arbeit nicht beteiligt. Insbesondere habe ich hierfür nicht die entgeltliche Hilfe eines Promotionsberaters oder anderer Personen in Anspruch genommen. Niemand hat von mir weder unmittelbar noch mittelbar geldwerte Leistungen für Arbeiten erhalten, die im Zusammenhang mit dem Inhalt der vorgelegten Dissertation stehen.
Die Arbeit wurde bisher weder im In- noch im Ausland in gleicher oder ähnlicher Form einer anderen Prüfungsbehörde vorgelegt.

I hereby declare that I have written this thesis independently and have not used any sources or aids other than those indicated. Data and concepts taken directly or indirectly from other sources are marked with references.
No other person was involved in the content or material production of this thesis. I have not used the paid assistance of a doctoral advisor or other people for this purpose. No one has received any monetary compensation from me, either directly or indirectly, for work related to the content of the submitted dissertation.
The work has not previously been submitted to any other examination authority in the same or a similar form, either in Germany or abroad.

Regensburg,

Laure Gauthier-Manuel

“Il faut chercher avec le Cœur”

Le Petit Prince, Antoine de Saint Exupéry

Acknowledgments-*Danksagungen- Ringraziamenti-Remerciements*

I would like to express my gratitude to my supervisor Prof. Dr. Christine Ziegler and my co-supervisor Prof. Dr. Pierre Koch, for the trust they have placed in me to work on such ambitious but fascinating projects. Thank you both for giving me the opportunity to pursue my dream of becoming a researcher.

I thank Prof. Dr. Thomas Stoeckner for his investment in Neurotrans Network, and the funding Marie Sklodowska Curie Actions. I thank all my Network mates: Alberto, Ana Sofia, Anna, Erika, Francesca, Iris, Leticìa, Manan, Petros, Zaid, and especially those that came until Regensburg to learn about protein purification and cell culture with me: Anton, Despoina, Judith and Rocco. I wish you all the best for the future!

To the whole Ziegler Team, thank you Gregor to represent this "old school science" that I enjoy so much! I am so thankful to you and Lifei for sustaining me in the vitrification of GAT1 WT until late at night and to you, Lifei, for supporting me in the data processing!
Benedikt, Georg, Veronika, Jan, Johannes, Tamara, Timo, Nataliya, Katja, thank you all for your help, advice or good time in and out of the lab! Ich bin so dankbar zum Robert, Claudia, Sabine und Maria, den technischen und administrativen Mitarbeitern des Ziegler-Teams. Ohne Ihr Engagement würde das Labor nicht so gut funktionieren. Vielen Dank für alles!
I permit myself to dedicate special words to Felix, that even with our opposite characters, became what I dare to say, "my lab bestie". Thank you for your presence, your patience, and all the good times during these years!

I thank Prof. Dr. Elena Bossi and her whole team, Prof. Dr. Cristina Roseti, Dr. Raffaella Cinquetti, and all the people with whom I had the pleasure of working in Varese: Angela, Chiara, Giulia, Manan, Mattia, Tiziana. Thank you all for welcoming and integrating me as if I belonged to the chair. I particularly thank you, "Angie" and "Mani", for your patience and kindness to teach me the methodologies of electrophysiology the first weeks I was in (big) troubles with the oocytes and the set-up! Grazie Mille a tutti!

I thank Marko Roblek for furnishing me the cell lines for expressing rGAT1 WT and L300Q mutant. The project would have stuck without your help, thank you so much!

I thank Despoina Kapiki for her investment in testing new fluorescence assays with rGAT1 proteoliposomes and therefore giving a sense to my work! Ευχαριστώ!

I thank Beatrice Amigues and Vincent Delauzin for their welcoming and all the knowledge they transmitted to me during my stay at CytobodX. A vous deux, merci pour tout!

I truly thank all my students, Nadine, Sebastian, Amani, Iman, Victoria and Tatjana that teach me how to transmit my passion and give me a reason to keep working on scientific research. I especially thank them for their work, their personal investment and their courage to have me as supervisor!

I thank Prof. Dr. med. Richard Warth, Dr. Anna-Lena Forst, Dr. Allen Plain and the whole chair of Medical Cell Biology for their kindness, their availability and their unconditioned help for my sample preparation and epifluorescence/confocal imaging.

I thank Prof. Dr. Reinhard Sterner and its whole chair for these four years shared together. I address particular words for the technical assistant team that helped when I and/or the Ziegler Team needed it. Danke euch!

I thank Prof. Dr. Reinhard Rachel for the precious knowledge he transmitted to me on light and electron microscopy, and for challenging me to write my thesis on time!

I warmly thank Thomas, Povilas, Algirdas and Caroline. More than colleagues, I felt for a while being part of your respective families. Danke. Ačiū. Takk !

I thank Carolin and Kinga from the doctoral school of Regensburg (RIGEL). You are an essential support to achieving our PhD duties. Thank you for your good mood and your help the last weeks before submitting my manuscript!

I also want to thank the 5th floor of the Department of Biosciences of Milan and especially my research team Prof. Dr. Stefano Ricagno, Cristina, Davide, Federica, Giulia, Luca, Melissa, Nour, and the graduated students Brando e Ricardo. Thank you for your trust, and for having welcomed me so well in the lab! Grazie a voi!

Un grazie speciale alla mia coinquilina Laura, con cui ho condiviso più di quattro anni della mia vita. Grazie per esserti sempre preoccupata per me, spesso più di quanto lo facessi io! Grazie per tutte le persone che mi hai fatto conoscere, per non avermi mai lasciata sola e per i momenti indimenticabili che abbiamo vissuto e che continueremo a vivere insieme.

Ringrazio Rocco per le risate, per il lavoro fatto insieme in laboratorio, per le serate folli e per aver convinto il suo amico a venire a mangiare sushi in Germania!

Infatti, tu, Giorgio, sei stato coraggioso ad affrontare la distanza e soprattutto la mia personalità! Senza scrivere chilometri di righe che so che non leggeresti, ti ringrazio per l'attenzione che mi dedichi, per il modo in cui riesci a capirmi, anche senza essere sempre d'accordo con me, e per la presenza costante. Semplicemente, grazie per volermi così bene. Je t'aime.

Ringrazio con affetto anche Floriana e Fabio Botta, Anna e Damiano, per avermi accolta e integrata nella loro famiglia.

Un pensiero speciale va agli Emiliani, ai Parmigiani, ai Milanesi e alla mia Lucana d'oro: grazie per farmi sentire a casa, come una di voi. Grazie di cuore!

Il me vient maintenant le besoin de parler de ceux sans qui je ne serai pas là à écrire ces mots. Bien entendu je remercie tendrement mes parents pour les valeurs qu'ils m'ont transmis, notamment la rigueur du travail, le bon sens, le bon vivre, et leur courage de supporter une fille globe trotteuse comme moi ! Du fond du cœur, je vous remercie pour tout. Je n'oublie pas Lucienne et mon frère Geoffrey. Je remercie ta générosité pour ne pas voir pris tout le potentiel d'intelligence de la famille et de m'en avoir laissé un peu !

Je remercie toutes les personnes que j'ai pu rencontrer à Morbier, Morez, Besançon, Marseille, Lyon et Bordeaux, qu'elles soient professeurs, amis, colocataires, ou camarades. Notamment à ces derniers qui sont devenus camarades de vie, pour la vie. Merci à vous !

Pour conclure, je souhaite citer mes quatre mousquetaires de la science. Merci à Matthias grâce à qui j'ai trouvé ma vocation (et quelle vocation, me diras-tu !). Merci à Roberto de m'avoir fait répéter ma présentation pour la sélection au financement Marie Curie. Ces 250 pages sont « tutta colpa tua » ! Merci à Nicolas de m'avoir « tenu les pouces » pendant les moments difficiles du clonage… Vois-tu, tout a fini par joué ! Enfin bien-sûr, Sylvain, merci du fond du cœur pour ton soutien inconditionnel tout au long de ces années et l'amitié que nous essayons de pérenniser tant bien que mal au travers de notre «Reel»ationship !

Abstract

GABA transporter 1 (GAT1) and L-type amino acid transporter 1 (LAT1) are secondary transporters belonging to the solute carrier (SLC) families 6 and 7, respectively. GAT1 is a monomeric sodium dependent symporter playing a crucial role in regulating GABA concentrations within the synaptic cleft. Recent findings indicated that GAT1 interacts and transport betaine, a methylammonium solute usually transported by Betaine/GABA Transporter 1 (BGT1). The molecular mechanism, however, remains unknown. To understand the specificity and characteristics of betaine transport in GAT1 and BGT1, we identified three residues in GAT1 (Ser133, Leu300, and G403) that align with three residues in BGT1 (Glu126, Gln299, and Cys402) that might account for the differences observed between the two transporters. We revealed that GAT1 L300Q has a BGT1-like kinetics, highlighting the crucial role of a third sodium ion in BGT1 for promoting the inward-open state. Conversely, we showed that betaine reduces the affinity for sodium in GAT1 WT and L300Q indicating a transport highly sodium dependent. We propose that osmotic stress facilitates betaine transport in the GABA transporter family, a mechanism conserved from the ancestral BetP, an obligate betaine transporter from *Corynebacterium glutamicum*.

The SLC7 transporter LAT1 is associated with the type II transmembrane protein CD98 from the SLC3 family. The heterodimer is a sodium independent amino acid antiporter and mainly expresses in cancer cells, enhancing their survival and proliferation. Thus, it is a highly relevant target in pharmacology. The LAT1 inhibitor Brasilicardin A is a diterpenoid isolated from *Nocardia brasiliensis* and has low toxicity and a potent IC_{50}. However, its interaction mode with LAT1 is still unknown. Therefore, LAT1 complex was expressed and purified in order to determine its structure with BraA. This is a crucial step for identifying rudimentary functional groups to simplify the molecule synthesis. LAT1 was detected at the surface of PC-3M cells, that are *ex vivo* prostatic bone metastasis (BM). These hormone refractory cells are drug-resistant, however BraA represents a promising molecule to eradicate the proliferation of BM *in vitro*.

Our findings provide new insights into the molecular mechanisms that modulate the activity of two distinct solute carrier families, opening up promising avenues for therapeutic intervention in various diseases.

Zusammenfassung

Der GABA-Transporter 1 (GAT1) und der L-Typ-Aminosäuretransporter 1 (LAT1) sind sekundäre Transporter, die jeweils zur Solute Carrier (SLC)-Familie 6 und 7 gehören. GAT1 ist ein monomerer natriumabhängiger Symporter, der eine entscheidende Rolle bei des synaptischen Spaltes spielt. Jüngste Erkenntnisse deuten darauf hin, dass GAT1 mit Betain interagiert und dieses transportiert, einem Methylammonium-Osmolyt, das normalerweise vom Betain/GABA-Transporter 1 (BGT1) transportiert wird. Der molekulare Mechanismus ist jedoch noch unbekannt. Um die Spezifität und Eigenschaften des Betaintransports in GAT1 und BGT1 zu verstehen, haben wir drei Aminosäuren in GAT1 (Ser133, Leu300 und G403) identifiziert, die mit drei Aminosäuren in BGT1 (Glu126, Gln299 und Cys402) übereinstimmen und möglicherweise für die zwischen den beiden Transportern beobachteten Unterschiede verantwortlich sind. Wir haben gezeigt, dass GAT1 L300Q eine BGT1-ähnliche Kinetik aufweist, was die entscheidende Rolle eines dritten Natriumions in BGT1 für die Förderung des nach innen offenen Zustands unterstreicht. Umgekehrt haben wir gezeigt, dass Betain die Affinität zu Natrium in GAT1 WT und L300Q verringert, was auf einen stark natriumabhängigen Transport hindeutet. Wir schlagen vor, dass osmotischer Stress den Betaintransport in der GABA-Transporterfamilie erleichtert, ein Mechanismus, der vom ursprünglichen BetP, einem obligaten Betaintransporter aus *Corynebacterium glutamicum*, übernommen wurde.

Der SLC7-Transporter LAT1 ist mit dem Typ-II-Transmembranprotein CD98 aus der SLC3-Familie assoziiert. Das Heterodimer ist ein natriumunabhängiger Aminosäure-Antiporter und kommt hauptsächlich in Krebszellen vor, wo es deren Überleben und Vermehrung fördert. Daher ist es ein hochrelevantes Ziel in der Pharmakologie. Der LAT1-Inhibitor Brasilicardin A ist ein aus *Nocardia brasiliensis* isoliertes Diterpenoid mit geringer Toxizität und einer potenten IC_{50}. Seine Wechselwirkungsweise mit LAT1 ist jedoch noch unbekannt. Daher wurde der LAT1-Komplex exprimiert und aufgereinigt, um seine Struktur mit BraA zu bestimmen. Dies ist ein entscheidender Schritt zur Identifizierung rudimentärer funktioneller Gruppen, um die Molekülsynthese zu vereinfachen. LAT1 wurde an der Oberfläche von PC-3M-Zellen nachgewiesen, bei denen es sich um ex vivo-Prostataknochenmetastasen (BM) handelt. Diese hormonresistenten Zellen sind medikamentenresistent, jedoch stellt BraA ein vielversprechendes Molekül dar, um die Vermehrung von BM in vitro zu unterbinden.

List of Abbreviations

2/3D	2/3 Dimension
4F2hc (CD98)	4F2 heavy chain
8-His	Poly-histidine Tag
APC	Amino Acid-Polyamine-Organocation Family
AR	Androgen receptor
ATP	Adenosine Triphosphate
Au/Pd	Gold/Palladium
BBB	Blood Brain Barrier
BCA	Bicinchoninic Acid
BCCTs	Betaine-Carnitine-Choline transporters
BGT1	Betaine/ GABA transporter 1
BM	Bone metastasis
BraA	Brasilicardin A
BSA	Bovine Serum Albumin
Ca^{2+}	Calcium ion
CD	Cluster differentiation
CHS	Cholesteryl hemi-succinate
Cl^-	Chloride ion
CNS	Central Nervous System
Cryo-EM	Cryogenic Electron Microscopy
CTF	Contrast Transfer Function
Cu	Copper
CV	Column Volume
DDM	Dodecyl-ß-D-maltoside
DMEM	Dublecco’s modified Eagle's Medium
DNA	Deoxyribonucleotidic Acid

E.coli	*Escherichia coli*
EBNA	Epstein-Barr virus nuclear antigen
ED	Ectodomain
EDTA	Ethylenediaminetetraacetic Acid
EL	Extracellular loop
EV	Extracellular vesicle
FBS	Fetal Bovine Serum
GABA	Gamma Amino Butyric Acid
GAT	GABA transporter
G-C	Guanine-Cytosine
GCN2	General Control Non Depressible 2
GlyT	Glycine Transporter
$GnTI^-$	N-acetylglucosaminyltransferase I
GO	Graphene oxide
GSS	Glycine-Serine-Serine
HEK	Human Embryonic Kidney
Hepes	4-(2-hydroxyethyl)-1-piperazineethanesulfonic acid
I/V	Intensity/Voltage
IC_{50}	Inhibiting concentration
Imax	Maximal Intensity
K^+	Potassium ion
$K_{0.5}$	Affinity constant
LAT	L-Type Amino acid Transporter
LeuT	Leucine Transporter
LMNG	Lauryl Maltose Neopentyl Glycol
LN	Lymph nodes
LPR	Lipid Protein Ratio
MFS	Major Facilitator Superfamily

Mg^{2+}	Magnesium ion
mTOR	mechanistic Target Of Rapamycin
Na^{+}	Sodium ion
Na1/2/3	Sodium binding sites 1/2/3
NSS	Neurotransmitter Sodium Symporter
P/S	Penicillin/Streptomycin
PBS	Phosphate buffered saline
PC	Prostate cancer
PC-3M	Prostate cancer 3M cell line
PCR	Polymerization Chain Reaction
PDB	*Protein Data Bank*
PEI	Polyethyleneimine
PIP_2	Phosphatidylinositol 4,5-bisphosphate
PL	Phospholipid
PSA	Prostate Specific Antigen
RNA	Ribonucleic Acid
rpm	Rotation per minute
RT	Room temperature
SAR	Structure-activity relationship
SDS PAGE	Sodium dodecyl-Sulfate Poly-Acrylamide Gel Electrophorese
SEC	Size Exclusion Chromatography
SLC	Solute Carrier
Sn	*Stereospecific numbering*
SPA	Single Particle Analysis
TAE	Tris-Acetate-EDTA
TBS	Tris Buffered Saline
TEM	Transmission Electron Microcopy
TEVC	Two Electrode Voltage Clamp

TM	Transmembrane helix
Tris	Tris(hydroxymethyl)aminomethane
WT	Wild Type
YFP	Yellow Fluorescent Protein

List of Figures

Figure 1: Plasma membrane complexity..... 2
Figure 2: Polar heads and aliphatic chains..... 3
Figure 3: Computational lipidomics of phospholipid composition. 4
Figure 4: Characteristic LeuT, MFS, Glt_{Ph} and NhaA-folds.. 9
Figure 5: Repeats and transmembrane domains alignment with the corresponding α-helices foldings for the APC, NSS, and BCCT families..... 10
Figure 6: Detailed folds. 11
Figure 7: Secondary transporters at a glance. 12
Figure 8: Model of the transition from occluded to inward-open state 15
Figure 9: Residues alignment from different mammalian NSS, LeuT and BetP involving in the respective sodium binding sites. 16
Figure 10: Osmolyte classes 18
Figure 11: GABAergic system in the human brain 19
Figure 12: GATs sequence alignment..... 21
Figure 13: Hypothesis of Betaine binding site in GAT1 WT 26
Figure14: NSS, LeuT and BetP super-alignment 28
Figure 15: Localization of residues mutated and their respective TMs in GAT1 30
Figure 16: Diagram explaining the divers HATs systems. 32
Figure 17: LAT1 heterodimer structure (PDB 6IRT). 34
Figure 18: Lipid and inter-monomer interactions involved in complex stabilization.. 35
Figure 19: LAT1 inhibitors interacting in the binding site. 37
Figure 20: LAT1 tissue expression. 38
Figure 21: Molecule structures of LAT1 inhibitors..... 40
Figure 22: Cellular mechanism after amino acid deprivation..... 44
Figure 23: Structure of Brasilicardin A. 43
Figure 24: Synthetic analogues of Brasilicardin A 46
Figure 25: Brasilicardin A biosynthesis by *N. Brasiliensis* 48

Figure 26: Structures of Brasilicardin A intermediates BraC and BraE 48
Figure 27: Focus on the prostatic gland 50
Figure 28: Metastases associated with prostate cancer 51
Figure 29: Vector carrying rGAT1 WT with the YFP modified by PCR 56
Figure 30: PCR workflow used to generate pHIS-FLAG rGAT1 57
Figure 31: Representation of the linear product after PCR 58
Figure 32: Reconstitution of the final template pHis-FLAG *r*GAT1 58
Figure 33: Chemical structure of branched Polyethyleneimine (PEI) 66
Figure 34: Different maturation stages of oocytes from *X. laevis* 89
Figure 35: Two electrode voltage clamp principle and set up 90
Figure 36: Fluorescence signal of the eYFP expressed at the N-terminal of rGAT1 after 72 h of expression.. 103
Figure 37: Analysis of GAT1 WT-eYFP expression 104
Figure 38: Cloning of pHF rGAT1 105
Figure 39: Western blot to verify the expression of the new construct pHis-FLAG rGAT1 in the ration DNA:PEI 1:3. 106
Figure 40: Western blot of rGAT1 after membrane extraction and Ni-NTA resin elution, expressed with different cell culture conditions. 108
Figure 41: Western blot of rGAT1 after membrane extraction and Ni-NTA resin elution, expressed in shaking flask at 125 rpm after 72 h 109
Figure 42: TEM images of rGAT1 WT in DDM/CHS micelles 109
Figure 43: Comparison between the forward and the reverse purification of *r*GAT1 111
Figure 44: Purification of *r*GAT1 before vitrification for Cryo-EM 110
Figure 45: Data collection of *r*GAT1 in LMNG/CHS micelles 112
Figure 46: Comparison of rGAT1 particle density on graphene oxide or standard carbon film. 113
Figure 47: 2D classes of *r*GAT1 on 1.2/1.3 graphene oxide coated grids. 114
Figure 48: Micrographs of *r*GAT1 particles at the surface of GO coated grids 114
Figure 49: Lipidic composition of the brain total extract used. 115
Figure 50: Analysis of rGAT1 reconstituted in proteoliposomes 116

Figure 51: Thermophoresis experiment showing the binding of GABA on rGAT1 reconstituted in proteoliposomes 117
Figure 52: Scavenged fluorophore used for chemosensor-based transport assay..... 118
Figure 53: Chemosensory-based transport assay for rGAT1 WT reconstituted in proteoliposomes with the LPR 1:10. 118
Figure 54: Purification and further analysis of rGAT1 expressed in EVs 120
Figure 55: TEM images of rGAT1 in EVs 121
Figure 56: Response of rGAT1 WT, L300Q and non-injected oocytes. 124
Figure 57: Response of rGAT1 WT, S133E, G403C and non-injected oocytes 125
Figure 58: Average currents of rGAT1 WT, S133E/L300Q, L300Q/G403C and non-injected oocytes 126
Figure 59: Entire oocytes for immunolocalization of rGAT1 WT and mutants..... 127
Figure 60: Vegetal oocyte poles for immunolocalization of rGAT1 WT and mutants 129
Figure 61: Animal oocyte poles for immunolocalization of rGAT1 WT and mutants..... 131
Figure 62: Expression of GAT1 L300Q at different DNA:PEI ratios after 72 h compared to the WT. 133
Figure 63: Cellular localization and fluorescence quantification of rGAT1 WT and L300Q 134
Figure 64: Analysis of the expression of e-YFP rGAT1 WT and L300Q 135
Figure 65: Kinetic parameters of rGAT1 WT and L300Q 136
Figure 66: Sodium affinities in presence of 300 µM GABA or 30 mM betaine for GAT1 WT and GAT1 L300Q 138
Figure 67: Intensity voltage analysis at various sodium concentrations 300 µM GABA for rGAT1 WT and L300Q. 140
Figure 68: rGAT1 L300Q Expression/Purification on two affinity chromatography resins 141
Figure 69: rGAT1 L300Q polishing 142
Figure 70: Micrographs and 2D classes for different grid types.. 144
Figure 71: Typical micrographs for rGAT1 L300Q on Quantifoil grids 1.2/1.3 5 s blotting..... 145
Figure 72: 2D classes of rGAT1 L300Q..... 145
Figure 73: rGAT1 WT inward-occluded structure fitted in the initial map of GAT1 L300Q.... 146

Figure 74: GABA and sodium binding in GAT1 WT (from 7Y7W) and L300Q generated by AlphaFold.. 147
Figure 75: Subunit detection of LAT1/CD98 complex according to the antibodies used..... 149
Figure 76: Condition screening for expression of LAT/CD98 expression in suspension cell culture.. 150
Figure 77: Non-transfected HEK293 GnTI$^-$ cells for detecting nonspecific interactions..... 152
Figure 78: Heterodimer LAT1/CD98 expressed in DNA ratio 1:1 or 1:2. 156
Figure 79: Expression of CD98 as single subunit..... 157
Figure 80: Confocal images of CD98 expressed in HEK293 GnTI$^-$ as single subunit..... 159
Figure 81: Expression of LAT1 as single subunit 159
Figure 82: Confocal images of LAT1 expressed in HEK293 GnTI$^-$ as single subunit..... 161
Figure 83: Confocal images of *r*GABA transporter 1 ΔEL2 transfected in HEK293 GnTI$^-$..... 161
Figure 84: FLAG affinity chromatography steps..... 162
Figure 85: Analysis of fraction F2 during concentration before SEC 162
Figure 86: Analysis of LAT1/CD98 purification post SEC..... 163
Figure 87: Analysis of the 100 kDa molecular cut-off flow through 164
Figure 88: Analysis of SEC columns washed with 2 CV of 500 mM NaOH..... 165
Figure 89: Second affinity chromatography steps on StrepTactin Superflow XT..... 166
Figure 90: Western blot analysis on PC-3M cells lysate 168
Figure 91: LAT1 and CD98 cellular localization in the bone metastasis PC-3M 170
Figure 92: Nonspecific signal associated with the PC-3M cells..... 170
Figure 93: Scheme of GAT-SERT concatemer 171
Figure 94: Superposition of rGAT1 WT in inward-open and occluded conformations 175
Figure 95: Successive events in GAT1 L300Q from GABA binding to retention in the binding site.. 175
Figure 96: GABA and sodium release in GAT1 L300Q.. 176
Figure 97: Putative betaine binding site..... 177
Figure 98: Betaine transport mechanism in GAT1 WT..... 178
Figure 99: Betaine transport mechanism in GAT1 L300Q..... 180

Figure 100: Selection and specification of GAT1 and BGT1 along evolution..... 184
Figure 101: Molecular cascade for cellular adhesion. 187
Figure 102: Model of bone colonization by malignant prostatic cancer cells after proteomic burden accumulated in neuroendocrine cells in the prostate epithelium 188

List of Tables

Table 1: List of the main LAT1/CD98 structures.. 33
Table 2: Plasmids used for molecular biology cloning and further experiments. 55
Table 3: Bacterial strains used for molecular biology methods. 55
Table 4: Primers used for 8-His-FLAG insertion on pC1-eYFP *r*GAT1 template. 57
Table 5: PCR thermocycling conditions for the cloning of pHis-FLAG *r*GAT1 vector. 58
Table 6: Primers used for site directed mutagenesis in pHis-FLAG rGAT1 or pAMV-PA rGAT1 plasmids. 59
Table 7: Primers for inserting $(GSS)_4$ linker in pC1-eYFP *r*GAT1 60
Table 8: Thermocycling condition for touchdown protocol. 61
Table 9: Bacterial strains and selective agent according to each plasmid used for cloning. 62
Table 10: Primers used for sequencing. 63
Table 11: Cell lines used, media and supplements for adherent or suspension cell culture and transient transfection. 64
Table 12: Volumes used for cultivating and splitting depending on the flask size. 65
Table 13: Transient transfection conditions for *r*GAT1 (eYFP and HF) and LAT1/CD98. 67
Table 14: Transient transfection conditions for GAT1 eYFP tagged and LAT1/CD98 for immunofluorescence experiments 68
Table 15: Composition of GAT1 and LAT/CD98 solubilization buffers for expression tests. 68
Table 16: Conditions tested for small scale expression of *r*GAT1 WT. 70
Table 17: LAT1/CD98 small scale expression conditions 71
Table 18: Conditions used for large scale expression of *h*LAT1/CD98 based on the previous conditions tested in small scale. 71
Table 19: Solutions used for gel fast silver staining. 74
Table 20: Primary antibodies used 76
Table 21: Secondary antibodies used for Western blot and/or immunofluorescence with associated dilutions 77
Table 22: Molar extinction coefficients of the proteins purified 78

Table 23: Calibration proteins used for SEC columns associated with the Stokes radius according to their elution volume 79
Table 24: SEC buffers, and concentrator molecular weight cut-off used according to the protein purified. 80
Table 25: Glow discharging conditions according to the grid type. 84
Table 26: Different grids and blotting conditions tested for the different proteins studied in this work. 85
Table 27: Conditions of linearization of the plasmid with rGAT1 (WT/mutants) gene, with the restriction enzyme SalI. 91
Table 28: Conditions for *in vitro* RNA synthesis (to be continued in Table 29) 91
Table 29: Conditions for *in vitro* RNA synthesis (end) 92
Table 30: Sample preparation for RNA analysis on agarose gel 92
Table 31: Solutions for oocytes preparation. 93
Table 32: Solutions for electrophysiology measurements 95
Table 33: Chronological order of antibody incubation. 99
Table 34: Epifluorescence microscope illumination channels characteristics and use. 101
Table 35: Laser scanning microscope illumination channels used according to the fluorophore... 102
Table 36: Kinetic and affinity parameters of rGAT1 WT and L300Q for GABA and betaine at constant concentration of sodium (98 mM). 136
Table 37: Kinetic and affinity parameters of rGAT1 WT and L300Q for sodium at constant concentration of GABA (300 µM) or betaine (30 mM).... 138
Table 38: Differences and similarities between SLC6 and 7 families 189

List of Equations

Equation 1: Concentration determination related to absorbance.. 78
Equation 2: System for electrophysiology solutions ND*X*. 94

Table of contents

Abstract I

Zusammenfassung III

List of Abbreviations V

List of Figures IX

List of Tables XV

List of Equations XVII

Introduction 1

I. Membrane proteins: challenges, diversity, functions, structures and mechanisms 1

1. Plasma membrane: structure, composition and exchange surface 2
2. Membrane Proteins are communicative biomolecules 4
   - i. Receptors 5
   - ii. Channels 5
   - iii. Transporters 6
     - ATP activated pumps and primary active transporters 6
     - Secondary Transporters 6
3. Secondary transporters folding families 7
   - i. LeuT-fold 7
   - ii. GltPh-fold 8
   - iii. NhaA-fold 8

iv. MFS-fold 8
4. General and individual mechanism of secondary transporters 11
i. Alternating access model 11
ii. Different folds, same mechanisms/different folds, different mechanisms 12
- Rocking bundle mechanism 12
- Elevator mechanism 13

II. Study I: Molecular mechanism evolution of the GABA transporter family 13
1. GABA Transporters are part of the SLC6 family 13
i. Co-substrate and sequential binding event 13
ii. Role of Na1 and Na2 sodium binding sites in conformational cycling 14
2. Osmolytes and Neurotransmitters are the substrates of SLC6 family 16
3. GABA Transporters (GATs) family 18
i. Role and function in the central nervous system 18
ii. Difference between GATs/GAT1/BGT1 22
4. Towards a conserved mechanism across BCCT and NSS 23
i. Parallels between NSS and BCCT families 23
ii. GAT1 interacts and transports betaine 24
iii. Na1' in BGT1 26
iv. Residues of GAT1 and BGT1 for substrate specificity 27
5. Aims of Study I 29
6. Procedure 30
i. Sodium and substrate interaction/translocation in GATs 30
ii. Role of Protein/Lipid interactions in GATs 31

III. Study II: L-type Amino Acid Transporter 1 (LAT1): pharmaceutical inhibition and potential application against bone metastasis from prostate cancer 31
1. L-type amino acid transporter 1 31
i. Nomenclature 31
ii. Structure and function of the heterodimer LAT1/CD98 32
iii. Structural elements stabilizing the complex 35
- In the plasma membrane 35
- In the extracellular space 36
iv. Substrate binding in LAT1 subunit and molecular mechanism 36
2. Physiological and pathological relevance of the heterodimer LAT1/CD98 37

i. LAT1 is specifically expressed in certain healthy tissues 37
ii. LAT1 is overexpressed in tumoral tissues 39
3. LAT1 as a pharmacological target 39
i. LAT1 as “drug carrier” 39
ii. LAT1 as drug target in se 39
iii. Limitations for LAT1 inhibitors design 41
- Molecule metabolization 41
- LAT1 alternating access model 41
- Inhibition of LAT1 or LAT1/CD98? 41
4. Brasilicardin A: a promising and challenging inhibitor of LAT1 42
i. Brasilicardin A is a potent bioactive natural secondary metabolite 42
- Brasilicardin A has an immunosuppressing activity 43
- Molecular pathway activated by BraA inhibits cellular proliferation 44
- Brasilicardin A is a promising drug candidate 45
ii. Availability and production of BraA is a limiting factor 45
iii. Modifying the original BraA to simplify the compound synthesis 46
iv. Bio and Semi-synthesis of BraA 47
- Discovery of the Brasilicardin “gene cluster” in N. brasiliensisis 47
- Optimizations of BraA Semi/Natural synthesis 48
5. BraA against prostatic bone metastasis: a putative treatment? 49
i. Prostate physiology, cytology and biochemistry 49
ii. Prostate Cancer (PC) and associated metastases 51
iii. Bone metastasis study: role of LAT1 and its inhibition by BraA 52
6. Aims of the Study II 52
7. Procedures 53
i. LAT1-BraA interaction: Sample preparation for Cryo-EM study 53
ii. BraA for treating aggressive bone metastasis: LAT1/CD98 target validation 54

Material and Methods 55

I. Molecular Biology 55
1. Plasmids and bacterial strains used 55
2. Principle and protocol for pC1-eYFP rGAT1 modification 56
3. Genetic modifications on rGAT1 gene 59

i. Primers design 59
- For site directed mutagenesis 59
- For loop insertion 59

ii. Procedure 60
4. General methods 61
i. Agarose gel 61
ii. Linear DNA purification and ligation 61
iii. Transformation, plasmid amplification and sequencing 62

II. Cell culture and expression of mammalian proteins 63
1. Generalities 63
2. Adherent cell culture 64
i. Cell thawing 64
ii. Cell splitting 65
iii. Cell seeding for protein expression test and immunocytochemistry 65
iv. Transient transfection 66
- For protein test expression 66
- For cyto-immunochemistry 67

v. Harvest and evaluation of expression tests for eYFP/His-FLAG rGAT1 WT and mutant and LAT1/CD98 68
vi. Semi quantification on ImageJ 69
- eYFP fluorescence of rGAT1 WT and L300Q mutant 69
- Expression of rGAT1 WT and L300Q mutant on western blot 69

3. Suspension cell culture 69
i. Cell adaptation to suspension 69
ii. Small scale expression for GAT1 WT 70
iii. Large scale expression for GAT1 WT 70
iv. Small- and large-scale expression of LAT/CD98 71

III. Protein purification protocols, analysis and reconstitution in proteoliposomes 72
1. Purification of HF-*r*GAT1 WT 72
2. Purification LAT1/CD98 73
3. Protein analysis by sodium dodecyl sulphate-polyacrylamide gel electrophoresis (SDS-PAGE) and western blot 74
4. Protein concentration determination 78

5. Size Exclusion chromatography (SEC) 79
6. Reconstitution of rGAT1 WT in proteoliposome 80

IV. Expression/Purification of *r*GAT1 WT in extracellular vesicles 81
1. Molecular biology 81
2. Cell culture, transfection and expression 81
3. Extracellular vesicles purification 82

V. Transmission (Cryo)-electron microscopy (TEM and Cryo-EM) 82
1. (Cryo)-Transmission electron microscopy principle 82
2. Grid type and vitrification for single particle analysis 83
3. Negative staining 85
4. TEM observation and image analysis 86
5. Cryo-EM GAT1 WT and L300Q data collection (Regensburg) 86
6. Cryo-EM GAT1 L300Q data collection (Würzburg) 86
7. GAT1 L300Q data processing, initial map and AlphaFold generated structure 87

VI. Electrophysiology methodologies 88
1. Two Electrode Voltage Clamp (TEVC) principle 88
2. Mutant preparation and RNA synthesis 90
3. Oocyte preparation 93
4. RNA Injection in oocytes 94
5. Two Electrode Voltage Clamp measurements 94
   i. Solution preparation 94
   ii. Two Electrode Voltage Clamp set-up 95
   iii. GABA or Betaine dose-response 96
   iv. Sodium dose-response 96
   v. Voltage-jump with variation of sodium concentration 96
6. Data analysis 97
   i. Dose-response 97
      - GABA and Betaine dose-response 97
      - Sodium dose-response 97
   ii. Voltage-Jump 97

VII. Sample preparation for epifluorescence and confocal imaging 98
1. Oocytes fixing and Cryo-Sectioning 98

2. Cyto-immunochemistry on oocytes 98
3. Cyto-immunostaining on HEK for LAT1/CD98 complex localization 99

VIII. Prostatic bone metastases PC-3M study 100
1. Cell culture 100
2. Immunocytochemistry 100
3. Western blot on cell lysate 101

IX. Light microscopy techniques for protein subcellular localization 101
1. Epifluorescence microscopy 101
2. Confocal microscopy 102

Results 103

I. Sample preparation for Protein/Lipid interactions study in GATs 103
1. Test expression of eYFP-rGAT1 WT 103
2. His-FLAG rGAT1 cloning and test expression 104
3. Expression/Purification optimizations for HF-rGAT1 WT 106
   i. Different cell culture conditions 106
   ii. Purification steps modifications 108
   - Wash buffer 108
   - Detergents 109
   - Forward/Reverse purification 110
4. Vitrification and grid type optimization 112
   i. Carbon coated grids 112
   ii. Graphene oxide coated grids 113
5. rGAT1 WT proteoliposome reconstitution 115
6. Biophysical characterization 116
   i. GABA binding assay 116
   ii. Fluorescent-based transport assay 117
7. rGAT1 Enriched extracellular vesicles Expression/Purification 119

II. GABA and betaine transport in GAT1 WT and L300Q, a BGT1-like mutant 123
1. Identification of functional mutants of rGAT1 by TEVC 123
   i. Single mutants 123

ii. Double mutants....125
2. Membrane expression observed by epifluorescence microscopy....126
3. Comparison of rGAT1 WT and L300Q expression....132
4. Impact of Gln300 on GABA and betaine transport....135
5. Sodium coupling and dependency in rGAT1 WT and L300Q for betaine transport....137
6. rGAT1 L300Q goes through structural biology....141
i. Obtention of protein material....141
ii. From micrographs to preliminary EM map....142
7. Structural differences between rGAT1 WT and L300Q....146

III. LAT/CD98 complex: challenges of expression, purification and heterodimer formation for Brasillicardin A drug design....149
1. Heterodimer expression test and recognition by different antibodies on western blot....149
2. Expression conditions optimization in suspension cell culture....150
3. Excess expression of CD98 does not improve heterodimers presence in the membrane....150
4. LAT1 and CD98 expressed as single subunits have unexpected subcellular localizations....157
5. LAT1/CD98 heterodimer purification....161
i. Establishing of initial protocol....161
ii. Challenges and shortcomings....164
- Concentrator flow-through....164
- Column washes....165

iii. Optimized protocol....165

IV. Prostatic bone metastasis: cell target validation for BrasilicardinA and LAT1/CD98 heterodimer paradox167
1. Heterodimer is detected on cell lysate western blot....167
2. Only LAT1 is present at the surface of PC-3M cells....168

Discussion....171

I. Probing GAT1 in a lipid environment: Insights from reconstitution studies....171

II. The Molecular Basis of GABA Transporter Function and Specificity....173
1. Molecular mechanism of GABA binding and transport in GAT1 and the mutant L300Q....173
2. Betaine binding and transport: WT versus L300Q mutant....177

3. From GAT1 WT and GAT1 L300Q to BGT1 mechanisms 181
4. Unraveling GAT1 and BGT1 Specificity: Linking Molecular Mechanism to Cellular Function 182
5. Limitations and outlooks to the mechanisms suggested 184

III. Prostatic bone metastases: invasion mechanism and new pharmacological target of Brasilicardin A 186

IV. SLC6 and SLC7 families: an evolutionary convergence? 189

Conclusions and outlooks 191

- GABA Transporters family 191
- LAT Transporter family 193

Bibliography 196

Introduction

I. Membrane proteins: challenges, diversity, functions, structures and mechanisms

From prokaryotes to eukaryotes, every species is a fascinating biomolecular organization. To be functional proteins require a three-dimensional folding in space determined by the amino acid sequence of the polypeptide chain. More than 50 years ago, structure predications showed that not only the information contained in the amino acid chain contributes to protein folding (Monod 1970). In fact, a polypeptide chain explores a folding landscape constricted also by the close environment and chemicophysical parameters like salinity, the pH, or the temperature. They are considered as epigenetic enrichment and contribute even more to the final stabilized three-dimensional protein structure than the original amino acid chain. This emphasizes that proteins need very specific mechanisms to avoid misfolding and/or inactivity. Structural biology is paramount in understanding protein function because a protein's three-dimensional structure directly dictates its activity. Even with advancements in computational methods like AlphaFold, accurately predicting protein folding in the presence of substrates, ions, activators etc. from its amino acid sequence remains a significant challenge due to the immense number of possible conformations a polypeptide chain can adopt. Therefore, experimentally determining these intricate structures through the well-established techniques (X-ray crystallography, cryo-electron microscopy, NMR spectroscopy) provides indispensable atomic-level insights into how proteins interact with other molecules, catalyze reactions, and perform their diverse biological roles. This direct structural information is crucial for rational drug design, understanding disease mechanisms, and advancing biotechnology.

Membrane proteins pose an even greater challenge than soluble proteins due to their unique and the complex phospholipidic environment they are embedded in. Studying them at the molecular level requires their extraction and stabilization in artificial membrane mimics (detergents, nanodiscs, liposomes) a process that often destabilize or alter their native conformation. Moreover, they are often low expression levels in heterologous systems for further purification, and their hydrophobic surfaces, inherent flexibility, are the primary bottleneck for crystallization and

structure determination by X-ray diffraction. In this context, cryo-electron microscopy (cryo-EM) has emerged as a revolutionary technique for membrane protein structural determination.

1. Plasma membrane: structure, composition and exchange surface

A plasma membrane is complex proteo-lipidic bilayer (Figure 1). It contains dominantly different phospholipid (PL) types, distinguishable by their aliphatic chain esterified on the glycerol molecule at the position *sn*-1 and *sn*-2 (Ingólfsson et al. 2017), but also Sphingolipids, Glycolipids and sterols. More precisely, monounsaturated or unsaturated fatty acids like stearic acid (18:0) or palmitic acid (16:0) are localized in position *sn*-1, while mono and poly-unsaturated lipids are found in position *sn*-2 (Choi et al. 2018; Farooqui, Horrocks, and Farooqui 2000).

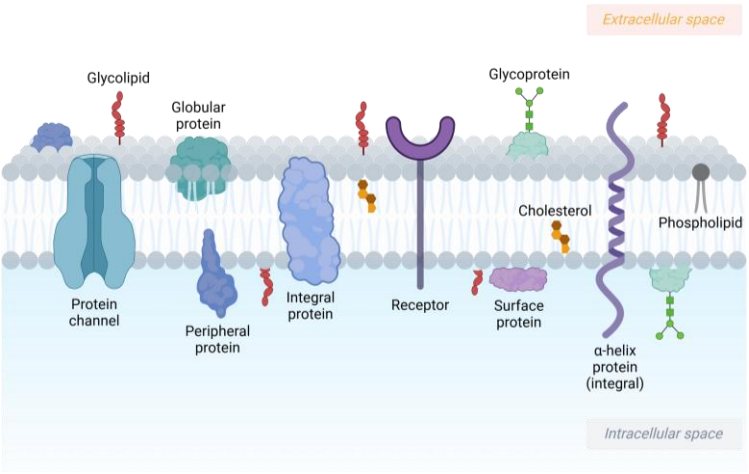

Figure 1: Plasma membrane complexity. Beside lipids and sphingolipids, it is enriched in various proteins, glycoproteins and glycolipids (figure created on Biorender.com).

The polar head of PL is constituted of a phosphate group at the position *sn*-3 of the glycerol molecule associated with charged or zwitterionic metabolites. The most common polar head groups in eukaryotic membranes (Figure 2) are the zwitterionic phosphatidylcholine (PC), phosphatidylethanolamine (PE) in both inner and outer leaflets, while the anionic phosphatidylinositol (PI) and phosphatidylserine (PS) are localized nearly exclusively in the inner leaflet (Jayaraman et al. 2021; Ingólfsson et al. 2017; Van Meer, Voelker, and Feigenson 2008; Farooqui, Horrocks, and Farooqui 2000).

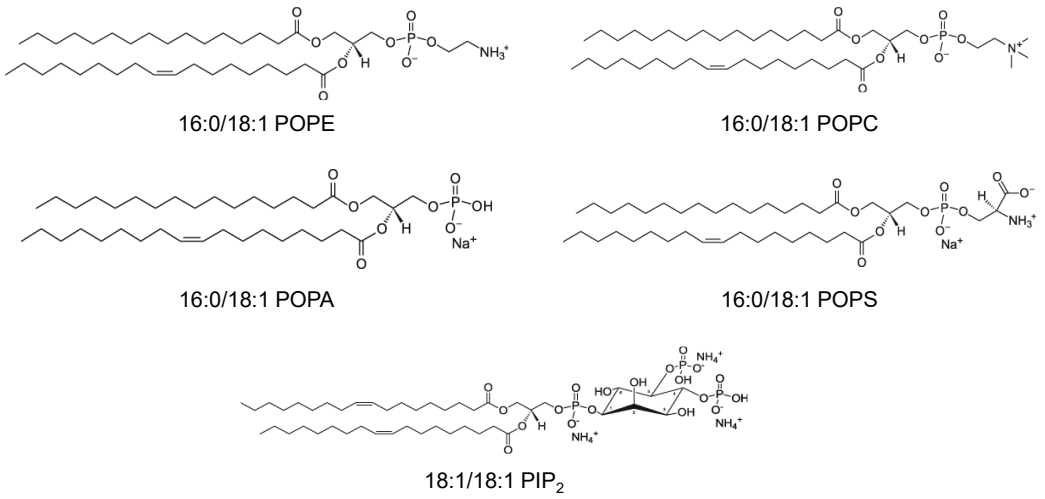

Figure 2: Polar heads and aliphatic chains (with length and unsaturation) of the most common phospholipids found in plasma membrane (PO: palmityl-oleoyl aliphatic chains).

Phospholipids assemble each other to form a bilayer, and each type of phospholipid is distributed asymmetrically between the inner and outer leaflets. This repartition counterbalances the difference of charges and enhances the overall stability of the plasma membranes (Ingólfsson et al. 2017). Moreover, it plays a role in cell signaling like initiation of phagocytosis or blood coagulation (Van Meer, Voelker, and Feigenson 2008). A disorganization or an imbalance of the PLs in the plasma membrane is linked to a large variety of pathological disorders like neurological diseases, heart, lung or kidney failures (Harayama and Riezman 2018; Ingólfsson et al. 2017; Farooqui, Horrocks, and Farooqui 2000).

Lipid composition of plasma membrane differs according to the type of membrane. At the subcellular scale, the reticulum endoplasmic membrane does not contain PIP_2 and has low level of cholesterol (Jayaraman et al. 2021; Harayama and Riezman 2018; Van Meer, Voelker, and Feigenson 2008). At the tissue scale, neuronal cells contain more cholesterol and unsaturated acetyl chains compared to liver, kidney or heart cells (Choi et al. 2018; Ingólfsson et al. 2017). The heterogenous organization of each phospholipid can result in membrane microdomains (Figure 3).

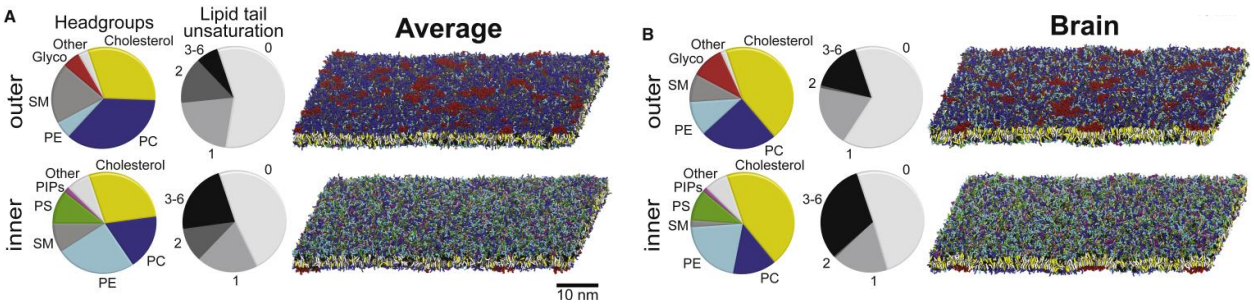

Figure 3: Computational lipidomics of phospholipid composition, unsaturation and repartition according the inner and the outer leaflets. a) Standard and b) neuronal plasma membrane (Ingólfsson et al. 2017).

It has a consequence on the other component of the membrane, especially proteins for their recruitment and precise localization. Phospholipids have a crucial role in the stabilization and conformation of a particular type of proteins that have evolved together with the apparition of the plasma membrane: the transmembrane proteins. Indeed, internalizing external stimuli becomes challenging by the presence of physical barriers. Therefore, membrane proteins appeared to promote cell homeostasis and allow communication with the extracellular space.

2. Membrane Proteins are communicative biomolecules

Membrane proteins can be classified into two groups: (i) The anchor membrane proteins, with an intracellular and one membrane domain, and (ii) the integral transmembrane proteins with an intracellular, a transmembrane and an extracellular (glycosylated or not) domain. The number of transmembrane domains, so called transmembrane helices (TMs) is proteo-dependent. There are three subclasses of integral membrane proteins: receptors, channels, and transporters. Receptors typically bind to a specific ligand, such as a hormone or neurotransmitter, on one side of the membrane. This binding event triggers a conformational change that initiates a signaling cascade inside the cell without directly transporting molecules across the membrane.

Channels form a pore through the membrane, allowing for the rapid and selective passage of specific ions or molecules down their electrochemical gradient. They are often gated, meaning they open or close in response to a stimulus like voltage change or ligand binding.

Transporters are distinguished between carriers and pumps. They bind to a molecule and undergo a conformational change to move it across the membrane. This process is generally slower than

channel transport and can be either passive (facilitated diffusion) or active, requiring energy in form of ATP or electrochemical gradients to move molecules against their concentration gradient.

i. Receptors

They sense stimuli from the extracellular space and integrate the following signal in the intracellular space to induce physiological responses like cell like motility, excitability, division or growth, and response to oxidative stress. G-protein coupled receptors (G-PCR) ubiquitously found on mammalian cells, are commonly dimers with seven transmembrane helices. They are subdivided in four families (A, B, C, and F) according to their amino acid sequences and their physiological functions (Yang et al. 2021). Various ligands like odors, hormones, neurotransmitters, chemokine but also photons interact with them, following the activation of secondary messengers like cyclic adenosine 3,5-monophosphate (cAMP) release, or inducing different responses like calcium mobilization or kinase phosphorylation. It initiates then a cascade of reactions in the intracellular space to regulate neurotransmission, immune or endocrine systems (Yang et al. 2021). Aside from G-PCRs, Cluster of differentiations (CD) are type-II glycosylated membrane protein, i.e. integral membrane protein with the N-terminus in the intracellular space, and the C-terminus facing the extracellular space. They are widely present on immune cells but also on dendritic, stem, epithelial, endothelial cells, platelets, or erythrocytes. They have diverse structural function like cellular adhesion (CD34), apoptosis (CD51) (Curse, Lewis, and Wang 2004) or endocytosis (CD98) (C. Zhang et al. 2023).

ii. Channels

In most cases, channels are an oligomeric assembly where each subunit contains pore forming transmembrane helices and often a selective filter acting as an entrance portal. Channels facilitate the diffusion of ions (Na^+, Cl^-, Ca^{2+}, K^+), or small charged molecules, in the direction of their respective concentration gradient. Open and closing of channels are tightly regulated. For example, the opening of the voltage gated ion channels is governed by membrane potential. Some channels are ligand gated like the $GABA_A$ receptors in post-synaptic neurons. They are pentameric proteins composed of combinations of different subunits (α1–6, β1–3, γ1–3, δ, ε, π, ρ1–3 and θ) (Sente et

al. 2022; Terunuma 2018; Sigel and Steinmann 2012). The combination of the different subunits depends on cellular localization and the function. Recently non canonical subunit assemblies in the extra-synaptic regions were discovered, allowing diverse molecular mechanisms (Sente et al. 2022). After release of GABA by the pre-synaptic neurons, its binding to the $GABA_A$ channels induces the conduction of chloride ions through the protein to hyperpolarize the post synaptic neuron, inhibiting consecutive neuronal communication. This activity can be regulated allosterically by benzodiazepine agonists or histamine (Sente et al. 2022; Sigel and Steinmann 2012). Interestingly, channels are not exclusively stimulated by chemical ligands but also physical stimulations like membrane tension in the case of the small conductance mechanosensitive channels (MscS) in bacteria. In an evolved form in Eucharia, the Piezo ion channels, research rewarded by the Nobel prize for physiology in 2021, are activated by an external physical stimulus, like touch, pain, and proprioception that induces nonselective cation permeation and later on, cognitive reactions by vertebrates (Martinac 2022).

iii. Transporters

Unlike channel proteins, which form open pores, pumps and carriers operate more like a revolving door, sequentially exposing their binding sites to one side of the membrane and then the other.

- *ATP activated pumps and primary active transporters*

In this case, energy for translocating substrate requires the hydrolysis of adenosine triphosphate (ATP). ATP binding cassette (ABC) transporters uptake their substrates in the direction of their chemical gradient and downhill, i.e. to the intracellular space. Contrastingly, the Na^+/K^+ pumps export sodium in extracellular space and import potassium in the cytoplasm against their respective concentration gradients.

- *Secondary Transporters*

Contrastingly to the primary transporters, they catalyze the substrate translocation energized by the existing electrochemical gradient. Secondary transport is often termed "coupled" because the movement of two or more different solutes is obligatorily linked. The term “solute” describes the substrate, i.e. the molecule to transported, and the co-substrate, bringing the energy required for

the transporter that is generally ion (Na^+, K^+, Cl^-). The uniporters transport only one substrate (in blue, Figure 4A). Those that are transporting two substrates in the opposite direction, like the sodium-calcium exchanger, are antiporters (in yellow, Figure 7A) and in the same direction, like the sodium-glucose cotransporter SGLT1, are symporters (red, Figure 7A).

3. Secondary transporters folding families

Membrane proteins with a transporting activity or supporting a transporting activity are called solute carriers (SLCs) and are organized in 66 different classes (Ferrada and Superti-Furga 2022), according to their cellular localization, the substrate transported, their accessory role, their molecular mechanism and their typical folding (L. He, Vasiliou, and Nebert 2009). According the latest evolutionary-based classification, SLCs are distributed in 24 different fold types (Ferrada and Superti-Furga 2022). However, four principal folds are largely studied: LeuT, MFS, GltPh and NhaA-folds (Ponzoni et al. 2018). Each characteristic fold is represented on the Figure 4.

i. LeuT-fold

This fold is highly conserved in numerous transporter families and its name originates from the Leucine transporter from *Aquifex aeolicus* ($LeuT_{Aa}$), which was the first structure of this specific fold determined in 2005. LeuT and the hydrophobic amino acid transporter MhsT from *Bacillus halodurans* are the bacterial homologs of the neurotransmitter sodium symporter family (NSS). Mammalian homologues belong to the SLC6 family. Bacterial or mammalian members are dominately sodium dependent transporters with a general stoichiometry of 1 Substrate:1-3 Na^+. The SLC6 family is notably represented by the γ- aminobutyric acid, i.e. GABA (GATs), the glycine (GLYTs) the serotonin (SERT), the dopamine (DAT) and the noradrenaline (NERT) transporters. LeuT and the NSS share 25% of sequence identity, but their common fold and the amino acids involved in sodium binding, substrate recognition and translocation were conserved along evolution (Yamashita et al. 2005). LeuT is 12- transmembrane helices transporter organized in two pseudo-symmetric inverted repeats of 5 TMs each (Figure 4). Two supplementary TMs are present at the C-terminal domain (TM11 and 12) and correspond to C-terminal hairpins, like in the Amino Acid-Polyamine-Organocation Family (APC), from which the LeuT fold is originating (Västermark and

Saier 2014). LeuT provided first insights into the rocking bundle mechanism (explained in the following part) highly conserved in the NSS family.

ii. GltPh-fold

GltPh is the archaeal aspartate transporter from *Pyrococcus horikoshii* and is the bacterial homolog of the glutamate transporters involved in animal neurotransmission (SLC1 family). Study of GltPh elucidated the elevator mechanism (also detailed in the next part). Its fold is constituted of 4 repeats with 3 TMs in each. In two repeats TMs are replaced by short hairpins helices (Figure 4).

iii. NhaA-fold

NhaA is a sodium/proton (Na^+/H^+) antiporter from *Escherichia coli* and is a general model for the SLC9 proton antiporters family. NhaA and SLC9 share also the elevator mechanism but contrastingly to GltPh, NhaA fold has only two repeats comprising each 5 TMs (Figure 4).

iv. MFS-fold

The human glucose transporters (GLUTs) belong to the Major Facilitator Superfamily (MFS). They are transporters with 4 repeats with 3 TMS in each (Figure 4).

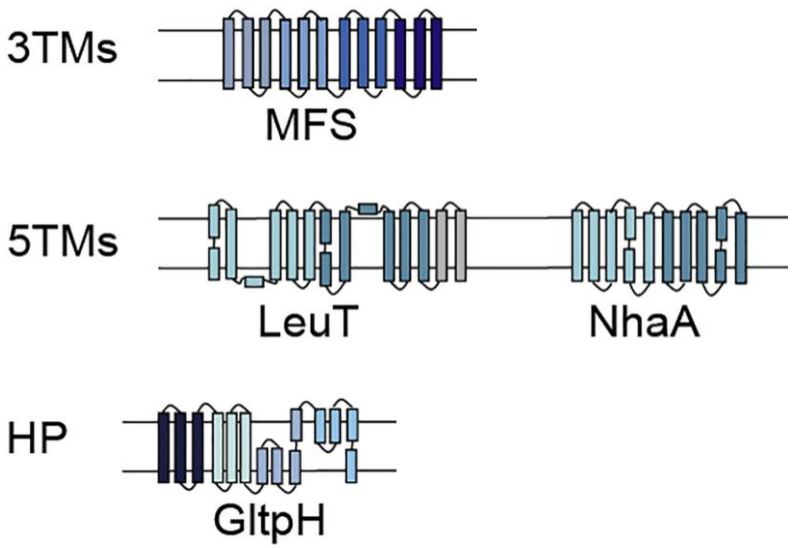

Figure 4: Characteristic LeuT, MFS, GltPh and NhaA-folds. TMs part of the same repeat unit have the same color. MFS is a 4 repeats fold with 3 TMs in each repeat. LeuT and NhaA are two pseudo-symmetric inverted repeats with 5 TMs in each repeat. LeuT spans two more TMs out of any repeat. GltPh is a 4 repeats fold with 3 TMs in each repeat; in two repeats, there is a pair of half TM hairpins (HP on the figure) (Figure modified from Xie et al. 2022).

This dissertation will focus on LeuT folded proteins and their close fold and mechanistic relation to another family, the so-called Betaine-Carnitine-Choline transporters (BCCTs). They are represented by the well-studied BetP from *Corynebacterium glutamicum*, a strict betaine-sodium coupled transporter (Ziegler, Bremer, and Krämer 2010; Krämer 2009; Krämer and Ziegler 2009). To compare different proteins from different families within the same fold, the TM nomenclature is A1, 2, 3, 4, 5 for the first repeat and B1, 2, 3, 4, 5 for the second repeat. The 5 TMs are represented with the letters I-U-V in the first repeat and I-Ω-Λ in the second, to illustrate the inverted helices in this repeat (Figure 5).

Compared to AdiC or LeuT, BetP exhibits a shift in the transmembrane helix numeration (Figure 5). This is due to a duplication at the N- terminal and a loss of the C-terminal hairpin along evolution (Västermark and Saier 2014). Structure alignment across families (APC-NSS-BCCT) shows that RMSDs may exceed 6.5 Å (Ponzoni et al. 2018), therefore, it exits structural differences inter-families.

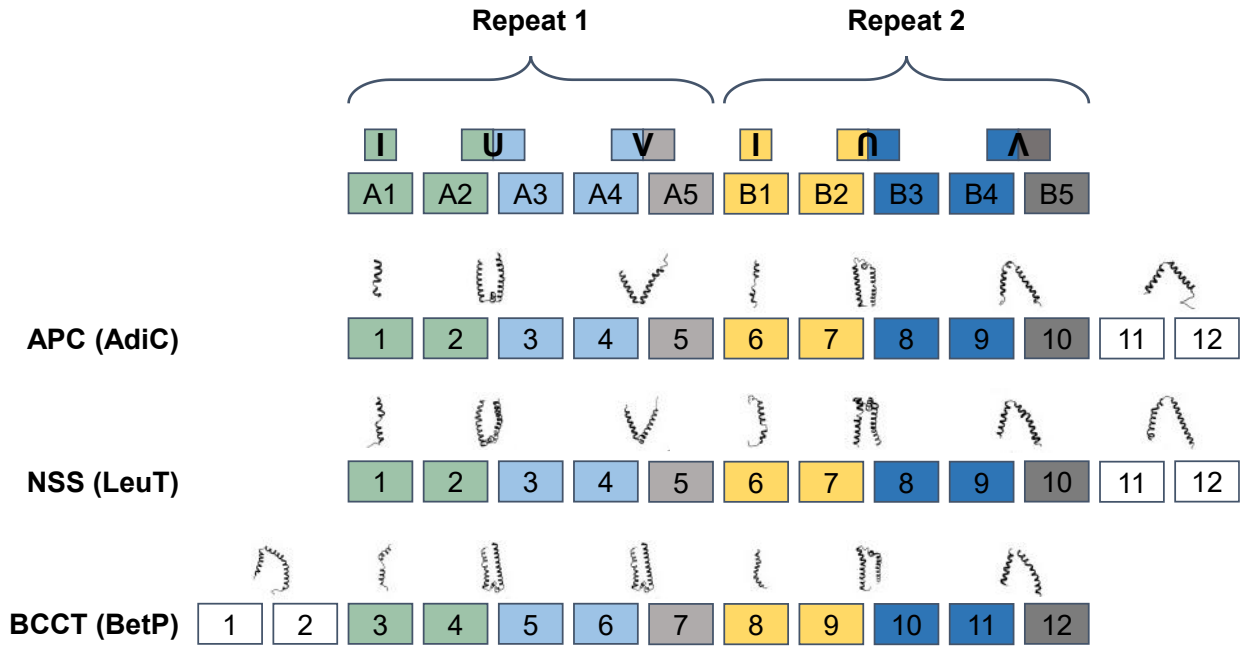

Figure 5: Repeats and transmembrane domains alignment with the corresponding α-helices foldings for the APC, NSS, and BCCT families (modified from Västermark and Saier 2014 and Khafizov et al. 2012)

However, on the standard nomenclature (Figure 5), the helices A1 and B1 of two model proteins LeuT and BetP are both broken halfway to the plasma membrane. This can also be seen on the detail fold of both proteins in Figure 7. This is a major common feature that creates a dipolar moment for facilitating the binding of sodium and the respective substrate together with TMs movement for their translocation (Yamashita et al. 2005) (Figure 6).

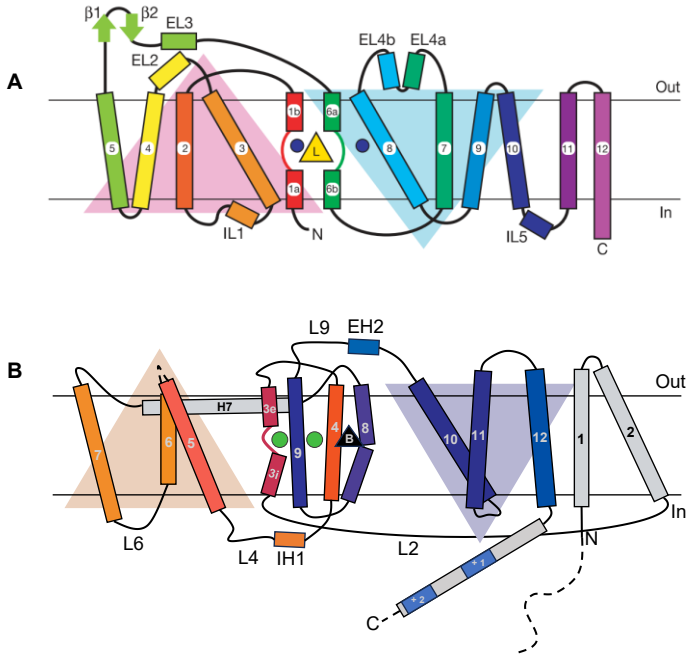

Figure 6: Detailed folds of a) LeuT bacterial homolog of the NSS family (from Yamashita *et al.,* 2005) and b) BetP from the BCCT family.

4. General and individual mechanism of secondary transporters

i. Alternating access model

The alternating access mechanism is a fundamental mechanism by which carrier and pumps facilitate a transport cycle in which a substrate is bound, transported, and released and the transporter is back to a state to redo the cycle again. This cycle of conformational changes within the protein, generally called outward facing/occluded/inward facing, ensures that the substrate binding site is never simultaneously open to both sides of the membrane. This prevents uncontrolled leakage of solutes and loss of electrochemical gradients. In outward-facing conformation, the substrate binding site is accessible from the extracellular space. A specific substrate molecule and the coupling ions, in the case of secondary active transporters, bind to this exposed site. Upon substrate binding, the protein undergoes a conformational change avoiding access from the initial side, and intracellular environment, trapping the protein within an occluded state. Further conformational changes are necessary to open the binding site to the intracellular space for releasing substrate and ions; the protein is then in inward facing state (Figure 7B). Such

a sequentially gated access mechanism ensures directional transport. To fulfil its function, the protein reverts to its initial outward-facing conformation, for another cycle of substrate transport. For antiporter systems, this step may involve the binding of ions, protons or other substrates like amino acids while for symporters, this step is known to be limiting, and the main actor is still not clear (Malinauskaite et al. 2016; Zomot et al. 2007).

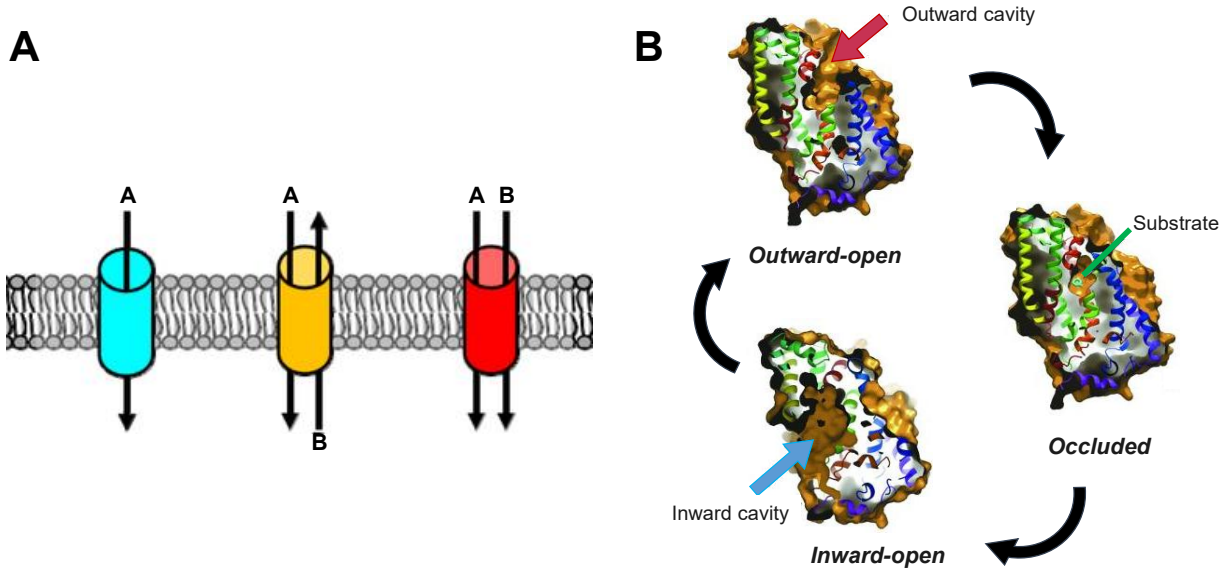

Figure 7: Secondary transporters at a glance. a) Scheme of a uniporter (blue), antiporter (yellow) and symporter (red) (modified from Almasi and El Hiani 2020) and b) Representation of the alternating access model (modified from Weyand et al. 2011).

ii. Different folds, same mechanisms/different folds, different mechanisms

While the alternating access mechanism provides a general framework for transporters function, the molecular details of how single protein, according to their fold presented before, achieves these conformational changes vary significantly.

- *Rocking bundle mechanism*

It is the most widely observed and is found in LeuT/NSS, BetP/BCCT and the Major Facilitator Superfamily (MFS) although their respective folds are different and have respectively inverted and symmetric repeats (Xie et al. 2022). In this model, the transporter consists of two domains so called bundles that symmetrically tilt against each other in a scissor like fashion around a central axis. Local amino acid interactions are gating access to cell interior/exterior, i.e. blocking or unlocking

the pathway through the cytoplasm or the extracellular space. Local noncovalent bonds rearrangements govern further global conformational changes of the transmembrane helices, inducing motions that alternatively expose the binding site to the extra or intracellular space.

- *Elevator mechanism*

First described for the glutamate transporter homolog GltPh (a member of the SLC1 family), it is a mechanism also shared by the proton antiporter NhaA in *E. coli*. It involves a motile transport domain and a static scaffold domain. Instead of tilting, the transport domain literally slides along the scaffold domain. The substrate binding site is located on this moving domain, so it is physically carried from one side of the bilayer to the other. This leads to a larger displacement of the substrate binding site across the membrane compared to the rocking-bundle model.

The diversity of these mechanisms highlights how different transporter families have unique structural solutions to achieve the fundamental alternating access principle, adapting their movements to the specific requirements of their substrates and the energy source used for transport.

II. Study I: Molecular mechanism evolution of the GABA transporter family

1. GABA Transporters are part of the SLC6 family

The SLC6 family transports a broad range of substrates: biogenic monoamines (serotonin, dopamine, and norepinephrine) modified amino acid (GABA, creatine) neutral amino acids (glycine) but also branched (alanine) and cationic amino acids, but also taurine, creatine and betaine. Except for biogenic amines, these substrates are considered as osmolytes and are widely explained later.

i. Co-substrate and sequential binding event

Typically, these transporters possess two sodium ion binding sites, designated Na1 and Na2, along with a substrate binding site known as S1 central binding site. An additional chloride ion (Cl^-) is required for the charge balance and the conformational changes from outward to inward-open state (Zomot et al. 2007). The ions, considered as co-substrates have a strict stoichiometry 2 Na^+: 1 Cl^- per substrate molecule for most of SLC6. Their electrochemical gradient driven energy ensures the intracellular accumulation of

substrate. It remains unclear whether both sodium ions bind simultaneously or if the substrate binds in between. It is also discussed if the sodium binds first in the Na1 (Malinauskaite et al. 2016; Zomot, Gur, and Bahar 2015) or Na2 (Noskov and Roux 2008). In bacterial NSS, in the BCCTs, and Nucleobase-Cation Symport 1 (NCS1) families, sodium ions stabilize the outward open states of transporters and sodium ion binding was described as the first step before substrate binding(Malinauskaite et al. 2014; Perez, Khafizov, et al. 2011; Weyand et al. 2011). Moreover, studies on GABA transporters showed no transport activity of GABA in the absence of sodium (Meinild and Forster 2012; Mari et al. 2006; Matskevitch et al. 1999). Therefore, ion-substrate coupling transport is a highly coordinated process essential for driving the uphill transport of the SLC6 substrate binding sites.

ii. Role of Na1 and Na2 sodium binding sites in conformational cycling

The Na2 sodium ion site acts on the transition from an occluded to an inward-open state. Structural studies on LeuT and MhsT showed that in the inward-occluded state, TM5, surrounding the amino acids coordinating sodium ions in the Na2 site (Figure 8. I), becomes unwinding and induces the hydration of Na2 (Figure 8. II). The weak interactions with the latter facilitates the liberation of sodium from the Na2 site (Stolzenberg et al. 2017; Malinauskaite et al. 2014). The release of Na2 triggers a significant shift in TM1 (Figure 8. III). Together with coordinated movements in other helices, particularly TM8, these movements propagate through the protein, driving the transition to the inward-open state. This new conformation allows the subsequent release of the substrate and the remaining sodium ion (in Na1) into the cytoplasm.

The evolutionary conservation of specific amino acid residues in the transmembrane helices 1 and 8 (TM1 and TM8) of the LeuT and BCCT fold families is explained by their critical role in coordinating sodium at the Na2 site. This sodium coordination is essential for the conformational transitions and helix movements that are indispensable for the transporter's function.

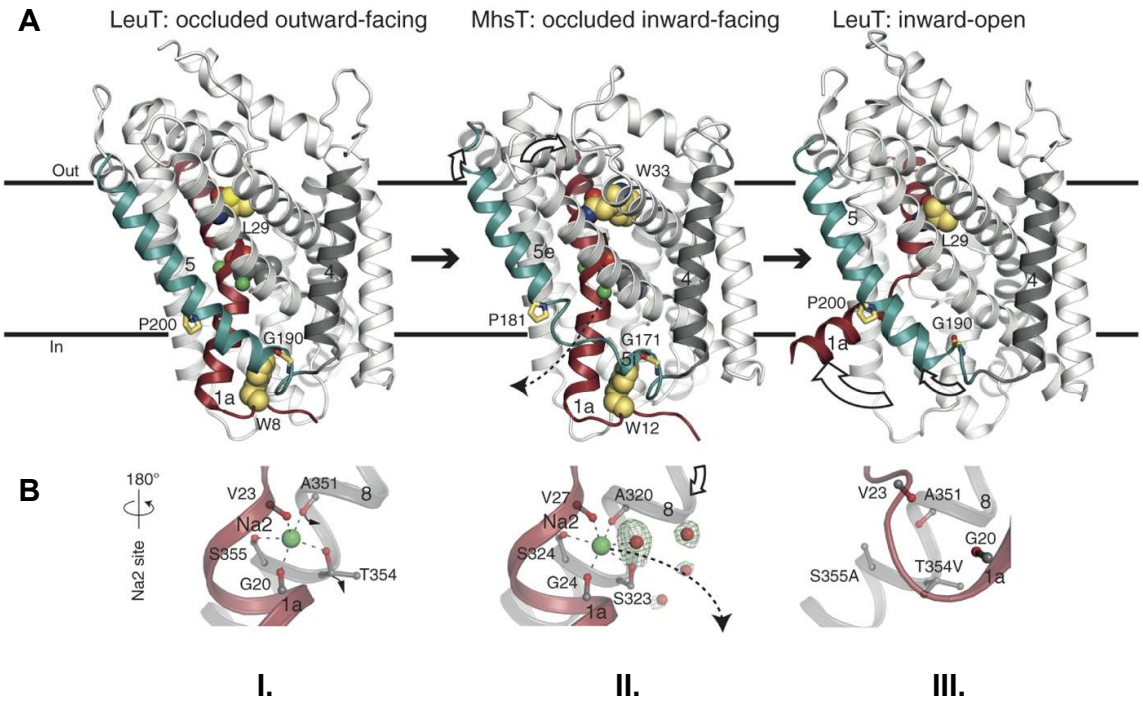

Figure 8: Model of the transition from occluded to inward-open state a) Ribbon representation of the whole proteins and b) Close-up on the Na2 sodium binding site (figure from Malinauskaite et al. 2014). (I) The folded TM5 (blue grey) unwinds (II) to break the sodium ion coordination following the hydration of the Na2 site. (III) The liberation of the ion allows TM1 (dark red) to also unwind and to shift to the left to create the inner cavity

The Na1 sodium site is only conserved within the NSS family (bacterial/eukaryotic homologs) and is coordinated octahedrally with residues of Alanine and/or Isoleucine, Asparagine, Serine and/or threonine, and with the substrate itself (Zhu et al. 2023; Yamashita et al. 2005). For example, in the GABA transporter 1 (GAT1), one of the oxygens of the GABA carboxylate group directly interacts with the sodium in Na1 (Zhu et al. 2023). However, Na1 is poorly conserved across the different transporter families. In the Nucleobase-Cation Symport 1 family, Na1 site in Mhp1 from Microbacterium liquefaciens is even absent (Khafizov et al. 2012; Perez et al. 2012; Weyand et al. 2011). In BetP, an alternative Na1´site was identified comprising four residues: T246, T250, S376, F380 and was not involving the substrate (Khafizov et al. 2012). The Figure 9 shows the alignment of the latter residues with NSS sequences according the standard nomenclature of the TMs.

	Na1' site (BetP)				Na1 site (NSS)				Na2 site (NSS)					
	A3		B1		A1		B1	B2	A1			B3		
$BetP_{Cg}$	T246	T250	S376	F380					A147	.	M150	F464	T467	S468
$LeuT_{Aa}$	P101	A105	S256	A261	A22	N27	T254	N286	**A17**	G20	V23	A351	T354	S355
$GAT1_{Hs}$	S133	N137	G297	S302	A61	N66	S295	N327	**S56**	G59	I62	L392	D395	S396
$BGT1_{Hs}$	E126	N130	A296	C301	I53	N58	S294	N326	**S48**	G51	I54	L391	D394	S395
$GlyT1_{Hs}$	S135	G139	G325	G330	A63	N68	S323	N355	**T58**	G61	V64	L420	G423	T424
$GlyT2_{Hs}$	S280	A284	S479	G484	A208	N213	S447	N509	**S203**	G206	V209	L574	D577	T578
DAT_{Hs}	S149	G153	G323	V328	A77	N82	S321	N353	**S72**	G75	V78	L418	D421	S422
$SERT1_{Hs}$	A169	A173	G338	V343	A96	N101	S336	N368	**S91**	G94	V97	L434	D437	S438

Figure 9: Residues alignment from different mammalian NSS, LeuT and BetP involving in the respective sodium binding sites. Their respective helices are numbered according to the standard nomenclature explained Figure 5. Residues in black are the effective residues involved in the Na1', Na1 and 2 sites. NSS/LeuT residues in grey correspond to BetP Na1'. Residues in orange show a one amino acid shift between BetP and NSS and are not involved in the Na2.

2. Osmolytes and Neurotransmitters are the substrates of SLC6 family

Osmolytes and neurotransmitters are both substrates of SLC6 family. Osmolytes are categorized in electrolytes (ions in solution like Na^+, K^+, Cl^-), present in high concentrations in the cell cytoplasm or extracellular fluids, and in small organic molecules (Pasantes-Morales and Cruz-Rangel 2010). They have heterogenous structures and are distinguished as (i) amino acids and derivates (glutamate, glycine, taurine, GABA, N-acetyl aspartate), polyalcohols (*myo*-inositol and sorbitol) and (ii) methylammonium solutes (glycerophosphorylcholine, betaine, (Phospho)-creatine) (Figure 10). Aside the osmoprotective properties of organic osmolytes, some of them , e.g., betaine act as folding agents and can stabilize protein structures by many inter- and intra-macromolecular interactions involving non-covalent bonds (Yancey and Somero 1979). Methylammonium solutes are also called "counteracting solutes" because they protect macromolecules in presence of denaturing agents like urea. However, in absence of the latter, they become perturbing solutes (Yancey and Somero 1979). In contrast, amino acids, their derivates, and polyalcohols are "non-perturbing" or "compatible" solutes, meaning that they do not disturb protein function or structure at high concentrations (Yancey and Somero 1979). Counteracting and compatible solutes are accumulated in the cytoplasm or release in the extracellular space during osmotic fluctuations. They result from electrolyte concentration imbalances that are common in external environments

like soils, in physiological conditions like glomerular filtration in kidney, or pathologic situations like ischemic strokes, brain and spinal cord trauma (Sheng et al. 2021; Pasantes-Morales and Cruz-Rangel 2010). During osmotic stress, the accumulation of betaine can reach 1 M in bacterial cells. In the animal kidney medulla, the hypertonicity can reach 1000-1200 mosmol/kg (Kempson, Zhou, and Danbolt 2014). To adapt to these conditions, kidney cells also accumulate betaine or glycerophosphorylcholine, where the main role is to counteract urea (Burg, Kwon, and Peters 1996).

In animal central nervous systems (CNS), GABA, glutamate and glycine are also neurotransmitters (NTs) i.e. signalling molecules released and integrated by neurons for generating motor or cognitive actions. The CNS is segregated into excitation (Glutaminergic neurons), and inhibition (GABAergic neurons) systems. Neurotransmitter-like osmolytes have the same cellular homeostasis function as any other organic osmolytes, thus their cytoplasm concentrations could be regulated by unspecified transporters after osmotic stress stimulation. However, NTs efflux against hypoosmotic conditions in the brain would create repetitive imbalances between cerebral excitation and inhibition (E/I). The CNS would be constantly dysregulated and could not complete its physiological roles. Consequently, it requires transporters dedicated to one specific role, i.e. neurotransmission or osmoregulation. Indeed, the osmolyte taurine maintains neuronal cells homeostasis (Pasantes-Morales and Cruz-Rangel 2010). Paradoxically, the Betaine/GABA transporter 1 (BGT1) transports either methylammonium solute (betaine) or NTs. This suggests a versatile role of this transporter, i.e. osmotic stress and neurotransmission, and therefore a tight control of their activity to avoid E/I imbalances. This will be explained in the next two parts.

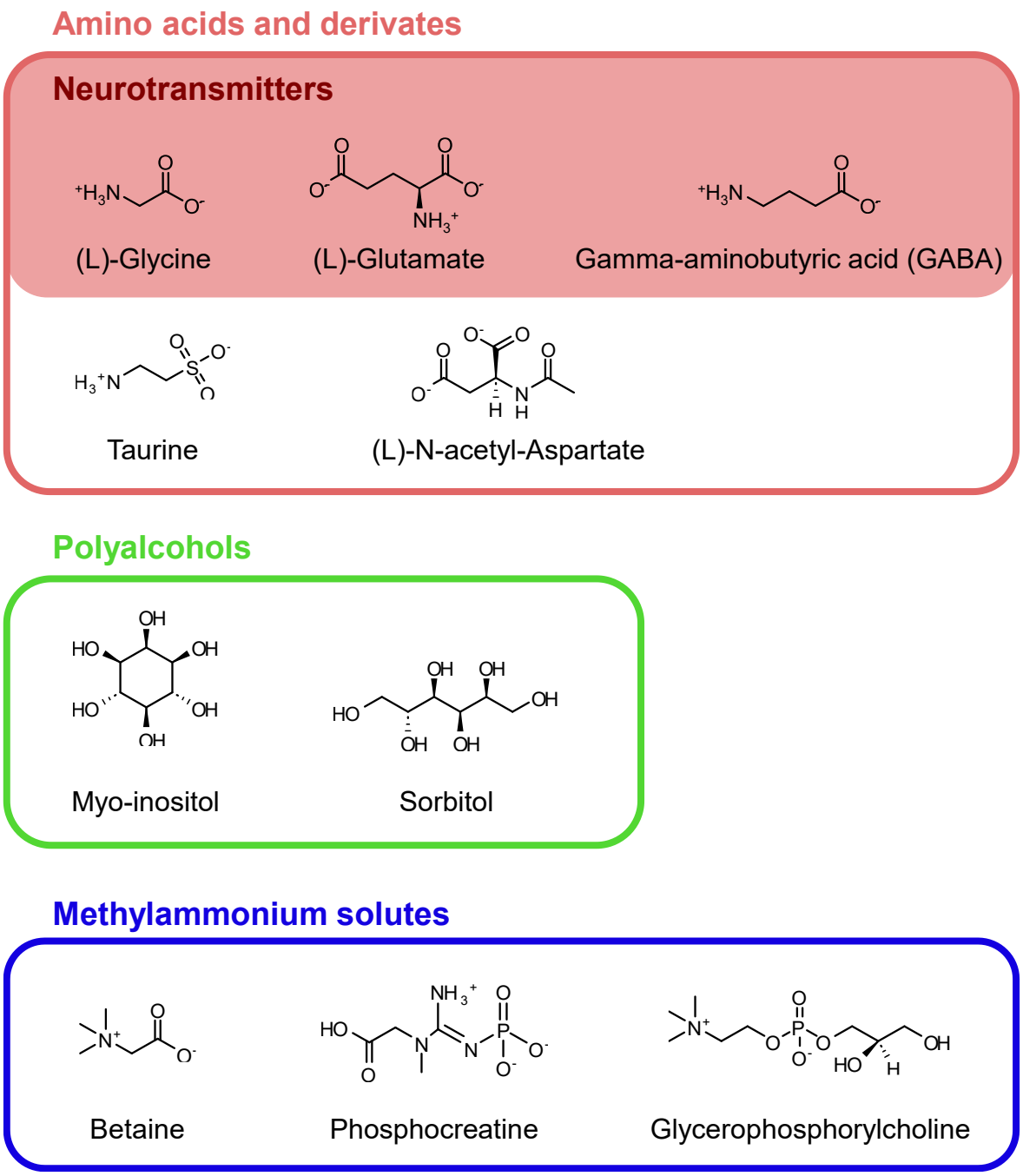

Figure 10: Osmolyte classes.

3. GABA Transporters (GATs) family

i. Role and function in the central nervous system

This sub-family of NSS counts four members that from a general point of view have a role in synaptic clearance in the GABAergic neuronal systems. They re-absorb extracellular GABA in the pre-

synaptic neurons or astrocytes (Figure 11B) to avoid an over inhibition due to an extend exposition of GABA on the post synaptic neuron receptors. GABAergic neuronal network is widely distributed in the brain and makes projections throughout diverse structure like amygdala, hippocampus, hypothalamus, prefrontal cortex, olfactory bulb, retina and the spinal cord (Figure 11A). GABAergic neurons regulate primordial functions such as motor control, sleep, or mood (Ochoa-de La Paz et al. 2021). Dysfunctions of GABAergic system or imbalance with the glutaminergic system is associated with diverse neuronal pathologies notably epilepsy (Nevitt, Marson, and Tudur Smith 2018; Ibrahim, Rutka, and Snead 2014; Lehre et al. 2011; Schmidt and Löscher 2005; Ängehagen et al. 2003; Storici et al. 1999; De Biase et al. 1991), alcoholism, sleep and psychological disorders (Ochoa-de La Paz et al. 2021). Being strategically localized on pre-synaptic neurons, the main regulator of external GABA concentrations is GAT1 (SLC6A1) followed by GAT3 (SLC6A11), mostly found on peripherical astrocytes (Ortega and Schousboe 2017). GAT2 (SLC6A13) is barely present in the human brain and BGT1, Betaine/GABA transporter 1 (SLC6A12) has a low impact on GABA transport (Kickinger et al. 2019; Kempson, Zhou, and Danbolt 2014).

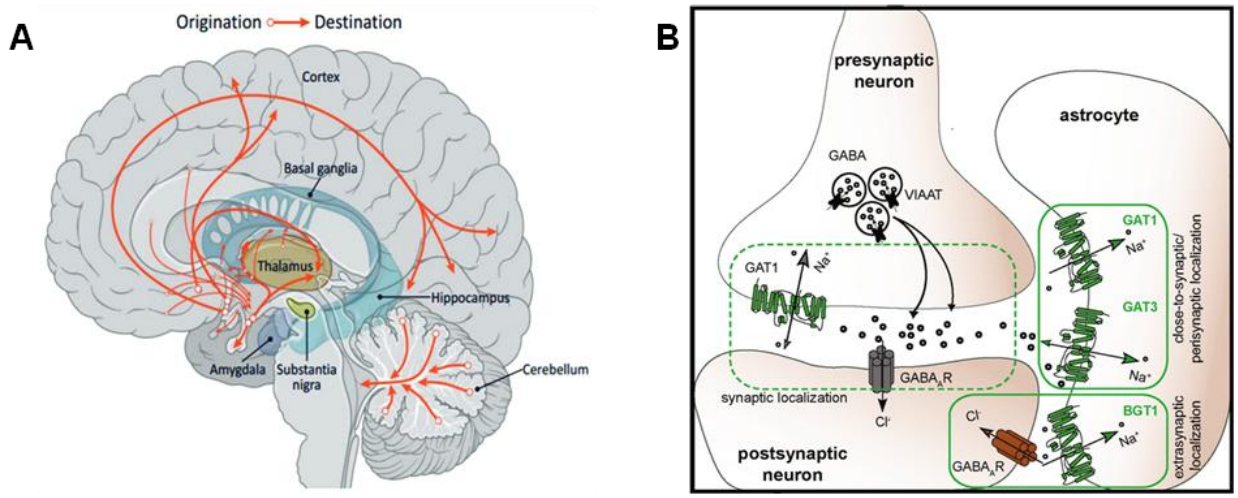

Figure 11: GABAergic system in the human brain. a) GABA projections through the diverse structures of the central nervous system in the brain (from Ochoa-de La Paz et al. 2021). b) Schematic representation of a GABA neuronal synapse (from Ortega and Schousboe 2017). GABA is loaded in vesicles thanks to a vesicular amino acid transporter (VIAAT, SLC32A1). After fusion with the membrane, GABA is released in the synapse and activates the $GABA_A$ receptors that are chloride channels. This ion influx enhances the hyperpolarization of the membrane and results in a post neuronal inhibition. To avoid an extended inhibition, GAT1, in the synaptic and peri-synaptic region, with GAT3, catalyse both reuptake of GABA

with 2 sodium ions (Na^+) and one chloride ion (not represented). BGT1 localized in the extra-synaptic region contributes only as “back-up” GABA transporter (Kickinger et al. 2019; Ortega and Schousboe 2017; Schousboe et al. 2004)

The GAT family members share over 50% sequence identity (black highlighted residues on their sequence alignment in Figure 12). The residues involved in ion binding (sodium and chloride), and the inner and outer gates are highly conserved within the family. They all possess a large glycosylated extracellular loop (EL2) that is known to be crucial for exporting the GATs to the plasma membrane (Schweikhard et al. 2015; G. Cai et al. 2005). Moreover, the last sialic acid of the oligosaccharide chain is essential for modulating the sodium affinity of the transporters (J. Hu et al. 2011; G. Cai et al. 2005). Mainly, the studies on GATs were made on GAT1 after the successful cloning of the rat homolog (Guastella et al. 1990). Before the publication of the first structure in 2022, numerous site directed mutagenesis, combined with uptake assays or electrophysiology experiments elucidated the transport mechanisms of GAT homologues and identified the key residues or TMs involved in the general topology (E. R. Bennett and Kanner 1997; Clark 1997; Kanner et al. 1994), conformational changes (Zomot and Kanner 2003; E. R. Bennett, Su, and Kanner 2000; Keshet et al. 1995), sodium binding (Meinild and Forster 2012; Mari et al. 2006; Yonggang Zhou, Zomot, and Kanner 2006; Zomot and Kanner 2003; Grossman and Nelson 2002; MacAulay et al. 2001), chloride binding (Zomot et al. 2007), substrate recognition (Rosenberg and Kanner 2008; Bismuth, Kavanaugh, and Kanner 1997), the external and internal gates (Dayan-Alon and Kanner 2019; Ben-Yona, Bendahan, and Kanner 2011; Ben-Yona and Kanner 2009) and in small molecule interaction (Cherubino et al. 2009).

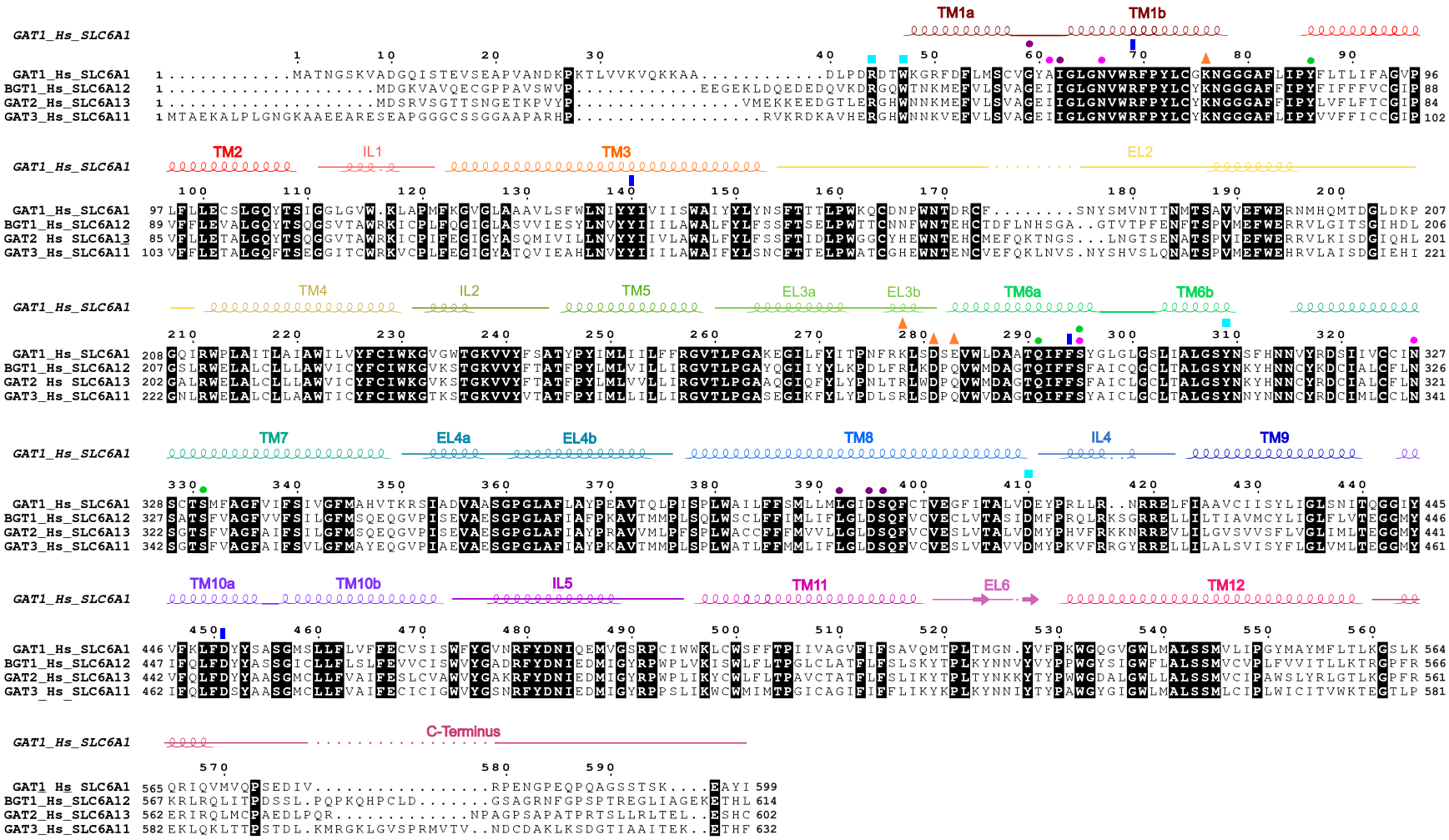

Figure 12: GATs sequence alignment. See detailed next page

Figure 12: Amino acid sequence alignment of the four human GABA transporters (GAT1-P30531; BGT1-P48065; GAT2-Q9NSD5; GAT3-P48066) with the secondary structures from *h*GAT1 structure, PDB 7SK2 (Motiwala et al. 2022) **.** Strictly conserved residues are highlighted in black. α-helices and β-strands in *h*GAT1 are shown as coils and arrows respectively. α-helices in intra/extracellular loops are represented with a strikethrough coil. The transmembrane helices are represented by simple coils and the unwound regions of the TM1, 6 and 10 are shown by a straight line joining both part of the helices. Different symbols represent amino acids involved in inner (■) and outer gates (▌), Na1 (●) and Na2 (●) sodium sites, Cl^- site (●) and allosteric site (▲) (modified from Bhatt et al. 2023).

ii. Difference between GATs/GAT1/BGT1

GAT1 was known to be exclusively specific for GABA while GAT2 or GAT3 both facilitated transport of β-alanine and taurine in addition (Tamura et al. 1995; Q. R. Liu et al. 1993), leading to modified GABA transport (Liu et al. 1993). BGT1 showed transport for GABA and betaine but displays significant functional differences from the other GATs members (Matskevitch et al. 1999). BGT1 $K_{0.5}$ for GABA is almost 2-fold lowest than GAT1 $K_{0.5}$ for the same substrate (Bhatt et al. 2024). Also, its stoichiometry is 3 sodium ions for one molecule of substrate (Matskevitch et al. 1999). Moreover, pharmacological modulation of BGT1 showed unusual inhibition (Lie et al. 2020).

BGT1 mRNA was reported in cultured astrocytes, and it was well described that it was not localized on neuronal but rather on glial cells (Kickinger et al. 2019; Kempson, Zhou, and Danbolt 2014; Schousboe et al. 2004) and the overall expression of BGT1 in the brain is low. Moreover, GABA transport by BGT1 would represent 0.1 to 1% of the total GABA synaptic clearance (Kempson, Zhou, and Danbolt 2014), explaining that BGT1 deficient mice are not presenting any seizure difference with the WT mice (Lehre et al. 2011). With a low concentration of betaine in rodent brains (0.5–0.8 mM VS taurine 4.2-7.1 mM, reviewed by Pasantes-Morales and Cruz-Rangel in 2010 or 0.02–0.1 µmol/g of tissue VS taurine 5-10 µmol/g of tissue, reviewed by Kempson in 2014) and even a none detectable concentrations in human brain (Pasantes-Morales and Cruz-Rangel, 2010), it raised the interrogation of the effective roles of betaine and BGT1 in the CNS. Surprisingly, it is highly expressed on leptomeninges (arachnoid and pia mater), therefore there is a potential role of BGT1 in the interstitial fluid clearance of betaine (Kempson, Zhou, and Danbolt 2014; Y. Zhou et al. 2012). On the other hand, BGT1 is highly expressed on hepatocytes,

and abundant on renal cells (medullary cells and renal papilla). It transports betaine respectively for catabolism as methyl donor for the methionine cycle in the liver and protecting medulla cell damages due to urea exposure (Kempson, Zhou, and Danbolt 2014). The expression of BGT1 can be stimulated by osmotic stress in the Madin-Darby canine kidney cells (Schweikhard et al. 2014) amplifying its importance for counteracting osmolyte transport, instead of GABA.

To summarize, it was suggested that GAT1 transports GABA in a stoichiometry substrate: sodium: chloride of 1:2:1, however it is 1:3:1 for BGT1. GABA transporters do not have the same affinity for GABA (GAT1/BGT1), they are modulated by other amino acid derivates osmolytes (GAT2/3) and their main GABA transporting function is biased (BGT1). Therefore, a functional segregation between neurotransmission and osmotic regulation have appeared within the GABA transporter family, but how did it happen?

4. Towards a conserved mechanism across BCCT and NSS

i. Parallels between NSS and BCCT families

BGT1 and the glycine transporter 2 (GlyT2, SLC6A5) have a similar substrate:Na^+:Cl^- stoichiometry of 1:3:1. The location and physiological meaning of this third sodium ion is vague but would induce a higher accumulation of glycine and constrains its efflux (Zafra and Gimenez 2008). An adaptation in GlyT2 and BGT1 allows them to couple their transport mechanism with a third sodium ion, a feature not seen in other NSS proteins. This evolutionary change enables these specific transporters to function differently by utilizing an additional sodium ion.

To understand the origin and the location of Na3 in GlyT2, Subramanian and coworkers performed molecular dynamics simulations. Interestingly, the supplementary sodium placed spontaneously at the location consistent with the alternative Na1' site of BetP (Subramanian et al. 2016), which is shifted from the Na1 in LeuT and mammalian NSS (table figure of Na1' residues). Some sub-families of the SLC6 transporter family may have evolutionarily conserved the ability to couple with a higher number of sodium ions. This mechanism could be an adaptation for the transport of complex substrates. For example, BGT1 may have adopted this strategy, as its low kinetic parameters suggest a higher energy requirement compared to GAT1 (Bhatt et al., 2024).

ii. GAT1 interacts and transports betaine

Recently, it was shown that GAT1 interacts and transports betaine, although with an affinity (11 mM) and a transport velocity (I_{max} -76 nA) respectively 360-fold and 3-fold lower than with GABA (Bhatt et al. 2024). The activity of GAT1 is also regulated by betaine; At high concentration of GABA and betaine, the methylammonium solute promotes a synergic effect, i.e., induces higher inward currents than in presence of GABA alone (Bhatt et al. 2024). Therefore, these results suggest that the molecular mechanism of GAT1, also adapted along evolution to fulfill its activity historically interacting only with GABA (Tamura et al. 1995). Indeed, the tertiary amine of betaine makes it bulkier than GABA (Figure 10). In addition to the two sodium ions, the protein is sterically compromised. The recent structures of GAT1 were solved with two GAT1 inhibitors, i.e. tiagabine and nipecotic acid (Zhu et al. 2023; Motiwala et al. 2022), in the Apo- and GABA-bound states (Zhu et al. 2023). A significant gap in current knowledge is the lack of a resolved structure for Betaine-GAT1. According to the structural similarities of the mammalian NSS with BetP, its structure with betaine and sodium bound (PDB 4AIN, Perez et al. 2012) was used to conjecture the position of betaine in GAT1 (Figure 13). The sodium ions in the Na2 in BetP and in GAT1 superposed almost perfectly and the carboxylic group of GABA is also co-localized with the one of betaine. However, its trimethyl ammonium group is located closed to serine 295, and the overall stability of betaine is probably sustained by the backbone of the Alanine 61 and Isoleucine 62 in the TM1 (Figure 13), resulting in steric and charges clashes with sodium in the Na1 site. Although the residues involved in Na1' in BetP are not always strictly conserved in GAT1, they are similar in terms of size and charge, except for Ser302 (Figure 9). Therefore, BetP Na1' might be conserved in GAT1 as a potential secondary Na1 in case of interaction with substrate like betaine. Moreover, in this position, the sodium ion would compensate for the absence of GABA in replacing its positively charged amino group. In other words, for transporting betaine GAT1 would remodel its Na1 site that probably moves towards the residues of Ser133, Asn137 (TM3) Ser302 (TM6b) and Thr400 (TM8) (Merge, Figure 13).

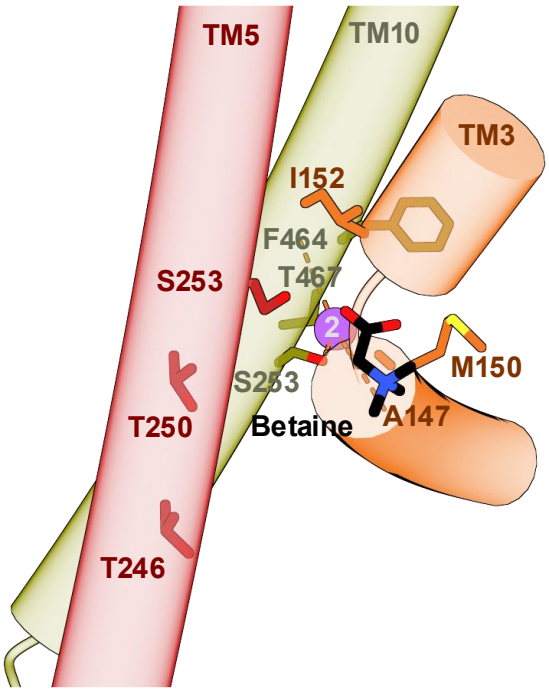

BetP WT

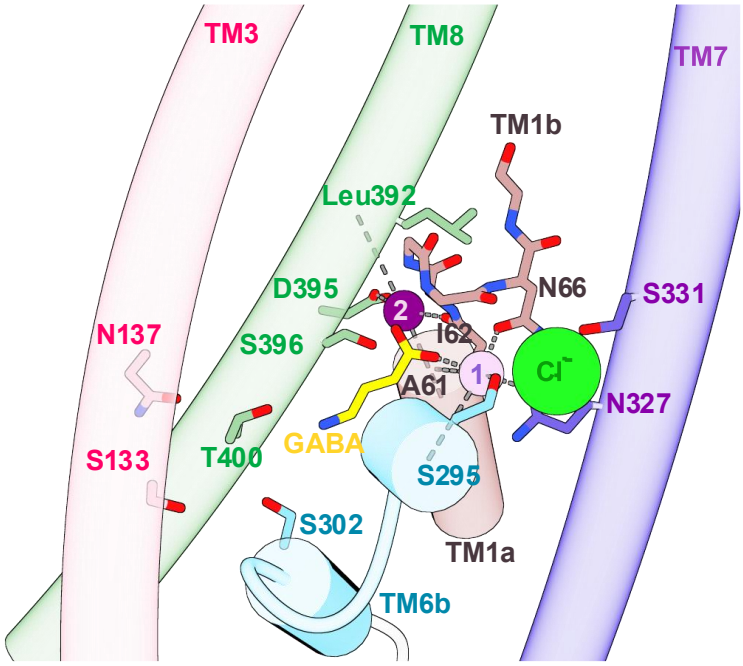

GAT1 WT

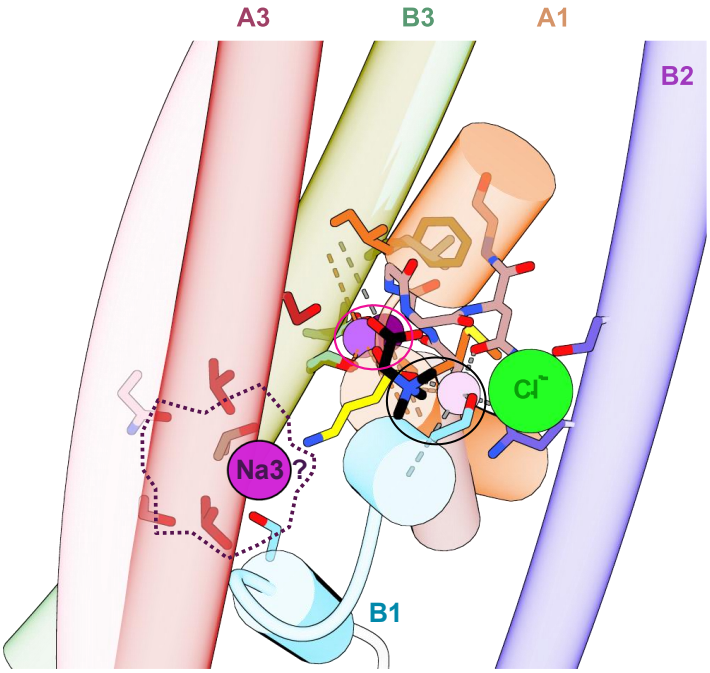

Merge

Figure 13: Hypothesis of Betaine binding site in GAT1 WT after structure superposition of GAT1 WT (PDB 7Y7W, Zhu et al., 2023) and BetP WT (PDB 4AIN, Perez et al. 2012). On the merge, the superposition of the Na2 sites from each protein is circled in purple and the replacement of sodium in Na1 site by the methyl ammonium group of betaine is circled in black. On the same image, the TMs are numbered like the standard nomenclature (Figure 5). the putative secondary Na1 in GAT1, equivalent to Na1' in BetP in represented with a sphere surrounded by an irregular dotted circle (magenta).

iii. Na1' in BGT1

If the second Na1 in GAT1 seems to be in concordance with the recent betaine transport activity, what about BGT1? Indeed, the conservation of BetP Na1' in BGT1 could be the rational explanation to the 3 sodium stoichiometry observed (Subramanian et al. 2016; Matskevitch et al. 1999). However, two residues of BetP Na1' are not well conserved in BGT1 (Figure 9). Glu126, is favorable for sodium coordination but not the Cys301 (Kish, Ohanessian, and Wesdemiotis 2003). Also, Thr400 in GAT1 corresponds to Cys399 in BGT1. Therefore, other residues in surroundings might support the creation of the third sodium site in BGT1 like Gln299 (Leu300 in GAT1). Indeed, glutamine is one of the amino acids with the highest affinity and stable interactions

with sodium (P. Wang et al. 2007; Kish, Ohanessian, and Wesdemiotis 2003; Bojesen, Breindahl, and Andersen 1993).

iv. Residues of GAT1 and BGT1 for substrate specificity

The specific recruitment of the substrate and its fast dissociation is essential for transporters to avoid any blockade during the conformational changes cycle and depends notably on the amino acid sequence. The NSS have a common conserved motif (G/A/C)ΦG in the unwound region of the TM6 (Focht et al. 2021). It is poorly conserved among NSS; thus, this loop polymorphism could be at the origin of its flexibility for transporting diverse substrates by the NSS. Indeed, MhsT and LeuT showed that larger amino acids could be transported if the side chain of the substituted residue was shorter (Focht et al. 2021; LeVine et al. 2019). In this so-called volumetric sensoring, the transporter constricts its binding core by a shift of the (G/A/C)ΦG motif to avoid its access to water molecules (Focht et al. 2021; LeVine et al. 2019). Enlarging the substrate diversity was also observed in BetP. A mutation (G153D) within the glycine stretch (three glycine residues between TM3e and TM3i, corresponding to the unwound TM1a and 1b in NSS) permitted to BetP to transport choline (Perez, Koshy, et al. 2011). Interestingly, the central position of the (G/A/C)ΦG motif corresponds to Leu300 in GAT1, Leu294 in GAT2 and Leu314 in GAT3 but to Gln299 in BGT1. Moreover, the NSS/BetP super-alignment (Figure 14) showed that BGT1 has a unique cysteine residue at the position 402, corresponding to Gly403 in GAT1, Ser497 in GAT2, Ser417 in GAT3. In the other transporters, Cys402 corresponds to small non-polar (glycine, alanine, valine, proline) or polar (serine, threonine) residues (Figure 14).

To summarize, the conservation of BetP Na1' associated with the single amino acid sequence polymorphism of GAT1 and BGT1 might account for their distinct molecular mechanisms and to favour methylammonium solute transport or neurotransmitter like osmolyte.

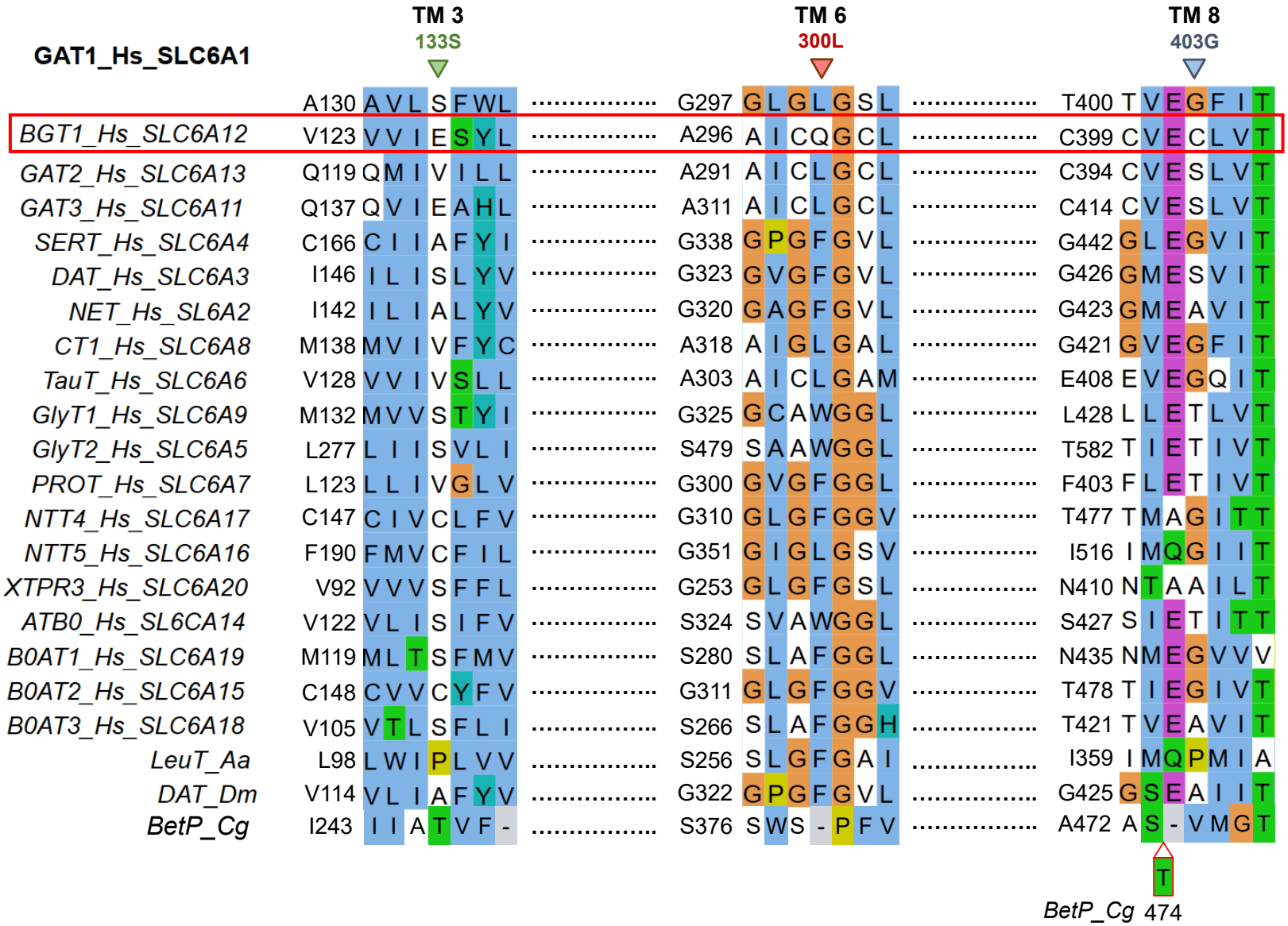

See legend next page.

Figure 14: Sequence alignment of the NSS super family. Residues of Ser133, Leu300, and G403 in GAT1 corresponding to Glu126, Gln299, and Cys402 in BGT1 are shown with head arrow respectively in green, red, and blue. TM3, TM6 and TM8 indicate the TMs these residues are located in.

5. Aims of Study I

Along this introduction we have reviewed generalities on membrane proteins, the importance of their phospholipidic environment, the molecular mechanism of secondary transporters, the past research on GABA transporter family and their ability to transport two different types of osmolytes (methylammonium solutes or amino acid derivates) or being regulated by them.

The aim of Study I is to investigate the molecular mechanisms that underpin the functional divergence between two members of the NSS superfamily: GABA transporter 1 (GAT1) and Betaine/GABA transporter 1 (BGT1). Specifically, this research will address two central questions: How do GAT1 and BGT1 achieve their distinct substrate preferences? What is the role of the third sodium ion binding site in BGT1? While GAT1 primarily transports the neurotransmitter GABA, BGT1 has evolved into a specialized betaine transporter, despite their sequence similarity. This study will examine the residues and structural motifs responsible for this substrate sub-selection. Another key objective is to unravel the significance of a unique feature of BGT1: its ability to couple with a third sodium ion. This adaptation may provide the extra energy required for high-capacity transport of accumulated substrates, a distinct mechanism from the rapid neurotransmitter uptake performed by GAT1.

To explore these mechanisms, we will investigate the potential role of Glutamic acid 126 (E126), a residue hypothesized to be crucial for forming this third sodium binding site (Na3). Our analysis will focus on how this residue impacts the transporter's affinity for sodium ions. Moreover, we will address several other key molecular players. We will first examine the role of Glutamine 299 (Q299) residue in substrate recognition. This residue is believed to be directly involved in binding either amino acid-based substrates or methylammonium osmolytes. Additionally, we will explore the potential role of this residue in supporting the function of the third sodium binding site. Finally, we will analyze the unique Cysteine 402 (C402) residue to determine its impact on the overall architecture and function of the transporter. By studying these specific residues and their contribution to substrate binding, ion coupling, and structural stability, this thesis aims to shed

light on the evolutionary and mechanistic innovations that have allowed these two transporters to specialize for their different physiological roles.

6. Procedure

i. Sodium and substrate interaction/translocation in GATs

The three key amino acid cited before will be substituted at their respective positions in GAT1 to convert it to a "BGT1-like" transporter. This method was already described for transposing the GABA transport function within the creatine transporter (Dodd and Christie 2007). By directed site mutagenesis, three single GAT1 mutants will be engineered

- S133E (role of Glu126 in sodium Na3 binding)
- L300Q (role of the Gln299 in sodium Na3 binding and GABA/betaine interaction)
- G403C (role of Cys402 in transporter structural rearrangement)

The localization of these residues in GAT1 is represented Figure 15.

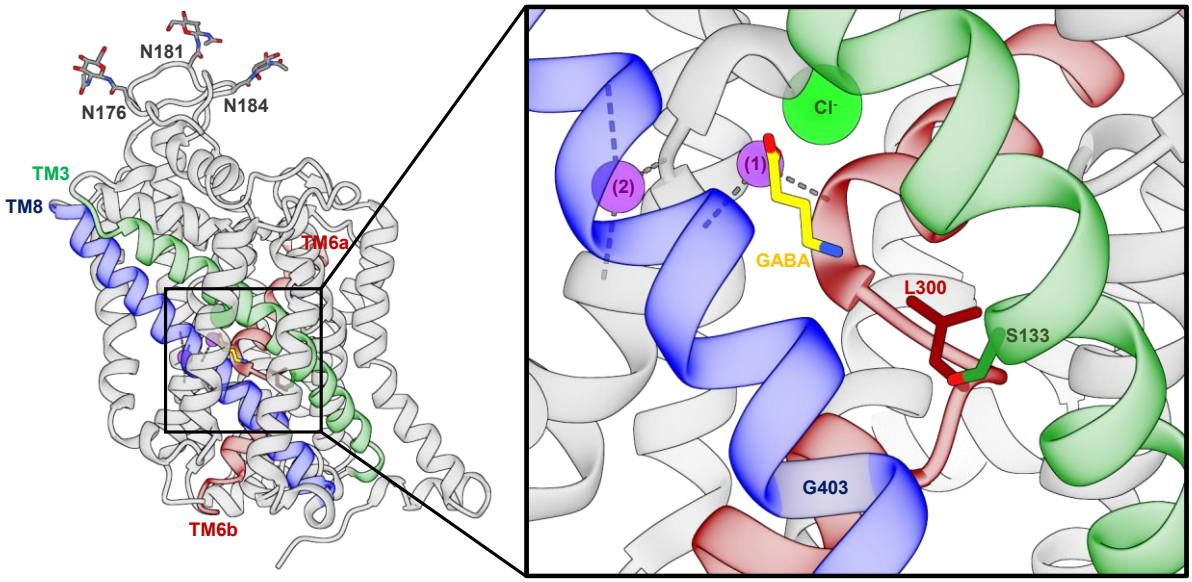

Figure 15: Localization of residues mutated and their respective TMs in GAT1. On the fully glycosylated transporter (Asn176, 181, 184), TM3 (green), TM6 (red) and TM8 (blue) are the TMs caring respectively the residues of Ser133, Leu300, and Gly403, represented in the same colors as stick (blue grey for G403). L300 is in the loop between the TM6a and b. (●) Sodium (●) chloride ions (▌) GABA (PDB 7Y7W, Zhu et al., 2023)

Double (S133E/L300Q, L300Q/G403C, G403C/S133E) and triple (S133E/L300Q/G403C) mutants will be also generated to recreate as much as possible BGT1 behavior in GAT1 (Dodd and Christie 2007). The DNA of each mutant will be injected into *X. laevis* oocytes for characterization by two electrode voltage clamp (affinity, maximal intensity, stoichiometry, voltage dependency) and epifluorescence microscopy (immunolocalization of the mutants/WT in oocytes). Mutants showing any differences with the WT will be recombinantly produced and purified for structural comparison by cryo-electron microscopy and single particle analysis.

ii. Role of Protein/Lipid interactions in GATs

The phospholipidic/sterol influence on GABA transporter is still understudied compared to biogenic amine transporters like DAT or SERT (Anderluh et al. 2017; Sitte and Freissmuth 2006; Seidel et al. 2005; Shouffani and Kanner 1990). For this purpose, GAT1 WT protein will be cloned, recombinantly expressed, purified and reconstituted into proteoliposomes. GAT1 is expressed on presynaptic neurons, therefore brain total extract lipids will be used to reproduce the standard lipidic environment for ensuring the stability and the functionality of GAT1. In collaboration with Despoina Kapiki (LMU munich), GAT1 reconstituted will be used for binding and fluorescence-based transport assays. GAT1 WT will be also expressed at the surface of extracellular vesicles (EVs) to further understand how a neo-native lipidic environment, with the correct lipid composition and balance between the inner/outer leaflet would influence structure and function of the protein.

III. Study II: L-type Amino Acid Transporter 1 (LAT1): pharmaceutical inhibition and potential application against bone metastasis from prostate cancer

1. L-type amino acid transporter 1

i. Nomenclature

L-type amino acid transport 1 (LAT1) is part of the heteromeric amino acid transporters (HATs) in the Amino acid-Polyamine-organo Cation (APC) superfamily (Scalise et al. 2018). Indeed the model commonly used to study molecular mechanisms of LAT1 is the bacterial transporter L-

arginine/agmatine AdiC (Ilgü et al. 2021; Jungnickel, Parker, and Newstead 2018). HATs are subdivided into 5 systems where the heterodimers are formed by a light chain (involving the SLC7 family) and a heavy chain (involving SLC3 family). The SLC7 family participates also to the formations of the cationic amino acid transporters (CATs) where the light chains of SLC7A1, 2, 3, 4 and 14 form monomeric transporters with 14 transmembrane helices (Brunocilla et al. 2023; Kantipudi et al. 2020; Scalise et al. 2018). The diagram below summarizes the different combinations possible to form the HATs (Figure 16). This precise classification distinguishes the HATs according to the amino acid transported, their sodium/pH dependency and the tissues where they are expressed (Wagner, Lang, and Bröer 2001).

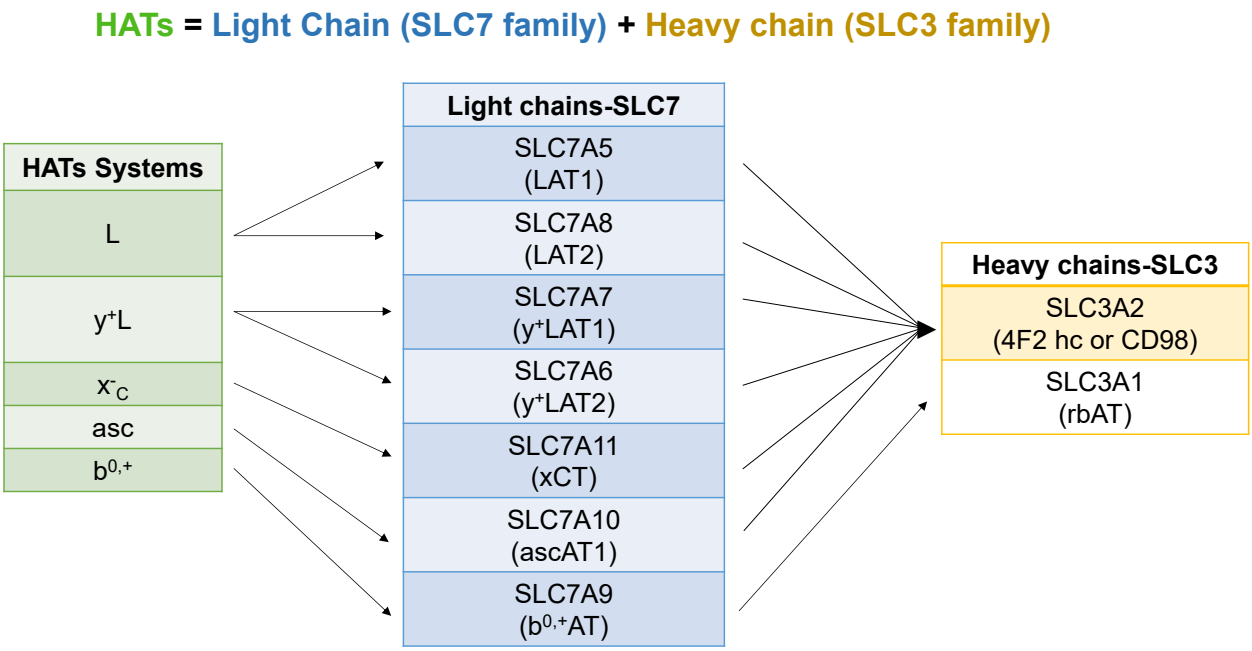

Figure 16: Diagram explaining the divers HATs systems associated with all the heterodimers combinations according to each system.

ii. Structure and function of the heterodimer LAT1/CD98

LAT1 is composed of the SLC7A5 light chain and the SLC3A2 heavy chain commonly called LAT1 and 4F2 heavy chain (hc) or Cluster of Differentiation 98 (CD98) respectively. Structures of LAT1 (Figure 17) showed that the light chain has a characteristic AdiC fold with 12 transmembrane helices where TM1 and 6 are unwound for substrate binding (Lee et al. 2023; Yan

et al. 2021; Lee et al. 2019; Yan et al. 2019). LAT1/CD98 structures solved in Apo state or with inhibitors are listed below (Table 1).

Technique	Resolution (Å)	PDB code	Structure details	Conformation	Ref.
Cryo-EM	3.50	6IRT	BCH*	Inward-open	Yan et al, 2019
	3.30	6IRS	APO		Yan et al, 2019
	3.30	6JMQ	+MEM-108 Fab		Lee et al., 2019
	2.90	7DSK	+JX-075*	Outward-occluded	Yan et al, 2021
	2.90	7DSL	+JX-078*		Yan et al, 2021
	3.10	7DSN	+JX-119*		Yan et al, 2021
	3.40	7DSQ	+Diiodo-Tyrosine*		Yan et al, 2021
	3.89	8KDF	+JPH203*	Outward-Open	Lee et al, 2023
	3.30	8XPU			Hu and Yan, 2024

Table 1: List of the main LAT1/CD98 structures. *LAT1 inhibitors (see structure on Figure 21).

LAT1 subunit catalyzes, independently from CD98, the import of one leucine into the cytoplasm and the export of one tryptophan to the extracellular space in an antiport mode being a generic antiporter of branched-chained and aromatic amino acids (Phe, Tyr, Trp, His, Leu, Ile, Met, Val, Gln) (Xinjie 2019; Scalise et al. 2018; Napolitano et al. 2015). LAT1 and CD98 are physically linked by a disulfide bond between Cys164 of LAT1 and Cys210' of CD98 (Lee et al. 2023; Yan et al. 2021; Lee et al. 2019; Wagner, Lang, and Bröer 2001). CD98 is a type-II membrane protein, with only one transmembrane domain (TM1'), the N-terminus in the cytoplasm and the C-terminus in the extracellular space (Figure 17). The ectodomain (ED) of CD98 has an α-amylase fold-like structure with 4 residues of asparagine glycosylated (Asn365', 381', 424', 506') allowing the trafficking of LAT1 subunit to the plasma membrane (Console et al. 2022; Fort, Nicolàs-Aragó, and Palacín 2021; Lee et al. 2019; Xinjie 2019; Fort et al. 2007) (Figure 17). The catalytic domain A (in cyan and navy blue, Figure 17) demonstrates a standard glucosidase (β/α)8-barrel fold with at its end, the domain C (in green in Figure 17) made of a four sheets β-sandwich topology (Fort, Nicolàs-Aragó, and Palacín 2021). CD98 was tested with a wide range of carbohydrates and glycans and has never showed catalytic activity. Therefore, the physiological role of the homology 4F2hc-ED with α-amylase family members is unclear but it was proposed to interact with proteins

having an immunoglobulin-like domain, like galectin-3 (Gal-3) (Fort, Nicolàs-Aragó, and Palacín 2021). It is a glycan-binding protein, ubiquitously expressed in various human tissues at the cell surface, nucleus and cytoplasm (Sundblad, Croci, and Rabinovich 2010). Indeed, CD98 was immunoprecipitated and colocalized on TEM images with Gal-3 (Dalton et al. 2007). The glycosylation patterns on asparagine residues of CD98 are distant from the interface with LAT1 supporting that they are not involved in the heterodimerization.

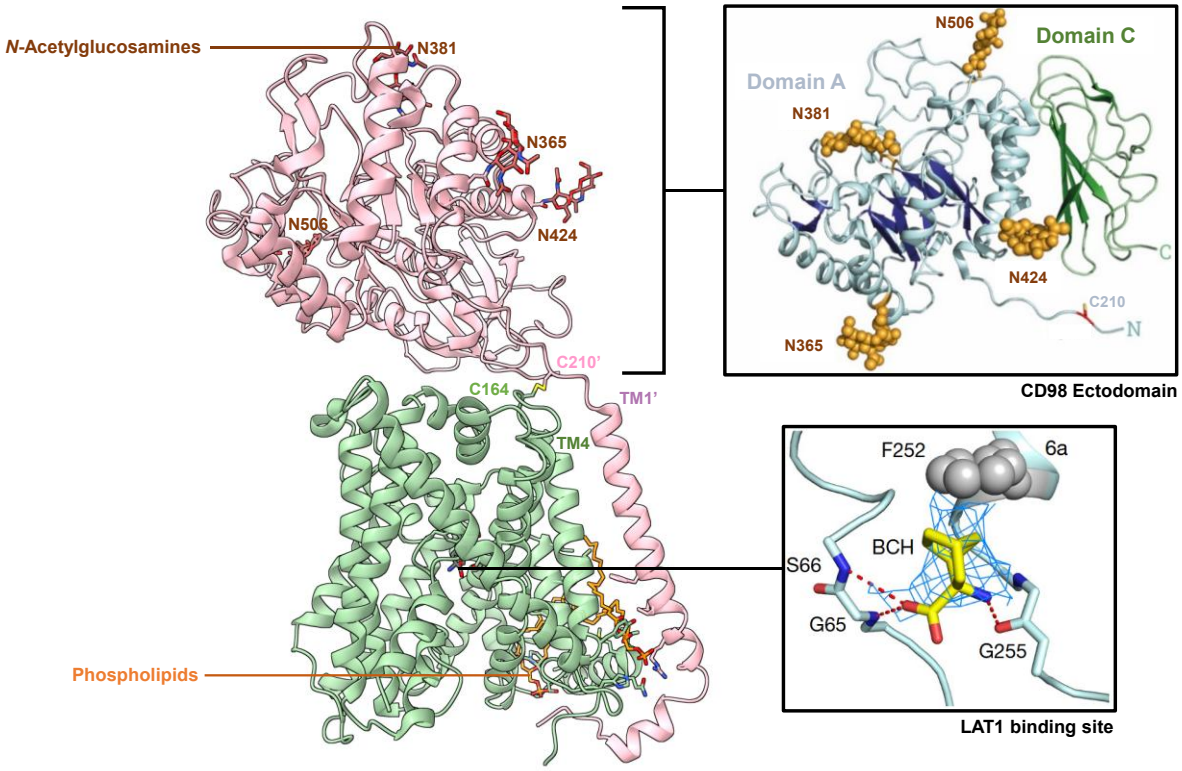

Figure 17: LAT1 heterodimer structure (PDB 6IRT). LAT1 light chain subunit (green) is linked to the heavy chain CD98 (pink) by disulfide bond (C164-C210'), two phospholipids (orange sticks) are present at the interface of the complex and each residue of Asn365', 381', 424' and 506' of CD98 are covalently bound to one N-acetylglucosamine molecule (maroon sticks). The detailed α-amylase fold of CD98 (Fort, Nicolàs-Aragó, and Palacín 2021) and the binding site of LAT1 with BCH (2-aminobicyclo (2,2,1) heptane-2-carboxylic acid) (Yan et al. 2019) are presented in the squares aside the respective subunits.

iii. Structural elements stabilizing the complex

- *In the plasma membrane*

The interfacial domain between the subunits comprises TM1' (CD98) and TM4 (LAT1). They are distant by 10 Å because of bulky amino acids from TM1' of CD98 (Phe189', Trp190', Phe193') and Leu180-181/Ala184 from TM4 of LAT1 (Lee et al. 2023; Yan et al. 2021; Lee et al. 2019) (Figure 18B, C). Therefore, one sterol molecule and two phospholipids are joining the gap between the two monomers (Figure 17 and Figure 18A). Four more sterol molecules in the membrane outer leaflet are associated with LAT1 (Figure 18A) which emphasizes that cholesterol and analogues stabilize the whole complex *in vivo* and *in vitro* (Lee et al. 2019; Dickens et al. 2017; Meury et al. 2014; Fort et al. 2007). Recently, not only 2 but 4 phospholipids were shown to interact at the interface TM1'-TM4 and were identified as phosphatidyl-ethanolamine polar head group (Wu et al. 2024).

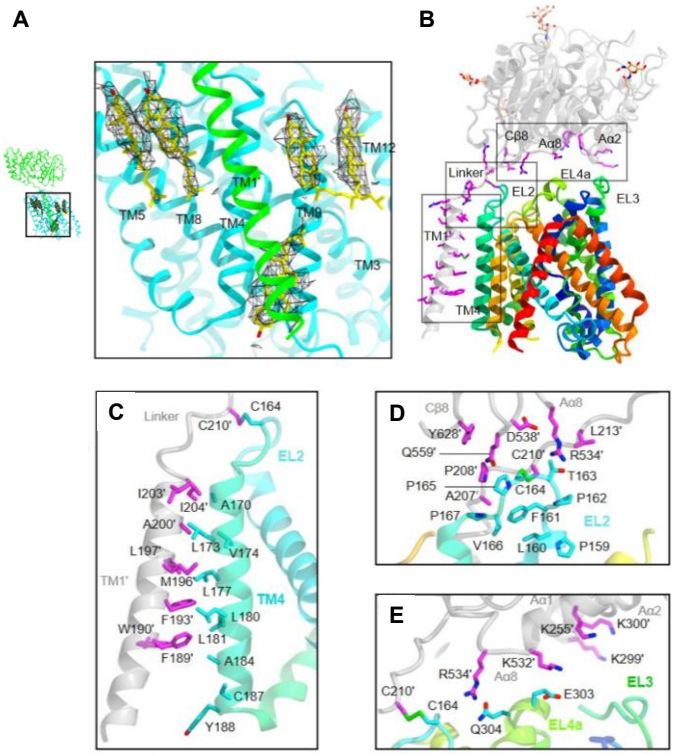

Figure 18: Lipid and inter-monomer interactions involved in complex stabilization. a) Cholesterol molecules around LAT1 in the outer leaflet and at the interface TM1'-TM4. b) Overview of LAT1-CD98 interacting residues. c) Helix-Helix interaction and interruption because of bulky amino acids on TM1' (Phe189', Trp190', Phe193' in pink) and small branch amino acids on TM4 (Ala164, Leu180, Leu181 in

cyan). d) and e) Shielding of the connecting neck and electrostatic interaction between LAT1 and CD98 subunit (see text) (Images from Lee et al., 2019).

- *In the extracellular space*

The connecting neck between TM1' and CD98 ED is a 33 Å loop that is shielded by interacting pair of residues from both monomers (Pro165-Gln559', Figure 18D). ED of CD98 and the extracellular domain of LAT1 have an electrostatic interface where Arg534', and Lys532', 255', 299' and 300' (CD98 residues in pink, Figure 18D and E) promote the interaction with Thr163, Gln304, Glu303 (LAT1 residues in cyan, Figure 18D) to enhance the partnership of the respective monomers (Chiduza et al. 2019; Lee et al. 2019).

iv. Substrate binding in LAT1 subunit and molecular mechanism

Like a typical APC family transporter, LAT1 shares the alternating access model which the transition from the outward to inward-open is triggered by substrate binding (Brunocilla et al. 2023; Lee et al. 2023; Yan et al. 2021). Analysis of LAT1 structures (Table 1) permits to differentiate the hash domain, scaffolding the core domain composed of unwound TM1 and 6 with the principal amino acids involved in the binding site (Figure 17 and Figure 19). Gly65 and Ser66 (TM1) form a positive pole that interacts with the carboxylate moiety of BCH, while the backbone of Gly255 (TM6) coordinates the amino group of the inhibitor. Phe252 (TM6) stabilizes its cyclic element with π-π interactions and is well known as a gating residue (Brunocilla et al. 2023; Z. Hu and Yan 2024; Yan et al. 2021; Lee et al. 2023, 2019). According to the TM movements, rotation of Phe252 temporizes the liberation or the binding of the substrate. In presence of BCH or other inhibitors, Phe252 is pointing toward the inhibitor cycle moieties resulting in occluded or inward-open conformations (Figure 19).

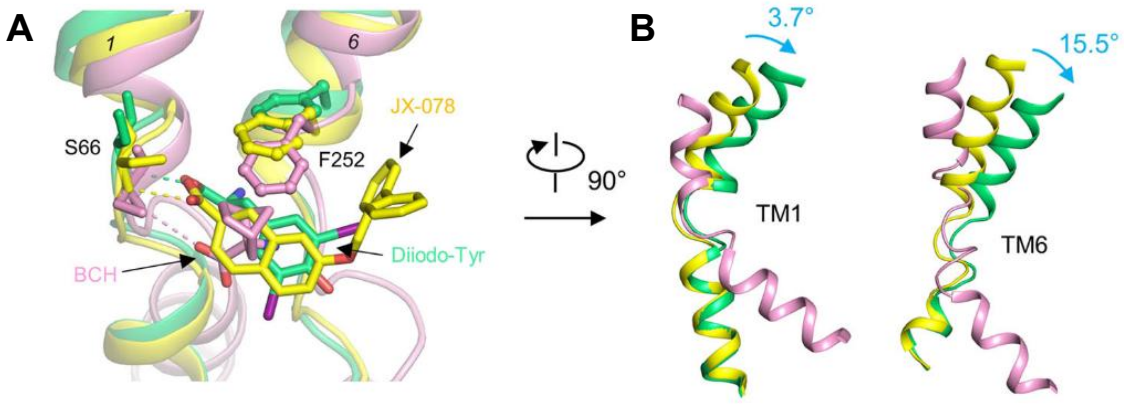

Figure 19: LAT1 inhibitors interacting in the binding site. The superposed structures correspond to LAT1 with BCH (pink), with JX-078 (yellow) and with diiodo-tyrosine (green). a) Phe252 is always pointing toward the cyclic groups of each inhibitor. b) different orientations of TM1 and TM6 according to each inhibitor bound to the protein (image from Yan et al., 2021).

On Figure 19B, TM1a and 6b are largely shifted in presence of BCH (pink structure), showing that LAT1 is in inward-open state while the distancing of TM1b and TM6a with JX-078 and diiodo-tyrosine demonstrates that LAT1 is in outward-occluded state. Therefore, JX-078 and diiodo-tyrosine avoid amino acid binding and/or influx inside and outside the cells (Yan et al. 2021). Instead, BCH probably binds after amino acid release in the cytoplasm and avoids the export of amino acids from the intracellular space by blocking LAT1 in the inward-open state.

In conclusion, according to their molecular structures, each ligand has a different inhibiting mechanism impacting the influx of the efflux of amino acids and the downstream cellular pathways they are involved in. This is an important feature to exploit, as LAT1 has high pathological implications.

2. Physiological and pathological relevance of the heterodimer LAT1/CD98

i. LAT1 is specifically expressed in certain healthy tissues

LAT1 is found on the B-cells, the endothelial cells of the blood brain barrier (BBB), and the syncytiotrophoblasts in the placenta (Figure 20).

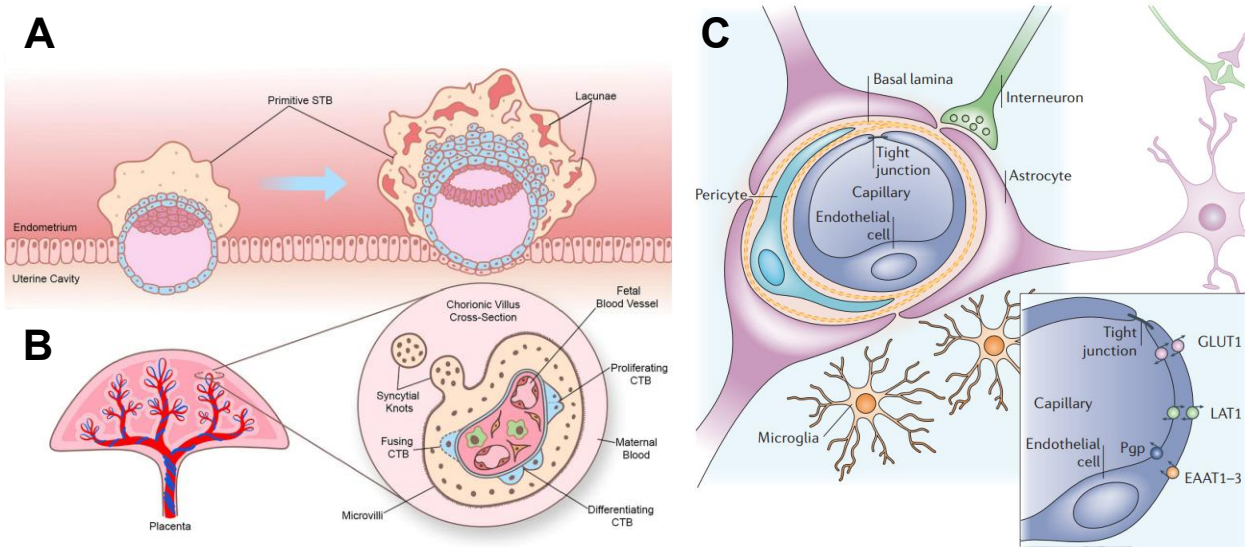

Figure 20: LAT1 tissue expression. LAT1 is expressed a) on the primitive syncytiotrophoblasts (primitive STB), b) on the lately chorionic villus of the placenta (CTB: cytotrophoblasts) (image from Jaremek et al. 2021) and c) on the blood brain barrier with a focus on the endothelial cells (navy blue) and the subcellular localization of LAT1 (image modified from Abbott, Rönnbäck, and Hansson 2006).

The expression of LAT1 on these cells is crucial. After infection, B-cells differentiate into plasma cells inducing a high rate of protein biosynthesis because of antibody production. Therefore, amino acid supply translocated by LAT1 is crucial for the immune response. On murine placentas, the transport of tryptophan by LAT1 is needed as a substrate for the enzyme indoleamine 2,3-dioxygenase (Munn et al. 2005), which suppresses the maternal immune response to fetus by inhibiting T-cells proliferation. Consequently, the system L-mediated tryptophan transport is a key player for maintaining the pregnancy (Usui et al. 2006; Munn et al. 2005; Wagner, Lang, and Bröer 2001). The BBB has a tight control on metabolites permeation, thus, LAT1 is the main amino acid regulator for physiological brain functions like cell nutrition, neurotransmission and immune protection. An impairment of LAT1 antiport activity is associated with diseases categorized as “aminoacidopathies”. Indeed, knock out of LAT1 favors the general imbalance of amino acid homeostasis in the brain and leads to autism spectrum disorders (Brunocilla et al. 2023). Consequently, LAT1 has a role in physiological but also pathological conditions.

ii. LAT1 is overexpressed in tumoral tissues

Highly expressed LAT1 neoplastic tissues (Xinjie 2019; Scalise et al. 2018; Wagner, Lang, and Bröer 2001) is critical for tumor growth, not only for protein synthesis but also for cellular signaling pathways that support tumor cell proliferation. Specifically, the intracellular uptake of leucine by LAT1 activates the mTOR pathway, a signaling cascade that stimulates cancer cell growth and proliferation by promoting cancer-associated reprogrammed metabolic networks and inhibiting autophagy (Norrsell et al. 2024; Brunocilla et al. 2023; Kahlhofer and Teis 2023; Häfliger and Charles 2019; Xinjie 2019; Scalise et al. 2018). LAT1 overexpression correlates with enhanced tumor aggressiveness and invasiveness, thus, is considered as an indicator of poor patient prognosis (Norrsell et al. 2024; Häfliger and Charles 2019; Xinjie 2019; Scalise et al. 2018). Consequently, LAT1 has garnered particular attention for pharmacological modulations in cancer therapies.

3. LAT1 as a pharmacological target

i. LAT1 as "drug carrier"

Gemcitabine was conjugated with threonine to increase the uptake of the cytidine mimic molecule by tumoral pancreatic cells (Nishikubo et al. 2023). Tyrosine functionalized nanoparticles and preloaded with irinotecan, an antimitotic molecule, were also using the transport activity of LAT1 for an anti-tumor effect (Norrsell et al. 2024). Considering the endothelial BBB expression of LAT1, these nanotechnology systems associated with its antiporter activity would give the possibility to cross the physiological barrier to treat cerebral diseases (Ahmed 2025; Puris et al. 2020). However, clinical data on these treatments are still limited (Norrsell et al. 2024).

ii. LAT1 as drug target in se

BCH and 3-aminobicyclo (3,2,1)octane-3-carboxylic acid (Figure 21) are widespread LAT1 inhibitors, commonly used for *in vitro* experiments and biophysical/structural characterization (Lee et al. 2019; Yan et al. 2019; Napolitano et al. 2017, 2015). BCH inhibits all system L transporters (LAT1, LAT2, LAT3, LAT4) and B^0AT1 (system B^0) and $ATB^{0,+}$ (system $B^{0,+}$). Therefore, it is not specific enough of LAT1 overexpressed in cancerous tissues (Jin et al. 2025;

Rii et al. 2024; Häfliger and Charles 2019; Singh and Ecker 2018), and could have deleterious secondary effect on other organs if used in clinics. LAT1 interaction with the synthetized molecules JX-075, 078, 119 and diiodo-tyrosine (Figure 21) was structurally determined and their inhibiting mechanism was already discussed earlier (*Cf:* ***iv. Substrate binding in LAT1 subunit and molecular mechanism***). Even if their inhibitory concentrations (IC_{50}) were in the range of 100-200 nM, any of them were tested for (pre)-clinical trials so far. One of the most promising molecule inhibiting LAT1 for antitumoral treatment, JPH203 (Nanvuranlat) (Figure 21), was discovered and synthetized around two decades ago (Endou et al. 2008). Its inhibiting mechanism avoids intracellular penetration of amino acid by blocking LAT1 in the outward-open conformation (Lee et al. 2023). After *in vitro* studies and the phase I clinic trials (Okano et al. 2020), JPH203 is now being evaluated in a phase II clinical trials for the treatment of biliary tract cancer (Jin et al. 2025; Z. Hu and Yan 2024; Rii et al. 2024; Okano et al. 2020). It has a high affinity for LAT1 (37.5 nM) while its metabolized counterpart, N-acetyl-JPH203 (Nac-JPH203, Figure 21), is 1.68 µM (Jin et al. 2025). Indeed when JPH203 is administered intravenously, it is taken up into liver cells, where it is predominantly acetylated to Nac-JPH203 by the N-acetyltransferase 2 (NAT2) (Wempe et al. 2012).

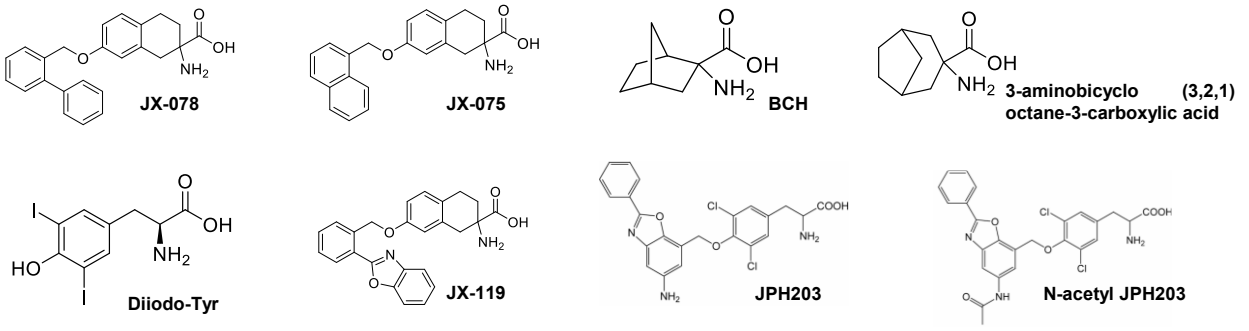

Figure 21: Molecule structures of LAT1 inhibitors mentioned in the text. So far, only (Nac) JPH203 are studied in clinical trials.

Although this metabolic transformation reduces LAT1 inhibition, the resulting N-acetyl-JPH203 accumulates preferentially in the biliary system. The localized concentration of the parent compound and its metabolite in the target tissue, combined with their respective inhibitory activity contributes to the observed therapeutic effect in biliary tract cancer (Jin et al. 2025).

iii. Limitations for LAT1 inhibitors design

- *Molecule metabolization*

JPH203 is highly efficient when slowly metabolized to its main metabolite N-acetyl JPH203. In order to increase benefit/risk the balance, patients must have a NAT2 phenotype which slowly produces Nac-JPH203 in the plasma (Okano et al. 2024, 2020; Furuse et al. 2023). However, 2/3 of pancreatic cancers are part of rapid metabolizer cancer groups, thus JPH203 has a little beneficial effect on these tumors (Norrsell et al. 2024). Therefore, the secondary metabolites and the overall pharmacokinetics of a new molecule must be the first thing to consider for ensuring that the activity of LAT1 will be impacted before the hepatic/kidney clearance of the molecule.

- *LAT1 alternating access model*

Because of its molecular mechanism, LAT1 is highly dynamic and each conformation (outward/occluded/inward) might not have the same affinity for one molecule, as it was shown for JPH203 (Brunocilla et al. 2023). Already in 2021, Yan and coworkers pointed to the rational question: how do the inhibitors get in the current binding site? Indeed, LAT1 inhibitor must be designed according to the conformation that will form its pharmacophore. Otherwise, the molecule would rather remain in systemic circulation than binding to the transporter, without optimal inhibition of the protein. Also, different molecule structures induce different inhibiting mechanisms and therefore do not have the same impact on the cellular fate.

- *Inhibition of LAT1 or LAT1/CD98?*

Golgi remodeling N-glycosylation of CD98 can have distinct roles in amino acids import for cellular maintenance. Indeed, the glycosylation site nearest the membrane, Asn365', promoted glycolipid-galectin-3-driven endocytosis (C. Zhang et al. 2023), an interacting partner of CD98 (Fort, Nicolàs-Aragó, and Palacín 2021; Dalton et al. 2007). Therefore, CD98 can be detected in the peripherical area of the plasma membrane instead of being embedded inside (C. Zhang et al. 2023). This is in accordance with different roles and/or the subcellular localizations held by CD98 in certain cancers. In liver tumor lesions, the nodule size measures 0.845 ± 0.232 mm² with positive detection of LAT1 and CD98, 0.524 ± 0.194 mm² with CD98 alone but only 0.097 ± 0.025 mm² with LAT1 alone. Therefore CD98 might have a consequence on tumor growth in a pathway

related to cell fusion (Ohkame et al. 2001). Moreover, in thymic carcinomas and thymomas, there is a positive correlation between high expression of CD98 and p53, vascular endothelial growth factors and micro-vessel density, proposing a supplementary role of CD98 in angiogenesis (Kaira 2010). In human gliomas, CD98 is predominantly found in the cytoplasm of tumor cells and not in the plasma membrane (Haining et al. 2012). This is in accordance with extracellular redox state alterations in pathological conditions such as cancer (Chaiswing and D'Oberley 2010), that could affect the disulfide bond between LAT1and CD98 and enhancing the role of the latter in endocytosis. Consequently, it was suggested that LAT1 single subunit could be a better pharmaceutical target than the whole LAT1/CD98 complex (Haining et al. 2012). In fact, in breast cancers, the expression of CD98 is not even evocated (Bodoor et al. 2020). Interestingly, the affinity of LAT1 for leucine was shown to be more than 2-fold higher than the complex LAT1/CD98, but the presence of CD98 permits to broaden the diversity of amino acids transported (Kantipudi et al. 2020). Therefore, the ancillary protein CD98 is not only a trafficking element but has independent roles including LAT1 regulation that could completely modify the interaction and inhibiting action of a pharmacological substance.

To summarize, rational drug design of LAT1 must consider the different conformational changes the protein undergoes to maximize its interaction with small molecules and the downstream cellular effect. The fast or low metabolization of the molecule could impair its efficiency for inhibiting LAT1. Therefore, pharmacokinetics should be studied carefully. In some rare cases, like in thymomas, LAT1 is not overexpressed (Kaira 2010). Hence, cancerous tissues, the grade of malignancy and aggressiveness must be considered for LAT1 targeted treatments. Finaly, LAT and CD98 positive tumoral tissues could have consequences on the interaction of a ligand with LAT1 subunit. Thus, the molecule should not be too specific to interact either with LAT1 alone or LAT1/CD98 complex.

4. Brasilicardin A: a promising and challenging inhibitor of LAT1

i. Brasilicardin A is a potent bioactive natural secondary metabolite

Molecule libraries of reversible/irreversible inhibitors or drug carrier systems for LAT1 gained interest since its involvement in cancers, but also in a wide range of pathologies like immune

diseases, insulin resistance, neurological disorders, and abortion risks (J. Zhang et al. 2020; Singh and Ecker 2018; Wagner, Lang, and Bröer 2001). However, few of them entered the clinical trials process, because too few *in vitro* information was available. Therefore, drug discovery for LAT1 is still ongoing and is also axed on active secondary metabolites produced by plants, fungi or microorganisms (Copp 2003). In 1998, a Japanese group continuously searching for bioactive metabolites from the pathogenic actinomycete strain *Nocardia brasiliensis*, isolated a molecule so-called Brasilicardin A (BraA) (Komaki et al. 1999).

- *Brasilicardin A has an immunosuppressing activity*

BraA (Figure 22) is tricyclic diterpenoid consisting of unusual anti/syn/anti-perhydrophenanthrene skeleton with an amino acid moiety, a 3-hydroxybenzoate, a L-rhamnose and a N-acetylglucosamine units (Botas et al. 2021; Yoshimura et al. 2018; Jung et al. 2015; Jung and Koch 2011; Usui et al. 2006; Komaki et al. 1999).

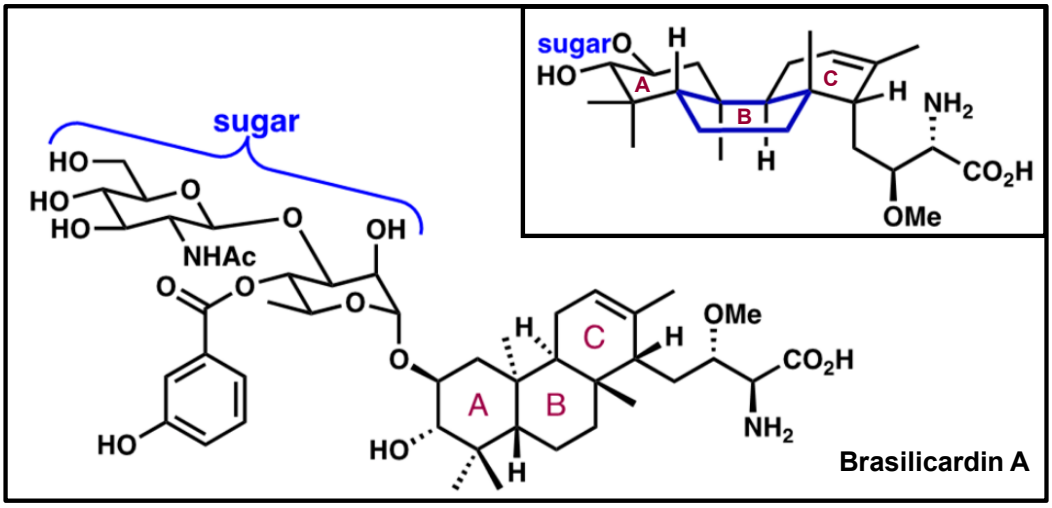

Figure 22: Structure of Brasilicardin A. The sugar moiety (blue) is formed (top to bottom) by an N-acetyl-glucosamine and L-rhamnose. NHAc indicates the acetyl group. L-rhamnose is associated with an hydroxybenzene by an ester bond (3-hydroxybenzoate) and to the ring system so-called anti/syn/anti-perhydrophenanthrene skeleton where A, B, and C represent the three cycles fused together. In the top right corner, a focus on the cycles shows that B (blue) has the boat configuration. The amino acid moiety terminates the molecule (image modified from Niman et al. 2023).

Its biological activity was tested on murine lymphocytes and showed an immunosuppressant activity with an IC_{50} of 63.90 nM, 2.6-fold lower than cyclosporin A (Komaki et al. 1999), a cyclic polypeptide used in clinics against immunological rejections after organ transplantation. However, the long terms complications associated with nephrotoxicity limit the use of cyclosporin A (Usui et al. 2006; Komaki et al. 1999; W. M. Bennett 1996). Indeed, its lethal dose (LD_{50}) is 107 mg/ml while no toxicity was observed with BraA at 100 mg/ml (Komaki et al. 1999). It was described that the immunosuppressant effect of BraA was not due to the inhibition of interleukin 2 (IL2) contrastingly to cyclosporin A. Therefore, BraA relies on another molecular pathway to stop lymphocytes proliferation.

- *Molecular pathway activated by BraA inhibits cellular proliferation*

When murine T-cells are treated with BraA, the molecule induces the activation of the General Control Non Depressible 2 (GCN2) amino acid sensitive pathway and promotes the phosphorylation of GCN2 kinase resulting in a rise of uncharged tRNAs (Usui et al. 2006; Munn et al. 2005). The downstream phosphorylation of eIF2α inhibits the global protein translation (Figure 23), inducing the specific loss of cyclin D1. This triggers the G1 phase arrest, associated with the entire cell-cycle interruption, and lately apoptosis (Usui et al. 2006; Munn et al. 2005).

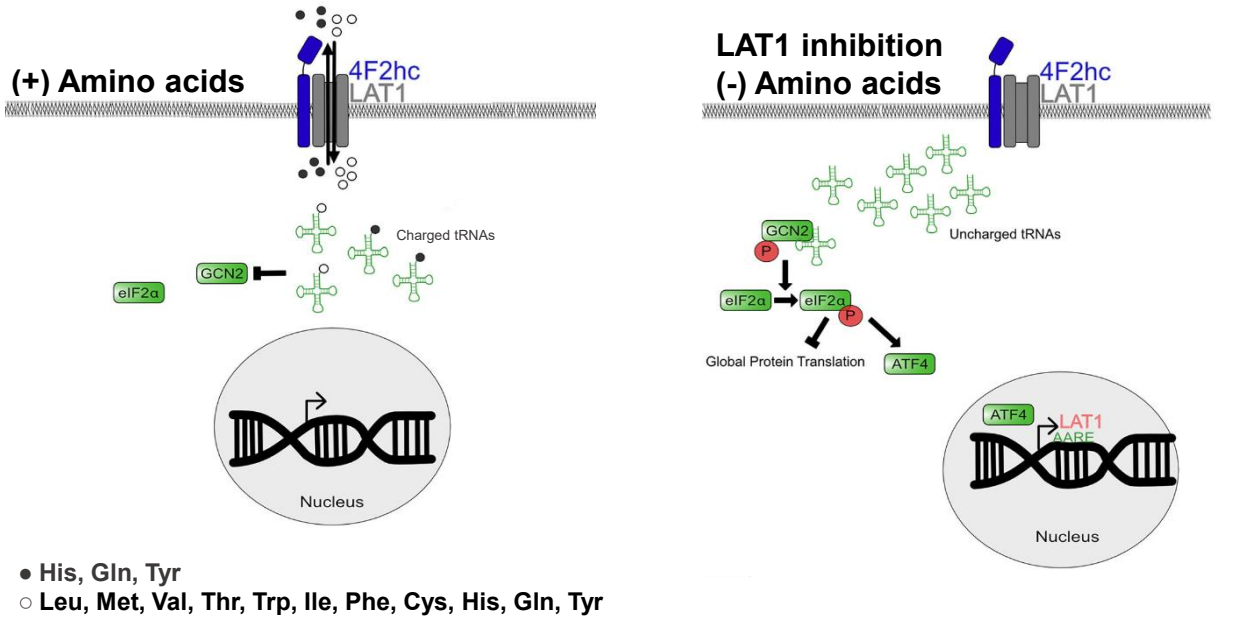

Figure 23: Cellular mechanism after amino acid deprivation. LAT1 inhibition or amino acid starvation induces the accumulation of uncharged tRNAs, because of the phosphorylated protein kinase GCN2

(General Control Non-Depressible 2) followed by the phosphorylation of eIF2α resulting in a global protein translation inhibition. Instead, the transcription factor ATF4 (controlling LAT1 gene expression) is preferentially translated. After ATF4 binding on the Amino Acid Response Element (AARE), LAT1 is expressed to restore amino acid import in the cytoplasm (image modified from Kahlhofer and Ties 2023).

In other words, the immunosuppressing effect of BraA resides in the inhibition of T-cell division. Additionally, it was shown that BraA has a cytotoxic effect on human leukemia cell lines (Komaki et al. 1999). Both immune and cancer cells overexpress LAT1 (J. Zhang et al. 2020), suggesting that the interaction BraA-LAT1 is an attractive molecule for immunosuppressive and antitumoral therapies (Usui et al. 2006).

- *Brasilicardin A is a promising drug candidate*

Further *in vitro* and *ex vivo* tests established the Administration-Distribution-Metabolization-Elimination (ADME) profile of BraA (Botas et al. 2021). It showed that BraA was almost not degraded by simulated gastric and intestinal fluids. Experiments with Caco-2 cells suggested that the molecule slowly penetrates through the intestinal epithelium by the P-Glycoproteins transport (X. Liu 2019). Once it reaches the systemic circulation, BraA is also highly stable in human plasma, and its catabolism by human hepatocytes seems to be slow (Botas et al. 2021). This first pharmacokinetics study on BraA suggests that after oral ingestion or intravenous injection, the probability of reaching LAT1 overexpressed tissues is high during (pre)-clinical studies in the future.

ii. Availability and production of BraA is a limiting factor

Natural production by *N. brasiliensis* requires particular laboratory precautions due to its pathogenicity and the production yields are not reliable (Wolański et al. 2024; Botas et al. 2021; Yoshimura et al. 2018; Jung et al. 2015; Hayashi et al. 2008). Total synthesis of BraA was reported but is not reproducible at an industrial scale due to its numerous 39 linear steps (Yoshimura et al. 2018). The difficulties related to BraA synthesis are the overall complex stereochemistry, the different functional groups (carbohydrates, amino acid moieties) and the tricyclic ring system with a chair-boat configuration visible on Figure 22 (Niman et al. 2023).

iii. Modifying the original BraA to simplify the compound synthesis

Structure-activity relationship (SAR) studies investigated the moieties essential for the biological effects observed, in order to simplify molecule synthesis. N-acetyl-glucosamine, 3-hydroxybenzoate and the amino acid moiety are required groups for both cell cycle and LAT1 inhibition (Usui et al. 2006). Later, new brasilicardins with simplified anti/syn/anti tricyclic core were synthetized to test their respective biological activity (Niman et al. 2023; Jung et al. 2015) In the analog BraL (Brasilogue A, Figure 24), it was replaced by a chiral tetrahydronaphthalene (tetralin) core. It was synthetized in only 10 steps, but did not prevent proliferation on human $CD4^+$ T cells (Jung et al. 2015). The high grade of flexibility due to the absence of hydrophobic methyl group and the whole C-ring might explain the absence of biological activity (Niman et al. 2023). Brasilicardin analog 3 (Figure 24), closer to the initial BraA, with a conserved rigid core, was supposed to sustain an immunosuppressive activity. However the analog 3 did not alter cell cycle (Niman et al. 2023).

To summarize, simplifying the global tricyclic core while shortening the distance (Jung et al. 2015) or integrating a rigid spacing unit (Niman et al. 2023) between the sugar and the amino acid portions of BraA is not sufficient for bioactivity. These chemical syntheses served also as SAR experiment saying that the original diterpenoid core is as critical as the two polar groups at each end.

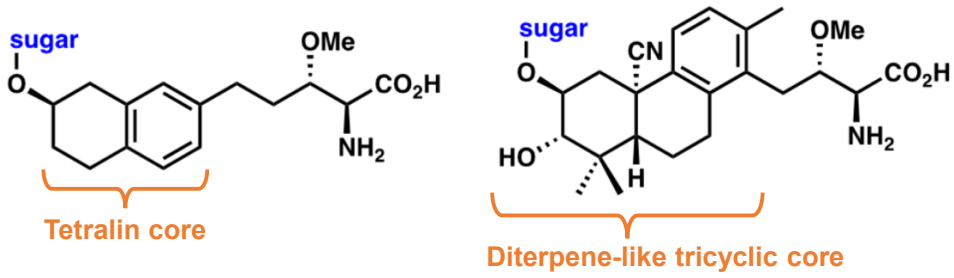

Brasilogue A (BraL) **Brasilicardin analog 3**

Figure 24: Synthetic analogues of Brasilicardin A with a simplified tetralin core for BraL (Jung et al. 2015) and a less flexible tricyclic core for brasilicardin analog 3 (Niman et al. 2023). “sugar” in blue refer to the disaccharide and the 3-hydroxybenzoate groups shown on Figure 22 (modified image from Niman et al. 2023).

Parallel synthesis with commercially available precursors (L-Rhamnose, D-glucosamine and cholesterol) showed a high efficiency production, with reasonable yield to synthetize an analog of BraA (Jung and Koch 2011). Although the absence of amino acid moiety compromises the biological activity, it raised the idea to formulate BraA via semi-synthesis i.e. via chemical modifications of a precursor to get the final product in a limiting number of steps. This strategy was used by Botas and coworkers in 2021 to get BraA in using biosynthetic precursors.

iv. Bio and Semi-synthesis of BraA

- *Discovery of the Brasilicardin "gene cluster" in N. brasiliensisis*

Dimethylallyl diphosphate (DMAPP) and isopentenyl diphosphate (IPP) are common precursors of isoprenoid production in actinomycetes (Hayashi et al. 2008). The first enzyme involved in biosynthesis of BraA is the geranylgeranyl diphosphate synthase (GGPPS, *bra2*) that metabolized DMAPP/IPP to geranylgeranyl diphosphate (GGDP, Figure 25C). The other genes responsible for the BraA biosynthesis were supposed to be in the flanking region of the gene coding for *bra2* (Hayashi et al. 2008). Indeed, 11 genes were identified, all oriented in the same direction and form the "Brasilicardin gene cluster" (Figure 25A). The function of seven genes (*bra1, 2, 3, 4, 5, 10*, and *11*) were determined by sequence homology (Figure 25B). The functions of the other genes are hypothesized (Figure 25B) according to the putative biosynthetic scheme (Figure 25C). Any trace of BraA was detected after gene cluster disruption (Hayashi et al. 2008). Therefore, the success of BraA production by *N. Brasiliensisis* resides in the tandem expression of each single gene.

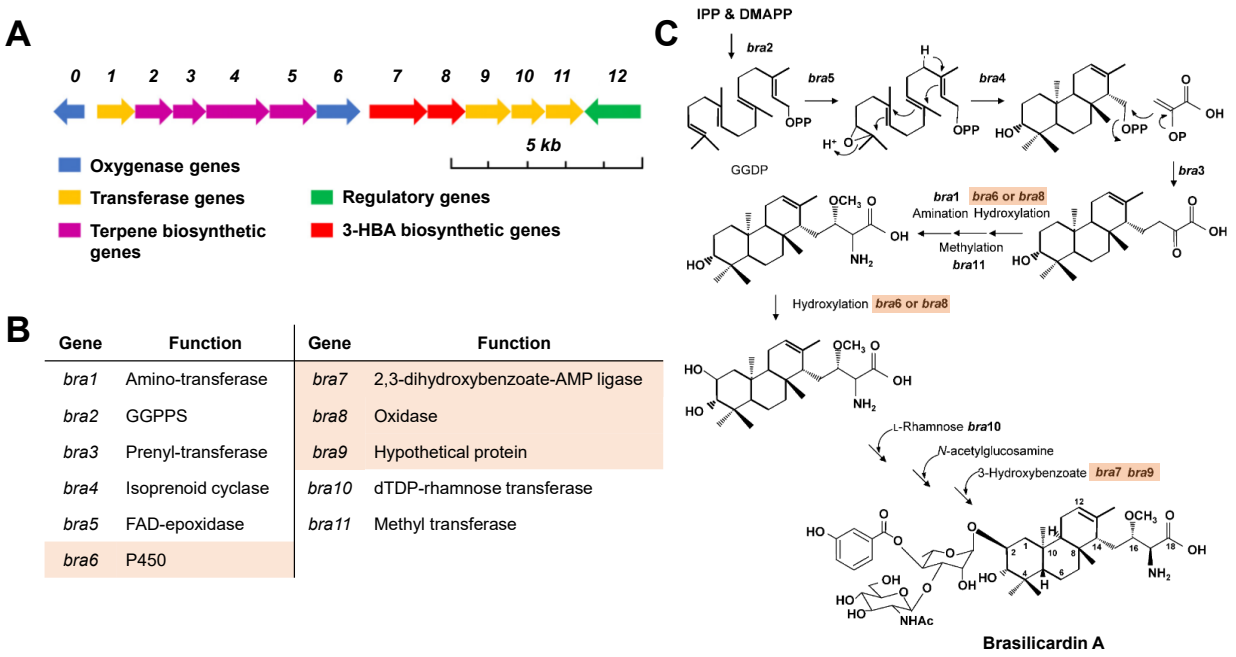

Gene	Function	Gene	Function
bra1	Amino-transferase	*bra7*	2,3-dihydroxybenzoate-AMP ligase
bra2	GGPPS	*bra8*	Oxidase
bra3	Prenyl-transferase	*bra9*	Hypothetical protein
bra4	Isoprenoid cyclase	*bra10*	dTDP-rhamnose transferase
bra5	FAD-epoxidase	*bra11*	Methyl transferase
bra6	P450		

Figure 25: Brasilicardin A biosynthesis by *N. Brasiliensis*. a) Gene cluster of the diverse enzymes catalyzing the metabolism of IPP and DMAPP to BraA (image from Botas et al. 2021). b) List of enzyme functions. The hypothesized functions are highlighted in orange. c) Proposed scheme of BraA biosynthesis with the enzymes involved for each step; the hypothetic function are highlighted in orange (image from Hayashi et al. 2008).

- *Optimizations of BraA Semi/Natural synthesis*

Based on this knowledge, the entire cluster was cloned, after strain screening, into the non-pathogenic *Streptomyces griseus* giving the best yields for BraA intermediates, named as BraC, and BraE, its aglycone counterpart (Figure 26). By optimizing culture medium, positive regulation of gene expression, and increasing the quantity of the initial precursor units IPP and DMAPP, the production BraC and BraE improved by 5-fold (Botas et al. 2021).

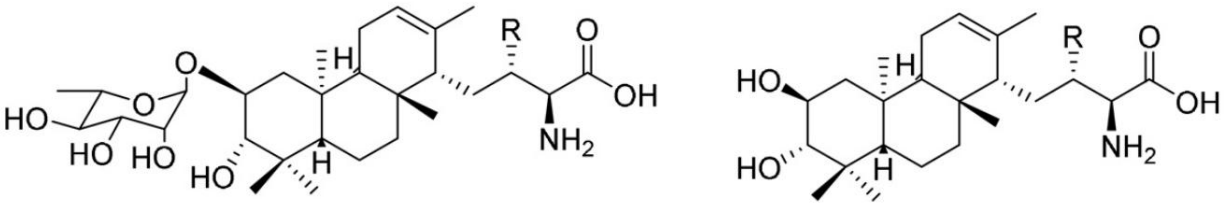

Brasilicardin C (BraC), R=OCH_3

Brasilicardin E (BraE), R=OCH_3

Figure 26: Structures of Brasilicardin A intermediates BraC and BraE. The latter is the aglycone form of BraC (image modified from Botas et al. 2021).

Rather than the heterologous production of the target compound BraA, the significant production of the stereochemical complex intermediate BraE was converted into the biologically highly active BraA by employing a 5-steps semi-synthetic strategy (Botas et al. 2021). Nowadays, efforts are concentrated on the gene cluster regulation to enhance the production of intermediates and/or the final product BraA (Wolański et al. 2024). *Bra12* was already known to positively regulate the gene expression (Botas et al. 2021) whereas other understudied translational factors like SpdR might downregulate *bra12* and *bra0*. Understanding the tight control of Brasilicardin gene cluster might ensure biosynthesis of the BraA compound (Wolański et al. 2024).

To summarize, BraA is a bioactive molecule inhibiting LAT1 that further stops cell division by activation of the GCN2 pathway. However, its use and molecular characterization are still limited because of its low availability. This could be overcome in the future by improving its biosynthesis by genetic engineering. Despite the potent IC_{50} of BraA (0.13 µM) against glioma cells compared to the JPH203 (15 µM) (Botas et al. 2021), it is meaningful to remind that IC_{50} of JPH203 against biliary tract cancer cells was 37.5 nM (Jin et al. 2025). LAT1 inhibition by a bioactive molecule seems to highly depend on the cancer cells treated. Therefore it is worth screening other tumors and/or metastases that could be efficiently treated by BraA to be used as new therapeutic solution, as cancer drug resistance is commonly observed in clinical practice (Lei et al. 2023).

5. BraA against prostatic bone metastasis: a putative treatment?

i. Prostate physiology, cytology and biochemistry

The prostate is a gland part of the reproductive male system, located below the bladder and is constituted of different regions and zones (Figure 27A), that sustains the production of semen. Prostate epithelial cells (on the peripheral zone, Figure 27B) are androgen dependent, i.e. respond to androgenic signals that are integrated by the androgen receptor (AR). It is a transcriptional factor activated following its interaction with steroid hormones. The high affinity of its Ligand Binding Domain (LBD) for testosterone or 5α-dihydrotestorone (DHT, stable form) disrupts the interaction with the heat shock protein and favorize the motility of the protein through the nucleus. With its DNA binding domain (DBD), AR binds to the androgen response element (ARE) (Figure 27D)

that promotes the expression of two specific prostate markers: the prostate specific antigen (PSA) and the transmembrane protease serin 2 (TMPRSS2) (Figure 27C).

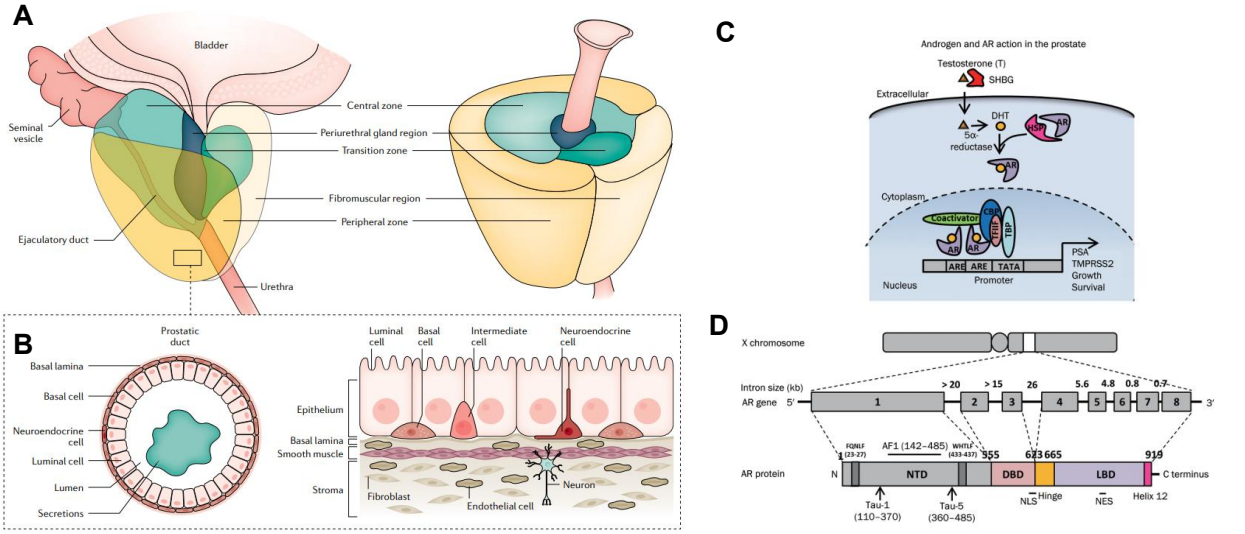

Figure 27: Focus on the prostatic gland. a) Prostate anatomy of the different lobes and the peripheral zone with b) the description of its epithelium. c) Molecular pathway for expressing PSA and TMPRSS2 after interaction of the androgen receptor (AR) with testosterone or its metabolized counterpart 5α-dihydrotestorone (DHT). d) Domains of the AR protein (modified images from Rebello et al. 2021; Tan et al. 2015).

PSA is a serine protease released in the lumen of the prostatic ducts where it cleaves semenogelin I and II, the predominant structural proteins of the coagulum produced by seminal vesicles, leading to release of free motile spermatozoa (Dash 2015; Williams et al. 2011; Lilja et al. 1987). PSA has a broad enzymatic activity and can activate or modify various growth factors (Williams et al. 2011). Thus, it has an essential role in prostate epithelial cell survival (Tan et al. 2015). When the prostate epithelium is disrupted after inflammation or neoplasia, it induces a leakage of PSA that reaches the blood stream. Consequently, an elevated concentration of PSA (above 10 ng/ml) in the systemic circulation is considered as a major biomarker for prostate cancer diagnostic (Rebello et al. 2021; Dash 2015; Giskeødegård et al. 2015).

ii. Prostate Cancer (PC) and associated metastases

In western societies, PC is the second cause of death after lung cancer and is commonly a malignant tumor, especially at the late stages of the diseases (Gupta et al. 2024; Rebello et al. 2021; Tan et al. 2015; Russell, Jackson, and Kingsley 2003). Metastases are often localized in the lymph nodes (LNs), in the bones, and in a lesser extend in the thymus, lung, liver, and the central nervous system (Rebello et al. 2021; Russell, Jackson, and Kingsley 2003) (Figure 28). Numerous lymph nodes are near the prostate (in green, Figure 28).

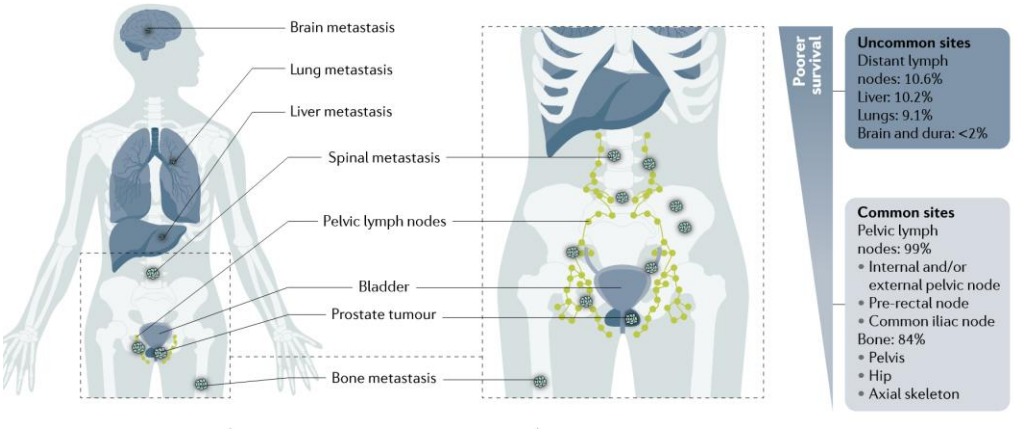

Figure 28: Metastases associated with prostate cancer: from common (pelvic lymph nodes, bones) to distant and rare sites (CNS, liver, lung) (image from Rebello et al. 2021).

Bone metastases (BMs) are originated from the neuroendocrine cells while LN metastases are formed by the epithelial cells of the prostate (Tai et al. 2011). Therefore, both metastasis types have different proteomic profiles. Contrastingly to LN metastasis, BMs highly express citrate transporters and other membrane proteins like integrins, sometimes associated with aberrant glycosylation patterns (Goode, Wang, and Munkley 2023; Mycielska et al. 2009). BMs present also deletion mutations of the oncogene p53 (Russell, Jackson, and Kingsley 2003; Carrol et al. 1993) and are AR independent (Goode, Wang, and Munkley 2023; Otsuki et al. 2017; Tai et al. 2011; Q. Wang et al. 2011). This sequential changes in protein expression or post translational modifications might promote distal invasion in the bones (Goode, Wang, and Munkley 2023). The common invasion mechanism of BMs is the inhibition of osteoblasts and an activation of osteoclasts following interleukin release, favorizing bone destruction, associated with pain and elevated fracture risks. Consequently, high serum level of osseous markers like phosphatase alkaline or calcium is correlated to BMs for diagnostic (Goode, Wang, and Munkley 2023).

iii. Bone metastasis study: role of LAT1 and its inhibition by BraA

The cell lines used to study bone metastasis are the PC-3 or the PC-3M subline, that differ from each other according to their proteome and respective metabolism. Indeed, the PC-3M cells increase their glutamine and citrate utilization to feed the Krebs cycle. This has a repercussion on energy production and therefore aggressiveness of the metastatic behavior (Zacharias et al. 2017; Mycielska et al. 2009). Also, glutamine modulates the mTOR pathway that promotes cell proliferation (Zacharias et al. 2017). Consequently, cell metabolism of PC-3M is related to amino acids. Confocal microscopy and western blots have showed that PC-3 cells express LAT1 (Otsuki et al. 2017; Q. Wang et al. 2011; Sakata et al. 2009). Treating PC-3 cells with LAT Silencing RNAs or the generic LATs inhibitor BCH decreased the relative cell growth, affecting the cell cycle progression after the G1 phase, but without dysregulating the mTOR pathway (Wang, 2011). Indeed, leucine free medium activated the expression of ATF4, that binds on the AARE (see Figure 23) enhancing LAT1 expression to restore the import of leucine (Wang, 2011). Therefore, the compensating amino acid sensitive GCN2 mechanism is responsible for PC-3 cells survival in absence of amino acids. Interestingly, Brasilicardin A impacts the same pathway (Usui et al. 2006), thus, the molecule seems to be an excellent candidate for stopping the proliferation of PC-3 cells *in vitro* by activating the GCN2 pathway.

6. Aims of the Study II

LAT1 interacts covalently by a disulfide bond with the protein CD98 which is implicated in the trafficking of LAT1 but also in amino acid recognition and other cellular mechanisms (C. Zhang et al. 2023; Kantipudi et al. 2020; Haining et al. 2012; Kaira 2010; Ohkame et al. 2001). Stability and activity of LAT1 are dependent on the phospholipids and the sterols composition of the membrane (Wu et al. 2024; Lee et al. 2019; Dickens et al. 2017; Meury et al. 2014). Numerous inhibitors of LAT1 are reviewed in the literature and LAT1 was structurally determined with some of them (Z. Hu and Yan 2024; Lee et al. 2023; Yan et al. 2021, 2019; Lee et al. 2019; Singh and Ecker 2018). However, no concrete pharmacokinetics, or ADME profile was performed in contrast to Brasilicardin A (Botas et al. 2021).

This study aims to investigate the molecular basis for BraA's inhibitory effect on the LAT1 antiporter. To achieve this, we will pursue two main objectives. First, we will identify the specific amino acids within LAT1 that constitute the binding site for BraA. This will allow for a detailed molecular structure-activity relationship (SAR) analysis, which is essential for determining which of BraA's functional groups and stereochemical features are required for its inhibitory activity. The insights gained from this analysis will be instrumental in the rational design of a simpler, more effective compound that is easier to formulate.

Second, we will determine the conformational state of LAT1 when it is bound to BraA. By identifying whether BraA traps LAT1 in an outward-open, inward-open, or occluded conformation, we can elucidate the precise inhibitory mechanism. This will, in turn, provide a clear explanation for the cellular effects that are observed.

LAT1 was described as a physiopathological relevant protein (J. Zhang et al. 2020). It is particularly studied in the case of cancers where its overexpression is almost always reported and associated with cell survival (Xinjie 2019). However, targeting LAT1 for tumor treatment is challenging because not all cancer cells respond uniformly to the same therapy. This variability in response is a key obstacle in developing effective LAT1-inhibiting drugs for a broad range of cancers. (Jin et al. 2025; Botas et al. 2021). Moreover, enlarging therapeutic solutions for tumors is crucial because of the common drug resistance mechanisms encountered in clinics (Lei et al. 2023). Interestingly, the survival of prostatic bone metastases relies on the amino acid dependent pathway GCN2 (Q. Wang et al. 2011), on which BraA has its biological activity (Usui 2006). Therefore, the second part of the work consists of identifying if bone metastasis *ex vivo* model PC-3M, subline of PC-3, is a cellular target for treatment with BraA.

7. Procedures

i. LAT1-BraA interaction: Sample preparation for Cryo-EM study

First LAT1/CD98 complex will be expressed in small scale to set the correct LAT1:CD98 plasmid DNA ratios for the ideal expression of the whole complex. Then, different purification strategies will be performed to optimize protein concentration for further vitrification and cryo-EM single

particle analysis. Confocal microscopy will also be used to understand the interaction between the subunits LAT1/CD98 and their dependency to each other for membrane trafficking.

ii. BraA for treating aggressive bone metastasis: LAT1/CD98 target validation

Ex vivo prostatic bone metastases will be cultivated for confocal microscopy and western blot analysis to identify the presence and the cellular localization of the complex and/or subunits LAT1/CD98. This study will help to understand the role of each subunit in this metastasis type.

Material and Methods

I. Molecular Biology

1. Plasmids and bacterial strains used

Plasmid name	Amplification	(Purification) Tag or use	Resistance	Origin
pC1-eYFP-*r*GAT1 WT	*Escherichia Coli DH5α*	eYFP-N-ter	Kanamycin	Prof. Harald Sitte, medical University Vienna (Austria)
pHis-FLAG-*r*GAT1 WT and mutants	*Escherichia Coli DH5α*	His-FLAG-Tags-N-ter	Kanamycin	This work
pAMV-PA-*r*GAT1 WT and mutants	*NEB Turbo*	For electrophysiological experiments	Ampicillin	Prof. Elena Bossi University of Insubria (Italy)
pcDNA3.1_Zeo_hSLC7A5_N-ter_FLAG (Referred to LAT1)	*Escherichia Coli DH5α*	FLAG-Tag-N-ter	Ampicillin	Invitrogen
pcDNA3.1_Zeo_hSLC3A2_N-ter_Strep (Referred to CD98)	*Escherichia Coli DH5α*	Strep-Tag-N-ter	Ampicillin	Invitrogen

Table 2: Plasmids used for molecular biology cloning and further experiments.

Bacterial strains			
Name	**Genotype and application**	**Internal Resistance**	**Source**
E. coli DH5α	F^- Φ80lacZΔM15 Δ(lacZYA-argF)U169 recA1 endA1 hsdR17(rk-, mk+) phoA supE44 thi-1 gyrA96 relA1 tonA **Suitable for DNA amplification**		Invitrogen™, ref: 44-0097
NEB® Turbo Competent E. coli (High Efficiency)	F' proA+B+ lacIq ΔlacZM15 / fhuA2 Δ(lac-proAB) glnV galK16 galE15 R(zgb-210::Tn10)TetS endA1 thi-1 Δ(hsdS-mcrB)5 **Suitable amplification of rGAT1 WT/mutants in pAMV-PA plasmid**	Tetracycline	New England Biolabs, Ref: C2984HVIAL

Table 3: Bacterial strains used for molecular biology methods.

2. Principle and protocol for pC1-eYFP rGAT1 modification

The initial plasmid pC1-eYFP *r*GAT1 was provided by the research team of Prof. Harald Sitte from the Medical University of Vienna (Austria). To purify the protein of interest, the yellow fluorescent protein (YFP) expressed at the N-terminus was replaced by an 8-His tag and a FLAG tag (DYKDDDDK peptide), joined by one glycine-serine linker. The choice of a double purification tag increases the chance of the protein to bind at least to one type of resin. In the best case, this offers the possibility to do a double purification, to improve quality of the protein sample. Both tags are present at the N-terminus because the C-terminus of all neurotransmitter sodium symporters is short, and contains an unfolded PDZ-binding domain (Goodspeed et al. 2020). Therefore, adding purification tags on the latter would enhance the non-stability of the protein. Further advantages of an N-terminal FLAG tag include a better stability against protease degradation and a better purification efficiency (Einhauer and Jungbauer 2001). The cloning strategy used to introduce these double purification tags and the glycine-serine linker, is a reverse PCR combined to a Golden Gate assembly for reconstituting the final vector shown on Figure 29.

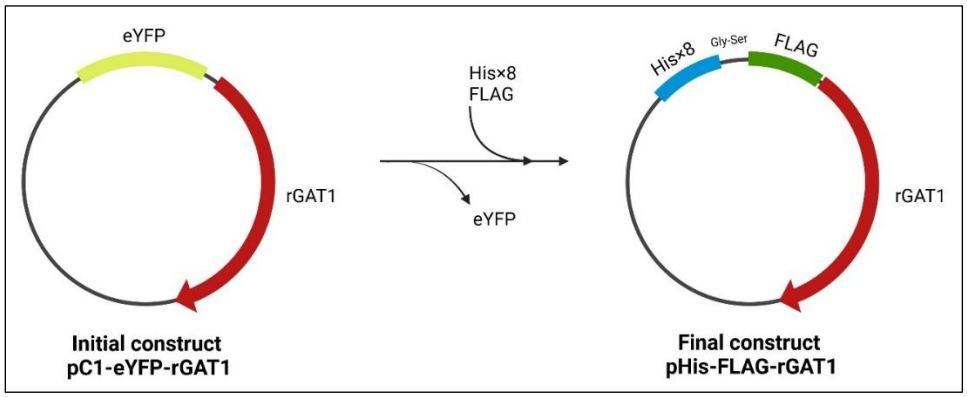

Figure 29: Vector carrying rGAT1 WT with the YFP modified by PCR to remove the YFP and introduce a 8-His and a FLAG tag linked by a Glycine-Serine linker (realized on Biorender.com)

The forward primer contains the FLAG-tag, the entire glycine-serine linker and anneals to the N-terminus of *r*GAT1. The reverse primer contains the 8-His tag, a part of the glycine-serine linker and anneals ahead of the start of the YFP gene. The primer sequences is detailed in the Table 4. Sticky ends at the 5' end of each primer are generated by using PaqC1 restriction enzyme, which is a type IIs restriction enzyme, allowing a scarless ligation after digestion. This principle was described previously and so called "Golden Gate Assembly" (Engler, Kandzia, and Marillonnet

2008; Marillonnet and Grützner 2020). Their annealing to the template is represented in Figure 30 with the detailed sequence of the enzyme PaqC1.

Primers for insertion 8-His -FLAG insertion on peYFP-C1		
Met-8-His FLAG insertion	Forward	5'GGAAACACCTGCATGCGGCTCAGATTACAAGGATGACGACGATAAGATGGCGACTGACAACAGCAAGG 3'
	Reverse	5'GGAAACACCTGCATGCAGCCGTGATGGTGGTGATGATGATGGTGCATGGTGGCGACCGGTAGCGCTAGC 3′

Table 4: Primers used for 8-His-FLAG insertion on pC1-eYFP *r*GAT1 template.

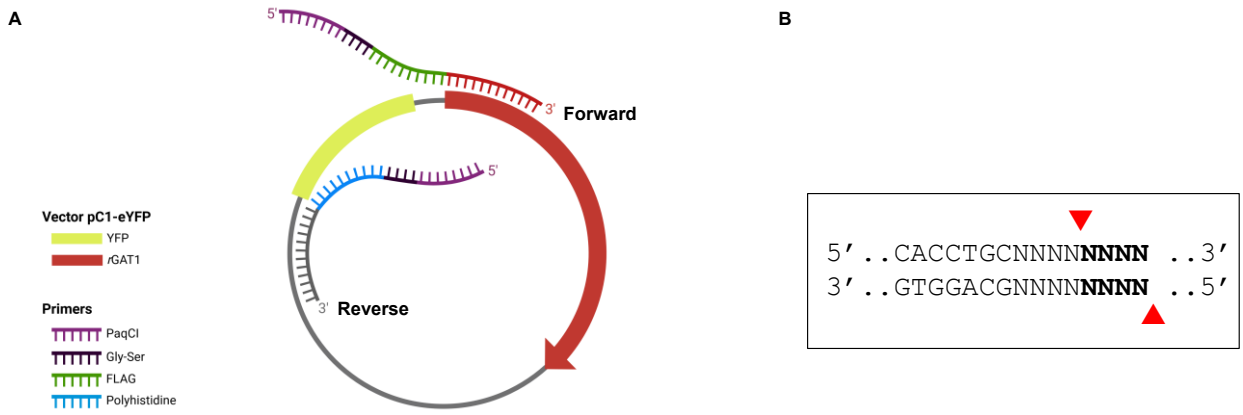

Figure 30: PCR workflow used to generate pHIS-FLAG rGAT1. a) Annealing of the forward and reverse primers on the pC1-eYFP template. Forward primer anneals to the N-terminus of *r*GAT1, and reverse primer anneals ahead of the start of the YFP gene. The sequences contained in each primer are also described. b) Sequence of the recognition and catalytic sites of the enzyme PaqC1. It binds on the 7 known nucleotides 5′ CACCTGC 3′, cleaves the sequence four nucleotides forward, and generate overhangs of 4 unspecified nucleotides shown as $(N)_4$ in bold.

After PCR, the PaqC1 site is present on both extremities of the linear product. After digestion, two sticky ends are generated, namely 5′GGCT 3′ on the top strand and 5′AGCC 3′ on the bottom strand (Figure 31).

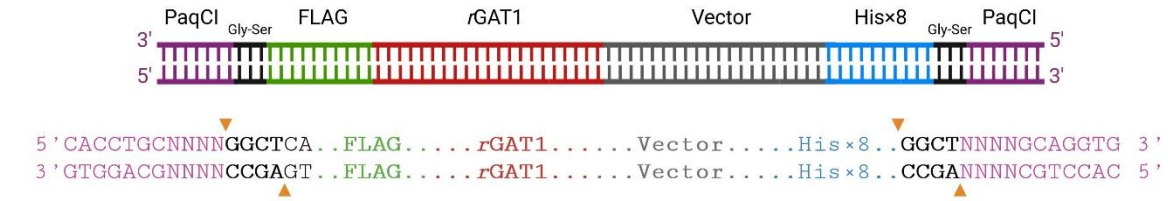

Figure 31: Representation of the linear product after PCR. The orange arrow heads show the restriction site of the PaqC1 to generate the sticky ends `5'GGCT3'` on the top strand and `5'AGCC3'` on the bottom strand.

During ligation, these sticky ends self-assemble to reconstitute the full glycine-serine linker and form the final desired circular plasmid with the help of a ligase (Figure 32).

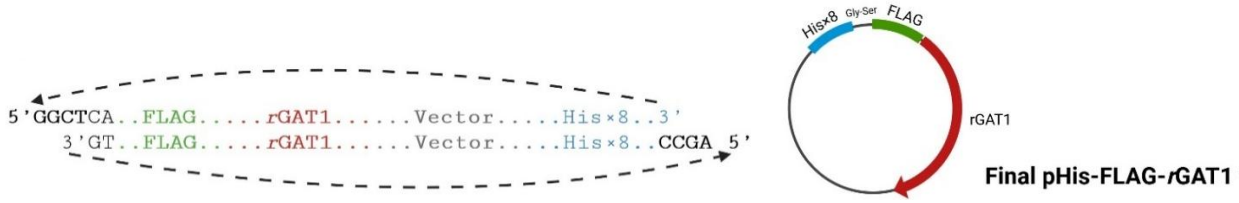

Figure 32: Reconstitution of the final template pHis-FLAG *r*GAT1 with the DNA sequences in the following order His-8-tag, glycine-serine linker, FLAG-tag and rGAT1 after ligation.

The PCR conditions used were the ones described for the Q5® high fidelity DNA polymerase (M0491S, New England Biolab) for a 50 µl volume reaction, with 10 ng of template DNA. The primers and the DNA template had a high G-C content (>50%), therefore the G-C enhancer provided was used. The PCR thermocycling procedure is detailed in the Table 5.

	Steps	Temperature	Time
	Initial denaturation	98°C	30 s
30 cycles	Denaturation Annealing Extension	98°C 58°C 72°C	10 s 25 s 25 s/kb
	Final extension	72°C	7 min
	Hold	4–10°C	

Table 5: PCR thermocycling conditions for the cloning of pHis-FLAG *r*GAT1 vector.

Then, the PCR product was digested with the PaqC1, to generate the overhangs, and DpnI to eliminate the methylated DNA template. The reaction was made with all the PCR reaction (ca.45

µl), 7 µl of Cutsmart® Buffer (B7204, New England Biolabs), 2 µl of DpnI (R0176L, 20 000 units/ml, New England Biolabs), 3 µl of PaqC1 (R07455, 10 000 units/ml, New England Biolabs) with 1 µl of PaqC1 activator, up to 70 µl with Rnase free water and incubated for 1 h at 37°C without shaking. The digested product was subsequently purified, ligated, transformed, and amplified as described later in the section general methods.

3. Genetic modifications on rGAT1 gene

i. Primers design

- *For site directed mutagenesis*

In these cases, primers were ordered online with the 5' extremity oligonucleotides phosphorylated (Eurofins, Germany). This avoids using a restriction enzyme generating overhangs for further ligation of the plasmids, but reverse PCR method was also used.

For point mutation on *r*GAT1 gene, the forward primer carries one modified codon corresponding to the downstream substituted amino acid; the reverse primer does not overlap the forward primer. They are listed in the Table 6.

Primers for site-directed mutagenesis in *r*GAT1		
GAT1 S133**E**	Forward	5' GTG CTG **GAG** TTC TGG CTG AAC 3'
	Reverse	5′ AGC TGC CGC GAG GCC C 3′
GAT1 L300**Q**	Forward	5′ G GGC **CAG** GGG TCC CTG ATT G 3′
	Reverse	5′ AGT CCG TAG GAG AAG AAG ATC TGG 3′
GAT1 G403**C**	Forward	5′ GTG GAG **TGC** TTC ATC ACT GCC 3′
	Reverse	5′ GGT ACA GAA CTG GCT GTC AAT G 3′

Table 6: Primers used for site directed mutagenesis in pHis-FLAG rGAT1 or pAMV-PA rGAT1 (used for electrophysiological experiment) plasmids.

- *For loop insertion*

For modifying the extracellular loop 2 (EL2) of *r*GAT1, the forward and the reverse primers anneal to the DNA strands outside its coding sequence. Each 5' extremity primer contains 2 pairs of 3 codons coding for a Glycine-Serine-Serine | Glycine-Serine-Serine sequence. In other words, after ligation and transcription, the EL2 will be replaced by a 12-amino acids peptide with the repeated

motif (Glycine-Serine-Serine)$_4$, supposed to give enough flexibility to the engineered loop connecting the associated transmembrane helices (Van Rosmalen, Krom, and Merkx 2017). The primers used are shown in the Table 7.

Based on the same primers, another set was designed with an asparagine in the middle of the linker sequence Table 7. This was introduced to help the trafficking of protein to the plasma membrane after glycosylation of Asparagine residue.

		Primers for insertion TM3-TM4 GSS linker	Remarks
GAT1 ΔEL2 GSS	Forward	5′ **AGC TCT GGT TCT AGT GGT** CGC TGG CCG CTA GCC ATC AC 3′	Non glycosylated
	Reverse	5′ **TCC GGA GGA GCC ACT GGA** GGA GTT GTA CAG GTA GTA G 3′	
GAT1 ΔEL2 GSS-Asn	Forward	5′ **AGC TCT GGT TCT AGT GGT** CGC TGG CCG CTA GCC ATC AC 3′	One position glycosylation
	Reverse	5′ **GTT TCC GGA GGA GCC ACT GGA** GGA GTT GTA CAG GTA GTA G 3′	

Table 7: Primers for inserting (GSS)$_4$ linker in pC1-eYFP *r*GAT1.

ii. Procedure

Briefly, 10 ng of plasmid DNA (*r*GAT1 WT, single/double mutant in pAMV-PA, pHis-FLAG or pC1-eYFP plasmids) were incubated with the reactants of the Q5® high fidelity DNA polymerase (M0491S, New England Biolab) for a 50 µl volume reaction. The GC enhancer was used according to the G-C content of the respective plasmid sequences.

The thermocycling used was the same as described earlier for pHis-FLAG cloning. When the PCR product was not detected after agarose gel analysis, a touchdown protocol was used. It consists of decreasing the initial annealing temperature of 1°C over 10 cycles. The final annealing temperature is used for the following 20 cycles (see Table 8 below). This procedure specifies initially the polymerization of the desired amplicon and avoids apparition of sporadic products (Don et al. 1991).

	Touchdown protocol		
	Steps	**Temperature**	**Time**
	Initial denaturation	98°C	30 s
10 cycles	Denaturation	98°C	10 s
	Annealing	65 → 56 °C (-1°C each cycle)	25 s
	Extension	72°C	25 s/kb
20 cycles	Denaturation	98°C	10 s
	Annealing	56°C	25 s
	Extension	72°C	25 s/kb
	Final extension	72°C	7 min
	Hold	4–10°C	

Table 8: Thermocycling condition for touchdown protocol.

4. General methods

i. Agarose gel

The presence of the PCR product was controlled on an agarose gel 0.8% (w/v) dissolved in Super buffer containing boric acid 36 mM, NaOH 10 mM (J.-H. Zhang, Wang, and Wang 2011). 500 µl of ethidium bromide were mixed to 25 ml of agarose preparation before casting. 5 µl of the PCR reaction and 1 µl of 6X gel loading dye purple (B7024S, New England Biolabs) were loaded on the gel with 3 µl of GeneRuler TM 1 kb DNA Ladder (Thermo Scientific^{TM}). The samples migrated at 120 V (constant) for 40 min in Super buffer. The presence of the PCR product was confirmed by the presence of a band at the expected size using UV lamp (GelDoc imaging system, Bio-Rad).

ii. Linear DNA purification and ligation

The PCR or digested products were purified with the QIAquick PCR purification kit (Qiagen). For elution, the Rnase Free water was previously warmed up (50 °C) and 20 µl were used to incubate the membrane (for 2 min) and elute the DNA. This concentrates the DNA. After centrifugation, the presence of DNA was controlled by measurement of the absorbance at 260 nm (Nanodrop one, double strand DNA mode, Thermo Scientific). For the ligation, 2 µl of T4 DNA ligase reaction buffer (B0202S, New England Biolabs) and 1 µl of T4 DNA ligase (M0202S, 400 000 units/ml

New England Biolabs) are used in a final reaction volume up to 20 µl with the purified linear DNA, to not dilute it. The reaction mix was incubated overnight (ca. 15 h) at 16 °C.

iii. Transformation, plasmid amplification and sequencing

50 µl aliquot of competent bacteria (see strain used according to each plasmid in the Table 9) were incubated with 10 µl of ligation product or 1 µl of purified plasmid at 100 ng/µl, for 5 min on ice. The transformation was made by heat shock for 1 min at 42°C (Engler, Kandzia, and Marillonnet 2008). For the recovery, the bacteria were incubated with 600 µl of SOC medium for 1 h, at 37°C with a constant agitation of 120 rpm. The bacterial suspension was then centrifuged for 3 min, at room temperature and 17 000×*g* (Heraus, Pico 17 centrifuge, Thermo Scientifc). The pellet was resuspended with 100 µl of supernatant, plated on agar plate (see antibiotic accordingly on Table 9Table 9) and incubated overnight at 37°C in a static incubator.

Plasmid	Bacterial strain	Selective agent on agar plate
pHF-rGAT1 WT and mutants	*E.coli* DH5α	Kanamycin 50 µg/ml
pcDNA3.1_Zeo_hSLC7A5 (LAT1)	*E.coli* DH5α	Carbenicillin 50 µg/ml
pcDNA3.1_Zeo_hSLC3A2 (CD98)		
pAMV-PA-GAT1 WT and mutants	NEB turbo competent *E.coli*	Carbenicillin 50 µg/ml Tetracycline 12.5 µg/ml

Table 9: Bacterial strains and selective agent according to each plasmid used for cloning.

The clones that grew were inoculated in 5 ml LB-Medium overnight at 37°C, 120 rpm for mini plasmid preparation. The next day, plasmid DNA was recovered and purified using the QIAprep® spin Miniprep (Qiagen, Germany) and sent for sequencing (Eurofins, Germany) to verify the accuracy of each cloning. The Table 10 summarizes the sequencing primers used according to each template.

	Primers for sequencing		Remarks
His-FLAG *r*GAT1 WT/mutant	Forward	5′ CGC AAA TGG GCG GTA GGC GTG 3′ (CMVFor, Eurofins)	
	Reverse	5′ CTT GAG GTA GTT GGA GAC 3′	
pC1-eYFP *r*GAT1 WT/ GSS linker	Forward	5' GTC GTA ACA ACT CCG CCC 3' (eGFPN1For, Eurofins)	
	Reverse	5′ CTT GAG GTA GTT GGA GAC 3′	
*r*GAT1 in pAMV-PA	Forward 1	5′ ACG CCA GGG TTT TCC CAG TC 3′	Sequencing from the 3' extremity to the middle of *r*GAT1 gene
	Forward 2	5' TGT TGT GGA AAG AGT TGT AG 3'	Sequencing from the middle of *r*GAT1 gene to the 5' extremity

Table 10: Primers used for sequencing.

II. Cell culture and expression of mammalian proteins

1. Generalities

All cell culture steps were performed under sterile conditions using a BIOAIR® Safeflow1.2 laminar flow hood. Consumables were purchased in sterile packaging and culture flasks were autoclaved to ensure sterility. Mammalian cell lines used in this worked with their associated media and uses are described in the Table 11. Prior to addition to the cells, all media were pre-warmed to 37 °C.

Mammalian cells

Name	Genotype and application	Source
Human embryonic kidney cells 293S GnT1$^-$ TetR$^+$	Gene knock-out of the glucose N-acetyltransferase (GnT1), for shorter glycosylation	CRL-3022, American Type Culture Collection (ATCC), Manassas (USA)
Human embryonic kidney cells 293S GnT1$^-$ TetR$^+$-*r*GAT1 or L300Q	HEK 293S GnT1$^-$ stably transfected with pHis-FLAG *r*GAT1 WT or L300Q, allowing its expression by doxycycline induction	Marco Roblek, Medical University of Vienna (Austria)

Cell culture	Media		Supplement
HEK Adhesion	$DMEM_c$ (culture)	Dulbecco's Modified Eagle Medium (Sigma-Aldrich)	1% (v/v) P/S (10000 U/mL Gibco®) 10% (v/v) FBS (CAPRICORN Scientific)
	$DMEM_t$ (transfection)	Dulbecco's Modified Eagle Medium (Sigma-Aldrich)	
HEK Suspension	$Freestyle_c$ (culture)	FreeStyle™ 293 Expression Medium (Gibco™)	1% (v/v) P/S (10000 U/mL Gibco®) 1% (v/v) FBS (CAPRICORN Scientific)
	$Freestyle_t$ (transfection)	FreeStyle™ 293 Expression Medium (Gibco™)	

Table 11: Cell lines used, media and supplements for adherent or suspension cell culture and transient transfection. P/S: Penicillin/Streptomycin, FBS: Fetal Bovine Serum.

2. Adherent cell culture

i. Cell thawing

Frozen cryo-stocks were quickly thawed at 37 °C, added to 13 mL pre-warmed $DMEM_c$ and centrifuged for 3 min at 300×g, room temperature (RT) (Allegra X-15R Beckman Coulter). The

supernatant was discarded, and the cell pellet was resuspended in 1 ml of $DMEM_c$ before being transferred into 7 ml $DMEM_c$ in a T25 adherent cell culture flask.

ii. Cell splitting

HEK293S GnTI$^-$ cells were grown in $DMEM_c$ at 37°C and 5% CO_2. Every 2 – 3 days, after reaching nearly 100% confluence, the culture medium was discarded, and cells were washed with Phosphate Buffered Saline (PBS) for 10 s before being incubated for 3 min at 37°C with the respective amount of Trypsin-EDTA (10X, sterile-filtered, 5.0 g porcine trypsin and 2 g EDTA, 4.Na per liter, T2610 Sigma-Aldrich) according to each flask size (Table 12). The action of trypsin was stopped by adding the corresponding amount of $DMEM_c$. After resuspension, the cells were split (usually 1:5 or 1:10) and $DMEM_c$ was added up to the growth volume (Table 12).

	T25	**T75**	**T175**
Growth volume	**7 mL**	**20 mL**	**40 mL**
PBS	1 mL	3 mL	5 mL
Trypsin-EDTA	1 mL	3 mL	4 mL
$DMEM_c$ for splitting	4 mL	7 mL	6 mL
Total splitting volume	5 mL	10 mL	10 mL
Volume of cell suspension associated splitting dilution	1 ml (1:5)	2 ml (1:5) 1 ml (1:10)	2 ml (1:5) 1 ml (1:10)
Volume of DMEMc up to the growth volume	6 ml	18-19 ml	38-39 ml

Table 12: Volumes used for cultivating and splitting depending on the flask size.

iii. Cell seeding for protein expression test and immunocytochemistry

After splitting, the adherent cells resuspended were counted manually with a glass counting chamber (Neubauer improved). For test expression, the cell suspension was diluted to a cell density of $4 \cdot 10^5$ cells/mL and used to seed a 6-well plate, with 2 mL per well. Contrastingly, for immunocytochemistry, adherent cells are seeded in 6-well plate at 1.10^5 cells/ml (2 ml per well) and grown on a glass circular coverslip (Siliconized glass circle cover slides 22 mm diameter, Hampton research) previously washed with ethanol 70%.

The plates are incubated at 37 °C, 5% CO_2 for 24 h. Before transient transfection, the media in each well was removed; the cells were washed with 1 ml PBS and incubated again with 2 ml of $DMEM_c$.

iv. Transient transfection

- *For protein test expression*

The transient transfection was performed following the work of Longo and co-workers (Longo et al. 2013) using the transfection agent polyethyleneimine (PEI) which the structure is represented on Figure 33.

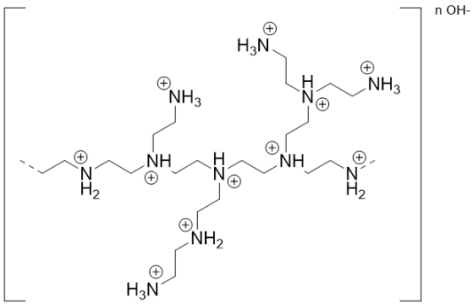

Figure 33: Chemical structure of branched Polyethyleneimine (PEI).

This highly positively charged polymer neutralizes the negative charge of the DNA backbone and facilitates the entry of exogenous DNAs into the cells and the nuclear envelope. According to the authors 1 µg of DNA per 1 mL of culture with a cell density of 1.10^6 cells/ml is used as standard while the quantity of PEI is variable and is a crucial factor for the final protein expression yield. Thus, the right DNA:PEI ratio needs to be determined for a given protein (Longo et al. 2013). DNA and PEI were diluted with $DMEM_t$ in 1/20 of the final well volume, i.e 100 µl when the final volume was 2 ml. To form the polyplex DNA-PEI, solutions were incubated 20 min and consequently dropped in the wells for expression.

For eYFP rGAT1 WT or L300Q, 2 µg of DNA was used while solutions of PEI varied between a range of 1:1, 1:2, 1:3, 1:4 1:5 DNA to PEI ratio (in weight). The expression occurred for 72 h at 37°C and was followed every 24 h with the fluorescence signal from the YFP, under the microscope EVOS FL (Invitrogen, Thermo Fisher Scientific, USA).

Based on the results for eYFP-rGAT1, 2 µg of DNA pHis-FLAG rGAT1 were tested with the DNA:PEI ratio of 1:3 with the same expression time (72 h).

For LAT1/CD98, which was expressed from two different plasmids, various DNA amounts and DNA:PEI ratios were tested to evaluate optimal transfection conditions. The expression occurred for 48 h. All conditions (DNA and PEI quantities) for any protein are summarized in the Table 13below:

	Protein	DNA:PEI	DNA (µg)	$DMEM_t$ (µl) to dilute DNA	PEI (µg)	$DMEM_t$ (µl) to dilute PEI
	eYFP-*r*GAT1 WT/L300Q	1:1	2	100	2	100
		1:2			4	
		1:3			6	
		1:4			8	
		1:5			10	
	HF-*r*GAT1	1:3	2	100	6	100
Heterodimer Co-transfection	LAT1 / CD98	1:2	2	100	8	100
	LAT1 / CD98	1:3	2	100	12	100
	LAT1 / CD98	1:4	2	100	16	100
	LAT1 / CD98	1:5	2	100	20	100
	LAT1 / CD98	1:3	2 / 4	100	18	100

Table 13: Transient transfection conditions for *r*GAT1 (eYFP and HF) and LAT1/CD98. A range of DNA:PEI ratio was tested for the different proteins. For LAT1/CD98 the ratio DNA to DNA was also tested with a total ratio DNA to PEI 1:3 (Last row).

- *For cyto-immunochemistry*

The same transient transfection protocol was used but with different quantities of DNA:PEI than previously. They are summarized in the Table 14.

	Protein	DNA:PEI	DNA (µg)	$DMEM_t$ (µl) to dilute DNA	PEI (µg)	$DMEM_t$ (µl) to dilute PEI
	eYFP-*r*GAT1	1:3	1.6	100	4.8	100
Heterodimer Co-transfection	LAT1 CD98	1:3	1.6	100	9.6	100
	LAT1 CD98	1:3	1.6 3.2	100	14.4	100
	LAT1 CD98	1:3	1.6 0	100	4.8	100
	LAT1 CD98	1:3	0 1.6	100	4.8	100

Table 14: Transient transfection conditions for GAT1 eYFP tagged and LAT1/CD98 for immunofluorescence experiments.

v. Harvest and evaluation of expression tests for eYFP/His-FLAG rGAT1 WT and mutant and LAT1/CD98

After 48 h (*h*LAT1/CD98) or 72 h (*r*GAT1) of expression, the medium was removed from each well, and the cells were washed with PBS. After its removal, cells were resuspended in 1 mL of PBS and centrifuged for 10 min at 17 000 × g, 4°C, (Centrifuge 5415R). The supernatant was discarded; the cell pellets were weighed and resuspended in 5 mL of solubilization buffer per milligram of cells. The buffer used for *r*GAT1 and *h*LAT1/CD98 are described in the following Table 15.

Protein	Solubilization buffer
eYFP/His-FLAG- *r*GAT1 WT/mutant	20 mM Tris pH 7,5, 150 mM NaCl, **4 % DDM, 0,8 % cholesteryl hemisuccinate (CHS)**, 0,01 mg/ml Dnase, 1 mM Pefabloc®, 0,5 mg/ml Pepstatine, 2 µg/ml Leupeptine, 1 µg/ml Aprotinine.
***h*LAT1/CD98**	20 mM Tris pH 7,5, 150 mM NaCl, **1,5 % DDM, 0,1 % LMNG, 0,3 %, cholesteryl hemisuccinate (CHS)** 0,01 mg/ml Dnase, 1 mM Pefabloc®, 0,5 mg/ml Pepstatine, 2 µg/ml Leupeptine, 1 µg/ml Aprotinine.

Table 15: Composition of GAT1 and LAT/CD98 solubilization buffers for expression tests.

After 1 hour of incubation on a rotary shaker at 4°C, the samples were centrifuged (17 000 × g, 4°C, 10 min) and 20 µl from the supernatants containing the solubilized proteins were mixed to 4 µl of 6X Lämmli loading buffer (Tris 350 mM pH 6,8, glycerol 30 % (v/v), SDS 10 % (w/v), β-mercaptoethanol 10 % (v/v), bromophenol Blue 10 % (w/v)) to dilute it to 1X, before being loaded onto an SDS-PAGE for protein expression analysis by western blot (For the procedure, ***Cf: Material and methods, III.3 Protein analysis***).

vi. Semi quantification on ImageJ

- *eYFP fluorescence of rGAT1 WT and L300Q mutant*

Images collected on the EVOS microscope were converted into 8-bit files and duplicated. One image is filtered with the gaussian blur with a 200 radius and used for background subtraction. After, a threshold is set to consider only the fluorescence present in the plasma membrane. Then the fluorescence signal is assessed by limiting the area measurement to the threshold. At least four images with more than 60 cells per image are used for each point plotted. Graphs are made on Graph Pad Prism 8 using the violin representation.

- *Expression of rGAT1 WT and L300Q mutant on western blot*

Images were converted into 8-bit and a threshold is set to select the bands of interest for quantification with the gel function. Each membrane is measured twice for technical replicate. For graphical representation, data are normalized with the values obtained for rGAT1 WT DNA:PEI ratio 1:3 expressed for 72 h.

3. Suspension cell culture

i. Cell adaptation to suspension

Adherent cells were split as already described and the cell suspension was centrifuged for 3 min at 300 × g, RT. The supernatant was discarded, the cell pellet was resuspended with 1 mL FreeStyle$_c$, added to 30 ml of the same media in a spinner flask ad grown at 37 °C, 5% humidity, 5% CO_2 with constant agitation of 75 rpm. Additional FreeStyle$_c$ was added every 2-3 days to keep the cell density at 1.10^6 cells/mL. Suspension cell culture is kept in spinner flask for rGAT1

cell lines (see ***Large scale expression for GAT1 WT***) or *h*ALT1/CD98 expression (see ***Small and large scale expression of LAT1/CD98)***. The cell suspension was transferred in a 2-litre vent cap Erlenmeyer (Corning) for rGAT1 WT transiently transfected; The cells are grown at 37 °C, 5% humidity, 8% CO_2 on a shaker plate at 125 rpm.

ii. Small scale expression for GAT1 WT

Different suspension cell culture conditions were tested (Table 16). In each case, 200 mL of cell suspension at 1.10^6 cells/mL were transiently transfected with 200 µg DNA pHis-FLAG-*r*GAT1 and 600 µg PEI diluted both in 20 ml of FreeStyle$_T$ and incubated 20 min before transfection. Cells were grown during 72 h for expression.

Condition	Bottle type	Circular agitation by	Speed (rpm)	CO_2 (%)	Temp. (°C)	Pellet weigh after harvest (g)
1	Spinner Flask	Stirring	75	5	37	1.4
2				8		0.517
3			120	5		0.977
4	Vent Erlenmeyer	Shaking	120	8		0.734

Table 16: Conditions tested for small scale expression of *r*GAT1 WT.

iii. Large scale expression for GAT1 WT

For large scale expression by transient transfection, 1 liter of cell suspension at 1.10^6 cells/ml in FreeStyle$_C$ are transfected with 1 mg of DNA and 3 mg of PEI (DNA:PEI 1:3), both diluted in 50 ml of Freestyle$_T$ and incubated for 20 min before incubation with the cells. Protein was expressed for 72 h in vent Erlenmeyer on shaking plate, 125 rpm at 37 °C, 8% CO_2.

For large scale expression by doxycycline induction, HEK293S GnTI$^-$ TetR$^+$ were permanently transfected with pHis-FLAG-rGAT1 WT and L300Q to form two stable cell lines kindly made by Marko Roblek (Medical university, Vienna). 1 liter of cell suspension at 1.10^6 cells/ml in FreeStyle$_C$ was induced with 5 µg/ml doxycycline. Protein was expressed for 72 h in spinner flask at 75 rpm, 37 degrees, 5% CO_2.

iv. Small- and large-scale expression of LAT/CD98

For small scale expression, the Table 17, summarizes the different conditions tested, inspired from initial results (Yan et al. 2021). The DNA and the respective amount of PEI were diluted with Freestyle$_T$ to 1/20 of the final culture volume to transfect (45 ml). After incubating the mixture at room temperature for 15 minutes, it was added to the cells, which were grown for 48 hours before being harvested.

Condition	DNA:PEI	LAT1:CD98	Culture (ml)	Cell density (cells/mL)	LAT1 (µg)	CD98 (µg)	DNA total (µg)	FreeStyle$_T$ (ml) to dilute DNA	PEI total (µg)	FreeStyle$_T$ (ml) to dilute PEI
Y	1:2	1:1	45	2×10^6	45	45	90	2.25	180	2.25
1	1:2	1:2		1×10^6		90	135		270	
2	1:3	1:2							405	
3	1:3	1:1				45	90		270	

Table 17: LAT1/CD98 small scale expression conditions tested in this work. The condition Y was tested from previous published results (Yan et al. 2021).

For larger scale expression, 500 ml of final culture volume at 1.10^6 cells/ml were transfected following the conditions 2 and 3 already tested and detailed in the Table 18.

Condition	DNA:PEI	LAT1:CD98	Culture (ml)	Cell density (cells/mL)	LAT1 (µg)	CD98 (µg)	DNA total (µg)	FreeStyle$_T$ (ml) to dilute DNA	PEI total (µg)	FreeStyle$_T$ (ml) to dilute PEI
2	1:3	1:2	500	1.10^6	500	1000	1500	25	4500	25
3	1:3	1:1				500	1000		3000	

Table 18: Conditions used for large scale expression of *h*LAT1/CD98 based on the previous conditions tested in small scale.

III. Protein purification protocols, analysis and reconstitution in proteoliposomes

1. Purification of HF-*r*GAT1 WT

Cells were harvested at 10 000×*g* at 4°C during 30 min. The cell pellet was resuspended in 10 ml of cell wash buffer (10 mM Hepes pH 7,5, 150 mM NaCl, 10 mM KCl, 1 mM $MgCl_2$, 10 µg/ml DNase, 0,5 mM Pefabloc) and centrifuged at 20 000×*g* at 4°C during 30 min. The cell pellet was resuspended and homogenized with glass homogenizer in buffer A (20 mM Hepes pH 7,5, 200 mM NaCl, 30 mM imidazole), supplemented with detergents. Initially DDM/CHS was used (2% DDM/0.4% CHS for solubilization and 0.05% DDM/0.01% CHS for the downstream purification steps), but further it was replaced by LMNG/CHS (see explanations in results section).
2% LMNG/ 0.2% CHS were added to the homogenized cell lysate and rGAT1 WT or L300Q mutant were solubilized for 2.5 h on a rotary shaker at 4°C and recovered in the supernatant after ultracentrifugation at 120 000×*g* at 4°C during 70 min (Optima XPN-100 ultracentrifuge, rotor Ti 70.1). The supernatant was then load on 0,5 ml bed volume of Ni-NTA beads (Ni-NTA Agarose 25 ml, Quiagen) previously equilibrated for 1 h on a rotary shaker at 4°C with 4 CV of buffer A Supplemented with 0.001% LMNG/0.0001% CHS. The protein was allowed to bind to the Ni-NTA beads overnight in batch on a rotary shaker at 4°C. The next day, the slurry was transferred to a gravity column, and the resin was washed with 10 CV of buffer A with 0,001% LMNG/0,0001% CHS. The protein was eluted with a buffer containing 20 mM Hepes pH 7,5 200 mM NaCl, 200 mM imidazole, 0,001% LMNG/0,0001% CHS. Finaly, the column was washed with a buffer containing 50 mM Hepes pH 7,5 200 mM NaCl, 500 mM imidazole, 0,001% LMNG/0,0001% CHS (0.05% DDM/0.01% CHS) to control if all the protein were washed off the resin during the elution.

To remove the imidazole from the protein sample, the elution fractions were pooled, and loaded on a PD-10 desalting column (Cytiva) to exchange the elution buffer against the buffer B (10 mM Hepes, 150 mM NaCl, 0,001% LMNG/0,0001% CHS). After desalting, the fractions containing the protein were pooled and loaded three times on 1 ml bed volume of anti-FLAG resin (Anti-FLAG M2 antibody resin, Sigma-Aldrich) previously equilibrated with 5 CV of buffer B. The resin was washed with 10 CV of the same buffer and the protein was eluted with 5 CV of

buffer B supplemented with FLAG peptide (F3290, Sigma Aldrich) at 150 µg/ml (150 µM). A final wash of the column was made with 5 CV of a solution of 100 mM Glycine pH 3.5.

All the different steps just described were analyzed by SDS-PAGE and Western blot to control the presence and the purity of the protein. The latter was also sent for a mass spectrometry analysis (performed by the Dr. Astrid Bruckman in Regensburg).

2. Purification LAT1/CD98

The complex LAT1/CD98 is well described in the literature and was expressed and purified according to previous results (Rodriguez et al. 2021; Yan et al. 2019, 2021).
Transfected cells were harvested by centrifugation for 30 min at 10.000×*g*, 4°C. The cell pellets were weighed and resuspended in 5 mL of buffer containing 25 mM Tris.HCl pH 8.0, 150 mM NaCl, 0.7 µg/mL Pepstatin, 5 µg/mL Leupeptin, 1.3 µg/mL Aprotinin. Cells were mechanically lysed with a glass homogenizer and supplemented with 1% LMNG/0.1% CHS (w/v) for solubilization during 2 h at 4 °C on a rotary shaker. Solubilized proteins were recovered in the supernatant after centrifugation for 70 min at 120 000×*g*, 4°C (Optima XPN-100 ultracentrifuge, rotor: Ti 70.1) and loaded on 1 ml bed volume of anti-FLAG® M2 affinity resin previously equilibrated with 5 CVs of LAT1 Equilibration Buffer I (25 mM TRIS/HCl pH 8.0, 150 mM NaCl, 0.01% LMNG/0.001%CHS). The flow-through was loaded twice to ensure optimal binding. Then, the resin was washed with 10 CV of LAT1 Wash Buffer (25 mM Tris.HCl pH 8.0, 150 mM NaCl, 0.04% GDN (w/v)). To elute the protein, 200 µg/ml (200 µM) of FLAG peptide was added to 5 CV of LAT1 Wash Buffer. The resin was restored with 5 CV glycine 100 mM, pH 3.5.
The eluted fractions containing protein (visible on SDS PAGE and/or western blot) were pooled and loaded on 2 mL bed volume of Strep-Tactin® Superflow (IBA Lifesciences) resin previously equilibrated with 5 CV of LAT1 Wash buffer. Again, the flow-through was loaded twice to ensure optimal binding on the resin. The latter was washed with 10 CV Wash Buffer LAT1 and the protein complex was eluted with 6 CV of the same buffer supplemented with 2.5 mM of Desthiobiotin.

3. Protein analysis by sodium dodecyl sulphate-polyacrylamide gel electrophoresis (SDS-PAGE) and western blot

All the purifications steps were analyzed by SDS-PAGE either by Coomassie blue staining or western blot. As the threshold of detection of Coomassie staining is lower (minimum 0.1 to 0.5 µg of protein per band (Brunelle and Green 2014)) than for western blot, 12 µl and 20 µl from each fraction were loaded respectively for western blot and Coomassie staining. To each fraction, Lämmeli sample buffer 6X (Tris 350 mM pH 6,8, glycerol 30 % (v/v), SDS 10 % (w/v), β-mercaptoethanol 10 % (v/v), bromophenol Blue 10 % (w/v)) was added to dilute it to 1X. 3 µl of PAGE ruler protein ladder (Thermofisher) was also loaded on a 13,5 % (v/v) acrylamide/Bis-acrylamide gel that covers the molecular weight range from 180 to 25-10 kDa. The migration was performed at 300 V, constant intensity of 45 mA for 35 min in a running buffer containing 25 mM Tris pH 8,0, 200 mM glycine, 1 % SDS.

For Coomassie blue analysis, the gel was stained for 30 min in a Coomassie blue solution (0.1% (w/v) Brillant R Coomassie, 30% (v/v) Ethanol, 10% (v/v) Acetic Acid), then quickly washed with water and destained for 30 min in a solution composed of ethanol 20 % (v/v), acetic acid 10 % (v/v).

Fast silver staining (nanogram detection threshold) was used to detect low amount of protein. All the solutions used are described in the Table 19.

	Final concentration	**Up to 50 ml water**
1. Fixing solution	40% (v/v) methanol	20 ml
	13.5% (v/v) formalin	18.2 ml (37% formaldehyde)
2. Sodium thiosulfate	0.02% (m/v) sodium thiosulfate	0.0157 g
3. Silver Nitrate	0.1% (m/v) silver nitrate	0.05 g
4. Developing solution	3% (m/v) sodium carbonate	1.5 g
	0.05% (v/v) formalin	68 µl (37% formaldehyde)
	0.000016% (m/v) sodium thiosulfate	40 µl from **2.**
5. Stopping solution	2.3 M citric acid	22 g

Table 19: Solutions used for gel fast silver staining.

Briefly, the gel was alternatively soaked 10 min in fixing solution, washed twice for 1 min in water, soaked 1 min in sodium thiosulfate solution, rinsed for 20 s in water, and soaked 10 min in silver nitrate solution. The next wash in water contains a small amount of developing solution (1 ml for 10-15 ml water). Finally, the gel was incubated in the developing solution, and stopping solution was added once bands appeared (after 2-3 min).

SDS-PAGE further used for mass spectrometry analysis were stained in Coomassie blue solution, or with a special silver staining kit (Pierce™ Silver stain for mass spectrometry, Thermofisher Scientific) when the detection threshold for Coomassie blue was not reached. Briefly, once bands appeared after staining, they were immediately cut and destained in acetonitrile solution for further mass spectrometry analysis.

After SDS PAGE migration, for western blot analysis, the protein samples were transferred with a semi-liquid system (Biometra, 8 W, 0.5 l/min, Analytic Jena Company) on a polyvinylidene fluoride (PVDF) membrane (Immobilon® -FL, 0.45 µm, Millipore) previously activated in absolute methanol. Whatman paper (GB003, Cytiva) are soaked in a transfer buffer containing 25 mM Tris pH 8,0, 150 mM glycine. The activated membrane and the gel were placed between four soaked Whatman papers. The transfer was operated in an electric field of 25 V, 5 W with constant intensity (0,2 mA) for 45 min. Then, the membrane was incubated in a blocking solution of Bovine Serum Albumin (BSA) 3 % (w/v), in Tris buffered saline (TBS, 10 mM Tris pH 7,5, 150 mM NaCl), for 1 h at room temperature. The membrane was quickly washed twice for 30 s with 5 ml of TBS and then incubated with the primary antibody diluted in 10 ml of blocking solution for 1 h at room temperature. The Table 20 summarizes the different dilutions and the primary antibodies used according to the protein studied during this thesis.
The membrane was washed again with PBS and then incubated with a secondary antibody conjugated with alkaline phosphatase and diluted in 10 ml of blocking solution. The secondary antibody used depends on the species in which the primary antibody was synthetized. Antibodies and dilutions are mentioned in the Table 21. Again, the membrane was washed before developing with 10 ml of alkaline phosphatase buffer (100 mM Tris pH 9, 150 mM NaCl, 1 mM $MgCl_2$, 0.25 mg/ml 5-bromo-4-chloro-3-indolyl-phophate (BCIP) and 0.5 mg/ml Nitro-blue tetrazolium (NBT)). After apparition of bands, the reaction was stopped by adding water.

Primary antibodies					
Target	**Antibody name**	**Specie production**	**Dilution used**	**Usage**	**Source/Company**
FLAG® tag	Monoclonal anti-FLAG® M2, F1804	Mouse	1:600 1:5000	Immunofluorescence Western blot	Sigma Aldrich, St Louis, USA
*r*GAT1	Anti-SLC6A1 antibody, HPA013341	Rabbit	1:200 1:1000	Immunofluorescence Western blot	
Green/Yellow Fluorescent protein	Monoclonal anti Green Fluorescent Protein, G6539	Mouse	1:2000	Western blot	
Poly-Histidine tag	Monoclonal Anti-polyHistidine antibody, H1029	Mouse	1:5000	Western blot	
*c*BGT1	Anti human, rat, mouse BGT1 antibody, 67700-1-Ig	Mouse	1:4000	Western blot	Proteintech Group, Inc, Rosemont, USA
*h*CD98	CD98/SLC3A2 Monoclonal antibody, 66883-1-Ig	Mouse	1:500 1:5000	Immunofluorescence Western blot	
*h*LAT1	SLC7A5 Polyclonal Antibody 28670	Rabbit	1:500 1:5000	Immunofluorescence Western blot	
Strep-Tag	StrepMAB-Classic IgG1, 2-1507-001	Mouse	1:5000	Western blot	IBA Lifesciences GmbH, Goettingen, Germany

Table 20: Primary antibodies used. The utilization (Western blot and/or immunofluorescence) and the associated dilution are also described.

Secondary antibodies						
Target	**Antibody name**	**Specie production**	**Conjugation**	**Dilution used**	**usage**	**Source/Company**
Primary antibodies produced in Rabbit	Anti-Rabbit IgG	Goat	Alkaline Phosphatase	1:5000	Western blot	Abcam Ltd., Cambridge, UK
Primary antibodies produced in mouse	Anti-Mouse IgG antibody, A2418	Rabbit	Alkaline Phosphatase	1:5000	Western blot	Sigma Aldrich, St Louis, USA
Primary antibodies produced in mouse	Anti-Mouse IgG (H+L) Highly Cross-Adsorbed Secondary Antibody	Donkey	Alexa Fluor™ Plus 647	1:600	Immunofluorescence	Invitrogen, Thermo Fisher
Primary antibodies produced in Rabbit	Anti-Rabbit IgG	Goat	Cy3 fluorophore	1:500	Immufluorecsence	

Table 21: Secondary antibodies used for Western blot and/or immunofluorescence with associated dilutions.

4. Protein concentration determination

To determine the protein concentration at the end of each purification the kit Pierce™ BCA protein assay (Thermo Scientific) was used. The threshold of detection is 5 µg/ml. A calibration curve is generated with known concentrations of BSA (0, 25, 125, 250, 500, 750, 1000, 1500, 2000 µg/mL). to limit the error, the standard curve was done in replicate, and four replicates were prepared for each sample. The assay was performed in a 96-well plate where 10 µl of protein (for the calibration curve or the protein of interest) are incubated with 200 µl of a mixture BCA reagent:copper (II) ion suspension in the volume ratio 50:1. After incubation at 37°C for 30 min, the absorbance at 562 nm was measured on a microplate reader (TECAN sunrise, Germany).

As a complement, the Nanodrop technology was also used in the mode 1 ABS=1 mg/ml with the baseline made at 333 nm (Nanodrop one, Thermo Scientific). 3 µl were used for blanking and measuring the sample concentration. The absorbance at 280 nm is correlated to the protein concentration according to the following Equation 1.

$$A = \varepsilon \times C \times l$$

Equation 1: Concentration determination related to absorbance. A: absorbance of solution, ε molar extension coefficient of the protein ($L.mol^{-1}.cm^{-1}$), C: protein concentration (mol/l), l: optical path (cm).

The Table 22 describes the molar extension coefficient of every protein studied in this work.

Protein		**Molar extinction coefficient with oxidized cysteine residues ($M^{-1}.cm^{-1}$)**
His-FLAG- rGAT1		157065
hLAT1/CD98	*h*LAT1	79590
	*h*CD98	85160
	*h*LAT1/CD98	164750

Table 22: Molar extinction coefficients of the proteins purified in this work. The parameters were computed on ProtParam (Gasteiger E., Hoogland C., Gattiker A., Duvaud S., Wilkins M.R., Appel R.D., Bairoch A.; Protein Identification and Analysis Tools on the Expasy server, Swiss Institute of Bioinformatics). Only the coefficients with oxidized cysteines were used as all buffers used for the different proteins were without reductive component.

5. Size Exclusion chromatography (SEC)

Size exclusion Chromatography is based on a mobile phase (sample running through the column) and a stationary phase constituted of a porous bead, allowing proteins to be eluted based on their Stokes radius. In the case of membrane protein, not only the protein but also the surrounding micelle plays a role in the elution volume. Therefore, a difference should be made between the elution volume related to standard calibration based on molecular weight, and the elution volume corresponding to the real Stokes radius of the protein/micelle complex. The Table 23 presents the corresponding molecular weight-Stokes radius-elution volume relationship for the column Superose^{TM} 6 increase 5/150 GL (molecular weight range 5 kDa to 5.10^3 kDa, 3 ml column volume) for ideal globular proteins.

Globular protein	**Source**	**Approximate Molecular weight (kDa)**	**Stokes radius (Rs) (nm)**	**Elution volume on Superose^{TM} 6 increase 5/150 GL (ml)**
Thyroglobulin	Bovine thyroid	669	8.6	1.7
Apo-Ferritin	Horse spleen	443	6.1	1.9
Aldolase	Rabbit muscle	158	4.8	2.1
Carbonic anhydrase	Bovine erythrocyte	29	2.1	2.3

Table 23: Calibration proteins used for SEC columns associated with the Stokes radius according to their elution volume ((La Verde, Dominici, and Astegno 2017; SEC principles and methods, handbook 2020) and SuperoseTM 6 increase 5/150 GL instructions).

This distinction is important; a membrane protein with an elution volume of 1.9 ml does not correspond to a protein of 443 kDa, but an effective Stokes radius of a 69 kDa protein surrounded by a LMNG/CHS detergent micelle like for *r*GAT1 (*Cf:* ***Results***).

Before vitrification, size exclusion chromatography was performed for every sample (*r*GAT1 WT/mutants, *h*LAT1/CD98 in detergent) with the automated chromatography system ÄktaMicro and the column Superose^{TM} 6 increase 5/150 GL (Cytiva).

The column, stored with ethanol 20 % (v/v), was first rinsed with 2 CV of water and then equilibrated with 2 CV of buffer (see Table 24 the buffer used according to the protein purified). Prior to the polishing step, the sample was concentrated to 50 µl (injection loop volume) with molecular cut of concentrator (Amicon, Merck) adapted to the protein purified (Table 24). The elution was executed with a flow rate set at 0.2 ml/min and was followed on the software Unicorn 7 (Cytiva) by measuring the absorbance at 280 nm.

The fractions covering the main absorption peak on chromatogram were pooled and concentrated with the appropriate concentrator to minimum 1 mg/ml (measured by BCA and Absorbance at 280 nm). In the case of rGAT1 WT/L300Q, the concentrated sample was incubated again with 10 mM GABA to saturate their binding sites to promote an occluded conformation before freezing (Zhu et al. 2023).

Protein	Size exclusion buffer	Concentrator molecular weight cut-off
*h*LAT1/CD98	25 mM Tris pH 8.0, 150 mM NaCl, 0.02% GDN	100 kDa
*r*GAT1 (WT and mutant)	10 mM Hepes, 150 mM NaCl, 10 mM GABA, 0,001% LMNG/0,0001% CHS	50 kDa

Table 24: SEC buffers, and concentrator molecular weight cut-off used according to the protein purified.

6. Reconstitution of rGAT1 WT in proteoliposome

As *r*GAT1 (WT and mutant) was solubilized and purified with LMNG/CHS, the protein was reconstituted following the method described by detergent removal, without using SM2-Biobeads (Godoy-Hernandez et al. 2023).

Brain total extracts lipids (Avanti) dissolved in chloroform at the concentration of 20 mg/ml were dried under nitrogen steam for 2 h. The lipidic film was resuspended under constant agitation for 1 h at room temperature at a final concentration of 10 mg/ml with intracellular buffer (30 mM Hepes pH 7.6, 140 mM KCl, 10 mM NaCl, 5 mM $MgCl_2$). The lipid suspension was extruded on a 0.4 µm polycarbonate membrane. For a Protein Lipid Ratio (LPR) of 1:10, 1:25, 1:30 or 1:50, respectively 1, 2.5, 3, 5 mg of suspension were destabilized for 5 min at room temperature with 0.5 % (v/v) Triton X-100. Then, 100 µg of protein were added and incubated for 45 min on a rotary

shaker at room temperature. To remove detergent traces, a G25 sephadex resin (8.2 ml column volume, Cytiva) was used and previously equilibrated with 2 CV of intracellular buffer. After buffer exchange, the protein reconstituted was centrifuged at 200 000 ×*g* 45 min 15°C. The resulting pellet was washed with 1 ml of 30 mM Hepes buffer pH 7.6 without salt and centrifuged again at 200 000 ×*g* 45 min 15°C. Finally, the pellet was resuspended with the same Hepes buffer to get a final concentration of 40 mg/ml of lipid. When proteoliposomes were used for measurement, they were diluted to a concentration of 1 mg/ml of lipid with Hepes buffer containing a physiological extracellular concentration of 140 mM NaCl.

IV. Expression/Purification of *r*GAT1 WT in extracellular vesicles

This method was made in collaboration with Vincent Delauzin and Beatrice Amigues at CytobodX (Marseille, France).

1. Molecular biology

Rat GAT1 with a FLAG tag at thr N-terminal extremity was cloned in pCAGGS-mcherry vector (Addgene plasmid #41583) and transformed in *E.coli* DH5α (New England Biolab) prior to selection on agar plate containing ampicillin at 50 µg/ml. Plasmid was extracted from bacteria and purified with a maxi plasmid preparation (NucleoBond Xtra Maxi EF, Macherey-Nagel).

2. Cell culture, transfection and expression

Confluent EBNA HEK293 cells (REF) were detached with 5 ml of trypsin-EDTA (10X, sterile-filtered, 5.0 g porcine trypsin and 2 g EDTA, 4.Na per liter, T2610 Sigma-Aldrich) and resuspended with 5 ml of DMEM media (Dulbecco's modified Eagles medium 4,5 g/l glucose L-glutamine and sodium pyruvate, CORNING) supplemented with 10 % Fetal bovine serum (FBS , 10270 Gibco). The whole suspension is seeded in two 175 cm² flask (Nunc™ EasYFlasks™ 175 cm², 159910, Thermo Scientific) containing 40 ml of DMEM media with 10 % FBS. For the transfection, the DNA to Lipofectamine® 2000 Invitrogen, 1 mg/ml,) ratio were previously determined (Delauzun et al. 2020). 60 µg of plasmid and 150 µl of Lipofectamine 2000 were both diluted in 4 ml of Opti-MEM media (Opti-MEM® 1X reduced serum Medium, Gibco). To form

the lipofection complex, both solutions were mixed, incubated for 10 min and then split into two flasks. After 15 h, the media was exchanged with 30 ml in each flask of medium FreeStyle™ 293 Expression medium GlutaMAX™ (12338, Gibco) without FBS, avoiding the contamination by extracellular vesicles that it contains. Cells are incubated at 37°C for 6 days for the enrichment of the culture media in extracellular vesicles.

3. Extracellular vesicles purification

The supernatant was then recovered and submitted to three centrifugation cycles (centrifuge 5910 Ri Eppendorf) 400×*g* 10 min, then 3000×*g* 10 min and finally 10 000×*g* 30 min, at 10 °C. 60 ml of supernatant was loaded on the column Hitrap Capto Core 700 (1 ml, Cytiva) previously equilibrated with 5 CV of DPBS (Dulbbeco's phosphate buffered Saline D8537 Sigma-Aldrich). The flowthrough (65 ml) was recovered and concentrated with a centrifugal concentrator of 10 kDa MWCO (Merck) up to 250 µl, then injected on the Superose 16/60 size exclusion chromatography column (Cytiva) previously equilibrated with 2 CV of PBS. The elution fractions under the absorbance peak are pooled and concentrated until having an optical density of 0,1 at 280 nm (NanodropOne, Thermo Scientific).

V. Transmission (Cryo)-electron microscopy (TEM and Cryo-EM)

1. (Cryo)-Transmission electron microscopy principle

They are imaging techniques of biological samples (proteins, extracellular vesicles, proteoliposomes) using electrons that are transmitted and collected on a camera. TEM is limited by a resolution of 2 nm therefore it is used to observe the overall shape of a sample. Cryo-EM is a three-dimensional electron microscopy technique enabling the determination of 3D structure from multiple 2D images. By combining higher electron acceleration, hardware modifications, new generation of camera with direct electron detection, different grid coatings and efficient particle selection and processing, Cryo-EM permits to determine high resolution structures (1.2 Å) since the last 4 years (Yao, Fan, and Yan 2020; Yip et al. 2020).

For TEM, electrons are generated by warming up a tungsten filament to 2500 °C and are then accelerated with a tension of 120 keV. This generates an electron beam that propagates through a

column under a vacuum of 10,6 mbar and cooled down by liquid nitrogen. For cryo-EM electrons are generated with electrons guns that required a higher vacuum (10^{-8} mbar at least) and accelerated from 200 to 300 keV according to the hardware. More powerful the acceleration is, better the resolution can be. Classical glass lenses used in optics are not powerful enough to diffract an electron beam. Therefore, a system of electromagnetic lenses is necessary for observing the sample. The diameter of the beam is reduced with the condenser, diminishing spherical aberrations on the final image. Only 10% of the electrons constituting the beam pass through the sample and are highly elastically scattered. They form the diffraction diagram in the Fourier Space where the image stability is visible thanks to the Thon rings shape. Elliptical over circular rings represent sample drift or lens astigmatism; Thus, the Fourier space contributes to the final image interpretation.

In TEM, the contrast between the background and the sample is enhanced by negative staining with uranyl acetate solution. Uranium atom (92^{nd} element in the periodic table) is a heavy metal and adsorbs on the carbon atom of biological samples. The latter will appear white, amplifying the contrast with the black background. Importantly, certain sample buffers, like phosphate buffers are incompatible with staining solutions, forming crystals on the grids. Therefore, buffer exchange is sometimes required to observe properly a sample. Contrastingly, with cryo-EM, the sample is fixed in a layer of vitrified ice, resulting in low contrast images, even though crucial for aligning the particles. Therefore, the contrast is created by under focusing the sample in the microscope.

2. Grid type and vitrification for single particle analysis

For structural analysis by cryo-EM, proteinaceous samples were applied on 3 mm diameter copper grid, covered by a so-called “Quantifoil film”. This consists of non-continuous holey carbon film where holes of 1.2 µm are separated from each other by 1.3 µm. Carbon is the standard film material, but other coatings can be considered (gold/palladium (Au/Pd) sputtered, graphene oxide, or graphene). They can improve the localization of particles in the hole centers instead of the air-water interface or avoid particle movement after exposure to electron beam. Au/Pd sputtered consists in applying nanoparticles of this alloy on a Quantifoil film. Gold is known to avoid particles movement (Weissenberger, Henderikx, and Peters 2021). Graphene oxide (GO) coating

helps to decrease the background noise on the micrographs since it is transparent to electrons (Pantelic et al. 2012) and is a major advantage for protein smaller than 100 kDa (Patel et al. 2021). However it remains a sensitive coating because it easily self-aggregates and therefore, not form a homogenous monolayer (Fan and Sun 2022). Also, studies led by Matthias Staudner in the team showed that the reproducibility of grid coverage is variable from 80 to only 10-20% of grid surface. In this regard, graphene represents an alternative, having the same advantage of GO without fragility.

Except for graphene oxide coating grids, all the other types were glow discharged (PELCO easiGlow™ Glow Discharge Cleaning System, Ted Pella, Inc.) before hydrophilic protein sample application. The plasma cleaning parameters depend on the coated type used in this work are summarized in the Table 25.

Type of coating	Reasons	Glow discharging parameters
Carbon	Most common, can be used for any sample	100 s, 0.39 mBar, 15 mA
Gold/Palladium sputtered	More stability of the particles	100 s, 0.39 mBar, 15 mA
Graphene Oxide (GO)	Better concentration of small particles in the middle of the holes but fragile coating	
Graphene	More stable than GO	30 s, 0.39 mBar, 12 mA

Table 25: Glow discharging conditions according to the grid type.

Vitrification consists in fixing protein sample previously loaded on grid in a layer of amorphous ice, preserving its different orientations and conformations in aqueous environment (Dubochet et al. 1982; Taylor and Glaeser 1974). The excess of liquid needs to be blotted away to avoid a thick ice layer. Blotting force and time can be varied, making the ice layer thinner or thicker. Different blotting papers exist: Standard 595 or Leica (47000-100 or 200, Ted Pella) or Whatman 1 (Cytiva), and their influence on vitrification is still unclear. Also, certain grid types require a waiting time before blotting to let the protein sample settle down. After being dipped into liquid ethane (-176°C) the sample is stored in liquid nitrogen. The challenge of vitrification is avoiding contamination by ice crystals. It greatly lowers the quality of the micrographs recorded during data collection. Consequently, numerous particles cannot be processed.

Taken together, sample preparation, choice of grid and vitrification conditions interplay a major role for further single particle analysis. Protein concentration influences the particle repartition on grid and its incubation with diverse substrates can promote a certain conformation as mentioned in the Size Exclusion Chromatography section and in the literature. Rational grid choice can help to concentrate the sample in the middle of the holes (graphene), and/or avoiding particle movements under electron exposure (gold). Finally, Screening of the blotting conditions during vitrification allows to select a suitable thickness of the amorphous ice layer without crystals to guarantee the quality of particles for SPA.

For every protein studied in this work, 3.5 µl of concentrated sample is vitrified with the plunge-freezer Vitrobot (Mark IV, Thermo Fisher Scientific), 4°C, 100 % humidity. The blot force was always set at 0. The other parameters (blotting/waiting time, filter paper) varied according to the protein and the grid type used are described in the Table 26.

Grid type	Waiting time	Blotting time	Blotting paper	Protein
Quantifoil 1.2/1.3 carbon coated	No	5 s or 6 s	Standard 595 (Ted Pella 47000-100)	*r*GAT1 WT *r*GAT1 L300Q
Quantifoil 1.2/1.3 AU/Pd sputtered	No	5 s or 6 s		*r*GAT1 L300Q
Quantifoil 1.2/1.3 GO coated	25 s	5.5 s		*r*GAT1 L300Q *r*GAT1 WT
Quantifoil 1.2/1.3 graphene coated	No	5.5 s		*r*GAT1 L300Q

Table 26: Different grids and blotting conditions tested for the different proteins studied in this work. All grids were screened in the microscope JEOL CryoARM 200.

3. Negative staining

The sample is loaded on circular copper grids of a 3 mm diameter, composed of 300 mesh (Plano, Germany) and manually coated by a carbon film averaging 15 nm thickness. Grids were glow discharged during 30 s, on the low mode current under a pressure of 0,2 mbar with the plasma cleaner PDC-32 **(**Harrick Plasma Inc., Ithaca, USA). This made the carbon film hydrophilic and able to absorb aqueous samples. 3 µl of sample were loaded and let over the grid for 30 s. The

droplet excess was eliminated with Whatman® paper 5. The sample was stained in two steps with a solution of uranyl acetate 2% (w/v). First, two quick stainings of 5 s with 3 µl of uranyl acetate were performed. Finally, an incubation with 3 µl of uranyl acetate for 1 min permanently stained the sample. The excess of staining solution was removed with Whatman® paper 5 and the grid was left 1 min at the air to dry before storage.

4. TEM observation and image analysis

It is recommended to wait at least 1 hour after the staining to observe the grids. This increases the efficiency of the staining and guarantees a better quality of the final images. The observations were performed with the microscope CM12 transmission electron microscope 120 keV (FEI Company, Hillsboro, USA) and images were collected with the camera TVIPS0124, 1k×1k pixels (TVIPS GmbH, Gauting, Germany). Measurements of particles diameter on the images collected were performed with the software ImageJ.

5. Cryo-EM GAT1 WT and L300Q data collection (Regensburg)

Data were collected at the cryo-EM facility of the university of Regensburg (Germany) thanks to the help of Dr. Gregor M. Madej, on the microscope CryoArm200 (Jeol) equipped with a cold field emitter gun, an acceleration voltage of 200 keV and an Omega energy filter of 20eV slit. The beam diameter of 1.0 µm was controlled by a Condenser lens aperture of 70 µm. The movies were collected with the camera Gatan K2 with, at magnification of × 80000 with a target defocus of 0.1 µm on a range from -0.6 to -1.6 µm. The pixel size was 0.7891 Å with a flux dose on camera of 1.4 electrons per pixel per second for a total dose of 60 electrons/ Å² and an exposure time of 6.67 s. A total of 43 frames were collected per movie and sets of 500 movies in average were recorded.

6. Cryo-EM GAT1 L300Q data collection (Würzburg)

Data were collected at the Biocentre of the University of Würzburg (Germany) thanks to the help of Dr. Bettina Böttcher, on the microscope Titan-Krios G3 (Thermo Scientific) equipped with a X-Field Electron Gun electron source, an acceleration voltage of 300 keV and an energy filter of 5 eV slit. The beam diameter of 1.3 µm was controlled by a Condenser lens aperture of 70 µm.

The movies were collected with the camera Falcon IVi direct Electron Detector in counting mode with two shots per hole, at magnification of × 130000 with a target defocus of 0.1 µm on a range from -0.4 to -1.6 µm. The pixel size was 0.946 Å with a flux dose on camera of 9.66 electrons per pixel per second for a total dose of 70 electrons/ Å² and an exposure time of 6.67 s. A total of 2052 frames were collected per movie and set of 14910 movies were recorded in the EER format (Electron Event Representation).

7. GAT1 L300Q data processing, initial map and AlphaFold generated structure

The movies were first imported in CryoSparc Live 5.0. After motion correction, and elimination of the worst micrographs, a blob picking, with 20000 particles were used for a preliminary 2D classification. The resulting two best classes were selected for template picking. To decipher the protein from the detergent micelles, micrographs are cleaned by the clamp solvent function to decrease pixel signal from the background. First *ab initio* model is created with 300 good particles to create an initial blob map that will be lately re-fine by adding better quality particles
For increasing the speed of the processing, pixels were binned 4 times, passing from a box size of 256 pixel to 64 pixel. Instead of measuring 0,946 Å, the pixels are now measuring 3.78 Å. Preliminary 2D classes from the pre-processing were used for a topaz extraction for a more powerful picking. At the end of the extraction, 3 208 863 particles were extracted out of 13 834 micrographs. Once the particles are extracted, a 2D classification can be started again. Number of 2D classes is set on 40 with a batch size of 500 particles per class, 20 iterations with 2 supplementary full iterations. For the next rounds of 2D classification, the number of classes is increased to 70, the function clamp solvent and enforce non negativity were used to normalize the intensity coming from micrographs with non-homogenous ice thickness. Thereafter, these 2D classes were used for hetero-refinement followed by a non-uniform refinement.

To visualize better how the top views of GAT1 mutant should look like, 100000 particles were generated from the EM map of *h*GAT1 WT (pdb 7Y7W) with “Simulate Data” function on CryoSparc. As the top views were low resolution and heterogenous compared to the model particles, data were transferred to Relion 4.0 to improve 2D classes quality.

Before, files needed to be converted because particle file format used by CryoSparc are not compatible with Relion. To do so, particles were again extracted from the micrographs and downloaded with the extension "`particles.star`". after that, the extension was changed again from "`.mrc`" to "`.mrcs`". Otherwise, the movies after motion correction can be directly uploaded in Relion 4. The advantage is that the micrographs have already the "`.mrc`" extension.

After importing in Relion, the CTF of the micrographs was refined and particles were extracted for 2D classes. To improve the quality of the top views, the particles were divided into 3 subsets to run independent iteration of 2D classes. Five iteration runs were performed on each subset before submitting a 3D classification and 3D refinement. Finally, the map obtained after post processing using "blush regularization" did not change the resolution of the preliminary maps obtained in CryoSparc. However, 2D classes from Relion were used for new *ab initio* model in CryoSparc and further post-processing improvements, notably Sharpening to restore the contrast and masking, to gain resolution on the protein, by removing solvent signal.

Finally, the structure of *r*GAT1 in inward-occluded state (pdb 7Y7W) was fitted the final map of *r*GAT1 L300Q that reached the resolution of 7 Å. This resolution was too low for deciphering amino acid chain. Therefore, AlphaFold 3 was used to generate a putative model of the mutant. This version offers the possibility to give as input the protein sequence of the mutant (glutamine instead of Leucine at the position 300), but also the ions (sodium and chloride) and the substrate (GABA). This structure was further used for hypothesizing the third sodium position and TM6 loop movement suggested by electrophysiological data (*Cf:* ***Results and Discussion***)

VI. Electrophysiology methodologies

1. Two Electrode Voltage Clamp (TEVC) principle

It is a suitable method to study electrogenic proteins, i.e. characterized by a flux of charged elements like (in)organic cations or anions. GAT1 has been already widely studied by TEVC, and here will be described the general principles of the technique and the different procedures used during this PhD work. TEVC uses oocytes from *Xenopus laevis* as a heterologous protein

expression system. With an average diameter of 1 mm (Bossi, Fabbrini, and Ceriotti 2007; Baumgartner, Islas, and Sigworth 1999) and a low amount of endogenous ion channels and transporters expressed (Guan, Chen, and Zhang 2013), it is an easy cellular system to manipulate, limiting non-specific signals leading to misinterpretations of the data. Excised from ovary lobes of female frogs, oocytes between maturation stages V to VI (Figure 34), with the animal (dark) and vegetal (light) poles distinguished are selected for experiments.

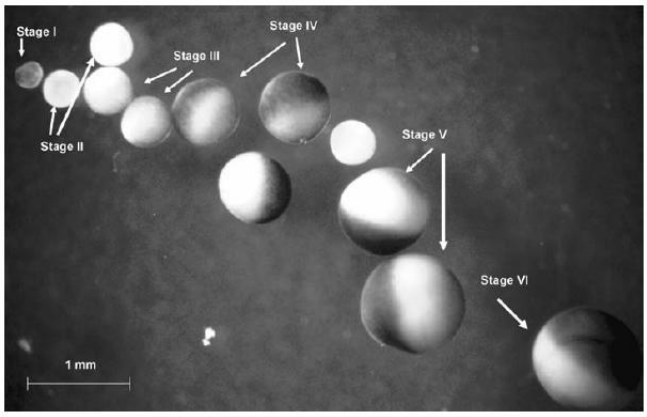

Figure 34: Different maturation stages of oocytes from *X. laevis* (from Bossi Fabbrini, and Ceriotti et al, 2007).

Synthetic cRNAs are injected into the vegetal pole (preferred because distanced from the nucleus), and the oocyte cell machinery will bio-synthesize the protein of interest. Mature protein molecules are functional after 2-3 days of expression according to the RNAs. Natural RNAs, cDNAs and membrane from animal or human tissues can be injected. In the latter case, membrane patches containing proteins will be directly integrated into the plasma membrane of the oocytes. This expression method is faster (24 h) and allow an *ex vivo* study of proteins (Bhatt et al. 2022)

When electrogenic membrane proteins are expressed at the surface of oocytes, they induce transmembrane currents due to the ion coupled transport and therefore change the membrane potential. In the TEVC method, a Silver/chloride electrode system measures the voltage (voltage electrode, Figure 35A, B, C) that is compared to the holding potential in the voltage clamping amplifier (Figure 35A). The current electrode (Figure 35A) contributes to readjust the desired voltage by injecting feedback current. It is this current compensation that is registered and analyzed

in TEVC to get information on the protein activity. The whole set-up is shown on the images on Figure 35B and C.

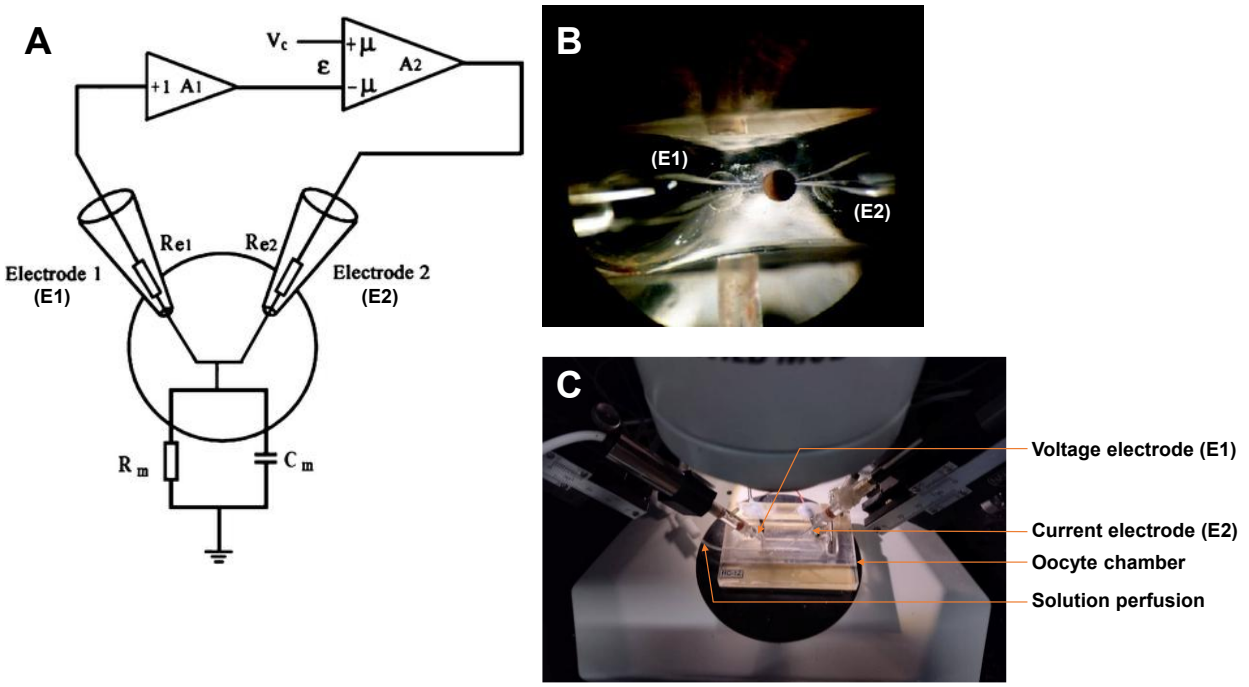

Figure 35: Two electrode voltage clamp principle and set up. a) Scheme of conventional TEVC on oocyte. Vm is monitored by connecting the voltage electrode (electrode 1, E1) to the input of a holding voltage (A1). The output of A1 corresponding to the Vm potential is connected to one input terminal of a clamping amplifier (A2), which compares Vm with the voltage command signal (Vc) applied to the other input terminal. The resulting output voltage of A2 forces a current proportional to the difference (ε) between Vm and Vc usually by means of a voltage-controlled current source mechanism, to flow through the current electrode (electrode 2, E2) into the cell. The current that passes through electrode 2 is measured (either upstream of electrode 2 or at the virtual grounding circuit) as the membrane current, since it counterbalances the Vm deviation the membrane current (image from Guan, Chen, and Zhang 2013). b) Stereomicroscopic view of the *Xenopus laevis* oocyte in the bath chamber and impaled with the two glass electrodes (from Guan et al, 2013). c) Overview of the experimental set-up.

2. Mutant preparation and RNA synthesis

Rattus norvegicus GAT1 WT (*r*GAT1) in pAMV-PA plasmid was modified by reverse PCR with the high fidelity Q5 DNA polymerase (M0491S, New England Biolabs) to design three single mutants S133E, L300Q, G403C. For the double mutants (S133E/L300Q, L300Q/G403C and G403C/S133E), a plasmid already containing one mutation was used as template and the primers

required to insert the second mutation were used. For the triple mutant (S133E/L300Q/G403C), a plasmid containing already two mutations was used as template and the primers to integrate the last mutation were used. All the primers are listed in the Table 6 and each mutant was verified by sequencing (Eurofins genomics, Ebersberg, Germany). For more details on the point mutation integration and plasmid DNA preparation, refer to the molecular biology section.

To transcript the gene (WT and or mutants), 8 µg of the respective plasmids are linearized in a final reaction volume of 200 µl, as described in Table 27, for 2 h at 37 °C.

	Quantity/Volume
Plasmid DNA	8 µg
New England Biolabs buffer™ 3 10X	20 µl
Acetylated BSA (10 µg/µl, Promega)	2 µl
Restriction enzyme SalI (10 U/µl, Promega)	2.4 µl
RNase free water	Up to 200 µl

Table 27: Conditions of linearization of the plasmid with rGAT1 (WT/mutants) gene,with the restriction enzyme SalI.

The linearized products were controlled on a gel 1% agarose (w/v) in TAE (Tris-Acetate-EDTA) buffer pH 8.3 and purified with the Wizard® SV PCR clean-up system (Promega, Italy). The transcription reaction is described in the Table 28 and its final volume was adjusted up to 90 µl with the purified linearized DNA.

	Volume	**Final [C]**
Transcription buffer 5X (Promega)	18 µl	1X
DTT 100 mM (Promega)	8 µl	10 mM
Rnase inhibitor 30 U/µl (Promega)	2 µl	0,6 U /µl
dNTP mix (A/U/CTP 5 mM, GTP 0,5 mM)	13 µl	A/U/CTP 0,7 mM and GTP 0,07 mM
CAP analogue 10 mM (Promega)	6,5 µl	0,7 mM
T7 RNA 20 U/µl (Promega)	8 µl	1,8 U/µl
DNA up 90 µl	34,5 µl	

Table 28: Conditions for *in vitro* RNA synthesis (to be continued in Table 29)

The mixture was incubated at 37°C and 1 µl of GTP at 25 mM was added at 20, 40 and 60 min after the initiation of the reaction. 20 min after the last addition of GTP, a mix without CAP analog (Table 29) was added for two more hours to complete the transcription.

	Volume	**Final [C]**
Transcription buffer 5X	2 µl	1X
DTT 100 mM	1 µl	10 mM
RNase inhibitor 30 U/µl	1 µl	3 U/µl
dNTP (A/U/CTP 5 mM, GTP 0,5 mM)	5 µl	A/U/CTP 2 mM and GTP 0,2 mM
GTP 25 mM	1 µl	2 mM
T7 RNA 20 U/µl	1 µl	1,8 U/µl

Table 29: Conditions for *in vitro* RNA synthesis (end)

The transcription product was analysed on 1% (w/v) agarose gel in TAE buffer. The migration was performed at 60 V for 45 min. Everything used for analyzing the RNAs was washed with autoclave water treated with diethylpyrocarbonate. Sample preparation for gel analysis is presented on Table 30.

	Volume
Transcription product	1 µl
RNA sample buffer	7 µl
Gel loading dye purple 6X (New England Biolabs)	2 µl
RNase-free water (up to 12 µl)	2 µl

Table 30: Sample preparation for RNA analysis on agarose gel. RNA sample buffer avoids RNA hairpin formation

To separate the RNA from contaminating proteins, DNA and free nucleotide phosphates present in the transcription product, the reaction products were incubated overnight at -80°C with 500 µl of lithium chloride 8 M. This reaction precipitated the RNA and after centrifugation for 30 min at 13000 ×*g*, 4°C, the pellet containing the RNA was resuspended with 500 µl of cold ethanol 70 % (v/v). The sample was centrifuged again for 30 min at 10000×*g*, 4°C. The pellet was air-dried for 15 min and resuspended with autoclave free RNase water constituting the final RNA solution. RNA quality was verified on agarose gel 1% (w/v) in TAE buffer. After measuring the

concentration by measuring the absorbance at 260 nm, the final solution of each RNA was diluted to 0,5 µg/µl in RNase free water and stored at -80°C

3. Oocyte preparation

Oocytes were obtained from adult Xenopus laevis females, the animal experimental protocol was approved locally by the Ethical Committee of the Organismo Preposto al Benessere degli Animali (OPBA) of the University of Insubria (OPBA permit no. 02_15 and no. 06_20) and by the Italian Ministry of Health (permit no. 1011/2015 and 440/2021-PR) and used in this project according the article 18 (tissue donation). The oocytes preparation followed the procedures described previously (Bossi, Fabbrini, & Ceriotti, 2007). Briefly, the oocytes collected were treated with 5 to 15 ml (according to the number of oocytes) of collagenase from Clostridium histolyticum (Sigma Aldrich) at 0.5 mg/ml in ND96 (Table 31) calcium-free to avoid overload in the oocyte during digestion (Guan, Chen, and Zhang 2013) for at least 1 h at 18°C, under constant agitation (Incubator MPM instruments, Bernarggio, Italy). Healthy and fully-grown oocytes, between stage V and VI, were manually selected and the follicular layer was removed to avoid the receptors and channels present on their surface to interfere with further measurements (Bossi, Fabbrini, and Ceriotti 2007). They were finally incubated in NDE (Table 31) for 24 h before use.

Solutions	**Compound**	**Concentration**
ND96 without calcium	HEPES pH 7.6	5 mM
	NaCl	96 mM
	KCl	2 mM
	$MgCl_2$	1 mM
ND96 with calcium	ND96	
	$+CaCl_2$	1.8 mM
NDE	ND96 with calcium	
	Pyruvate	2.5 mM
	Gentamicin sulphate	50 µg/ml

Table 31: Solutions for oocytes preparation.

4. RNA Injection in oocytes

The initial concentration of each rGAT1 RNAs was diluted to a final concentration of 0.25 µg/µl and 50 nl was manually micro-injected (Microinjector Type GJ-2, Narashinge, Japan) in each oocyte, 24 h after the selection. After 3 days expressing in NDE at 18 °C, oocytes were ready for electrophysiological measurements.

5. Two Electrode Voltage Clamp measurements

i. Solution preparation

For GABA and betaine dose-response, stock solutions of GABA and betaine were diluted to the expected concentrations with ND98 (Table 32). The concentrations used were 1, 3, 10, 30, 50, 100, 300 µM for GABA and 1, 3, 10, 30, 50 mM for Betaine.

For the experiments involving sodium concentration variation, GABA and betaine were kept at constant concentration (300 µM and 30 mM respectively). ND98 was diluted with a solution of trimethylammonium chloride at 98 mM (TMA98), also later called ND0 (0 mM sodium, Table 32), to get a variation of the concentration of sodium but a constant chloride concentration of 98 mM. The proportions of ND98 and TMA98 were calculated following the equation system 1 below.

$$\begin{cases} 98x + y = a \\ x + y = 1 \end{cases}$$

Equation 2: System for electrophysiology solutions ND*X*. Calculation of the factors x and y will determine the volumes of ND98 and ND0 respectively, necessary for the final solutions at different sodium concentration. a is the final sodium concentration fixed by the user.

To reach saturation, a solution of ND150 (150 mM NaCl, Table 32) was also prepared. The resulting sodium range used during the experiments was 0, 16, 32, 48, 64, 80, 98, 150 mM. For simplification ND*X* annotation is used to characterize solutions from 16 to 80 mM sodium.

Solutions for electrophysiology	Compound	Concentration
ND	Hepes pH 7.6	5 mM
	$CaCl_2$	1.8 mM
	$MagCl_2$	1 mM
ND98	ND +NaCl	98 mM
ND150	ND +NaCl	150 mM
ND*X*	ND +NaCl	16-32-48-64-80 mM
TMA98 ("ND0")	ND +TMA.Cl	98 mM

Table 32: Solutions for electrophysiology measurements. NDX solutions are prepared after mixing ND0 and ND98.

ii. Two Electrode Voltage Clamp set-up

The current and the voltage silver electrodes were chlorinated in bleach for 15 min and inserted in two Borosilicate microcapillaries filled with 3 M KCl after being sharpen with the Puller type PN-3 (Narashinge, Japan). After installing a flowing chamber (1 ml) filled with ND98, and two agar bridges (3% (w/v) agar in 3 M KCl) to connect it to the current and the voltage electrodes, the latter were soaked in ND98, and their resistance were set at 10 MΩ and 40 MΩ respectively. The oocytes were place in the middle of the chamber impaled with both electrodes and clamped at V_h= -60 mV with the amplifier (Oocyte Clamp OC-725, Warner Instruments, Hamden, CT, United States). Their holding current and the capacitance was verified on the monitor using Clampex 10.7. All the downstream measurements were followed and recorded with the same software.

Currents of each oocyte group (WT, single, double and triple mutants) were first recorded in presence of ND98 with saturating concentrations of substrate (GABA 300 µM or Betaine 30 mM) with a holding voltage V_h= -60 mV. Non-injected oocytes were subjected to the same test and used for negative control. Of note, ND98 was always perfused before and after the incubation of ND98

with substrates. This washed away the residual traces of substrate and allowed the recovery of the oocyte return to the initial baseline current.

iii. GABA or Betaine dose-response

The I_{Max} (current value characterizing the saturation rate of the transporter) and the $K_{0.5}$ for GABA and Betaine (concentration at half-saturation to determine substrate affinities) were determined with clamped oocytes at V_h= -60 mV alternatively perfused with ND98 (baseline) and ND98 with ascending concentrations of GABA (1, 3, 10, 30, 50, 100, 300 µM) or Betaine (1, 3, 10, 30, 50 mM) for the transport current measurement. The same oocyte was used for measuring a whole concentration range of GABA or betaine.

iv. Sodium dose-response

The I_{Max} and the $K_{0.5}$ for sodium were also determined with clamped oocytes at V_h= -60 mV. Oocytes (non-injected, WT and mutants) were first perfused with the solutions at different concentrations of sodium (0 to 150 mM) without any substrate. The baseline between each measurement was recorded using ND98. The currents values obtained in the measurements without substrate were used as baseline current values for the analysis (see later).

Thereafter, the oocytes were alternatively perfused with ND98 (baseline) and ND0, ND*X*, ND98 or ND150 with 300 µM GABA or 30 mM Betaine for the transport current measurement.

v. Voltage-jump with variation of sodium concentration

Current-voltage (I-V) relationship was obtained by applying a protocol with voltage jumps and used to understand the voltage dependency of the transporters. In this case, we wanted to understand the relation between sodium-substrate-voltage of GAT1 WT and mutants.

For this experiment, 5 different concentrations of sodium were used, 0, 16, 48, 98, 150 mM. Voltage jumps were performed from -100 mV to +40 mV with 20 mV of increment. For each sodium concentration, 3 consecutive series of voltage jumps were made: (i) with the sodium solution only, (ii) with the sodium solution supplemented with 300 µM GABA or 30 mM Betaine

and (iii) again with the sodium solution only. Each oocyte (non-injected, WT, and mutants) was submitted to this procedure for the five sodium concentrations.

6. Data analysis

i. Dose-response

The recorded current traces were analyzed with Clampfit 10.7. They were filtered with the gaussian lowpass and a cutoff of 5 Hz (425 coefficient) and the baseline was set manually.

- *GABA and Betaine dose-response*

The current values were obtained by subtracting the measured current with the baseline current. The values were plotted as $f([substrate]) = Current$ using the Michaelis Menten fit from Graph Pad Prism 8. Each value plotted represents the average current of all single oocyte at a specific concentration.

- *Sodium dose-response*

Transport currents registered with substrates in ND0, ND*X* and ND150 were subtracted to the baseline registered at the corresponding concentration of sodium. Current values obtained with ND0 were brought to 0 and used to rescale all the current values obtained with ND*X* and ND150. Finally, these values were plotted as $f([Sodium]) = Current$ using the nonlinear fit from Origin2024. Each current value plotted represented the average of all single oocyte used for the experiments. The fitted data were transferred to Graph Pad Prism 8 for figure drawing.

ii. Voltage-Jump

According to the value of the holding current, baseline values were averaged and then subtracted to the current values in presence of substrates. The resulting traces were filtered with the gaussian lowpass and a cutoff of 20 Hz (107 coefficients). A cursor was placed close to the end of the pulse trace, to assess the different current values associated with each different voltage. The data were plotted as $f(Voltage) = Current$ where the voltage current relationship associated with the five concentration of sodium was represented on the same graph for one substrate for one group of oocytes. The data were also represented with the heat-map where $f([sodium]) = Voltage$ and

the related currents were represented with a color gradient. The baseline color value was set as the current value obtained at -60 mV according to the oocyte group and the substrate.

VII. Sample preparation for epifluorescence and confocal imaging

1. Oocytes fixing and Cryo-Sectioning

After being tested on the TEVC set-up with ND98 and 300 µM GABA or 30 mM Betaine, 5 oocytes of each group (non-injected and injected with GAT1 WT or variants) were used for immunocytochemistry to localize the protein in the oocyte membrane. Oocytes were washed twice for 5 min at room temperature with 500 µl of buffer ND96 with calcium, consequently fixed with 500 µl of paraformaldehyde 4% (w/v) (diluted in PBS pH 7.5) for 15 min under gentle agitation at 4°C, and finally washed three times for 5 min with 500 µl of ND96 with calcium to remove any traces of the fixing agent. Oocytes were placed in plastic molds (Tissue-tek cryomold biopsy disposable specimen molds for use with the tissue cryo3 10 mm×10 mm×5 mm 7805 sakura finetek USA), filled with tissue freezing medium (Electron Microscopy Sciences, Hatfield, USA) and flash frozen in liquid nitrogen. They were stored at -80°C at least 24 h before slicing, to avoid resin crumbling.

For cryo-sectioning, the Cryostat chamber, the holding sample disks, and the blade were held at -20°C (CryoStar NX70, Thermo scientific). The blade was set by default at 45° to the sample and the slice thickness at 12 µm; it was thin enough for imaging and thick enough to avoid the self-rolling of the oocyte slices. Once sectioned, they adhered by simple contact to a poly-L-lysine coated glass slide (25mm x 75mm x 1 mm, Electron Microscopy Science). 10 oocytes slices were positioned on one slide, and were stored at 4°C for immediate immunostaining; otherwise, they were stored at -20 °C.

2. Cyto-immunochemistry on oocytes

Oocyte slices were hydrated in PBS for 10 min. Unspecific reacting sites were blocked with a solution of 2% (w/v) BSA/Tween^{20} 0.1% (v/v) in PBS for 1 h at room temperature. Then, the slides were slightly dried and incubated dropwise with the primary antibody anti-GAT1 (see Table 20 for dilution) in the blocking solution overnight at 4°C. The next day, the primary antibody solution

was removed with three PBS washing steps. The secondary antibody conjugated with Cy3 fluorophore (see Table 21 for dilution) in blocking solution was incubated for 1 h at room temperature in the dark to avoid fluorophore quenching. After removing the secondary antibody and washed again three times with PBS, the slides were dried and covered by a coverslip sealed with mounting medium (Glycerogel Mounting medium, C0563 15 ml, DAKO) previously warmed-up in a water bath at 50 °C. Mounted oocytes are stored at 4°C until observation.

3. Cyto-immunostaining on HEK for LAT1/CD98 complex localization

The different antibodies used for (co)-immunostaining, associated with their dilution, are presented on Table 20 and Table 21. 48 h after transient transfection and expression, $DMEM_c$ was removed, cells were washed with PBS and fixed with 10 % (v/v) formalin in PBS for 15 min at RT. After three PBS washes, cells were permeabilized with 0.1% Triton X-100 (v/v) in PBS for 15 min at RT. Cells were washed again 3 times with PBS and unspecific reacting sites were blocked for 30 min with 3% BSA/0.1% Tween[20] in PBS. The same solution was used to dilute the diverse antibodies. The primary antibody was loaded dropwise on the coverslips and incubated overnight at 4 °C. The next day, after three PBS washes, the cells were incubated with the secondary antibody with 1 µg/ml of Hoechst 33342 (62249, aqueous solution 20 mM, 5 ml, ThermoScientific) for 1 h at room temperature. For co-immunostaining, the coverslips are washed again with PBS and incubated with the other primary antibody overnight at 4°C. After PBS washes, the associated secondary antibody is incubated 1 h at room temperature without Hoechst dye. Finally, coverslips were washed with PBS and mounted on a poly-L-Lysine glass slide as mentioned. The different combinations and chronological order of antibody incubations are listed in the Table 33.

Protein and/or tags co-immunolocalized	First primary antibody	Associated secondary antibody	Second primary antibody	Associated secondary antibody
LAT1-CD98	anti-LAT1	anti-Rabbit	anti-CD98	Anti-Mouse
Strep-FLAG	anti-Strep		anti-FLAG	
LAT1-FLAG	anti-LAT1			
Strep-CD98	anti-Strep		anti-CD98	

Table 33: Chronological order of antibody incubation.

VIII. Prostatic bone metastases PC-3M study

1. Cell culture

Ex vivo PC-3M subline (Elabscience Bionovation Inc. USA) was isolated in the bone from a 62-years old man with prostate carcinoma. After thawing, cells were cultivated in T75 Flask with 15 ml RPMI 1640 medium without Phenol red and L-Glutamine (Lonza Bioscience, Switzerland) supplemented with 10% (v/v) FBS, 0.075% (v/v) sodium bicarbonate (7.5% solution, 25080-060, Gibco), 1 mM sodium pyruvate (100 mM solution, S8636, Sigma-Aldrich) and 4 mM L-Glutamine. Cells are maintained at 37°C in a humidified incubator with 5% CO_2. Cells are split every 2 days to keep cell confluency at 80% and avoiding metabolism stress. Supplemented RPMI medium is discarded, and the cells are washed with 5 ml PBS before 10 minutes incubation with 1 ml Trypsin-EDTA (10X, sterile-filtered, 5.0 g porcine trypsin and 2 g EDTA, 4.Na per liter, T2610 Sigma-Aldrich) at 37°C. Reaction is stopped by adding 4 ml of supplemented RPMI 1640 medium and the sub-cultivation ratio is kept at 1:4. For cryogenic storage, cells are resuspend in freezing medium 60% (v/v) supplemented RPMI, 30% (v/v) FBS, 10% DMSO (v/v) after centrifugation. 1 ml aliquot at 1.10^6 cells/ml are distributed in each vial.

2. Immunocytochemistry

PC-3M cells are also seeded in 6-well plate at 1.10^5 cells/ml (2 ml per well) and grown on siliconized glass circular coverslips (22 mm diameter, Hampton research). After 24 h, cells are already confluent and therefore supplemented RPMI medium was discarded cells are washed, fixed, and co-stained with the primary antibodies anti-LAT1, anti-CD98 and Hoechst 33342 (See detailed procedure in section ***Cyto-immunostaining on HEK for LAT1/CD98 complex localization***) and their associated secondary antibodies (see Table 20 and Table 21 for antibody dilutions). After mounting, PC-3M cells were observed by confocal microscopy.

3. Western blot on cell lysate

For western blot on total cell lysate, 25 ml of PC3-M cell suspension was centrifuged for 3 min at 3200×*g*, 4°C. The pellet was weight (100 mg) and washed with 1 ml of PBS. The suspension was divided in two, and each 500 µl was centrifuged for 5 min at 17 000×*g*, 4°C. One pellet was resuspended with the standard LAT1/CD98 solubilization (See composition on Table 15) while the other one with the "Otsuki solubilization buffer" 50 mM Tris-HCl pH 8.0 150 mM NaCl 0.5 mM EDTA, 1% Triton X-100, Aprotinin 1 µg/ml, Leupeptin 2 µg/ml, Pepstatine 0.5 µg/ml (Otsuki et al. 2017). Both suspensions were let for 1 h on a rotary shaker at 4°C to solubilize the plasma membranes. Then cell debris were pelleted by centrifugation for 5 min at 17 000×*g*, 4°C. The supernatants containing the solubilized protein complex were loaded on SDS-PAGE for further western blot analysis. For reductive conditions, 40 µl of sample were mixed with 8 µl the usual 6X lämmeli sample buffer while for the non-reductive conditions the sample buffer does not contain β-mercaptoethanol.

IX. Light microscopy techniques for protein subcellular localization

1. Epifluorescence microscopy

Oocytes were imaged with the epifluorescence microscope Axio Observer.Z1/7 equipped with the Axiocam 506 camera (Zeiss Jena, Germany) kindly provided by the Chair of Prof. Dr. Richard Warth. The objects were first localized with transmitted light (TL halogen lamp) through the microscope oculars then observed on live with the ZEN PRO software. The channels used according to the element/proteins observed are summarized in the Table 34.

Channel	**Reflector**	**Beam spliter (nm)**	**$\lambda_{ex.}$ (nm)**	**$\lambda_{em.}$ (nm)**	**Light source**	**Fluorophore illuminated**	**Observation**
EGFP	38 HE GFP	495	488	509	Shutter Lambda DG-4	Cellular co-factors	Oocytes auto-fluorescence
DsRed	43 HE DsRed	570	545	572		Cy3	*r*GAT1 WT/mutants

Table 34: Epifluorescence microscope illumination channels characteristics and use.

Oocytes were observed at magnification ×63 with immersion oil objective, where a unique portion of the oocyte membrane was imaged where the effective numerical aperture was 1.4, and the pixel size is 0.144 µm×0.144 µm. The image size in pixel was 1376×1104, and the scaled image size was 198 µm×159 µm. For full oocyte imaging at the same magnification, 3×3 images were taken in tile mode. Tiles were fused by stitching for better-quality images and background was subtracted with an under focused image of an empty region. where the effective numerical aperture was 0.5, and the pixel size is 0.454 µm×0.454 µm. The image size in pixel was 3941×3174, and the scaled image size was 1.79 mm×1.44 mm.

2. Confocal microscopy

Immuno-stained and mounted PC-3M and HEK cells are observed with the laser scanning microscope LSM 980 Airyscan 2 Multiplex Mode (Zeiss) at magnification ×63 with immersion oil objective. Sample observation was made with live imaging monitor ZeissPro. To avoid signal saturation laser power and camera gain were adjusted for each image and channel. Single cell images size was 2221×2221 pixels (78.38 µm× 78.38 µm) with 16 bits per pixel and a pixel time recording of 1.87 µs for super resolution mode. For wide field images, 12 tiles were used for a final size of 8302×6259 pixels (292.98 µm× 220.86 µm) with a pixel time and a frame time recording of 0.93 µs and 16.57 s. To increase the speed of acquisition, bits per pixel decreased to 8. The channels used according to the element/proteins observed are summarized in the Table 35.

Channel	**$\lambda_{ex.}$ (nm)**	**Fluorophore**	**$\lambda_{em.}$ (nm)**	**Element observed**
H3342-T3	348	Hoechst dye	455	Nucleus
CY32-T2	548	Cy3	561	LAT1 or Strep-Tag (N-Ter of CD98)
AF647-T1	653	Alexa Fluor 647	668	CD98 or FLAG-Tag (N-ter of LAT1)

Table 35: Laser scanning microscope illumination channels used according to the fluorophore.

Results

I. Sample preparation for Protein/Lipid interactions study in GATs

1. Test expression of eYFP-rGAT1 WT

The plasmid pC1-eYFP containing the sequence of rGAT1 WT was kindly provided by Prof. Harald Sitte (Medical University Vienna, Austria). First, the expression was tested at different DNA:PEI ratios and the fluorescence signal from eYFP was tracked every 24 h. The Figure 36 showed it after 72 h, before cell harvesting for total cell lysate western blot.

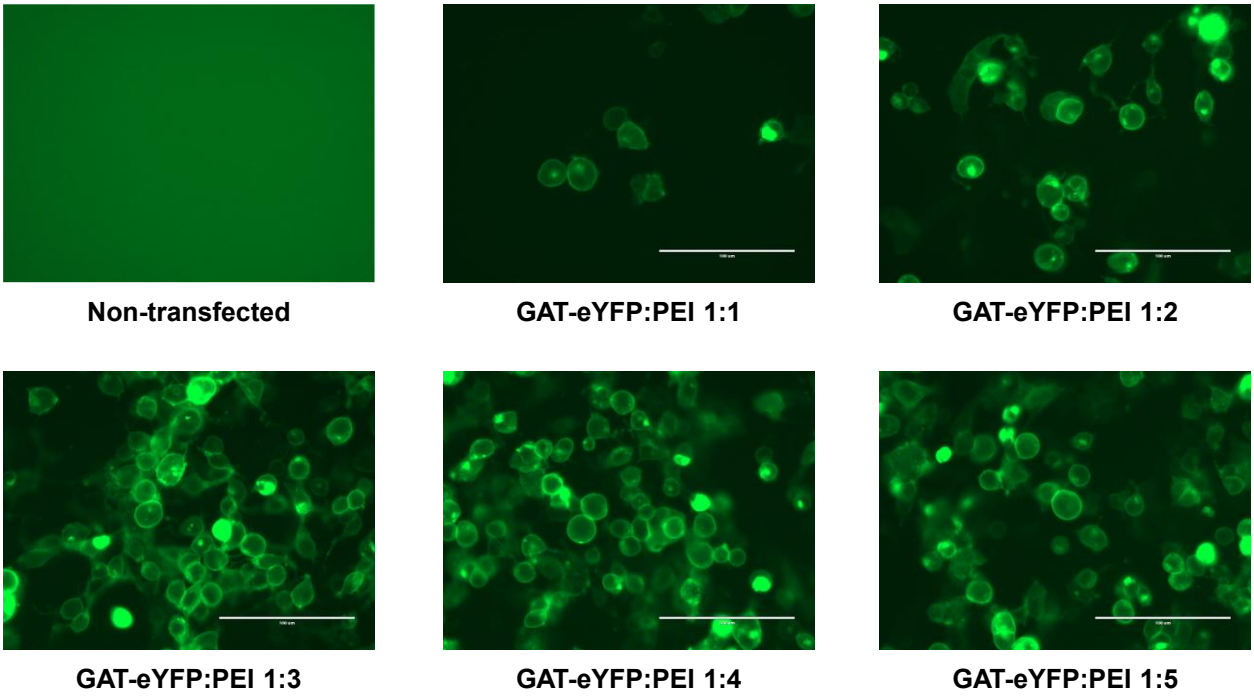

Figure 36: Fluorescence signal of the eYFP expressed at the N-terminal of rGAT1 after 72 h of expression. Picture are taken with the microscope EVOS (Invitrogen), Mag. ×40 in GFP mode, intensity 60% (scale bar 100 µm).

The florescence signal from the eYFP is in the plasma membrane coherently with the subcellular localization of rGAT1. This is true for any DNA:PEI ratio. However, higher the ratio is, more cells showed a positive fluorescence signal, associated with enhanced expression of the chimeric

construct eYFP-rGAT1. Indeed, on the western blot (Figure 37A) a positive band at 100 kDa is visible for every transfection condition except for the 1:1 ratio. Moreover, the relative expression (Figure 37B) is more than 50-fold higher with 1:3 and 1:5 ratios than with a 1:1 ratio. This is in accordance with the florescence images (Figure 36). As mentioned previously in the literature, polyethyleneimine is toxic for the cells, and it is judicious to choose a lower DNA:PEI ratio for protein expression (Longo et al. 2013). Thus, rGAT1-eYFP will be further transiently transfected with a 1:3 ratio.

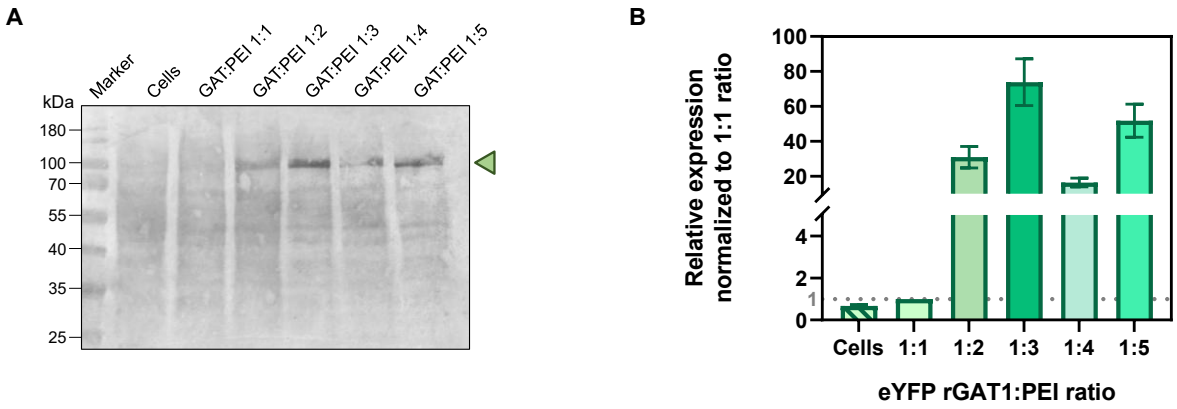

Figure 37: Analysis of GAT1 WT-eYFP expression. a) Western blot associated with b) the relative expression of the chimeric protein. The band intensities on the western blot corresponding to eYFP rGAT1 (100 kDa) is measured twice on ImageJ after background subtraction. All values are normalized with the intensity obtained with the 1:1 ratio. “cells” corresponds to non-transfected cells.

For the 1:4 ratio, it seems that as many cells are transfected as for the 1:3 or 1:5 ratios on the microscope images (Figure 36). However, the histogram on the Figure 37B showed that it corresponds to an expression 2.5-fold lower compared to these two ratios. This is associated with a misdetection of the western blot signal.

2. His-FLAG rGAT1 cloning and test expression

After testing the expression of rGAT1-eYFP and determining the correct ratio with the transfection agent, the construct was modified by molecular engineering to deplete the YFP tag while introducing a double tag poly-Histidine-FLAG for protein purification. The linear product

obtained after PCR is visible by a positive signal at 6 000 pb on agarose gel (Figure 38A). The ligation and reconstitution of the circular plasmid is confirmed by sequencing (Figure 38B).

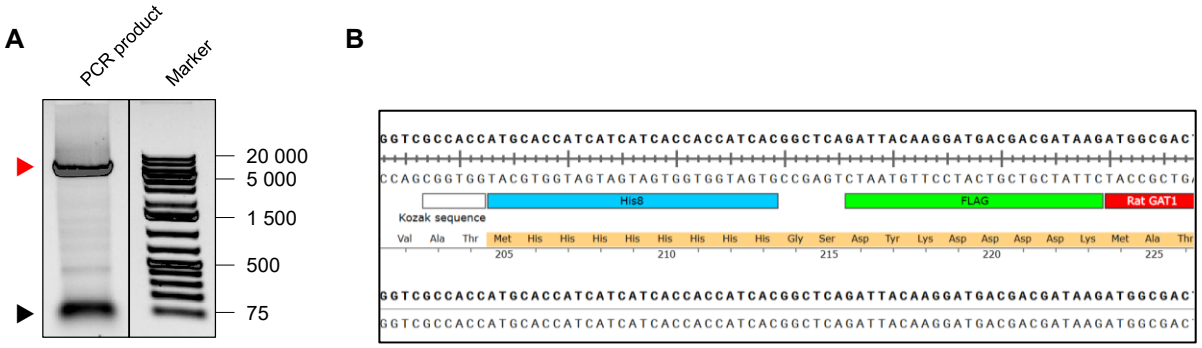

Figure 38: Cloning of pHF rGAT1. a) Agarose gel (negative image) showing the linear PCR product after depletion of eYFP and insertion of the double purification tag (6180 pb, red arrowhead) and the primers (75 pb, black arrowhead). B) Sequencing results confirming the insertion of poly8×His tag, glycine-Serine linker and FLAG tag (from SnapGene Software).

To verify the expression of the new construct, cells are transfected with a 1:3 DNA:PEI ratio, harvested after 72 h and a western blot on total cell lysate was performed. The protein, i.e His-FLAG rGAT1 was detected with a primary antibody anti-FLAG, between 55 and 70 kDa (Figure 39). The lower molecular weight compared to the Figure 37A is in accordance with the YFP depletion. Another protein expressing the FLAG tag was used as control (Ctr FLAG-tag). Therefore, the modification integrated by molecular has no influence on the expression of rGAT1 and the expression condition determined before for rGAT1 eYFP (i.e ratio DNA:PEI) can be identically used.

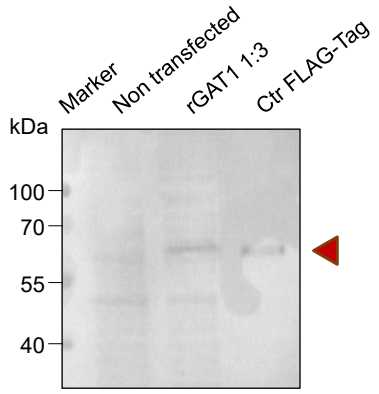

Figure 39: Western blot to verify the expression of the new construct pHis-FLAG rGAT1 in the ratio DNA:PEI 1:3. Incubation with primary antibody anti FLAG-tag (F1804, Sigma Aldrich).

3. Expression/Purification optimizations for HF-rGAT1 WT

i. Different cell culture conditions

For high yield protein expression, different suspension cell culture conditions were tested (listed in Table 16 in ***Materiel and Methods***). Each culture volume was 200 ml and yielded in the same range of cell mass (between 0.5 g to 1.4 g). The protein was extracted from the membrane with 2% DDM/ 0.4% CHS and purified on Ni-NTA resin before analysis on western blot (fig XZY below). Every blot showed a positive band between 55 and 70 kDa, meaning that the protein was expressed, extracted from the membrane, and bound/eluted from the Ni-NTA resin in any cell culture condition.

On the figure Figure 40B and D, any non-specific binding of the antibody was visible, thus they might be the two best condition in terms of sample purity. However, in conditions at high speed (Figure 40C and D) the resin wash with 60 mM imidazole highly eluted already the protein. This showed the resin saturation, potentially because more protein was produced at higher shaking speed.

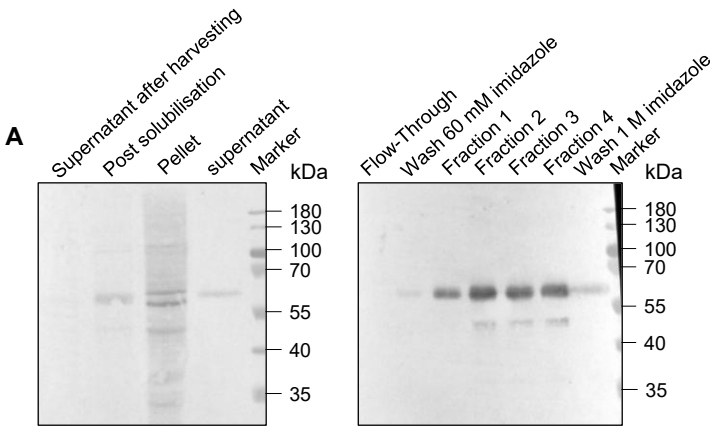

Spinner Flask at 75 rpm, 5% CO2, 37 °C (w=1,4 g)

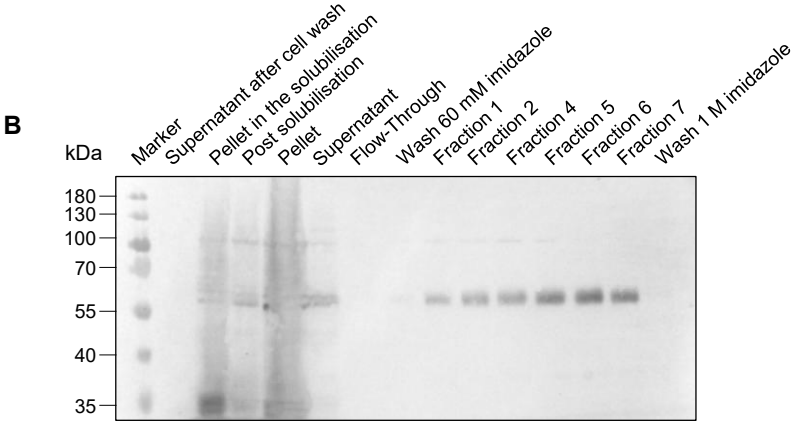

Spinner Flask at 75 rpm, 8% CO2, 37 °C, w=0.51 g

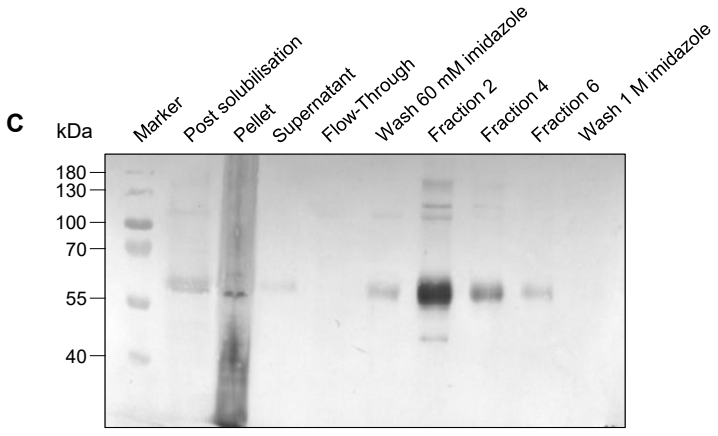

Spinner Flask at 120 rpm, 5% CO2, 37 °C, w= 0.98 g

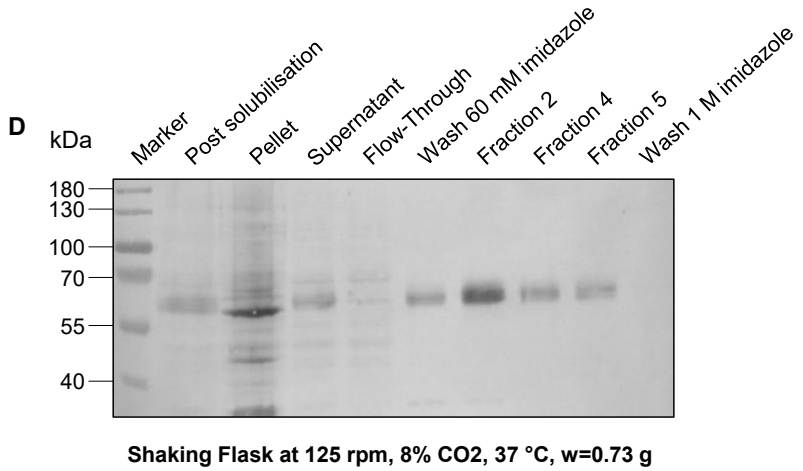

Figure 40: Western blot of rGAT1 after membrane extraction and Ni-NTA resin elution, expressed with different cell culture conditions. The primary antibody used was anti His-tag. Each line of each western blot was loaded with the same sample volume (12 µl).

Protein production in glass spinner flask at high speed is associated with technical issues. Shaking platforms do not always purpose higher speeds than 75 rpm and there is the risk of glass bottle breaking. Therefore, the shaking flask at 125 rpm at 8% CO_2 was ulteriorly used for rGAT1 WT expression.

ii. Purification steps modifications

- *Wash buffer*

As noticed previously, the concentration of imidazole for Ni-NTA resin wash was decreased from 60 to 30 mM to avoid the loss of protein. As shown on the western blot on Figure 41 no protein was detected in the wash fraction.

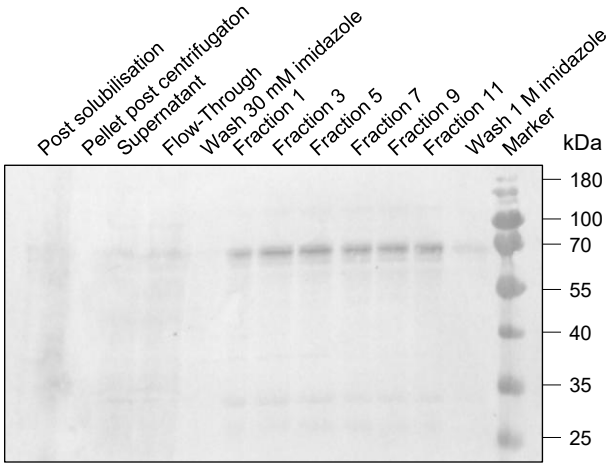

Figure 41: Western blot of rGAT1 after membrane extraction and Ni-NTA resin elution, expressed in shaking flask at 125 rpm after 72 h. The primary antibody used was anti His-tag. The protein quantity loaded was the same as on the figure XZW.

- *Detergents*

According to the western blot on the figure Figure 41 is detectable. However, the TEM images (Figure 42) showed only white spheres corresponding to aggregates of empty DDM micelles, suggesting that *r*GAT1 is not stable after purification.

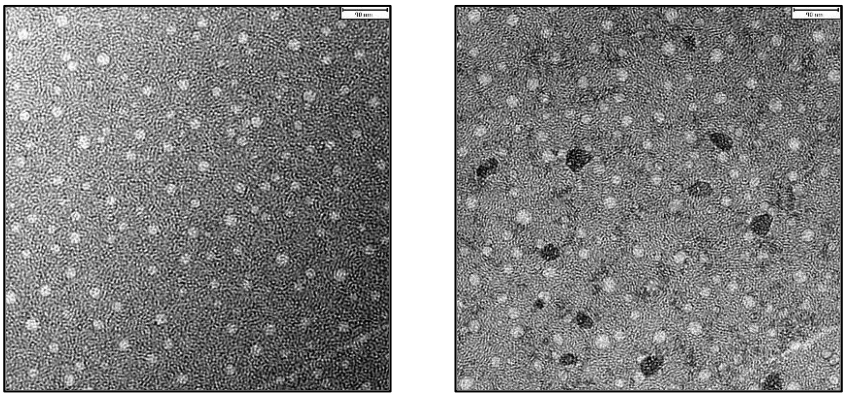

Figure 42: TEM images of rGAT1 WT in DDM/CHS micelles. Observation made at magnification 22 000× with the microscope CM12 (Philips). These two images show mainly detergent micelles (white spheres). The two images correspond to two different spots on the same 300-mesh copper carbon coated grid.

Indeed, the use of DDM for GAT1 is controversial. Zhu and coworkers got the best resolution for human GAT1 by cryo-EM (2.2 Å) in DDM/CHS micelles. Contrastingly, Motiwala and coworkers showed that DDM decreases the melting temperature by 12°C compared to the use of LMNG. The higher stability of proteins in LMNG micelles comes from the phospholipid-like shape of LMNG alkyl chains and is conventionally used at concentration much under the CMC (Godoy-Hernandez et al. 2023; Motiwala et al. 2022; Breyton et al. 2019). It offers the possibility to get less blurred movies for SPA. Also, LMNG is recommended for proteoliposome reconstitution without using SM2-Biobeads (Godoy-Hernandez et al. 2023). Therefore, cell plasma membranes were solubilized with 2% LMNG/ 0,2% CHS, (w/v). The concentration of LMNG/CHS was kept at 0,001% LMNG/0,0001% CHS (w/v) all along the purification. The Figure 43 shows the chromatogram after microAekta run and the associated SDS PAGE gel, with the other steps of purification before size exclusion. The monodisperse peak at 2 ml elution demonstrates that the structural integrity of the protein is kept.

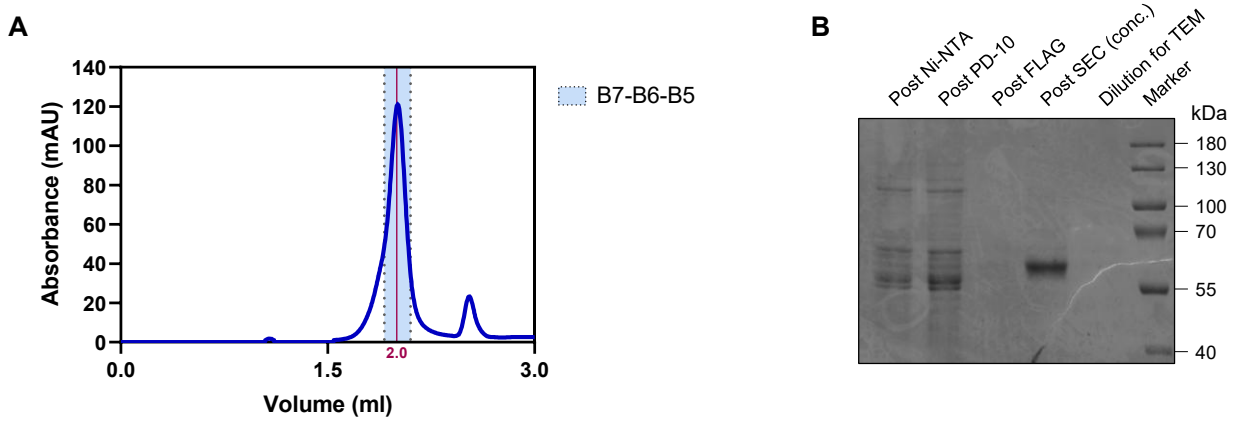

Figure 43: Purification of *r*GAT1 before vitrification for Cryo-EM. a) Chromatogram from SEC (column Superose^{TM} 6 increase 5/150 GL) and b) SDS PAGE analysis of the different step of purification. "Post SEC conc." represents the concentration of the fractions under the peak at 2 ml elution volume. It will be used for further negative stain and vitrification.

- *Forward/Reverse purification*

Finally, the succession of the affinity chromatography steps was also analyzed. The order Ni-NTA resin/desalting column/Anti-FLAG resin is called "forward purification" while the order anti-FLAG resin/Ni-NTA resin is called "reverse purification". The latter strategy was thought to avoid the desalting step.

According to the silver staining SDS PAGE, the purity of the sample is low either if the first purification step is the Ni-NTA or anti-FLAG resin (Line “elution post Ni-NTA” and “elution post FLAG” respectively on Figure 44C and D). The band associated with rGAT1 is slightly more visible after the second step purification in the reverse purification than in the forward purification, where no protein is detected (line “elution post anti-FLAG”, “elution post Ni-NTA” respectively on Figure 44C and D). Therefore, the reverse purification does not dilute the sample too much. However, the protein peak associated with *r*GAT1 elution is 4-fold higher for the forward purification than for the reverse purification (Figure 44A and B). Moreover, a supplementary band is visible around 40 kDa (Figure 44D, lines “Fractions C2, C3, C4”) for the reverse purification, while absent in the forward purification (Figure 44C line “ Post SEC”).

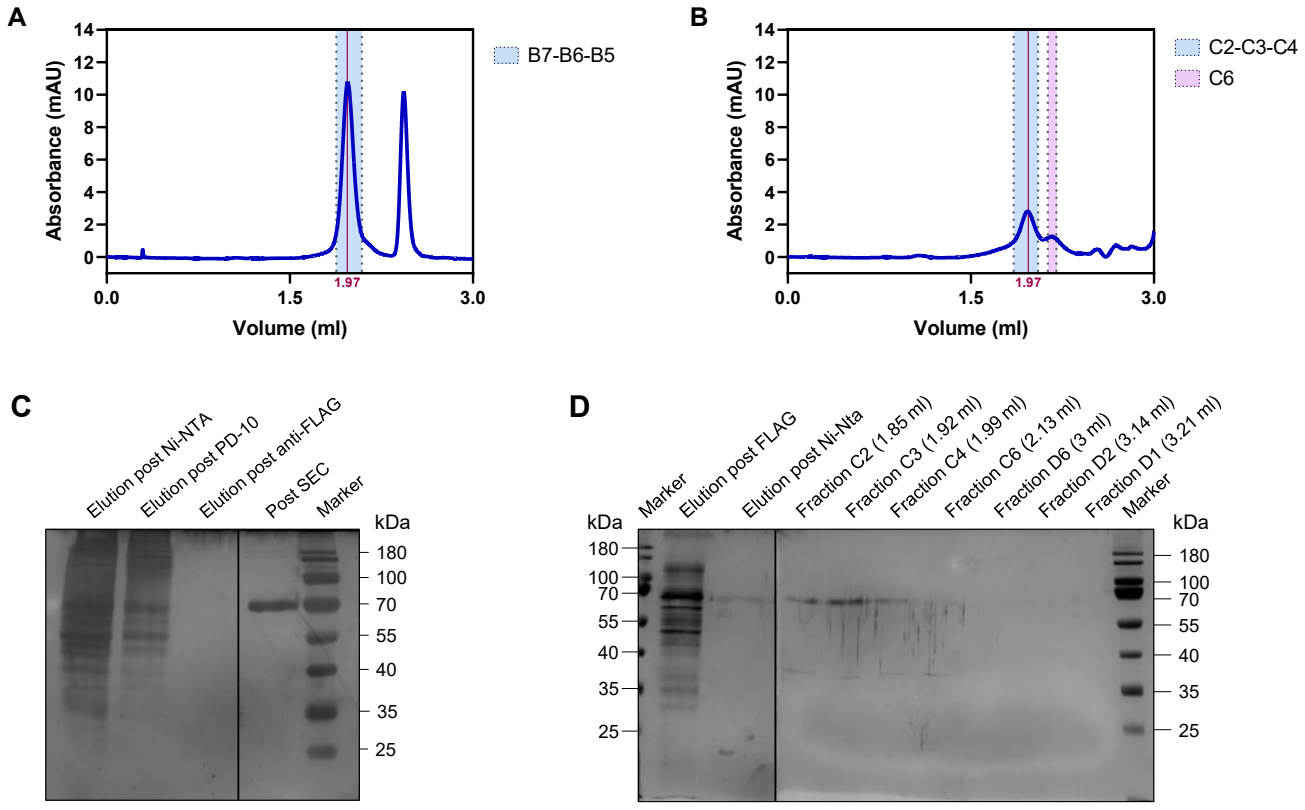

Figure 44: Comparison between the forward and the reverse purification of *r*GAT1. Chromatograms of a) forward purification and b) reverse purification. Associated silver staining gels summarizing the steps of c) forward purification and d) reverse purification.

All together, these results showed that the forward purification of *r*GAT1 maximizes the final protein yield for further applications.

4. Vitrification and grid type optimization

i. Carbon coated grids

After size exclusion chromatography (Figure 43.), rGAT1 WT was vitrified on different grid types to determine the coating offering the best particle density for data collection by cryo-EM.
The Figure 45 shows a typical micrograph and some 2D classes after vitrification on 1.2/1.3 300 mesh carbon coated grids. In total 7000 micrographs and 20000 particles were collected.

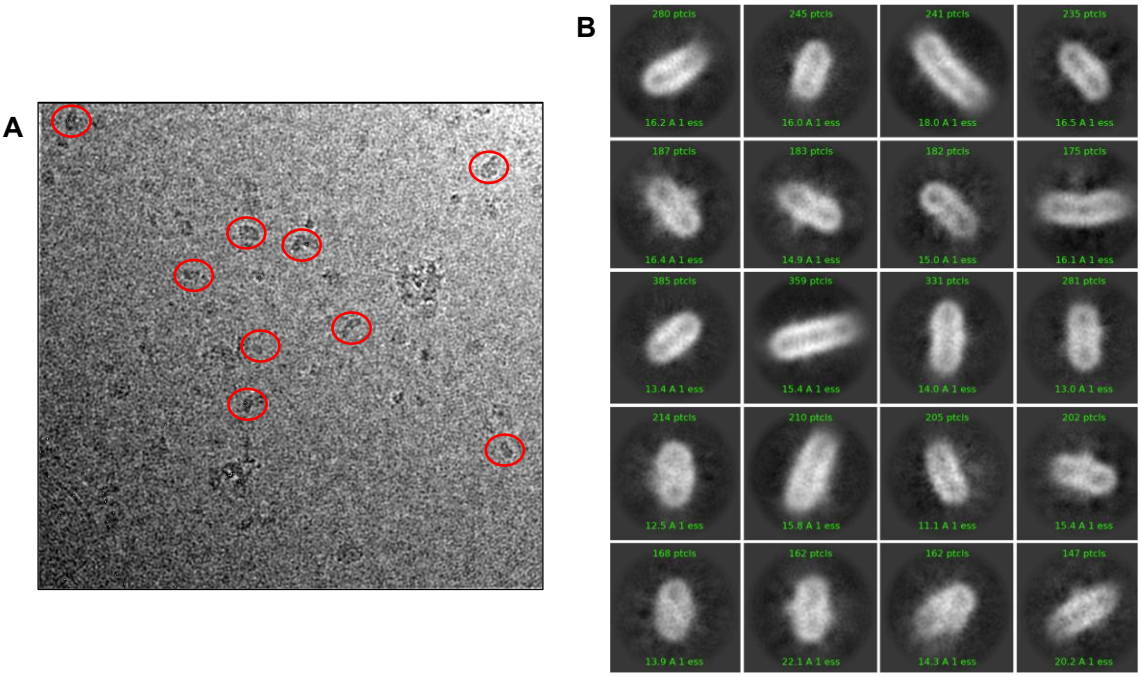

Figure 45: Data collection of *r*GAT1 in LMNG/CHS micelles (0.001%/0.0001%) vitrified on 1.2/1.3 300 mesh carbon coated grids with the microscope cryoARM 200 at magnification ×80 000. a) Micrograph where some particles are circled in red. b) 2D classes.

The cylinder shape on the Figure 45B represents the LMNG/CHS micelles. The protein is orientated perpendicularly in the middle of the micelle. Certain protein domains like the extracellular loop 2, the N and C-terminus are visible as small extensions getting out of the micelles. However, these are low resolution 2D classes because any secondary structures of the protein can be deciphered in the inner part of the micelle. This is partially due to the very few numbers of particles present in the hole center of the holey foil (Figure 45A). This problem was already reported in by Motiwala *et al.,* in 2022 where the particles were mostly located at the edge of the holes. Moreover, most of the particles might be located at the air-water interface and adsorbed on the blotting paper during the vitrification.

ii. Graphene oxide coated grids

Grid coating promoting the concentration of particles into the holes of the grid film is required for rGAT1. Graphene oxide (GO) was already reported for being advantageous for this purpose, especially when particles are smaller than 100 kDa. (Fan and Sun 2022; Pantelic et al. 2012; Patel et al. 2021). Therefore, rGAT1 was vitrified also on 1.2/1.3 300 mesh carbon grids with supplementary graphene oxide particles suspension forming layers upon the original carbon film. The Figure 46 shows the different particle density on the two coating types.

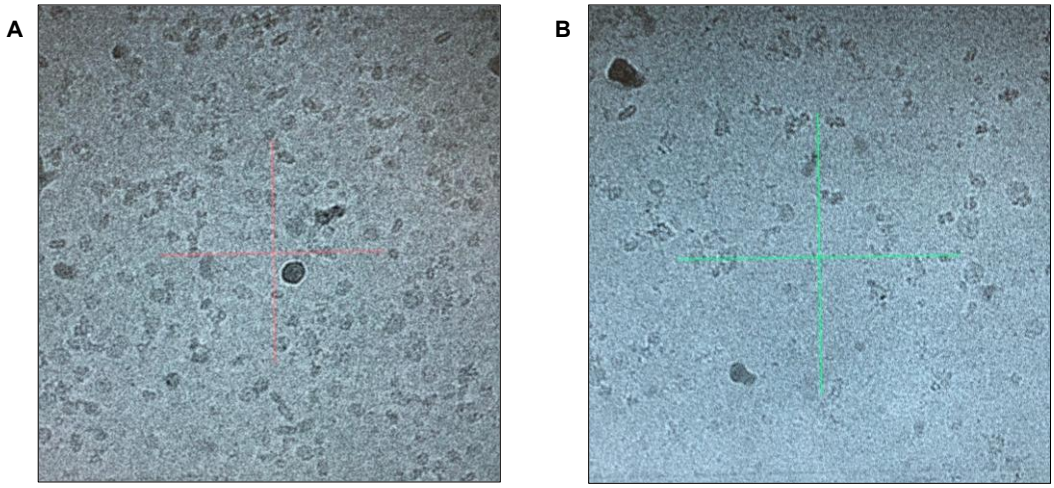

Figure 46: Comparison of rGAT1 particle density on the same type of grid 1.2/1.3 300 mesh coated with a) supplementary graphene oxide layer and b) standard carbon film. The grid screening was performed with the microscope cryoARM200 (Jeol) at the magnification ×80 000.

With the same protein sample, grid type, blotting time before vitrification (6 seconds) and the same magnification, graphene oxide coating improved the quantity of particles in the grid region observed. The 2D classes averaged from GO coated grids (Figure 47) are comparable to those presented on the Figure 45.

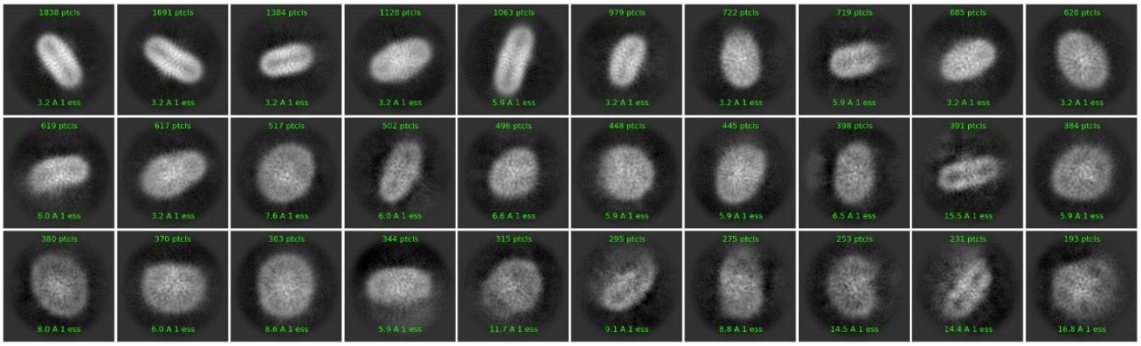

Figure 47: 2D classes of *r*GAT1 on 1.2/1.3 graphene oxide coated grids.

However, the Figure 48 is showing the superposition of graphene oxide sheets when it lays on the grid surface. Consequently, it hides the particles and cannot be used for further processing. Here it reveals the challenge in working with graphene oxide coated grid (Matthias Stauber's Master thesis) and consequently, it will not be used lately.

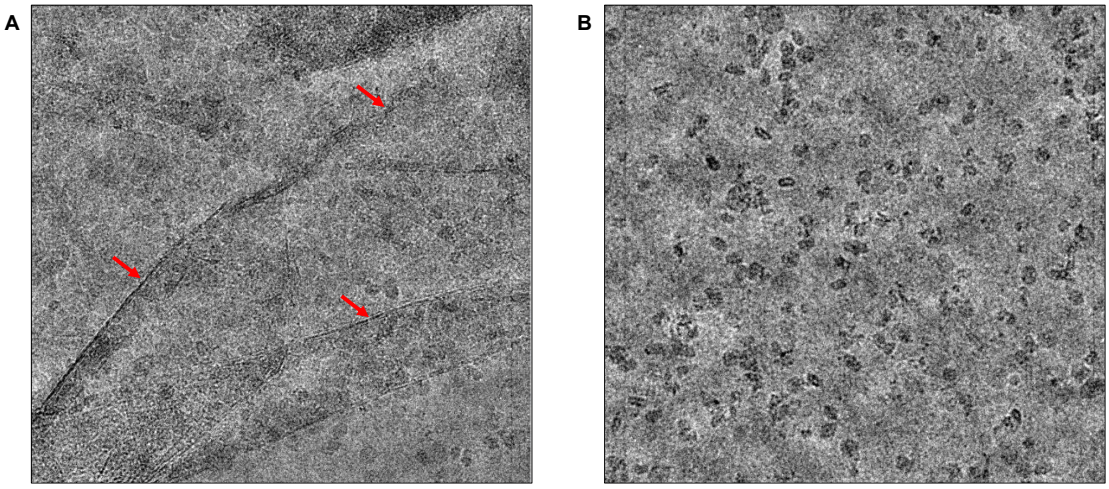

Figure 48: Micrographs of *r*GAT1 particles at the surface of GO coated grids. a) GO sheets overlaying (red arrow). b) Uniform GO film.

To summarize, rGAT1 WT was transiently transfected in DNA:PEI ratio 1:3, expressed in shaking flask at 125 rpm and 8% CO_2 for 72 h. It was extracted from the membrane and solubilized in 2% LMNG/0.2% CHS for more protein stability. The concentration of detergent was kept at 0.001% LMNG/0,0001% CHS for all the following purification steps (affinity and size exclusion chromatography). The Ni-NTA resin wash after binding was decreased to 30 mM imidazole to avoid protein loss. The passage on Ni-NTA resin must be made before the passage on anti-FLAG resin ("forward purification") to increase the protein yield after SEC. rGAT1 WT was vitrified on

two different grid coated type: carbon and graphene oxide. However, the latter demonstrated that it is not ideal for further data processing. Establishing rGAT1 expression, purification and vitrification condition screening constitute the basements for further biophysical assays to determine the transport and regulation mechanisms of GAT1.

5. rGAT1 WT proteoliposome reconstitution

After rGAT1 WT purification, it was reconstituted in proteoliposomes for further investigations with functional assay. Following the method described by Godoy-Hernandez and co-workers in 2023, rGAT1 was reconstituted in proteoliposomes with brain total extract lipids (composition on Figure 49).

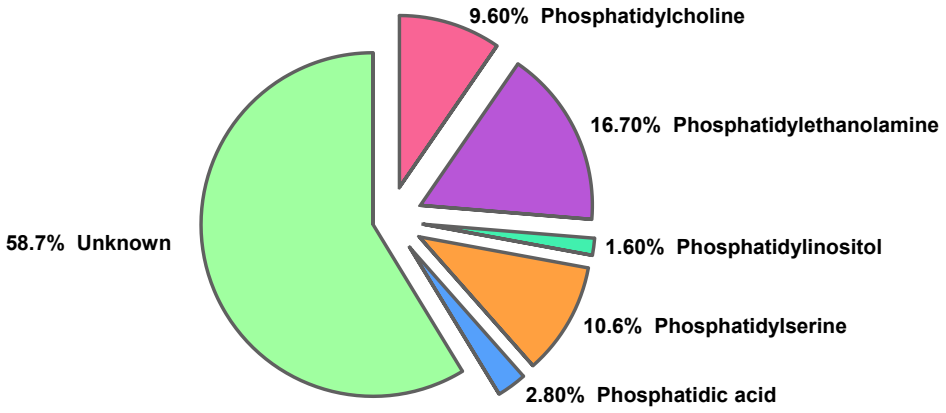

Figure 49: Lipidic composition of the brain total extract used for proteoliposome reconstitution of rGAT1 WT (Data from Avanti Polar Lipid, USA).

Three different Lipid to Protein Ratio (LPR) were used and rGAT1 is detectable in each sample by western blot (Figure 50A). Moreover, negative stain images (Figure 50B) showed flat spherical structures characteristic of proteoliposomes. Altogether, these results show the reconstitution of the protein.

.

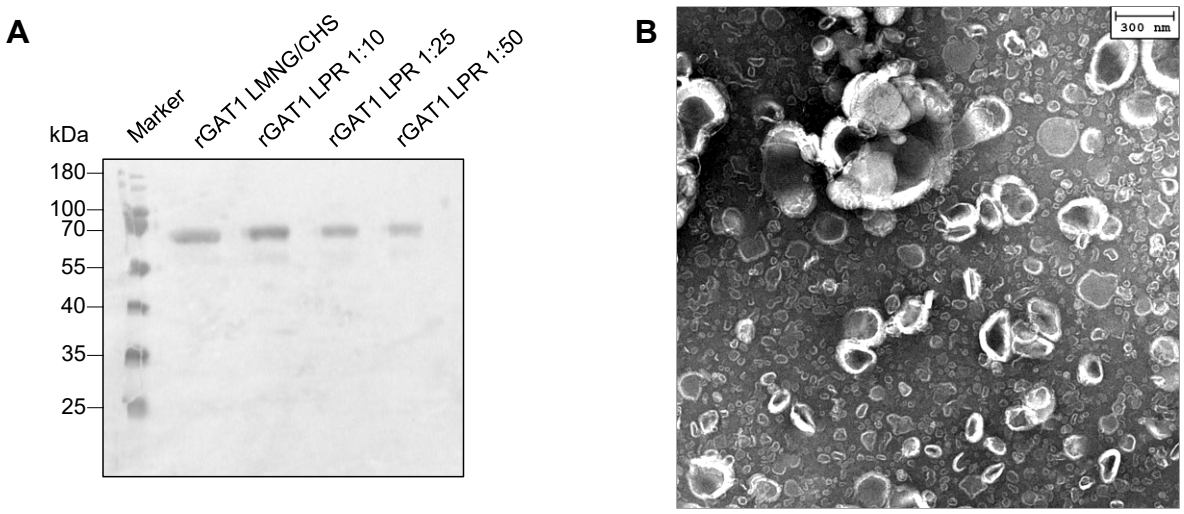

Figure 50: Analysis of rGAT1 reconstituted in proteoliposomes according to the method proposed by Godoy Hernandes and coworkers. a) Western blot of rGAT1 in detergent micelle for control and reconstituted in PL with different LPR (1:10, 1:25, 1:50). Detection of the protein was made with an antibody anti-GAT1. b) TEM image (CM12, Philips Mag.×6300) of rGAT1 in proteoliposome LPR 1:10.

6. Biophysical characterization

i. GABA binding assay

Based on collaborative work with Despoina Kapiki (LMU, Munich), rGAT1 WT reconstituted was used for thermophoresis assay to attend its capacity to bind it canonical substrate, GABA. On the Figure 51, in presence of GABA, the melting temperature peak shifted of 5°C. This means that more energy is required to unfold the protein because residues involved in the coordination of the substrate protect the protein core. Therefore, reconstituted rGAT1 can bind GABA and therefore is properly folded in the circular lipid bilayer.

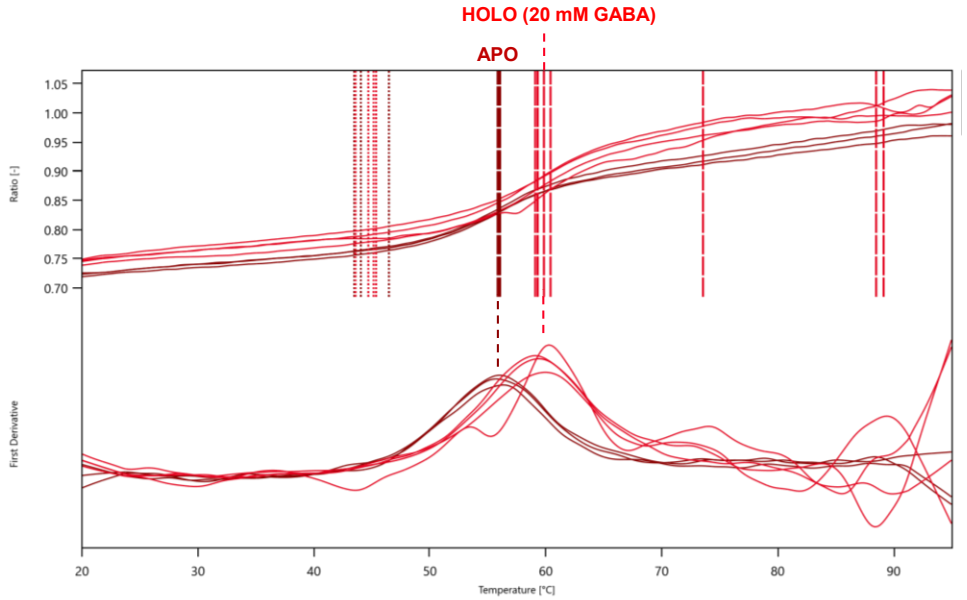

Figure 51: Thermophoresis experiment showing the binding of GABA on rGAT1 reconstituted in proteoliposomes (experience performed by D. Kapiki, LMU). 50 µl of proteoliposome rGAT1 (LPR 1:10) was diluted in 2000 µl of buffer Tris/MES with 150 mM NaPi, 20 mM GABA. Each temperature (Apo and holo) was measured 4 times.

ii. Fluorescent-based transport assay

rGAT1 reconstituted in proteoliposomes was also used for a chemosensor-based transport assay (elaborated by D. Kapiki). First, rGAT1 proteoliposomes are pre-loaded with a scavenged fluorophore complex so called *para-sulfonatocalix[4]arene-Atto655* (Figure 52). While GABA is up taken the fluorophore becomes unshielded and can emit at 680 nm.

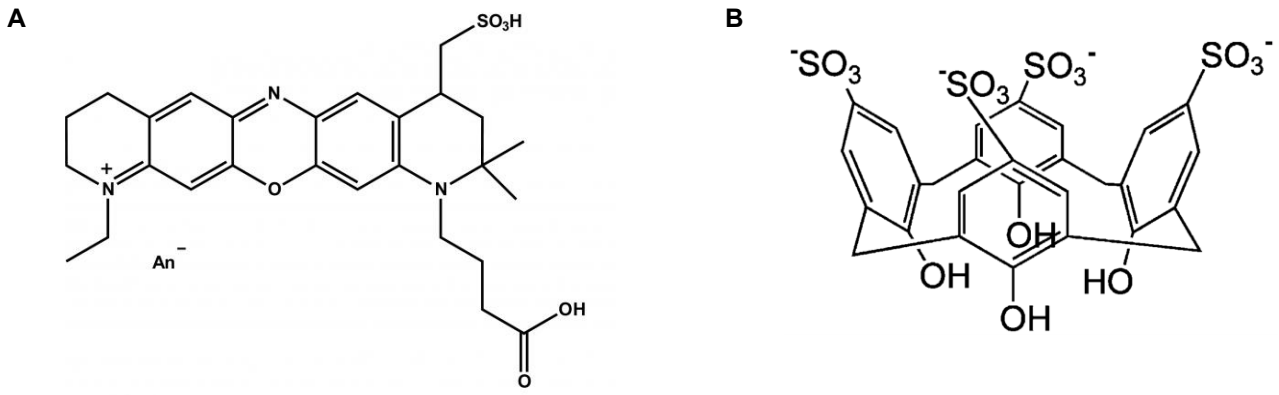

Figure 52: Scavenged fluorophore used for chemosensor-based transport assay. a) Fluorophore *Atto655* (Atto-Tech, GmbH, Germany). b) Scavenger *para-sulfonatocalix[4]arene* (SCX) (image from Harvey 2002) . The cavity like-conformation of the latter promotes the formation of an inclusion complex with Atto655, that consequently quenches its fluorescence (Gawhale et al. 2014; Guo and Liu 2014).

On the Figure 53, the fluorescence emission increased stepwise when the external concentration of GABA gradually increased. This suggests that rGAT1 reconstituted can transport GABA through the lipid bilayer of the proteoliposomes, as it was already proved. Moreover, this result is a proof of concept for the chemo-sensor based transport assay.

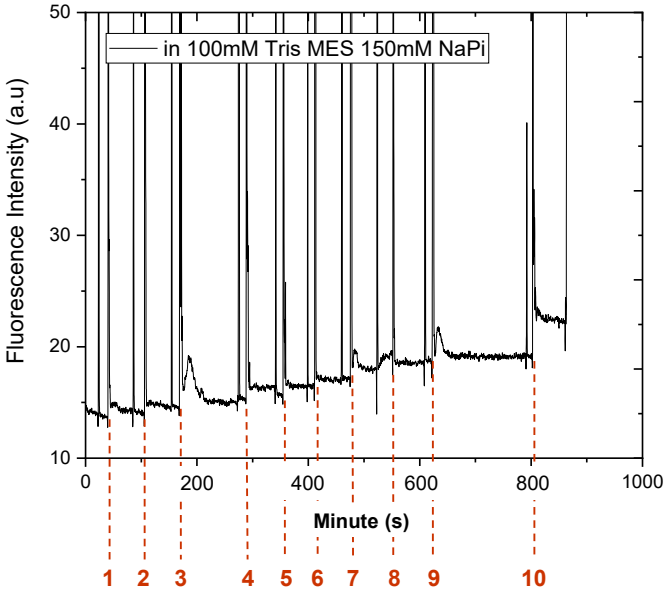

Legend	[GABA]
1	2 mM
2	4 mM
3	6 mM
4	8 mM
5	10 mM
6	12 mM
7	14 mM
8	16 mM
9	18 mM
10	30 mM

Figure 53: Chemosensory-based transport assay for rGAT1 WT reconstituted in proteoliposomes with the LPR 1:10 pre-loaded with 1 µM of Atto655 (fluorophore) and 10 mM SCX4 (scavenger) in 250 mM KPi. Gradual concentrations of GABA (0 to 30 mM) are buffered in Tris/MES with 100 mM NaPi (experience performed by D. Kapiki, LMU).

7. rGAT1 Enriched extracellular vesicles Expression/Purification

Following a collaboration with Dr. Beatrice Amigues and Dr. Vincent Delauzin (CytobodX, Marseille, France), rGAT1 WT was also expressed and purified in extracellular vesicles. It presents two main advantages: avoiding the use of detergent and studying the protein in a neo-native phospholipidic environment. rGAT1 enriched EVs are secreted in the culture media. They are purified and selected by size exclusion chromatography (Figure 54A). The peak is not monodispersed and corresponds to two different populations of EVs distinguished as peak 1 (8 ml, red area) and 2 (9 ml, green area). On western blot (Figure 54B), the smeared bands between 60 and 100 kDa for peaks 1 and 2 correspond to the different glycosylated isoforms of rGAT involving the 3 asparagine residues (Asn176, Asn181, Asn184) subjected to glycosylation. The bands of rGAT1 on western blot are identical. Therefore, the two different EVs population depends on the intrinsic and structural properties of the EVs. Indeed, the dynamic light scattering analysis (Figure 54C) showed that the peak 2 (green line) has no gaussian distribution and contains 1.5-fold less EVs with a 300 nm radius compared to peak 1 (red line). This sustains that the shape of the EVs from the peak 2 is flexible and heterogenous, instead of circular; this is clearly visible on the negative stain images recorded by TEM on Figure 55.

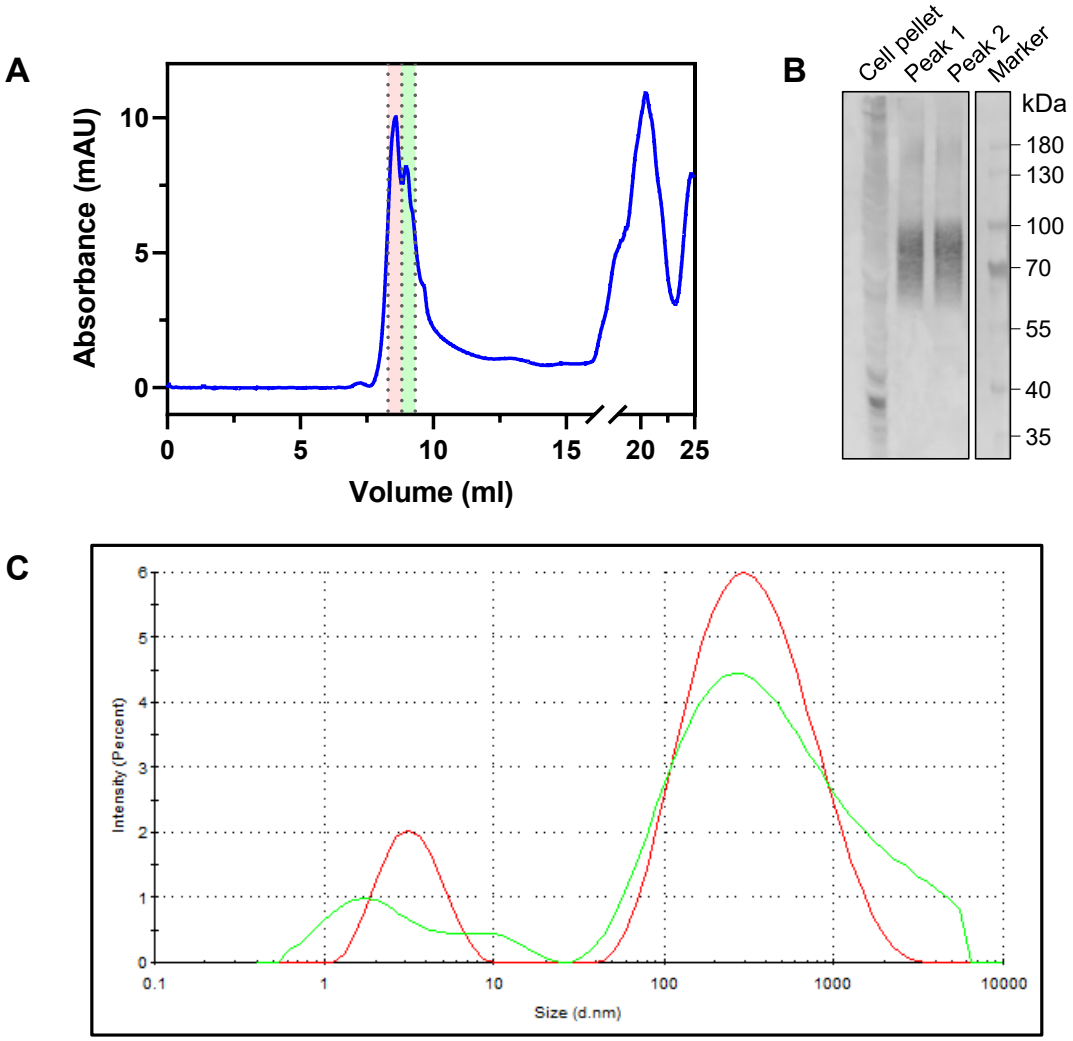

Figure 54: Purification and further analysis of rGAT1 expressed in EVs. a) Chromatogram after size exclusion chromatography (Superose 16/60, Cytiva). The area colored in red and green correspond respectively to peak 1 and peak 2. b) Western blot analysis of both peaks (with primary antibody anti-FLAG). The smeared bands visible between 60 and 100 kDa represent the different glycosylated isoforms of the protein in the EVs. c) Dynamic light scattering analysis. As for the chromatogram, peak 1 and 2 correspond respectively to the red and green lines. The peaks visible between 1 and 10 nm do not correspond to EVs but to impurities in the sample for both EV populations.

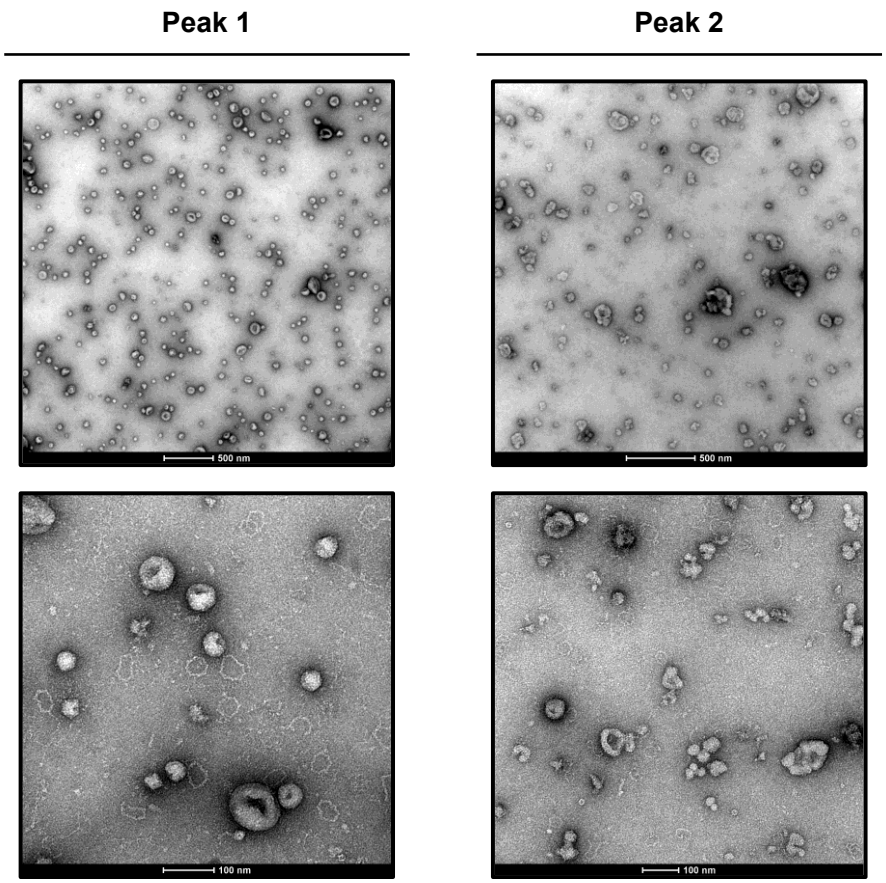

Figure 55: TEM images of rGAT1 in EVs corresponding to peak 1 and peak 2 obtained after SEC (Mag.×97000 Microscope FEI 120 keV, Thermo Fisher). Scale bar 500 nm for images on the top and 100 nm for the images on the bottom.

rGAT1 were successfully expressed at the surface of extracellular vesicles and according to results, they offer a batch of advantages compared to proteoliposomes. First, all GAT1 molecules are oriented inside-in i.e. with the N and C terminus in the intracellular space. Moreover, GAT1 expressed in EVs is highly glycosylated, presumably with long patterns (Figure 54B). The presence of sialic acid (last glycosylation moiety of the pattern) on GAT1 showed that the uptake of GABA increases by 25% than in its absence. This is because terminal sugars of oligosaccharide chains are involved in molecular recognition and communication (J. Hu et al. 2011). More precisely, the absence of sialic acid decreases the V_{Max} and the sodium affinity by 4-fold. However, it does not impair the GABA affinity. Sialic acid is supposed to facilitate the translocation of GABA and sodium ion trough the transporter (G. Cai et al. 2005). As sialic acid is anionic, it is also hypothesized that it has a role in recruiting the second sodium ion, known to be in a low

affinity and a versatile binding site in the transporter. Therefore, both the right orientation and correct high glycosylation of GAT1 expressed on EVs offer good reproducibility and reliable results for studying GAT1 transport mechanism by functional chemosensor assays proposed by Despoina Kapiki (fig. fluo assay Despoina). The importance of the neo-native phospholipidic environment in EVs is extendedly explained in the ***Discussion***.

II. GABA and betaine transport in GAT1 WT and L300Q, a BGT1-like mutant

1. Identification of functional mutants of rGAT1 by TEVC

i. Single mutants

As mentioned in introduction, there are three key residues in BGT1, Glu126, Q299, and Cys402 that are hypothesized to confer the transport selectivity to this protein. Following the procedure of Dodd and Christie in 2007, these residues are substituted into rGAT1 at their respective positions to convert it to BGT1-like transporter.

After RNA injection of rGAT1 WT and single mutants in *X.laevis* oocytes, they were perfused with 300 µM or 10 mM betaine both in a baseline solution containing 98 mM sodium chloride (*c.f.:* ***Material and Methods***). Figure 56 presents the results for L300Q mutant while Figure 57 for S133E and G403C mutants.

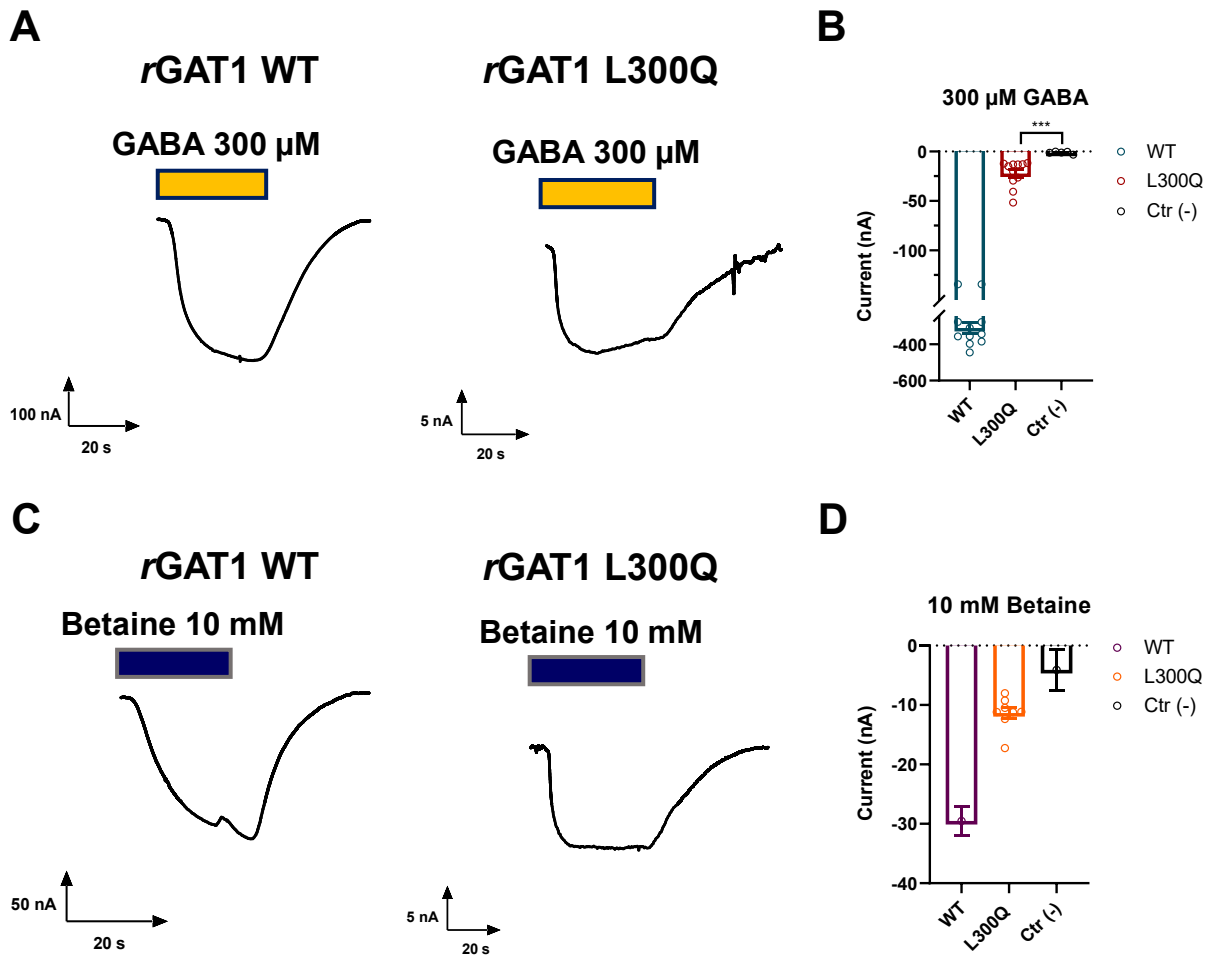

Figure 56: Response of rGAT1 WT, L300Q and non-injected oocytes after perfusion of GABA or betaine with constant concentration of sodium chloride (98 mM) at the holding voltage of -60 mV. Traces after perfusion of rGAT1 WT and L300Q with a) 300 µM GABA and c) 10 mM betaine. Summary graphs with single values plotted and unpaired T-Test with Welch correction (GraphPad8) to compare the average currents of rGAT1 WT, L300Q and non-injected oocytes (data± SEM, with at least 5 oocytes from 2 different batches). b) 300 µM GABA and d) 10 mM betaine.

In presence of 300 µM GABA, the typical traces visible on figure Figure 56A showed that the mutant is able to elicit a current like the WT but of reduced amplitude. This inward current is elicited by the translocation of GABA with the sodium ions into the intracellular space. However, the amplitude for the mutant is 16-fold lower (Figure 56B). In presence of 10 mM betaine, the typical traces (Figure 56C) was recorded in the WT and L300Q mutant, interestingly, the average current of L300Q was larger than in the presence of GABA and the WT current was only 3-fold higher (Figure 56D). Overall, these preliminary results showed that the mutant saturates more easily than the WT, probably due to an impairment of the successive conformations that the transporter should adopt to complete its cycle. The average currents are significantly higher than a negative control (non RNA-injected oocytes) with GABA but not with not with betaine (Figure 56B, D). However, there is a clear tendency of the mutant to induce transport currents in presence of the methylammonium substrate (Figure 56C). This contrasts with the two other single mutants (S133E and G403C) where in presence of GABA or betaine, the typical traces correspond only to background noise (Figure 57A, C) and the average currents were equivalent to non-injected oocytes (Figure 57B, D).

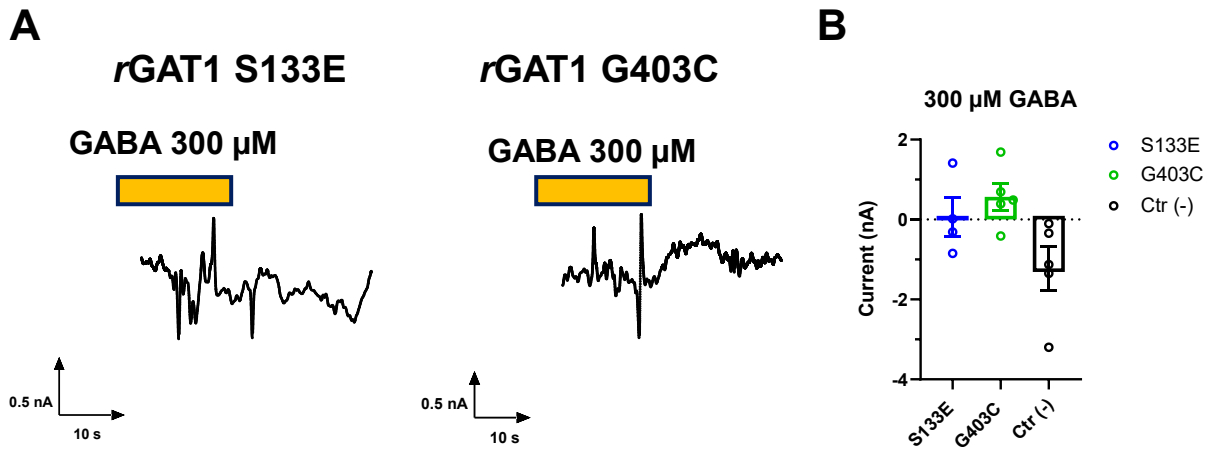

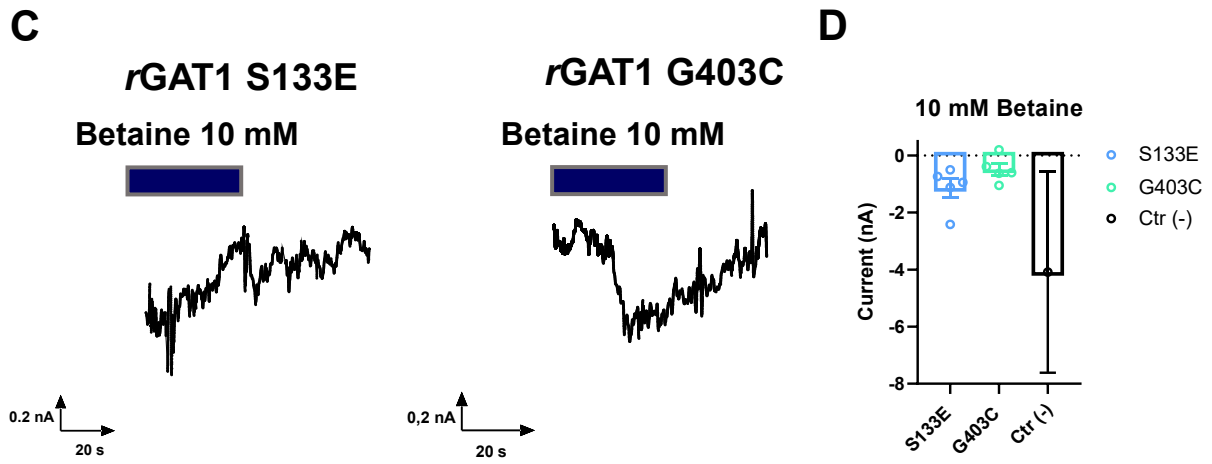

Figure 57: Response of rGAT1 WT, S133E, G403C and non-injected oocytes after perfusion to GABA or betaine with constant concentration of sodium chloride (98 mM) and holding voltage of -60 mV. Traces after perfusion of rGAT1 WT, S133E and G403C with a) 300 µM GABA and c) 10 mM betaine. Summary graphs with single values plotted to compare the average currents of rGAT1 WT, S133E, G403C and non-injected oocytes (data± SEM, with at least 3 oocytes) with b) 300 µM GABA and d) 10 mM betaine.

ii. Double mutants

As written by Dobb and Christie in 2007, more than one single point mutation promoted better transport function transposition. Therefore, all double combinations (S133E/L300Q, L300Q/G403C, S133E/G403C) and the triple (S133E/L300Q/G403C) mutants were generated.
No signal was recorded with the triple mutant and S133E/L300Q. For L300Q/G403C a significant difference compared to the negative control was recorded in the absence of Na (0 mM) as positive current and at the highest (150 mM) sodium concentrations with a constant concentration of 300 µM GABA (Figure 58). This peculiar behavior can be explained: for the outward current at 0 Na, this is the block of the leak of Na current that in this transporter is larger than the WT.

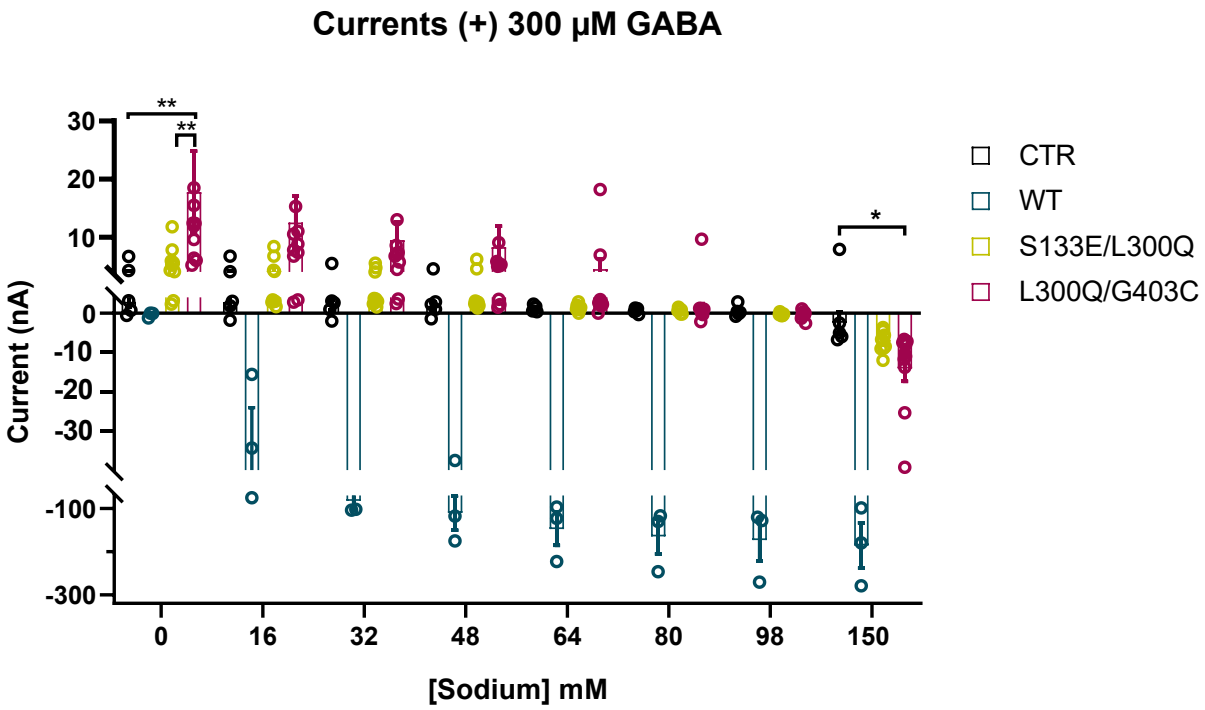

Figure 58: Average currents of rGAT1 WT, S133E/L300Q, L300Q/G403C and non-injected oocytes with a constant concentration of 300 µM GABA and a range of sodium chloride concentrations (holding voltage -60 mV, data± SEM, with at least 5 oocytes from 2 different batches).

2. Membrane expression observed by epifluorescence microscopy

To understand why every mutant has lower current intensities, they were immunolocalized in oocytes. If the subcellar localization of GAT1 mutants is compromised, it cannot fulfil its transport function, explaining that no current intensity is recorded by two electrode voltage-clamp.

Oocytes have a huge autofluorescence signal due to lipidic droplets present in their cytoplasm (spherical intracellular structures Figure 59Figure 60 and Figure 61). The red signal corresponds to the fluorescence of the dye conjugated to the secondary antibody and permits to detect the presence of GAT1 in the subcellular compartments. Yellow-orange fluorescence corresponds to the superposition of the protein signal and the autofluorescence showing the localization of the protein in the cytoplasm.

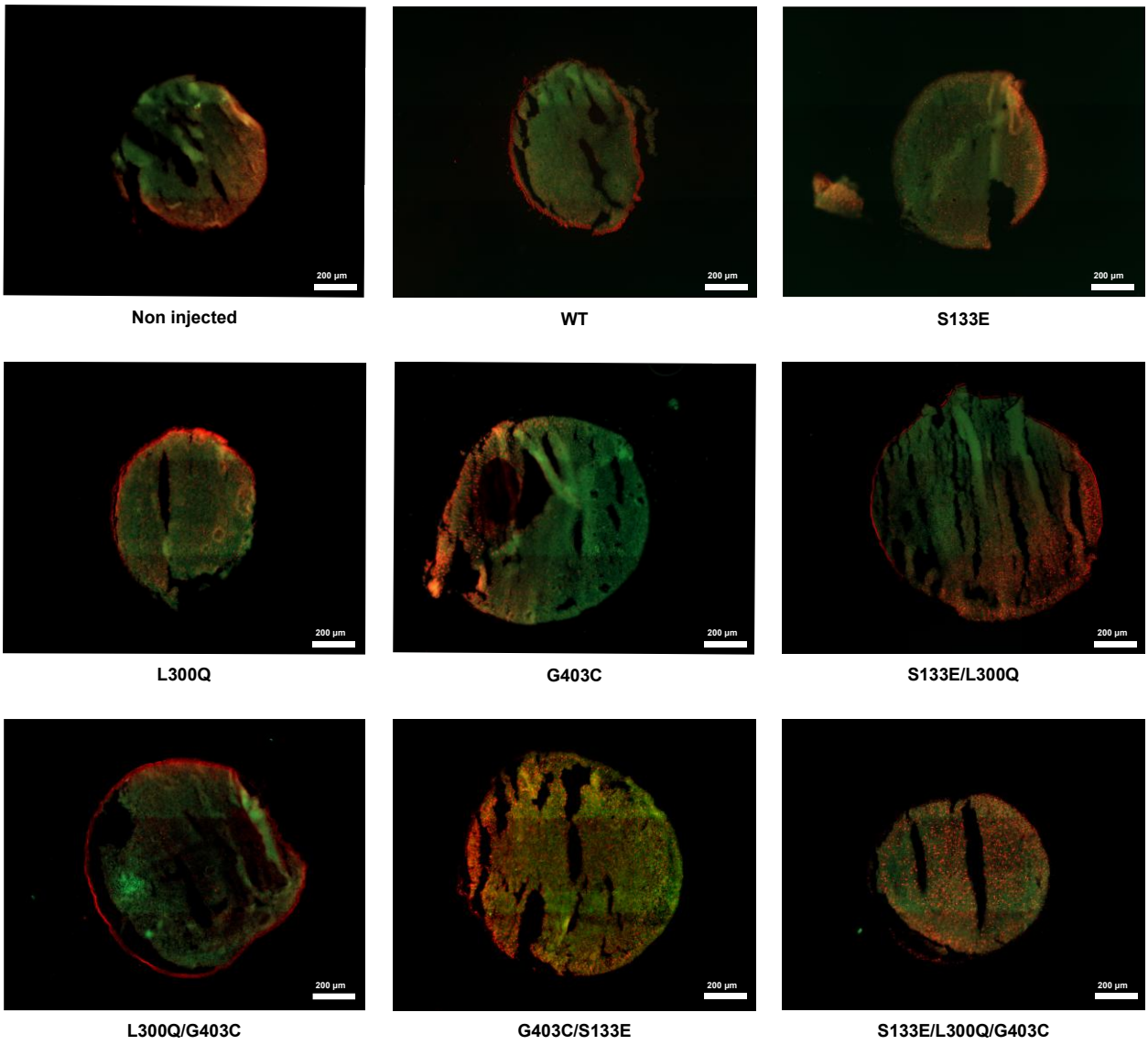

Figure 59: Entire oocytes for immunolocalization of rGAT1 WT and mutants (Mag. ×20, Axio observer Z1/7, Zeiss). Red signal on the oocyte plasma membrane corresponds to the presence of the protein. Non injected oocytes were also incubated with primary anti-GAT1 antibody for negative control. The experiment was repeated twice with oocytes from two different batches.

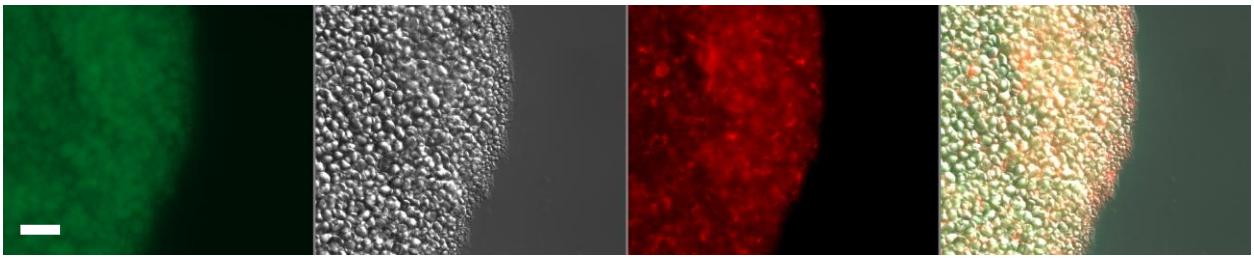

Non injected

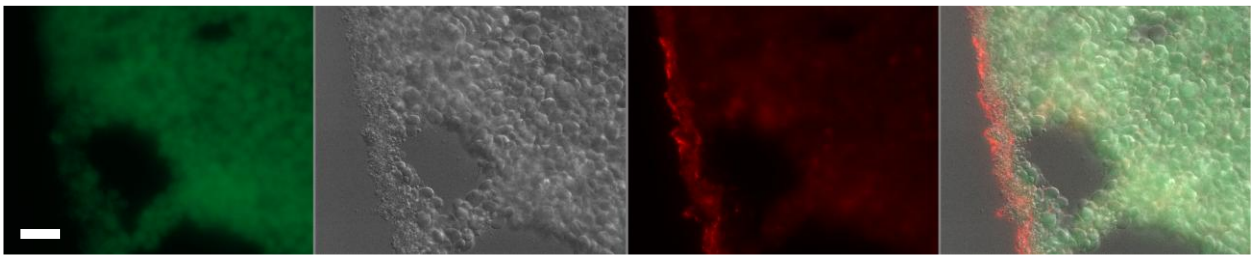

WT

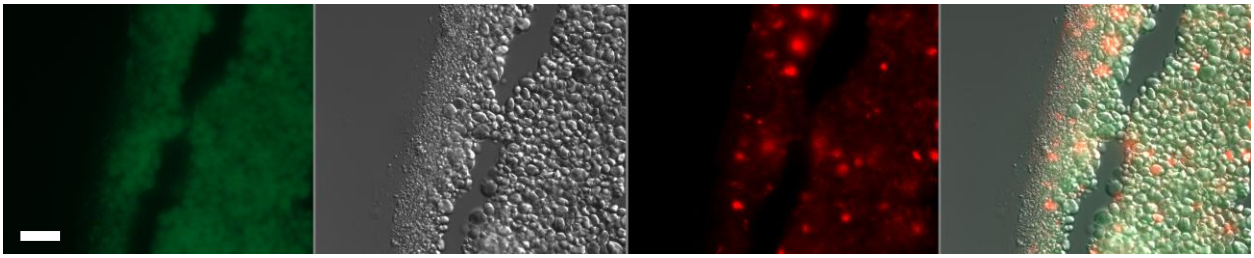

S133E

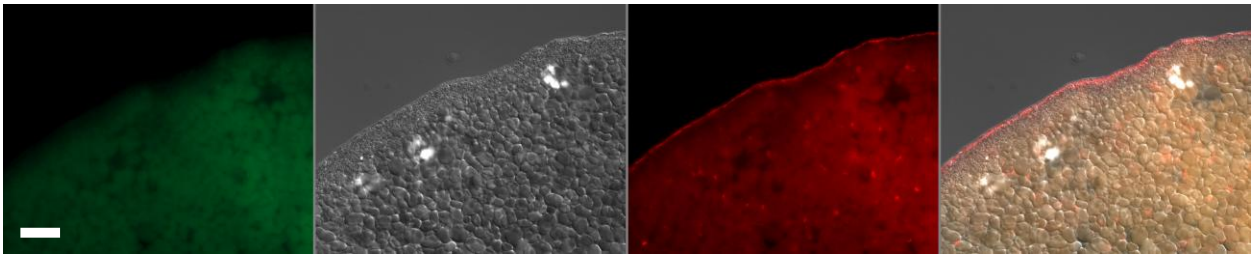

L300Q

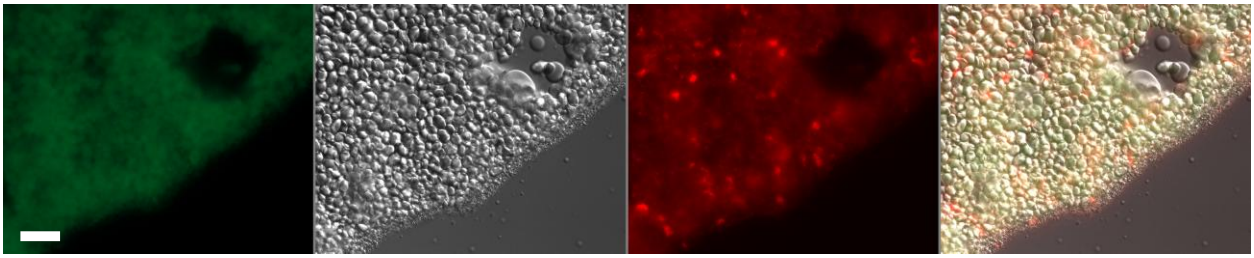

G403C

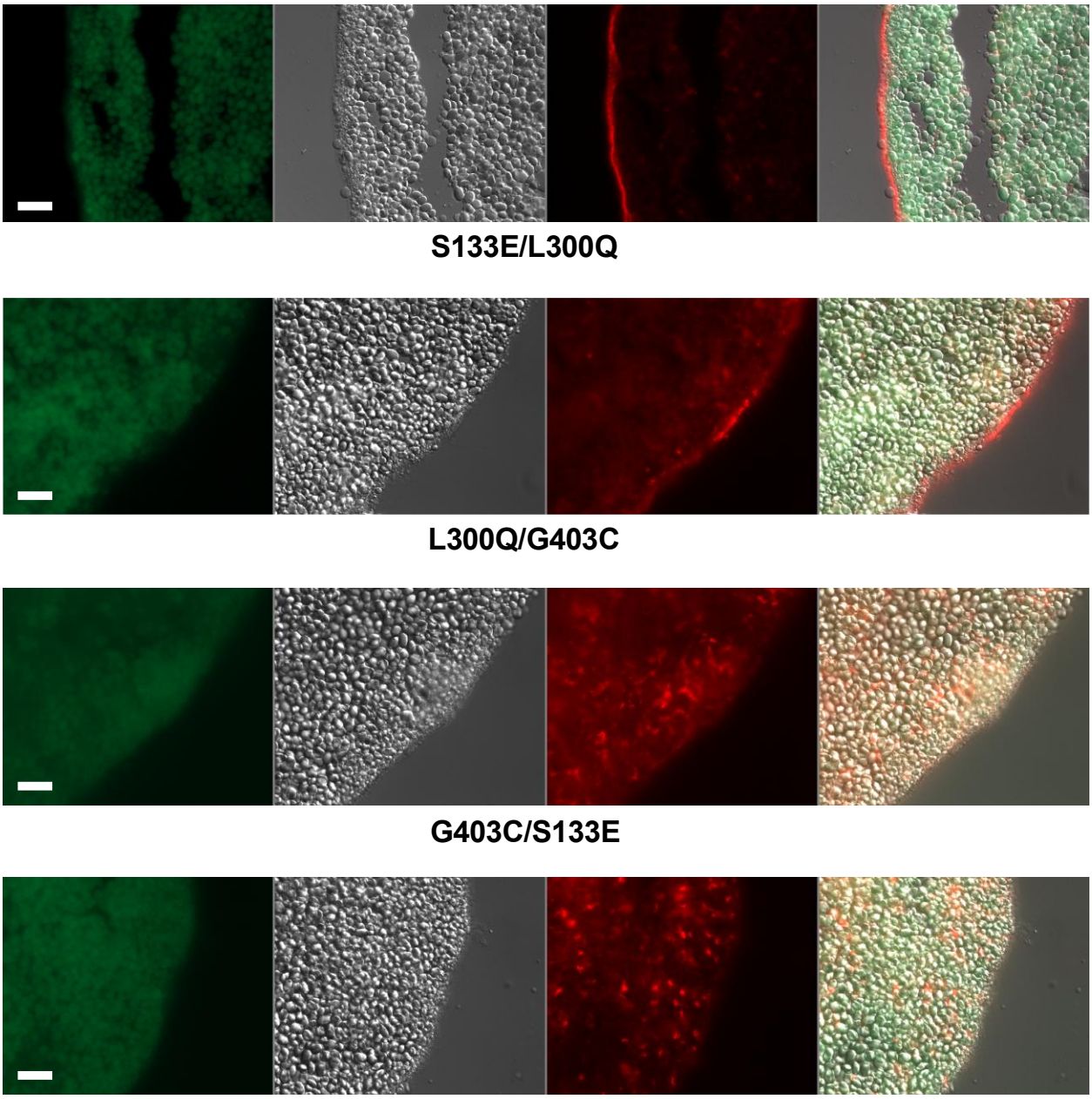

Figure 60: Vegetal oocyte poles for immunolocalization of rGAT1 WT and mutants (Mag. ×63 with immersion oil, Axio observer Z1/7, Zeiss, scale bar 20 µm).

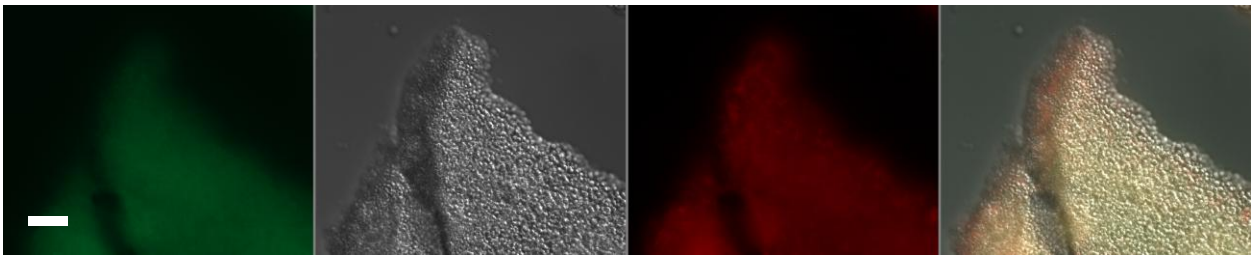

Non injected

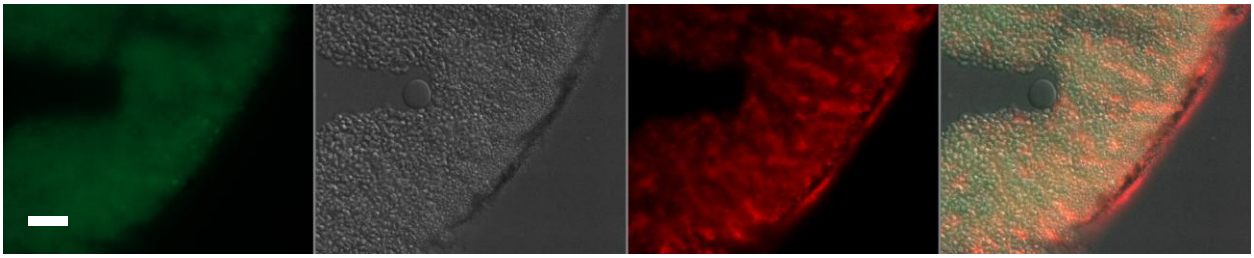

WT

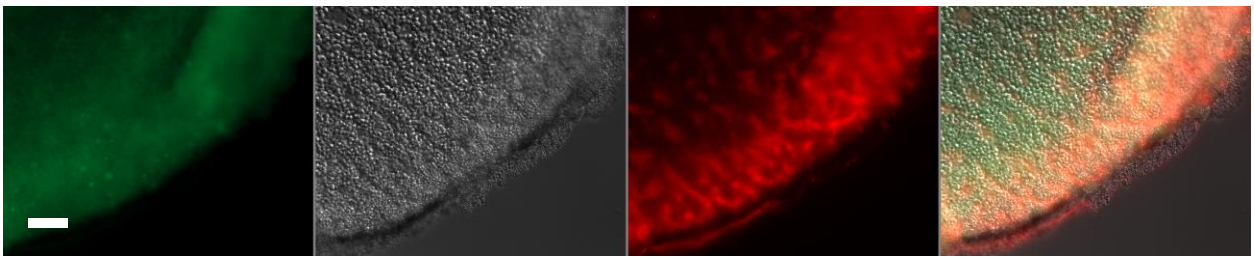

S133E

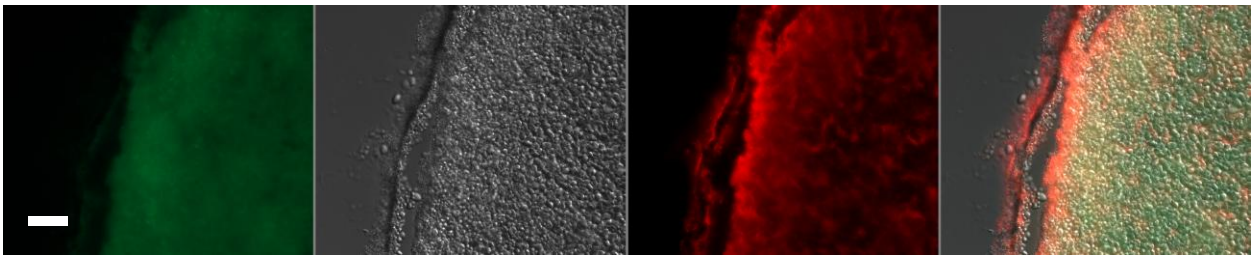

L300Q

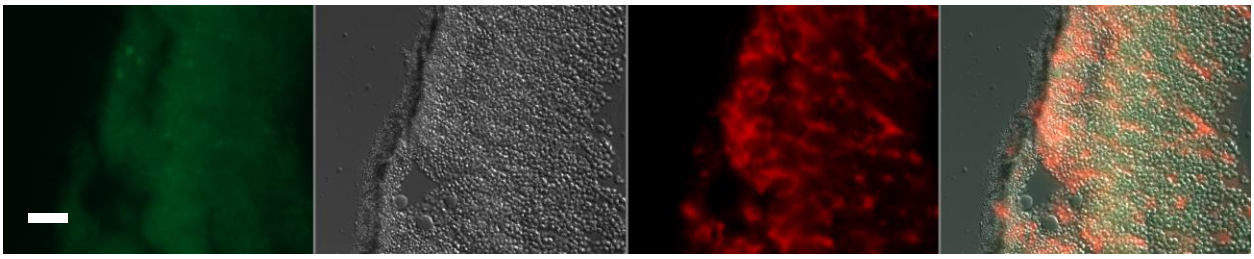

G403C

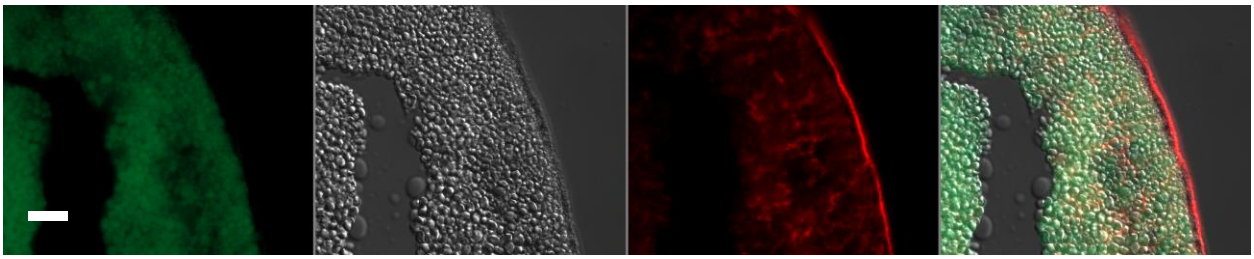

S133E/L300Q

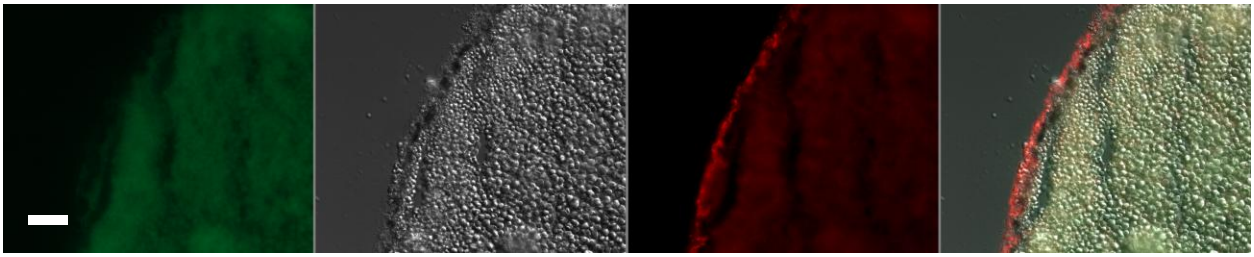

L300Q/G403C

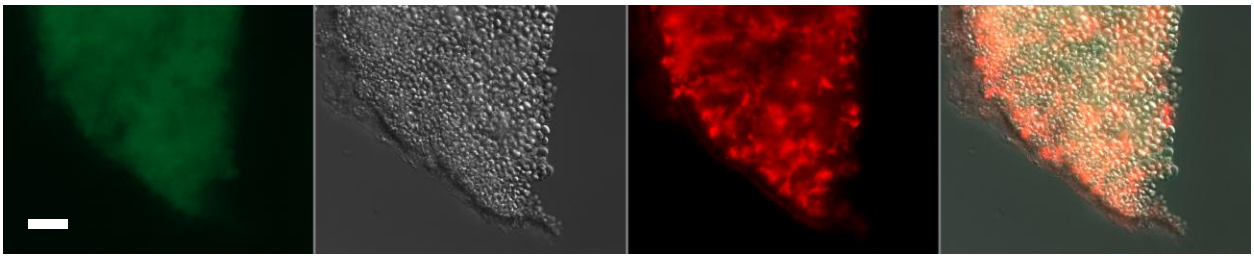

G403C/S133E

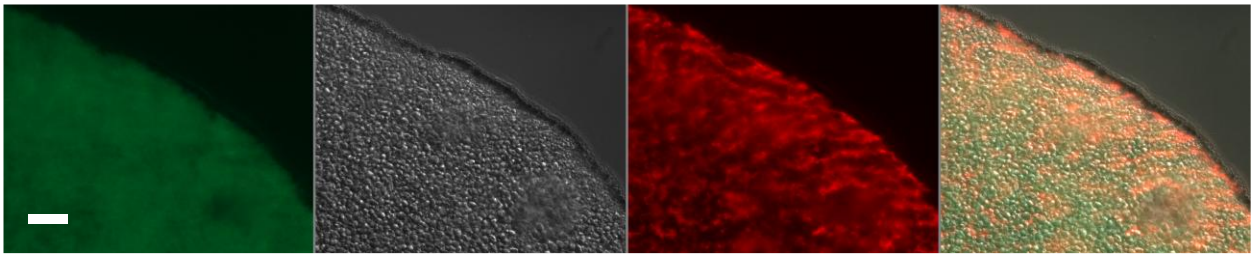

S133E/L300Q/G403C

Figure 61: Animal oocyte poles for immunolocalization of rGAT1 WT and mutants (Mag. ×63 with immersion oil, Axio observer Z1/7, Zeiss, scale bar 20 µm).

The mutants L300Q, S133E/L300Q and L300Q/G403C are present on the whole periphery of the oocytes (Figure 59), on the vegetal (Figure 60) and on the animal (Figure 61) poles like for the WT. The expression of S133E is controversial, because is slightly visible in the animal but not in the vegetal pole (Figure 60 andFigure 61). Its partial localization in the membrane and the potential

impact of the mutation on the transport make that this mutant did not show any specific transport currents (Figure 57). In contrast, the fluorescence signals from G403C, S133E/G403C and S133E/L300Q/G403C mutants are equivalent to the negative control. The protein is detected only as aggregates in the cytoplasm and not in the membrane (Figure 60 andFigure 61). Therefore, these point mutations are highly deleterious for protein stability.

To summarize, GAT1 L300Q, S133E/L300Q, and L300Q/G403C have a reduced activity but are present in the membrane. This demonstrates that they have intrinsically properties generated by the mutations impacting the transport activity, although, without knowing the exact reasons. The Figure 58 reinforces the hypothesis that these mutants have also an impact on sodium interaction in the transporter. The differences observed in L300Q mutant (Figure 56) might confirm the potential versatile role in substrate and sodium binding mentioned in introduction. Therefore, it will be extensively studied.

3. Comparison of rGAT1 WT and L300Q expression

To confirm that lower currents of GAT1 L300Q were not due to lower amount of protein expression compared to the WT, eYFP-rGAT1 WT and L300Q were expressed in HEK cells to follow their respective fluorescence signal, and the expression was semi-quantified after total cell lysate western blot.

First, eYFP-rGAT1 L300Q was expressed in HEK cells with different DNA to PEI ratios over 72h to define the correct expression conditions. Like the WT (Figure 36) the favorable expression conditions for the mutant is a DNA:PEI ratio of 1:3 or 1:5 (Figure 62). The ratio 1:3 was further used to be in the same conditions as for the WT (control conditions).

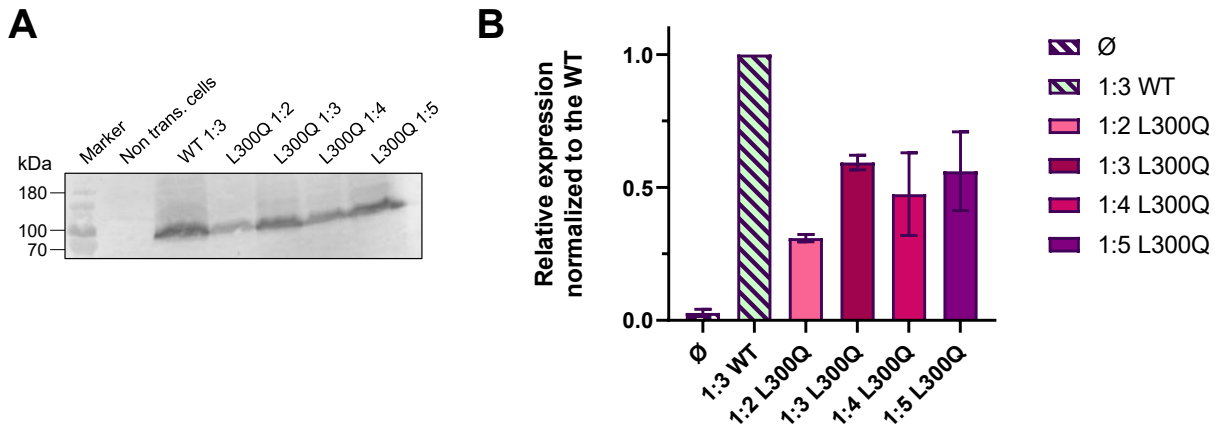

Figure 62: Expression of GAT1 L300Q at different DNA:PEI ratios after 72 h compared to the WT. a) Western blot (incubation with primary antibody anti-GFP). b) Semi-quantification of the bands measured twice with ImageJ. All the values were normalized with the values of the WT expression at DNA:PEI ratio 1:3.

However, after 72 h, the expression of the mutant is not exactly equivalent to the WT. Therefore, it was followed through the fluorescence signal of the eYFP along 96 h and semi-quantified by western blot for expression kinetics over 4 days.

On the Figure 63A, C, E, G, the full or single images showed that the protein, WT or mutant are localized in the plasma membrane. Although, saturated spots are visible for the mutant and mean that it is a potential aggregation-prone mutant. After 24 h, the fluorescence signal of the mutant is significantly lower than the WT. After 48 h, it is scattered (high and low values) meaning that the expression is less homogenous than in the WT and sustains that the mutant is more unstable (Figure 63B, D). Moreover, on the western blot and the associated kinetics, the expression of the mutant is at its lowest points after 24 and 48 h (Figure 64A, B). However, after 72 h, the fluorescence signal of the WT and the mutant is equivalent (Figure 63E, F) and the expression of the mutant reached the WT at 96 h (Figure 64B). Surprisingly, the fluorescence signal at 96 h decreased for the WT and the mutant and can be explained by the photobleaching of the YFP along time (Figure 63G, H).

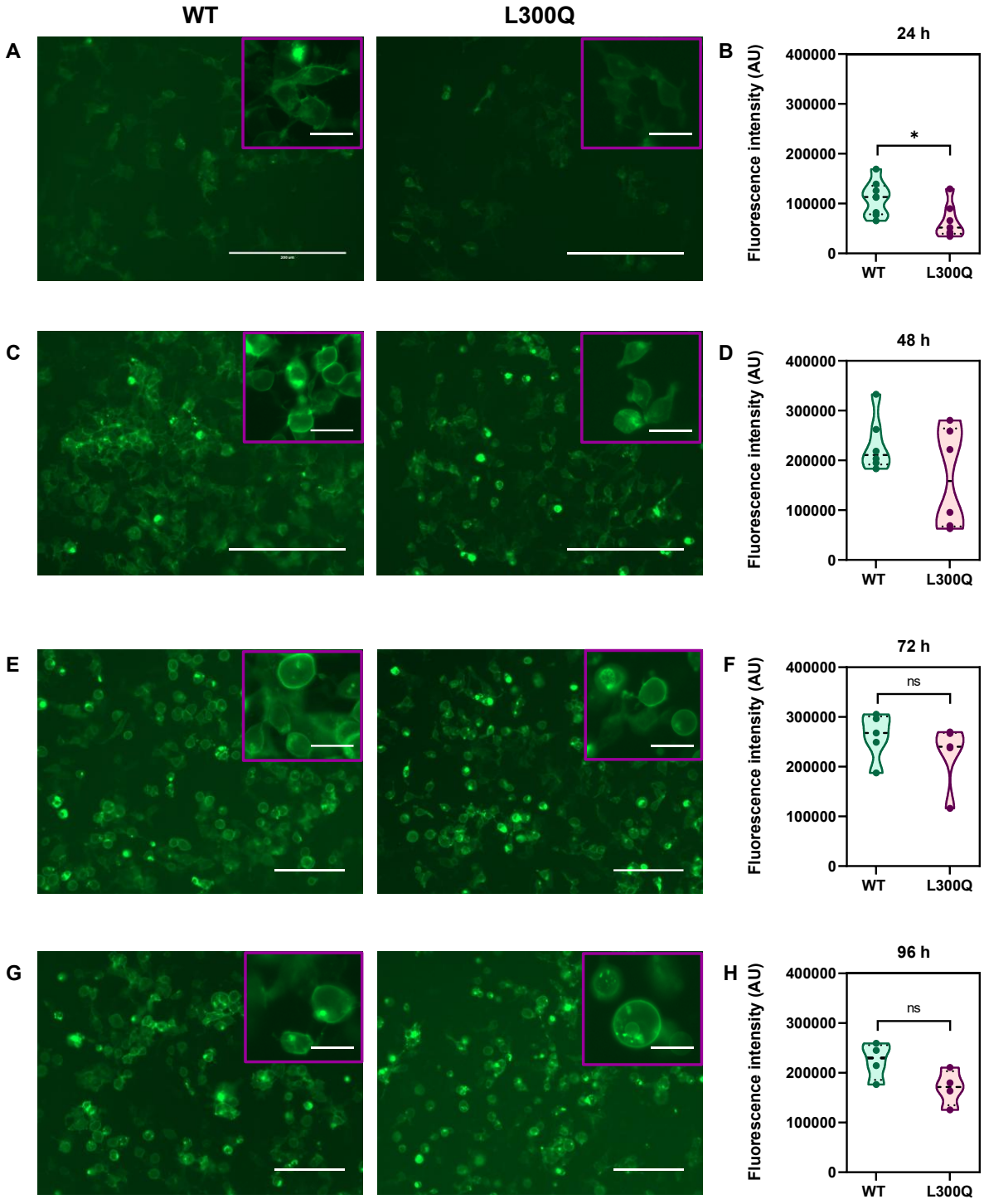

Figure 63: Cellular localization and fluorescence quantification of rGAT1 WT and L300Q. a, c, e, g) images of HEK cells transfected with rGAT1 WT (left) or L300Q (right) with eYFP at the N-terminus (GFP mode intensity 60%, EVOS microscope, ThermoFisher. Full images Mag. ×20, scale bar 200 µm and single cells zoom ×40, scale bar 25 µm). b, d, f, h) Fluorescence intensity quantification of eYFP-rGAT1 WT or L300Q.

The images were treated with ImageJ, where the background was subtracted by gaussian blurred before setting a threshold to avoid the saturated points. 4 to 10 images from 2 to 4 independent experiments were used.

All together, these data showed that the expression of rGAT1 WT and L300Q is equivalent after 96 h. Therefore, the lower currents visible by the preliminary electrophysiology data (Figure 56) is a characteristic from the mutant.

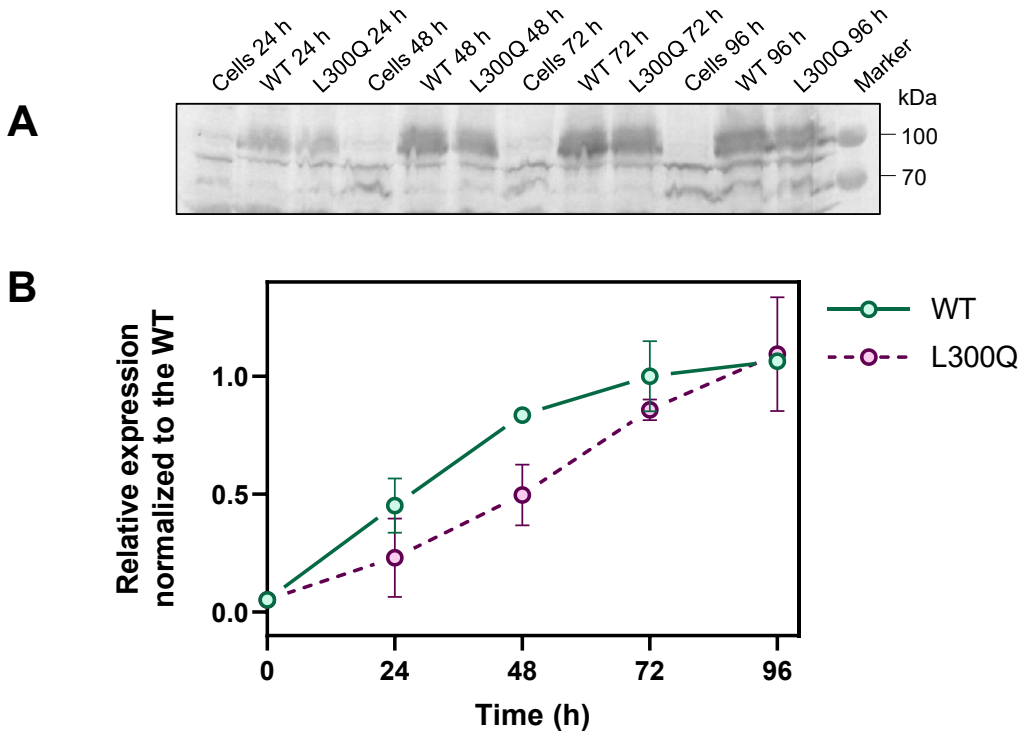

Figure 64: Analysis of the expression of e-YFP rGAT1 WT and L300Q. a) Western blot (detection with anti-GFP antibody). b) Kinetics over 96 h of the relative expression of the proteins. The western blot bands were analyzed on ImageJ. Each value is normalized on the values of the WT at 72 h. The experiment was repeated twice.

4. Impact of Gln300 on GABA and betaine transport

GAT1 L300Q was further investigated to decipher its affinity respectively for GABA and betaine. For this purpose, WT and mutant were exposed to ranges of betaine and GABA concentrations in presence of constant sodium chloride concentration (98 mM). The Figure 65 represents the dose-

responses for each substrate and each protein. The kinetics parameters are summarized in the Table 36 below.

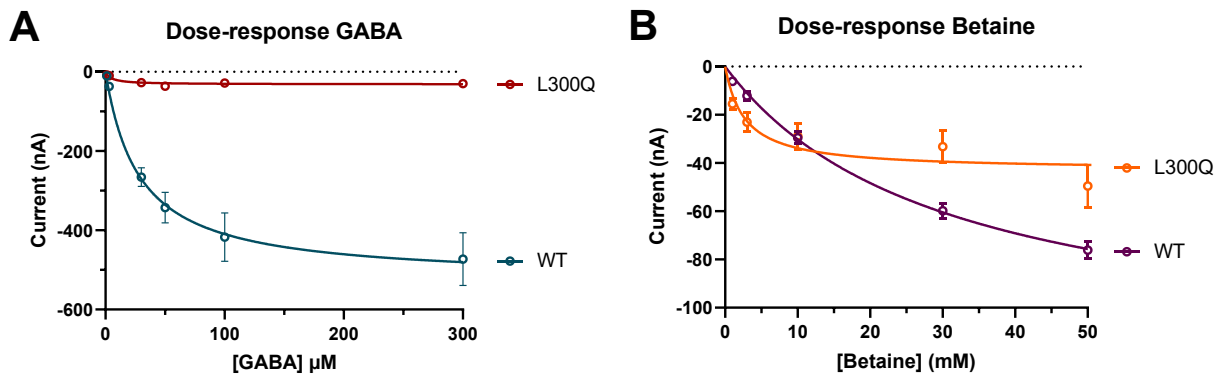

Figure 65: Kinetic parameters of rGAT1 WT and L300Q for a) GABA and b) Betaine. Measurements performed with a holding voltage of -60 mV on at least 5 oocytes from 2 different batches. Data were plotted ± SEM with nonlinear fit with GraphPad Prism 8.

	GABA			Betaine		
Parameters	WT	L300Q	cBGT1*	WT	L300Q	cBGT1*
I_{max} (nA)	-526 ± 47.9	-31.6 ± 2.60	-29.87 ± 1.32	-122 ± 7.53	-43.0 ± 6.20	-23.0±1.21
$K_{0,5}$ †	28.4 ± 9.42	4.87 ± 2.64	29.12 ± 7.12	30.3 ± 3.9	2.70 ± 1.73	1.69±0.21
TE (nA/mM)	18785.7	6488.7	1030.0	4.1	15.9	13.7

Table 36: Kinetic and affinity parameters of rGAT1 WT and L300Q for GABA and betaine at constant concentration of sodium (98 mM).TE for Transport Efficiency. † $K_{0,5}$ unit is µM in presence of GABA and mM in presence of betaine. *Values for cBGT1 were obtained from published results (Bhatt et al. 2024).

For GABA, the $K_{0,5}$ value of the WT is higher than in literature (ca. 15-20 µM) but the I_{max} and transport efficiency are equivalent. The mutant shows a maximal intensity (I_{max}) 16-fold lower and an apparent affinity ($K_{0,5}$) 7-fold higher than the WT (Table 36), meaning that GAT1 L300Q GABA transport is highly inhibited at low concentrations of GABA. Consequently, this impairs the efficiency of the catalytic cycle of the transport by decreasing its transport efficiency by almost 3-fold compared to the WT (Table 36). Interestingly, BGT1 has the same I_{max} as L300Q mutant, but the same affinity as GAT1 WT (Table 36). Therefore, the glutamine located in the (G/A/C)ΦG loop of the transports has a consequence for recruiting or liberating the substrate in the mutant and

another independent mechanism makes that BGT1 has a lower transport efficiency than GAT1 WT.

For betaine, the $K_{0,5}$ and I_{max} values of the WT (Table 36) are higher than in literature (Bhatt et al. 2024) but the transport cycle efficiency is equivalent, meaning that the parameters from the present data set are coherent with the previous published data.

Every transporter (GAT1 WT, L300Q, BGT1) shows an affinity for betaine with an order of magnitude 1000-fold lower than for GABA (µM for GABA and mM for betaine). This suggests that GABA and betaine have two distinguished binding sites like it is supposed on the Figure 13 (*Cf:* ***Introduction***).

The mutant has an I_{max} almost 3-fold lower but an affinity 11-fold higher than for the WT. In fact, the curves on the Figure 65B showed that the WT does not saturate compared to the mutant. This corresponds to non-specific transport as suggested also by the low affinity (30 mM). This contributes to decrease the transport efficiency of the WT by a factor of 4 compared to the mutant. Apart from the I_{max}, L300Q mutant and BGT1 have similar kinetics parameters (Table 36). The Gln300 introduced in GAT1 permits to reproduce almost perfectly the transport activity of BGT1. Therefore, a mechanism related to the residue of glutamine in the (G/A/C)ΦG loop permits to improve the efficiency of L300Q and BGT1 to transport methylammonium substrate compared to the WT.

5. Sodium coupling and dependency in rGAT1 WT and L300Q for betaine transport

In introduction, it was mentioned that the residues involved in the third sodium biding site in BGT1 were originally conserved from the Na1' sodium site in BetP. However, in BGT1 Gln299 might also sustain a role in the formation of the third sodium binding site. Consequently, the sodium affinities of GAT1 WT and L300Q were determined in the presence of constant and saturated concentrations of GABA and betaine (Figure 66A and B below and Table 37 below).

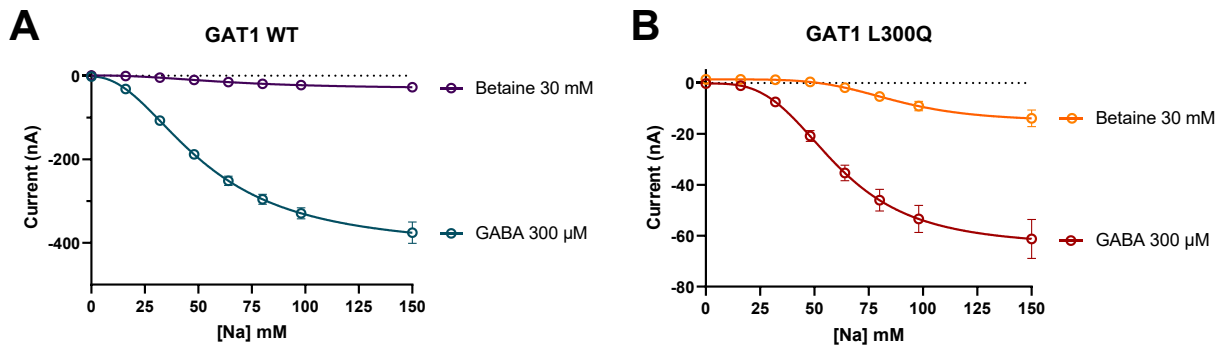

Figure 66: Sodium affinities in presence of 300 µM GABA or 30 mM betaine for a) GAT1 WT and b) GAT1 L300Q. Measurements were performed with a holding voltage of -60 mV on at least 8 oocytes from 2 different batches. Data were plotted ± SEM with the logistic fit on Origin.

	WT		**L300Q**	
Parameters	GABA	Betaine	GABA	Betaine
I_{max} (nA)	-415 ± 11	-31.7 ± 4.7	-64.4 ± 0.5	-15.1 ± 2.4
$K_{0,5}$ (mM)	52.7 ± 1.7	64.7 ± 9.9	60.4 ± 0.4	86.9 ± 8.1
TE (nA/mM)	7.87	0.50	1.06	0.17
Hill factor	2.1 ± 0.1	2.3 ± 0.6	3.3 ±0.1	4.6 ± 1.7

Table 37: Kinetic and affinity parameters of rGAT1 WT and L300Q for sodium at constant concentration of GABA (300 µM) or betaine (30 mM). TE for Transport Efficiency.

According to the sigmoidal curve shapes (Figure 66), GAT1 WT and mutant have a clear cooperativity with sodium, and this can be seen also with the Hill factor in Table 37. This is well known from the NSS stoichiometry of 1 substrate: 2 sodium ions. Interestingly, the sodium cooperativity of the mutant is more pronounced than for the WT and the Hill factor suggests that more than 2 sodium ions are involved in its transport activity. This is in concordance with the transporting parameters of BGT1 and sustains the role of Gln299 in remodeling the Na1' from BetP.

On Table 37, the I_{max} from the WT is coherent with current values recorded at saturating concentration of GABA, but the sodium affinity in this data set is higher than the literature values (35-45 mM from Bossi et al. 2002; Liu et al. 1998).

Betaine is reducing the I_{max} by 13-fold in the WT and by 4-fold in the mutant compared to the values with GABA (Table 37). The sodium affinity is also slightly decreased in these two cases. The low rates of GAT1 WT and L300Q with betaine compared to the rates values with GABA show that sodium ion binding and diffusion are limiting steps. Moreover, the transport efficiency of GAT1 L300Q is 7-fold lower than in the WT (Table 37). Therefore, betaine changes how the transporters (WT and mutant) interact with sodium, by creating secondary low affinity sodium sites in these two proteins. Indeed, in GAT1 WT, betaine and sodium are competing for the same site (Figure 13). Instead, in GAT1 L300Q, two sodium ions and betaine are competing for the same site. Therefore, this delays the successive conformational changes, explaining the very low I_{max} and transport efficiency in this case.

In presence of GABA, L300Q mutant (like the WT) remains voltage dependent (Figure 67A, B). Interestingly, WT and mutant show a huge step of the current amplitudes between 16 and 48 mM of sodium, at mid-low voltages (-40 to -100 mV) (Figure 67A, B). This means that 48 mM sodium is already sufficient for transporting GABA in the WT or in the mutant. This concentration corresponds to their sodium $K_{0.5}$, therefore in presence of GABA, sodium binding is not a limiting step for the alternating access cycle of the transporters.

Contrastingly, with betaine, the inward currents step for the WT is between 48 and 98 mM (Figure 67C). For the mutant, this step is not even visible; there is only a residual activity of 25 nA, at -100 mV and 150 mM sodium (Figure 67D). Therefore, saturating concentrations of sodium is required to transport betaine either in the WT or in the mutant, describing a clear rearrangement of sodium ions due to the presence of betaine in the respective proteins. Indeed, if only the residue of glutamine 300 in the mutant is responsible for high sodium dependency, then equivalent results would be observed for the values with GABA. Also, this particularity would not be observed in the WT. Therefore, there is another specific molecular mechanism in the GABA transporter family, independent of Gln299 present in BGT1, requiring high concentration of sodium for betaine transport.

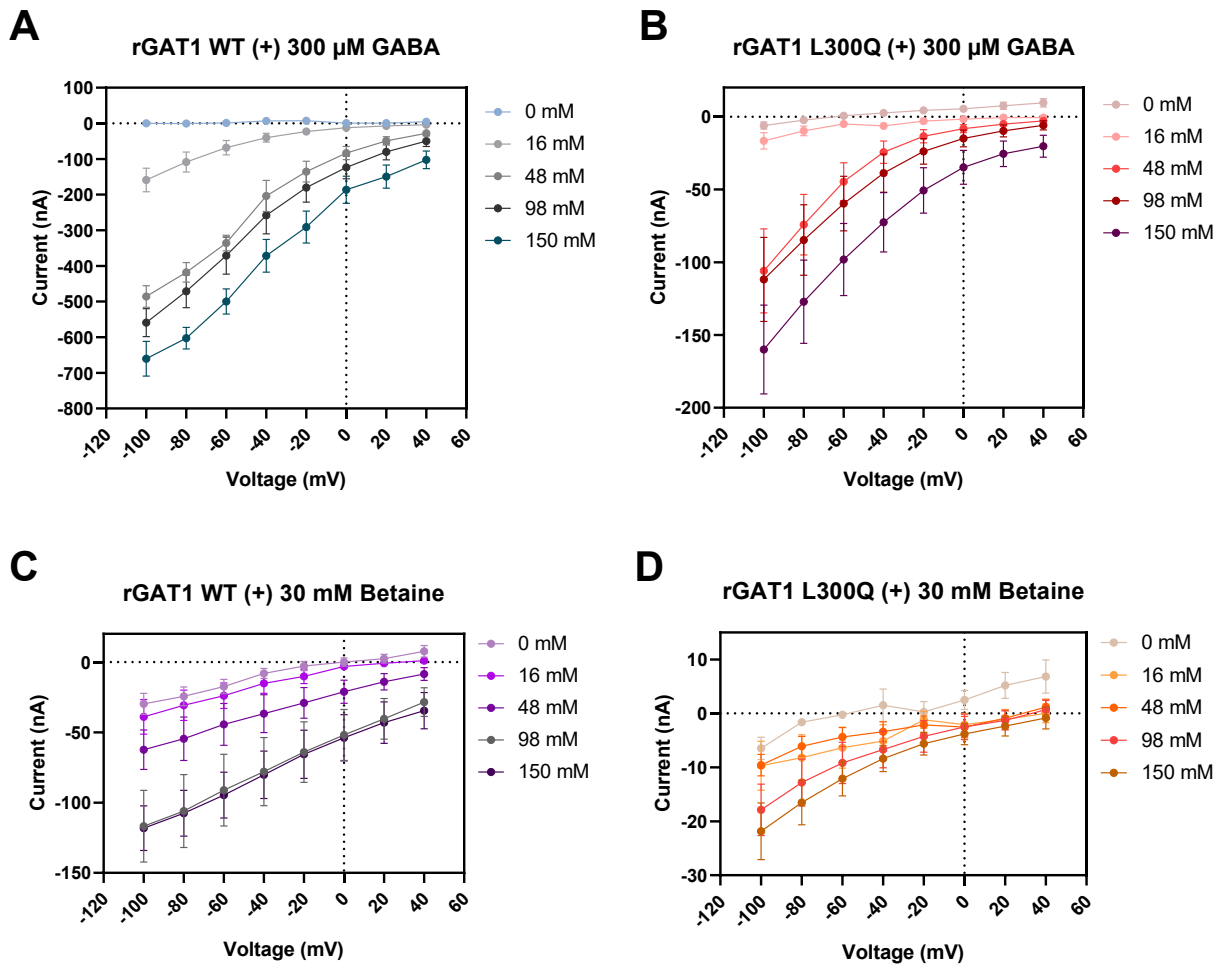

Figure 67: Intensity voltage analysis at various sodium concentrations 300 µM GABA for rGAT1 a) WT and b) L300Q, or 30 mM betaine for rGAT1 c) WT and d) L300Q.

To summarize, electrophysiology data on the single GAT1 mutant L300Q showed that this residue of glutamine, in combination with other GAT1 amino acids increases the affinity of the mutant transporter for GABA and betaine. Moreover, this specific residue reproduces the kinetics of BGT1 in presence of betaine, therefore it is responsible for betaine specificity in these two transporters (BGT1 and L300Q mutant). GAT1 L300Q has higher cooperativity with sodium in presence of GABA or betaine. However, this methylammonium solute has a repercussion on the sodium interaction either in GAT1 WT or mutant. It induces a high dependency to sodium, even higher in the mutant, probably to overcome to a competitive binding of sodium and betaine.

6. rGAT1 L300Q goes through structural biology

To understand how sodium/GABA/Betaine are cooperating in the mutant rGAT1 L300Q, it was studied by Cryo-EM and Single particle analysis. This would also serve as model to decipher the molecular mechanism specificities of GAT1 and BGT1 respectively for GABA and betaine.

i. Obtention of protein material

After expression (Figure 68A) and purification of GAT1 L300Q on Ni-NTA and FLAG resins (Figure 68B and C) the protein was concentrated to 2 mg/ml (Figure 68C) and polished by size exclusion chromatography (Figure 69A). The concentrated peak to 1 mg/ml (Figure 69B, second line) was vitrified on different grid types with different blotting time and glow discharging conditions (***Cf: Material and methods, vitrification of GAT1 L300Q***).

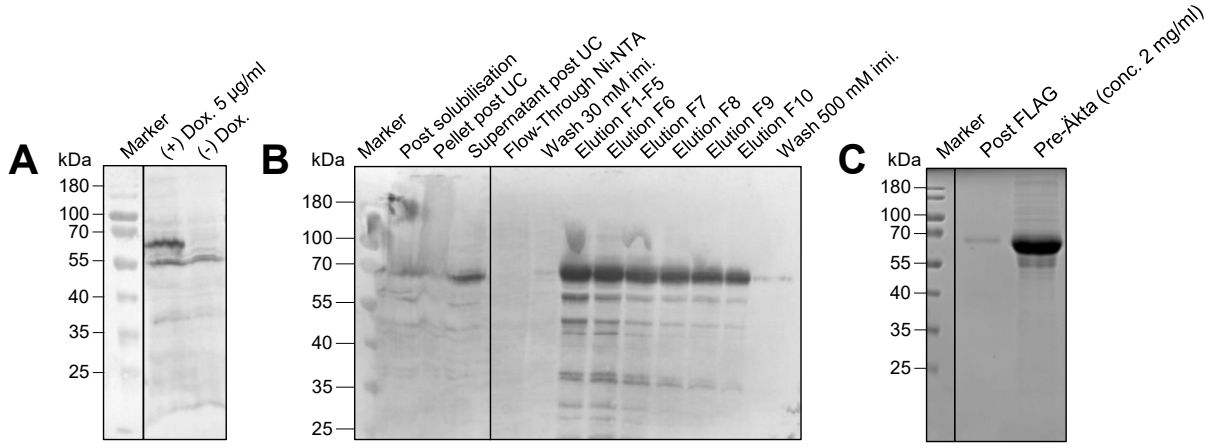

Figure 68: rGAT1 L300Q expression and purification on two affinity chromatography resins. a) Western-blot (primary antibody anti-FLAG) of (non)-induced rGAT1 L300Q cell line with doxycycline 5 µg/ml. A positive band at 70 kDa shows the presence of GAT1 L300Q in the induced culture. b) Western blot (primary antibody anti-HIS tag) of the purification steps on Ni-NTA resin. Positive bands at 70 kDa in the elution fractions showed the presence of the protein. c) SDS PAGE showing the purity of the protein after FLAG resin (first line before concentration, second line after concentration to 2 mg/ml).

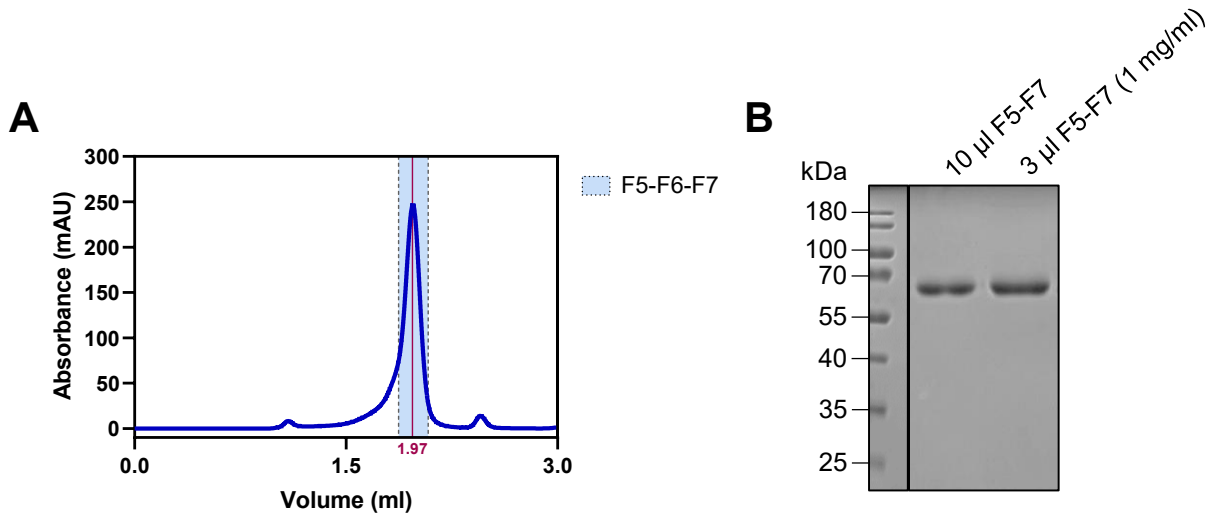

Figure 69: rGAT1 L300Q polishing. a) Chromatogram profile (column Superose6 Increase™ 150/30 GL, cytiva). b) SDS PAGE of the non-concentrated (first line, 10 µl of sample) and concentrated to 1 mg/ml (second line, 3 µl of sample) of rGAT1 L300Q. The latter was used for vitrification

ii. From micrographs to preliminary EM map

Some of these grids were screened in the CryoARM200 (Jeol) in EM microscopy platform in Regensburg. Small data set were recorded and typical micrographs and 2D classes associated with each grid are presented in the panel below (Figure 70).

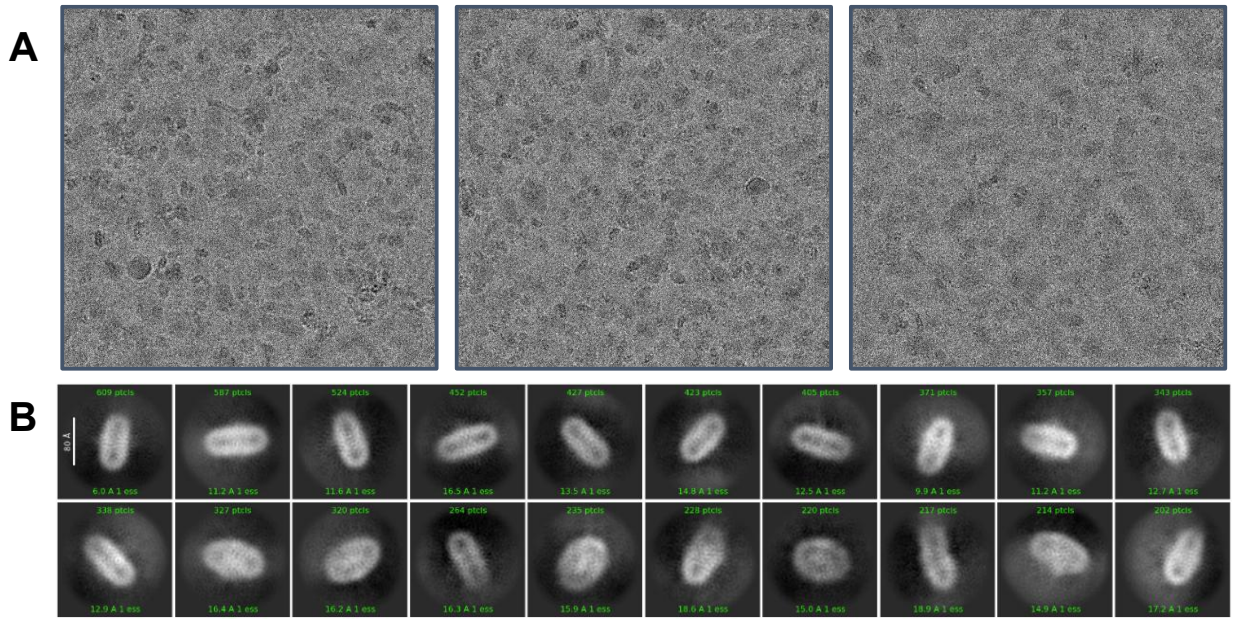

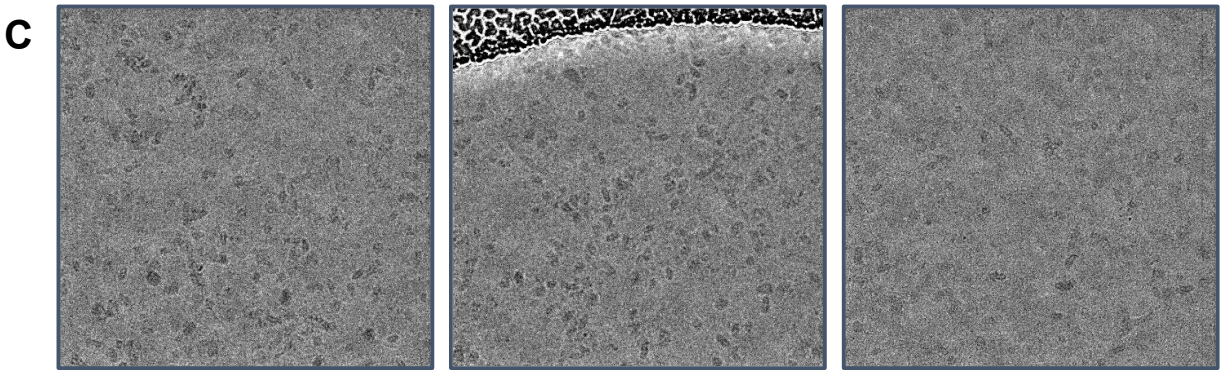
C

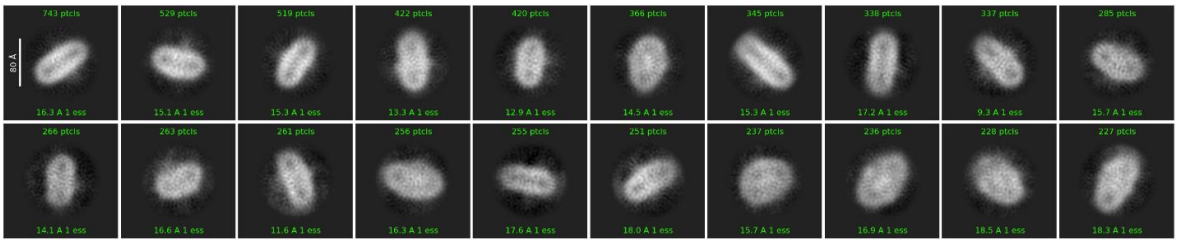
D
743 ptcls
529 ptcls
519 ptcls
422 ptcls
420 ptcls
366 ptcls
345 ptcls
338 ptcls
337 ptcls
285 ptcls
80 Å
16.3 Å 1 oss
15.1 Å 1 oss
15.3 Å 1 oss
13.3 Å 1 oss
12.9 Å 1 oss
14.5 Å 1 oss
15.3 Å 1 oss
17.2 Å 1 oss
9.3 Å 1 oss
15.7 Å 1 oss
266 ptcls
263 ptcls
261 ptcls
256 ptcls
255 ptcls
251 ptcls
237 ptcls
236 ptcls
228 ptcls
227 ptcls
14.1 Å 1 oss
16.6 Å 1 oss
11.6 Å 1 oss
16.3 Å 1 oss
17.6 Å 1 oss
18.0 Å 1 oss
15.7 Å 1 oss
16.9 Å 1 oss
18.5 Å 1 oss
18.3 Å 1 oss

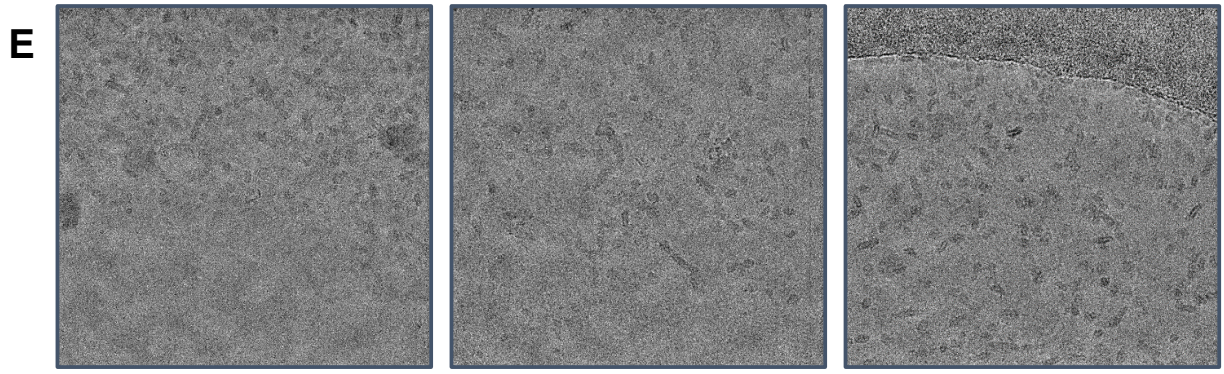
E

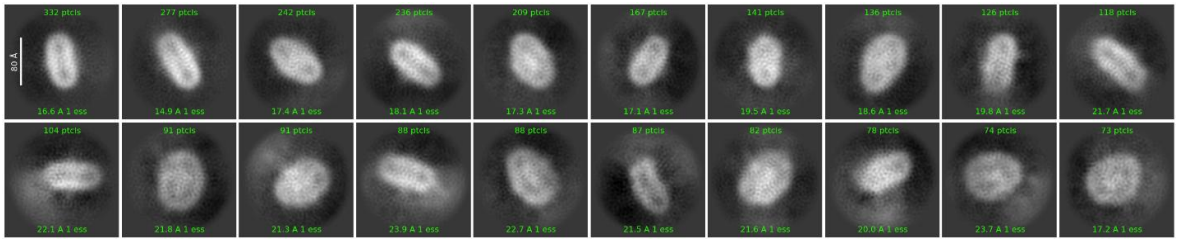
F
332 ptcls
277 ptcls
242 ptcls
236 ptcls
209 ptcls
167 ptcls
141 ptcls
136 ptcls
126 ptcls
118 ptcls
80 Å
16.6 Å 1 oss
14.9 Å 1 oss
17.4 Å 1 oss
18.1 Å 1 oss
17.3 Å 1 oss
17.1 Å 1 oss
19.5 Å 1 oss
18.6 Å 1 oss
19.8 Å 1 oss
21.7 Å 1 oss
104 ptcls
91 ptcls
91 ptcls
88 ptcls
88 ptcls
87 ptcls
82 ptcls
78 ptcls
74 ptcls
73 ptcls
22.1 Å 1 oss
21.8 Å 1 oss
21.3 Å 1 oss
23.9 Å 1 oss
22.7 Å 1 oss
21.5 Å 1 oss
21.6 Å 1 oss
20.0 Å 1 oss
23.7 Å 1 oss
17.2 Å 1 oss

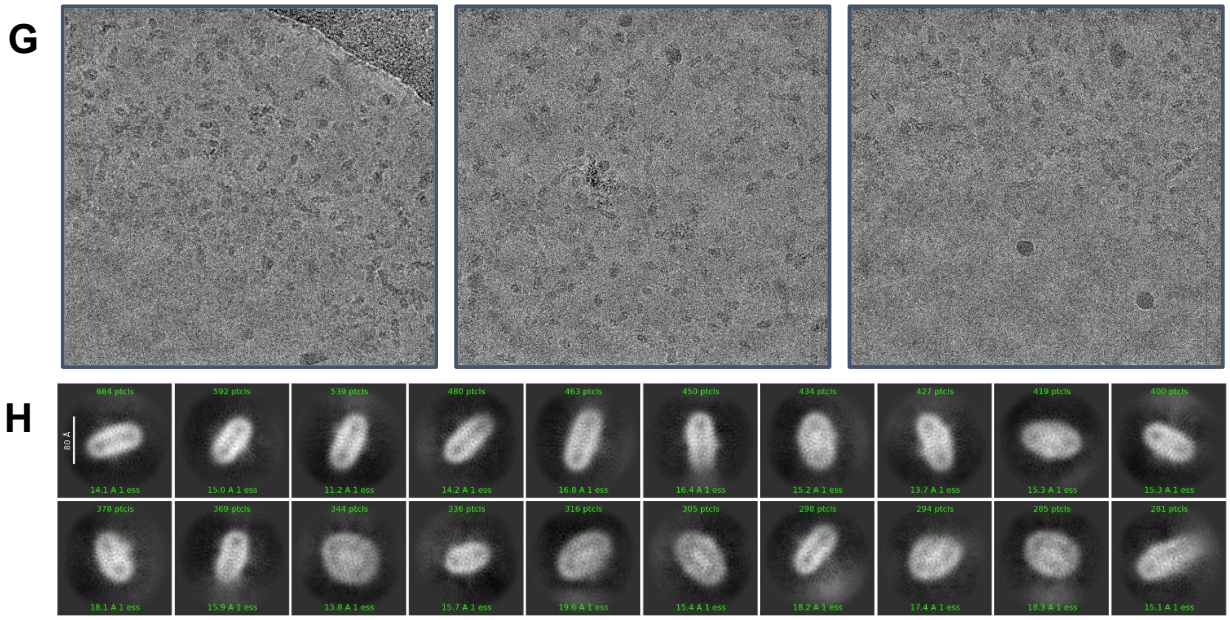

Figure 70: Micrographs and 2D classes for different grid types. a, b) Au/Pd 5 s blotting. c, d) Au/Pd 6 s blotting. e, f) Standard Quantifoil 5 s blotting. g, h) Standard Quantifoil 6 s blotting. Data were collected with CryoARM200 (Mag. ×60000) and processed with CryoSPARC 5.0, Pixel size 0.7891 Å, exposure 60 e^-/ Å.

Particles were found in all grids. On each micrograph, the particle distribution showed a gradient where the particle density was higher on the edge than in the center. Lower background signal was found in the 2D classes on Au/Pd 6 s blotting grid. However, the quality of the vitreous ice is another factor hardly controllable. The latter grid type showed a too thin ice layer and was highly contaminated. Therefore, data were collected on standard Quantifoil 5 s blotting in the cryo-EM facility of Wurzburg with the TITAN Krios (300 keV) revealing a better contrast for further data processing, although it also presented ice contamination (Figure 71).

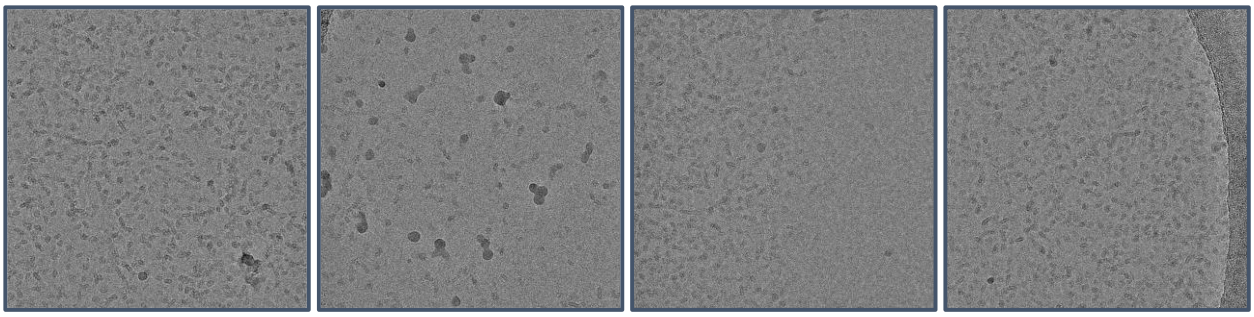

Figure 71: Typical micrographs for rGAT1 L300Q collected on Quantifoil grids 1.2/1.3 5 s blotting. Particles gradients and ice contamination can be noticed.

As mentioned (*Cf:* ***Material and methods***), data were processed in parallel in CryoSparc 5.0 and Relion 4.0 where 2D classes from both software are shown on the Figure 72.

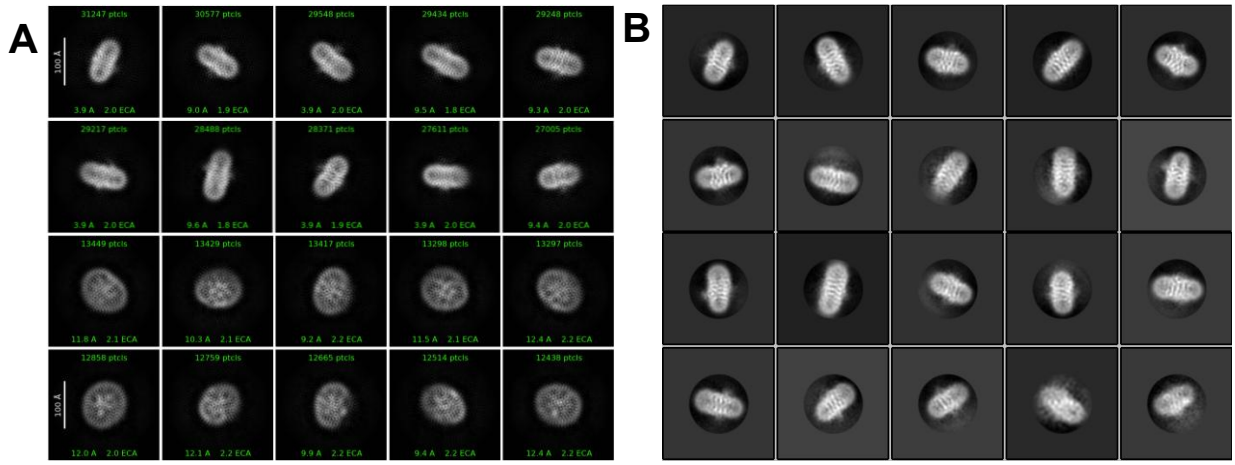

Figure 72: 2D classes of rGAT1 L300Q from a) CryoSparc 5.0 and b) Relion 4.0

After data processing, a map of 7 Å was obtained. As the mutant was purified in presence of 150 mM of NaCl and further incubated with 10 mM GABA before vitrification, the structure of GAT1 WT 7Y7W (Zhu et al. 2023) was used as a model to fit in the map (Figure 73)

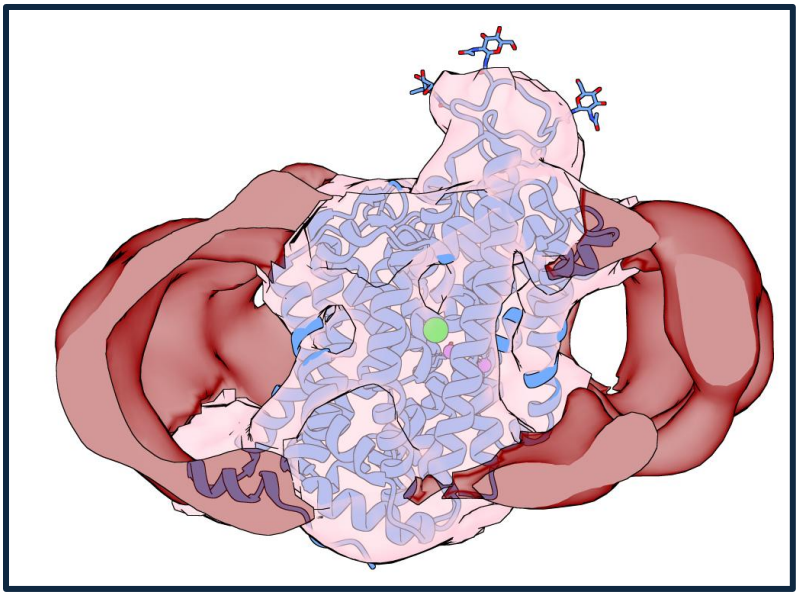

Figure 73: rGAT1 WT inward-occluded structure (7Y7W, in blue) fitted in the initial map of GAT1 L300Q (light pink: transmembrane domains, maroon: LMNG/CHS micelle)

7. Structural differences between rGAT1 WT and L300Q

Using AlphaFold 3, a structure of L300Q was generated after modifying the leucine in glutamine residue and giving as input two sodium, one chloride ions and the molecule of GABA. This permitted to model the inward-occluded state of GAT1 L300Q mutant that was then superposed to the WT structure 7Y7W (Figure 74).

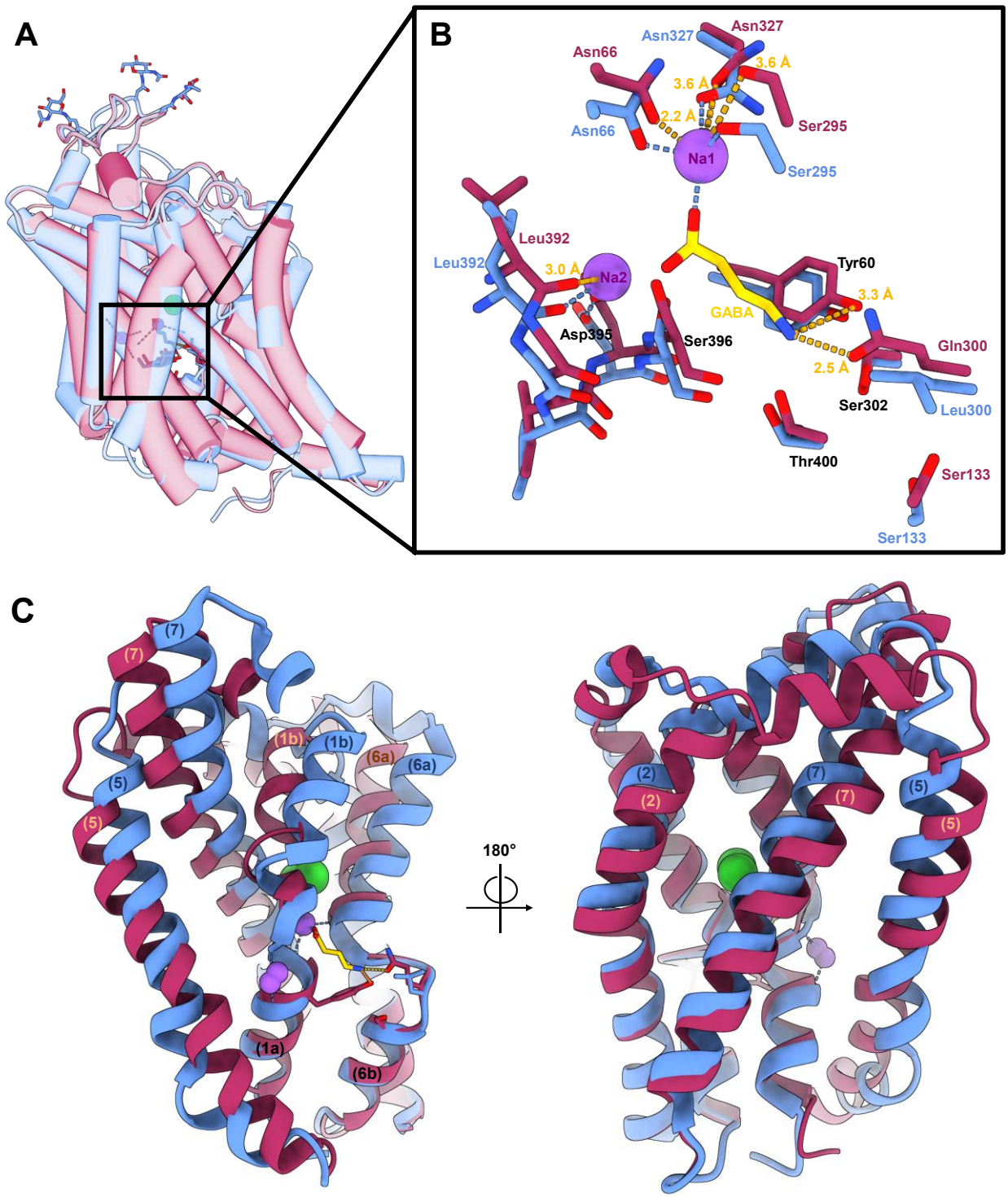

Figure 74: GABA and sodium binding in GAT1 WT (from 7Y7W) and L300Q generated by AlphaFold 3. a) Overall superposition of GAT1 WT (pale blue PDB 7Y7W) and L300Q (pale red). b) Close-up on sodium and GABA binding sites. c) Superposition of GAT1 WT (blue) and L300Q (red) transmembrane helices showing the main rearrangements. The numbers indicate the helice numeration.

In the inward-occluded state, TMs 1, 2, 5, 6 and 7 of the mutant are the helices moving the most compared to WT. This emphasizes that the mutation impacts mainly the bundle domain, i.e. the transmembrane helices related to substrates (GABA/betaine)/sodium binding (TM1, 6, 7) and releasing (TM5) (Figure 74C). Like in the WT, Tyr60 interacts with the amino group of GABA resulting in the occluded state of the protein. Interestingly the mutation of Leu300 into a glutamine creates a supplementary hydrogen bond of 2.5 Å with the GABA amino group. It stabilizes the position of GABA more than with only one hydrogen bond formed by Tyr60 in the WT. This creates a favorable binding site that explains the higher affinity of the mutant for GABA (Figure 65 and Table 36). Moreover, the coordination of Na2 is well conserved between the WT and L300Q. The backbone of Leu392 and Asp395 coordinate identically the sodium ion in the WT or in the mutant (Figure 74B). However, the sodium in the Na1 site might not be as well coordinated. Indeed, the Ser295 and Asn327 in the mutant are getting distant to form hydrogen bonds (3.6 Å distance between oxygen atom and sodium ion). This is supported by the global shift of the transmembrane helices 6a and 7 (Figure 74B, C) and could contribute to lowering the global affinity of the mutant for sodium. On the other hand, Ser133, hypothesized to be involved in the Na1' remodeling is moving by 1.45 Å forward compared to the WT and get closer to Ser302. This could allow the creation of the third sodium binding site observed in the mutant to also compensate the potential loss of coupling happening in the "loose" Na1 sodium site.

To summarize, structural information on GAT1 L300Q mutant suggests that the longer and polarized side chain of the glutamine (compared to leucine in the WT) favors a higher-grade GABA coordination. However, this impacts transport activity, as it is shown by electrophysiology data. Therefore, something is required to break the interaction of glutamine. Sodium ion in the Na2 site supports the movement of the TM1a for substrate/ions release in the intracellular space (Malinauskaite et al. 2014). According to the electrophysiology data, the cooperativity with more than two sodium ions in the mutant could constrict the movement of the (G/A/C)ΦG motif and the whole TM6 for downstream conformational change to the inward-open state.

III. LAT/CD98 complex: challenges of expression, purification and heterodimer formation for Brasillicardin A drug design

1. Heterodimer expression test and recognition by different antibodies on western blot

LAT1 and CD98 are expressed respectively with a FLAG and a STREP tag, where both are located at the N-terminus. Adherent HEK cells GnTI$^-$ were transfected in 6-well plate with DNA LAT1:CD98 in 1:1 ratio and DNA:PEI ratio 1:3. For the specific detection of the complex after 48 h expression, two sets of antibodies are used: one against the purification tags, i.e FLAG and STREP and one against the proteins themselves i.e. LAT1 and CD98 (Figure 75below).

Either the anti-FLAG or anti-LAT1 antibodies showed a band between 55 and 40 kDa for this subunit. Also, endogenous LAT1 was detected in the non-transfected cells with anti-LAT1 antibody (Figure 75A). For CD98, two bands were detected at 100 kDa with the anti-STREP characterizing two principal glycosylation states of CD98 (Figure 75B). In contrast, the smeared band between 55 and 100 kDa detected with anti-CD98 described a broader glycosylation state of the protein and truncated forms of CD98, explaining the detection of the protein below the 70 kDa. Moreover, endogenous CD98 with five distinguishable isoforms is detected in non-transfected cells (Figure 75B).

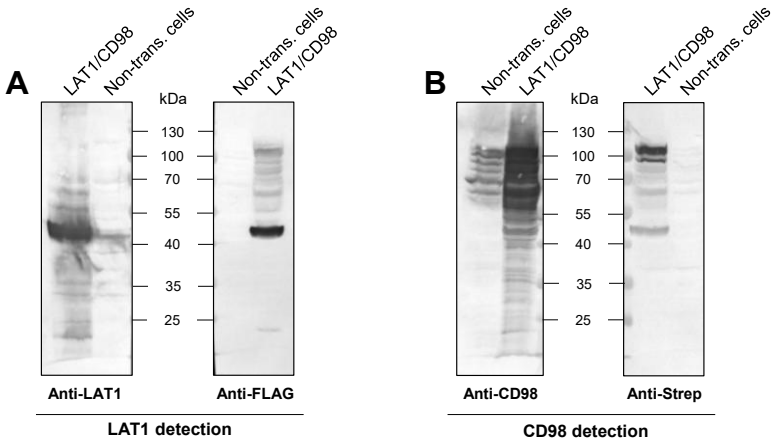

Figure 75: Subunit detection according to the antibodies used. a) LAT1 detected with anti-LAT1 and anti-FLAG tag antibodies. b) CD98 detected with anti-CD98 and anti-Strep tag antibodies. Reference and antibodies dilutions are described in the Table 20 and Table 21in ***Material and Methods***.

2. Expression conditions optimization in suspension cell culture

According to the literature, the common transfection conditions of the complex LAT1/CD98 is an equivalent DNA ratio (in weight) for both monomers, and a global DNA:PEI ratio of 1:2 (Rodriguez et al. 2021; Yan et al. 2021, 2019; Lee et al. 2019) and a least expression of 48 h. Indeed, after 48 h, the complex showed almost a 2-fold higher expression (Figure 76A). However, the transfection conditions described showed a low expression of CD98 (condition Y, Figure 76B). The expression of CD98 is still low even after increasing the DNA:PEI ratio to 1:3 (condition 3, Figure 76C). Therefore, the DNA amount of CD98 was doubled compared to the quantity of LAT1 DNA, and the polyplex were formed either with a DNA:PEI ratio of 1:2 or 1:3 (respectively condition 1 and 2). This resulted in a major improvement in the expression of CD98 (Figure 76C).

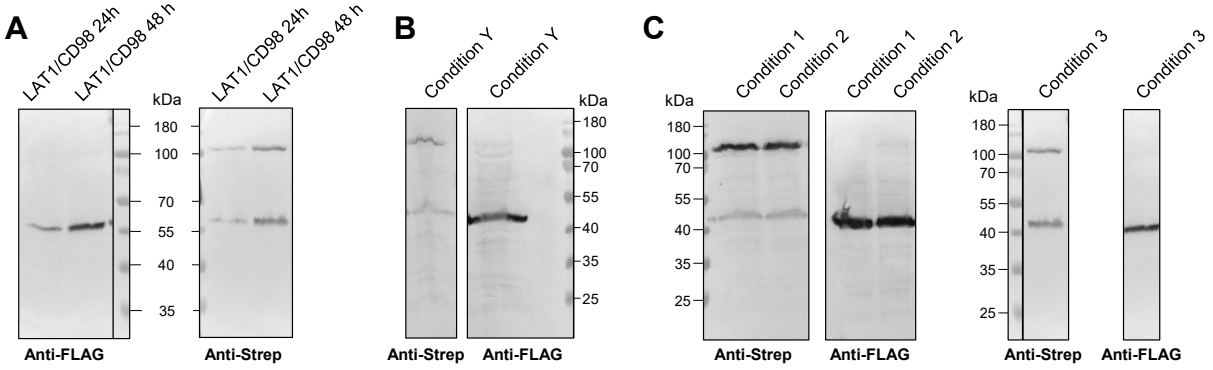

Figure 76: Condition screening for expression of LAT/CD98 expression in suspension cell culture. a) Conditions Y, described by Yan and coworkers in 2021. b) Conditions tested to improve the expression of CD98. All the different conditions are described in the Table 17 (*Cf:* ***Material and Methods***).

3. Excess expression of CD98 does not improve heterodimers presence in the membrane

To understand the impact of doubling the amount of CD98 DNA on the LAT1/CD98 complex formation, cells were transfected with LAT1:CD98 DNA ratios 1:1 or 1:2 (in weight) and observed by confocal microscopy. First non-transfected cells were incubated with the two sets of antibodies

to control nonspecific interactions (Figure 77). Endogenous LAT1 was detected in the membrane with the anti-LAT1 antibodies (Figure 77). That is why immunofluorescence staining will be performed with anti-LAT1/CD98 antibodies and with anti-FLAG/STREP antibodies to avoid background from endogenous expressed proteins. Whatever the expression condition, the heterodimer is detected in the plasma membrane either with the combination anti-FLAG/STREP and anti-LAT1/CD98 antibodies (Figure 78). Therefore, low or high expression of CD98 visible on western blot does not affect the complex formation in the membrane but the overall expression of CD98 involved in other pathways as a single subunit (see figures on the next pages).

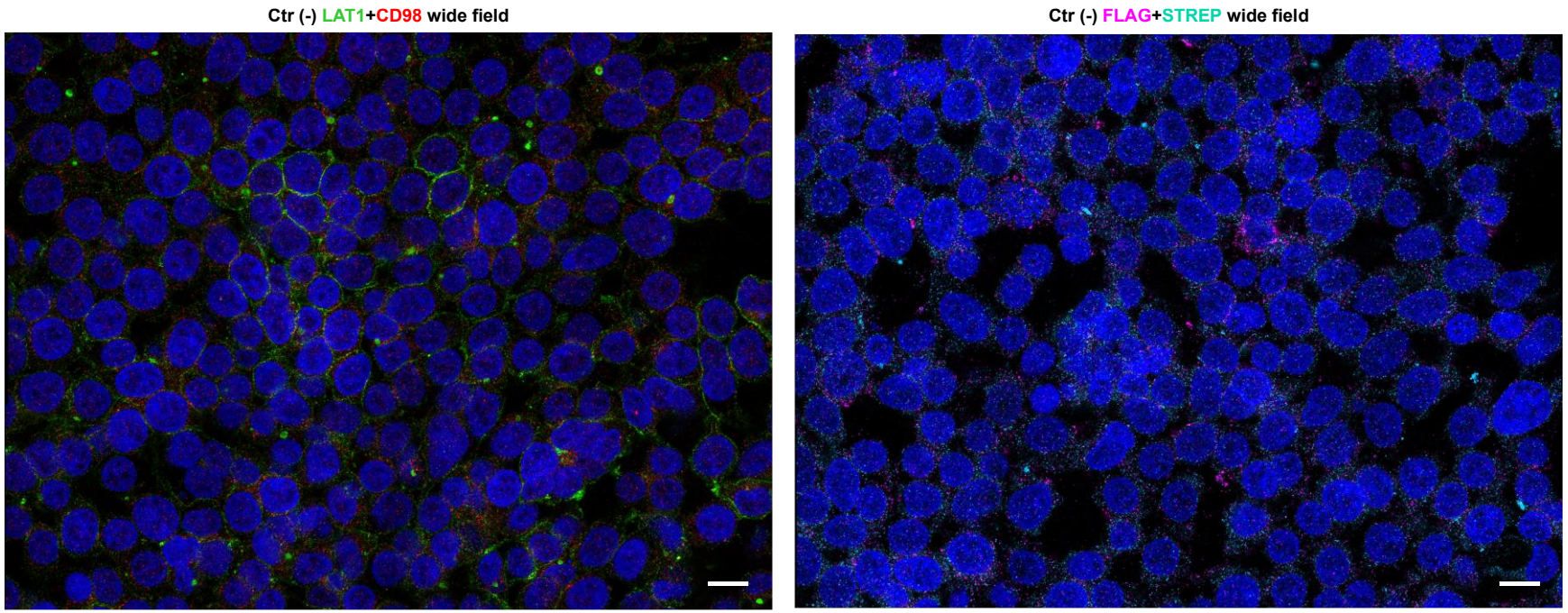

Figure 77: Non-transfected HEK293 GnTI$^-$ cells for detecting nonspecific interactions. Upper panel: anti-LAT1 and CD98 antibodies, lower panel: anti-FLAG and STREP antibodies (Scale bar: 20 µm). DAPI is used for nucleus staining. Images collected with microscope LSM 980 (Zeiss) at Mag. ×63 with immersion oil objective.

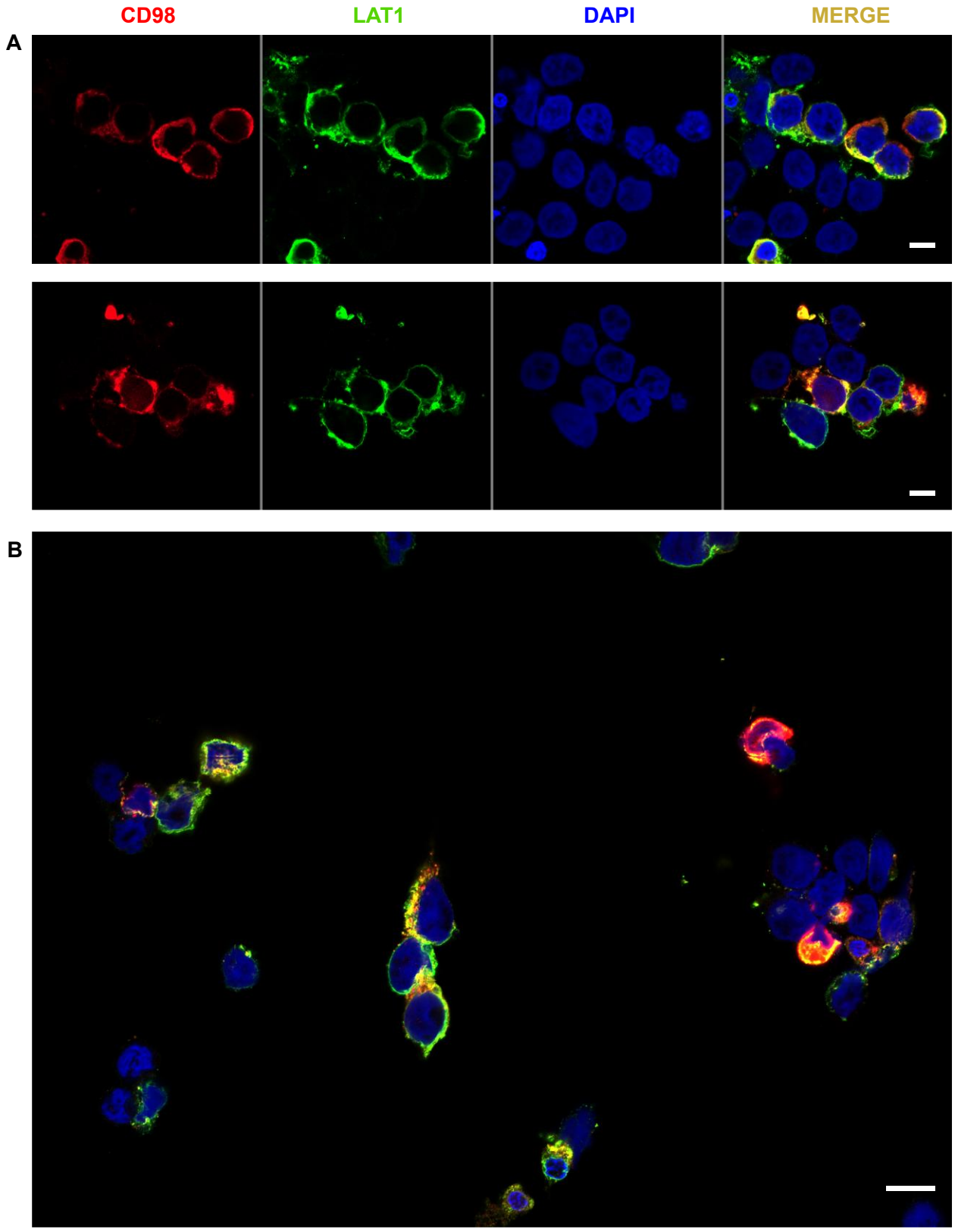

LAT1/CD98 1:1

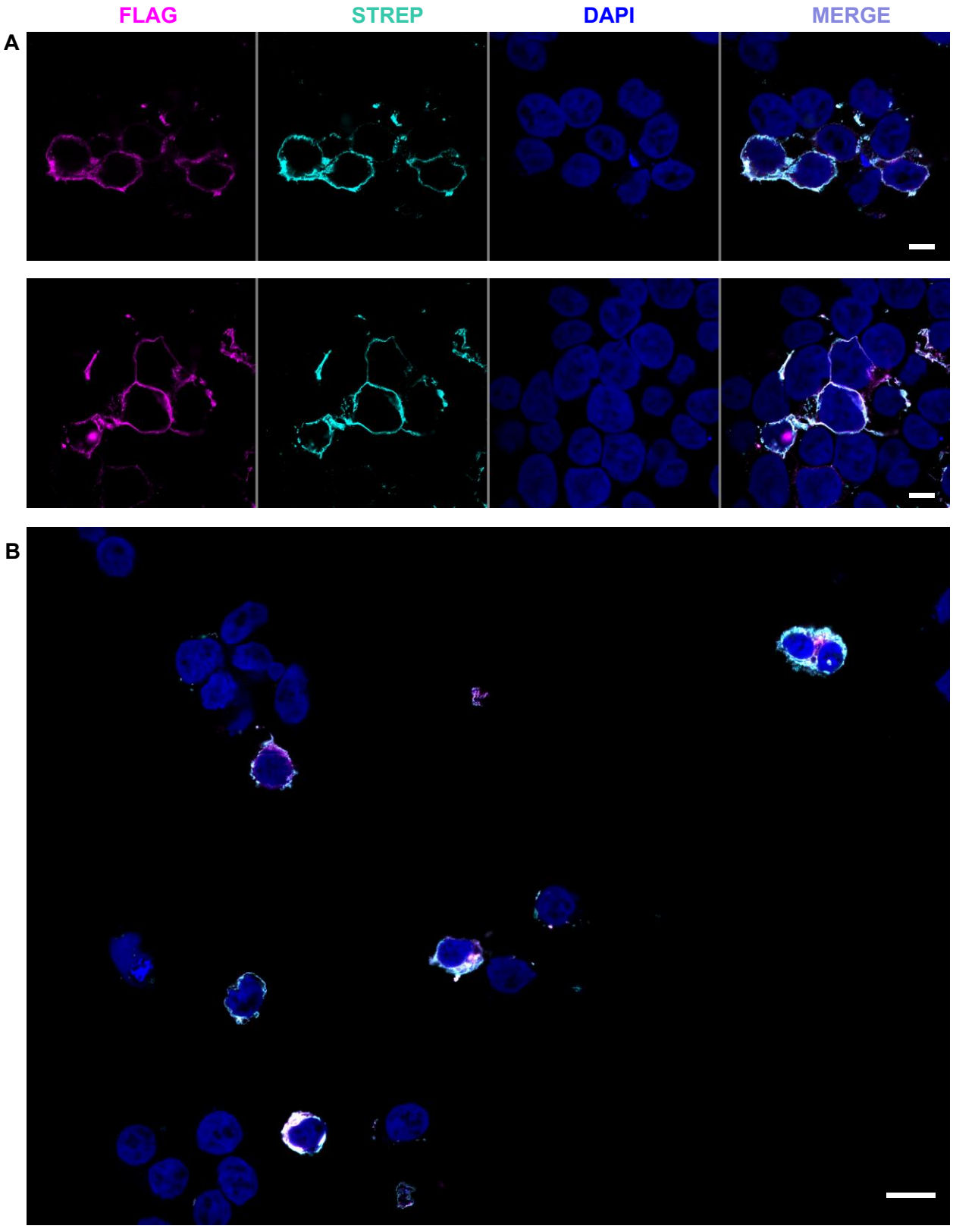

LAT1/CD98 1:1

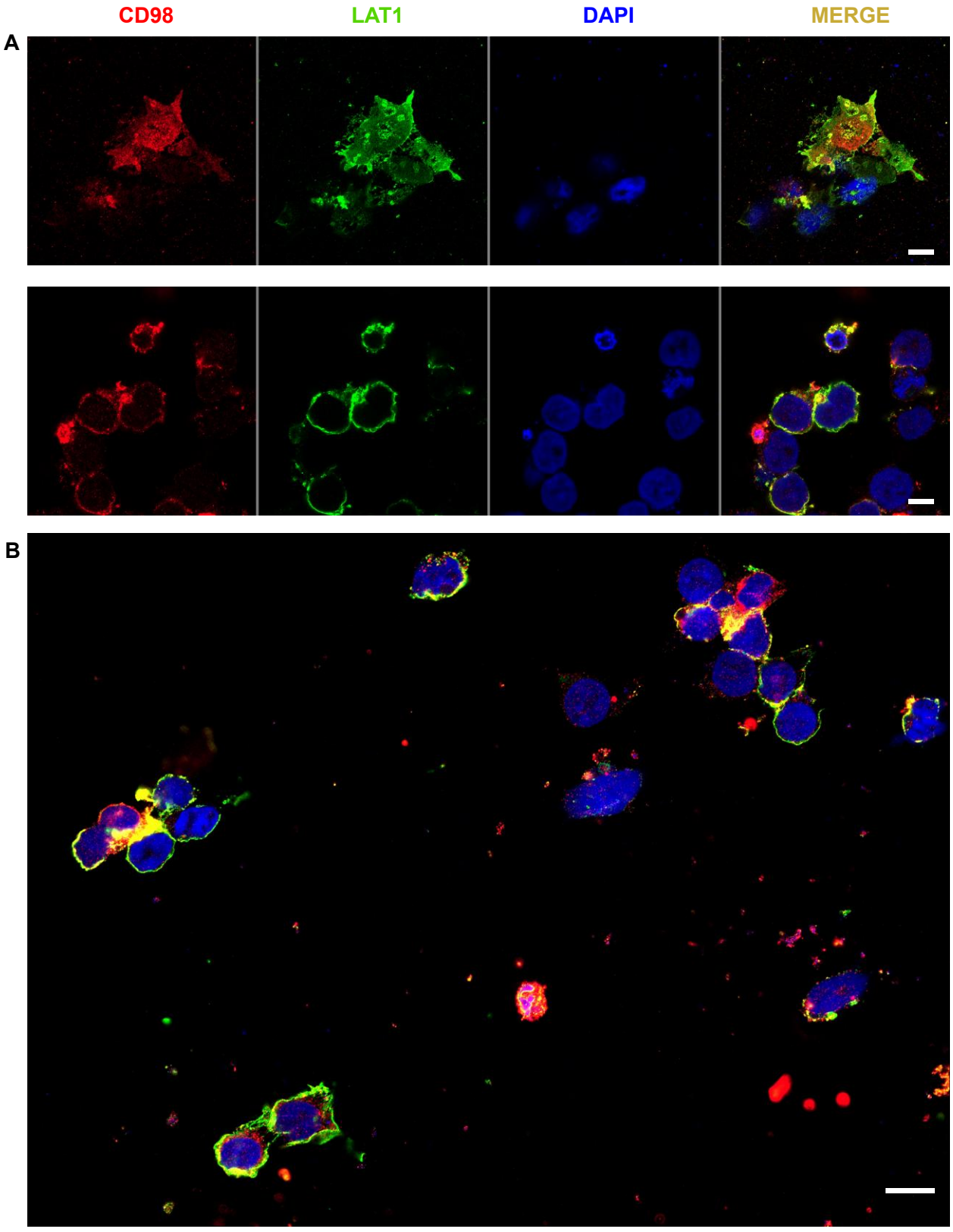

LAT1/CD98 1:2

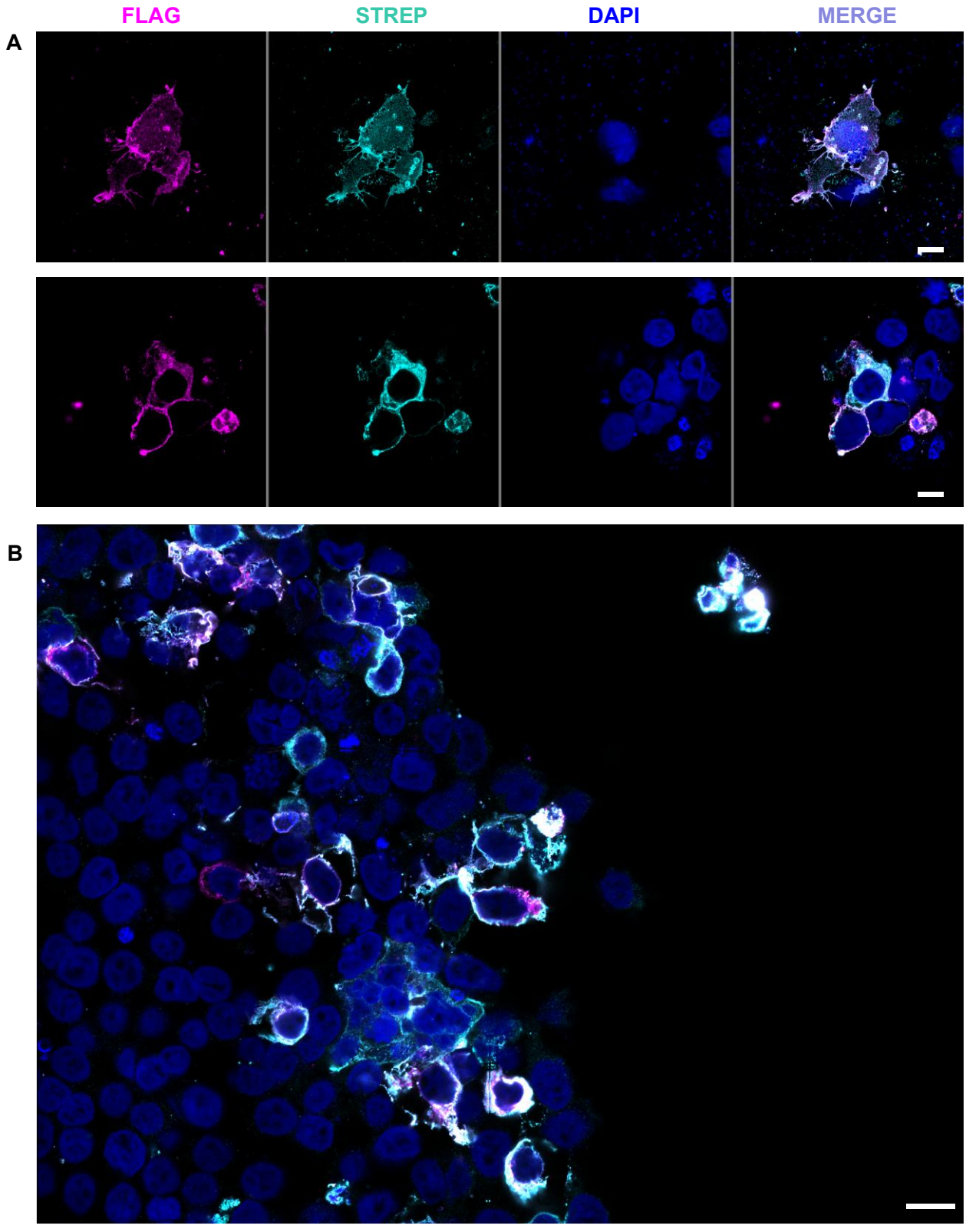

(Legend on the next page)

Figure 78: Heterodimer LAT1/CD98 expressed in DNA ratio 1:1 (first two panels) or 1:2 (last two panels) detected by immunofluorescence after incubation with primary anti-LAT1 (Green) and ant-CD98 (red) or anti-FLAG (Magenta) and anti-STREP (Cyan). a) single cells images (scale bar: 10 µm) b) wide field image (scale bar: 20 µm). Images collected on the microscope LSM 980 (Zeiss), Mag. ×63 with immersion oil objective).

4. LAT1 and CD98 expressed as single subunits have unexpected subcellular localizations

These "free molecules of CD98" might be impacted by the presence of LAT1. Indeed, when CD98 is transfected as single subunit, it showed a high expression level in DNA:PEI ratios from 1:3 to 1:5 (Figure 79) and is localized in the cytoplasm and the plasma membrane (Figure 80).

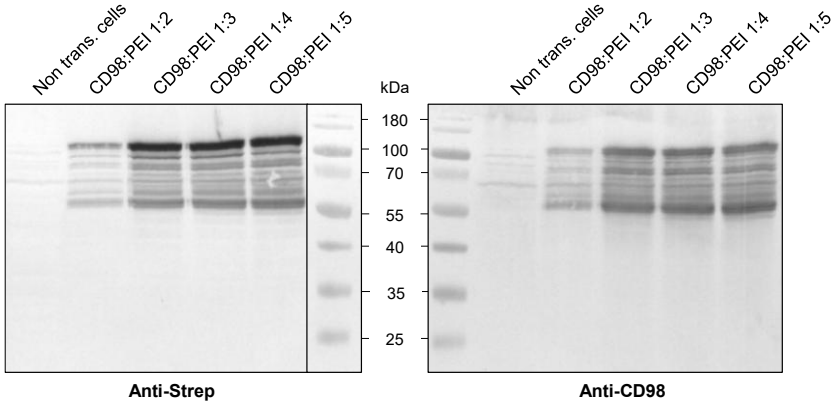

Figure 79: Expression of CD98 as single subunit after transfection in HEK cells at gradual ratios of DNA:PEI, detected by western blotting with anti-STREP and anti-CD98 antibodies.

Notably, CD98 in the plasma membrane was mainly detected with the anti-STREP antibody (supporting the membrane anchoring role of CD98) while cytoplasmic CD98 was mainly detected with the anti-CD98 antibody (Figure 80). As the antibody epitope is directed against the ectodomain of CD98, this means that the cytoplasm is enriched in proteolyzed form of CD98 emphasizing other cellular roles for endocytosis as already described (C. Zhang et al. 2023).

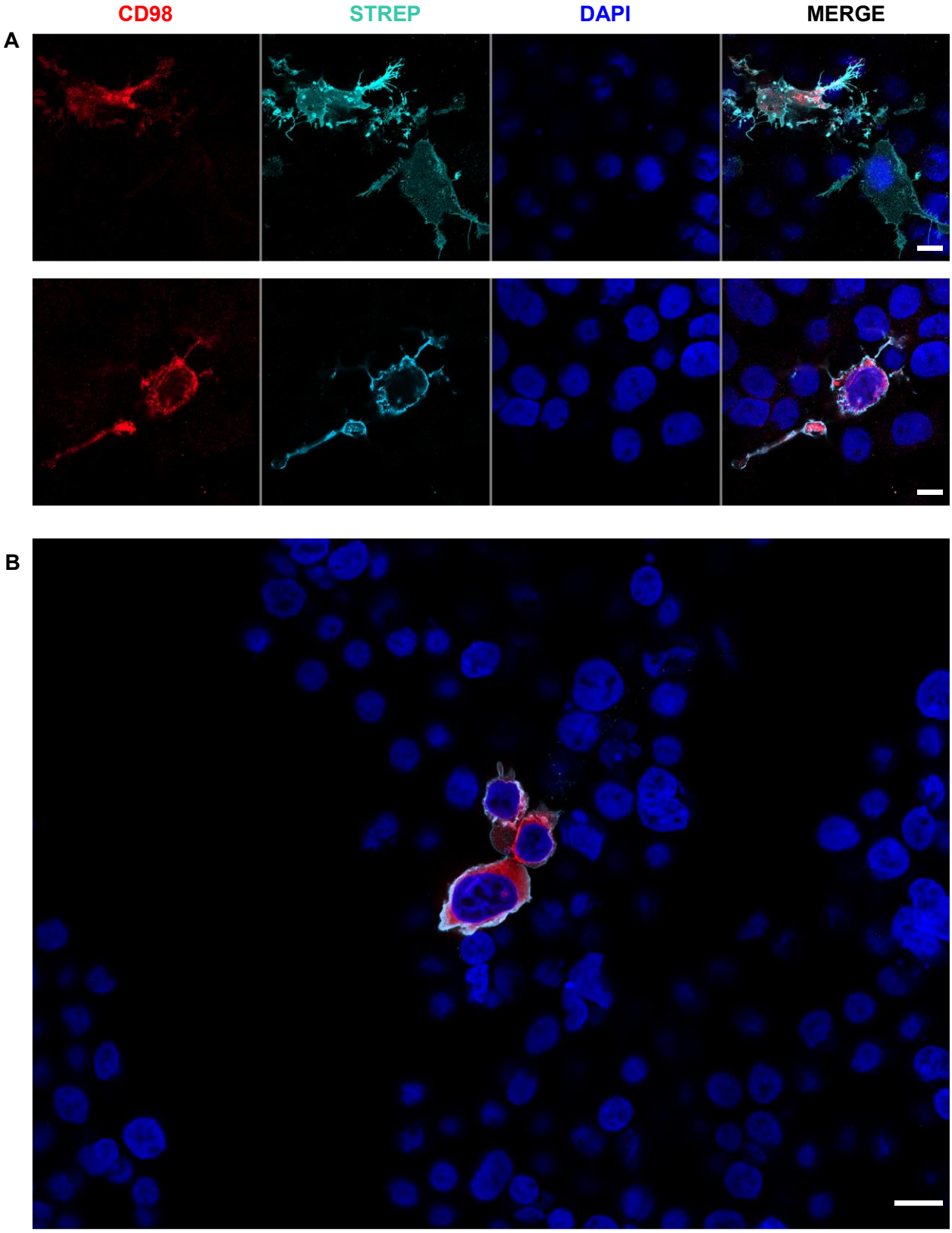

(Legend on the next page)

Figure 80: Confocal images of CD98 expressed in HEK293 GnTI$^-$ as single subunit. Single cells and wide field (lower panel) are presented. Red and cyan signals correspond respectively to the detection of the CD98, and Strep-Tag; They do not overlap in the cellular compartments. Images were collected on the microscope LSM980 (Zeiss) at Mag. ×63 with immersion oil objective.

While monomeric amino acid transporters possess a glycosylated loop to be exported to the membrane, LAT1 needs its anchoring protein CD98. Indeed, expressed as a single subunit, very low expression level is observed even at high DNA:PEI ratio (Figure 81). Therefore, high LAT1 expression depends on the presence of CD98 (Figure 75 and Figure 76).

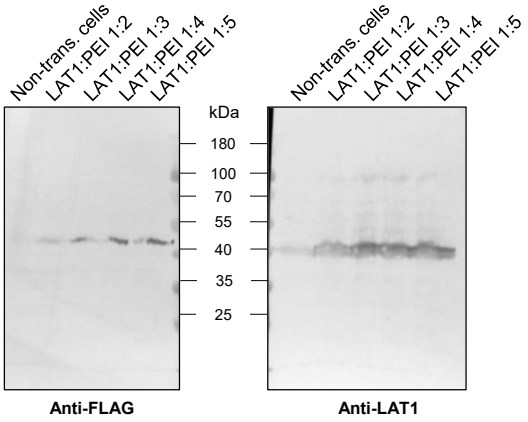

Figure 81: Expression of LAT1 as single subunit transfected in HEK293 GnTI$^-$ at gradual DNA:PEI ratios. Anti-FLAG and Anti-LAT1 antibodies were used for western blot detection.

Consequently, LAT1 single subunit molecules were supposed to be present rather in the cytoplasm, stacked in the endoplasmic reticulum. Surprisingly, confocal images revealed that LAT1 alone was localized in the plasma membrane like the heterodimer (Figure 82).

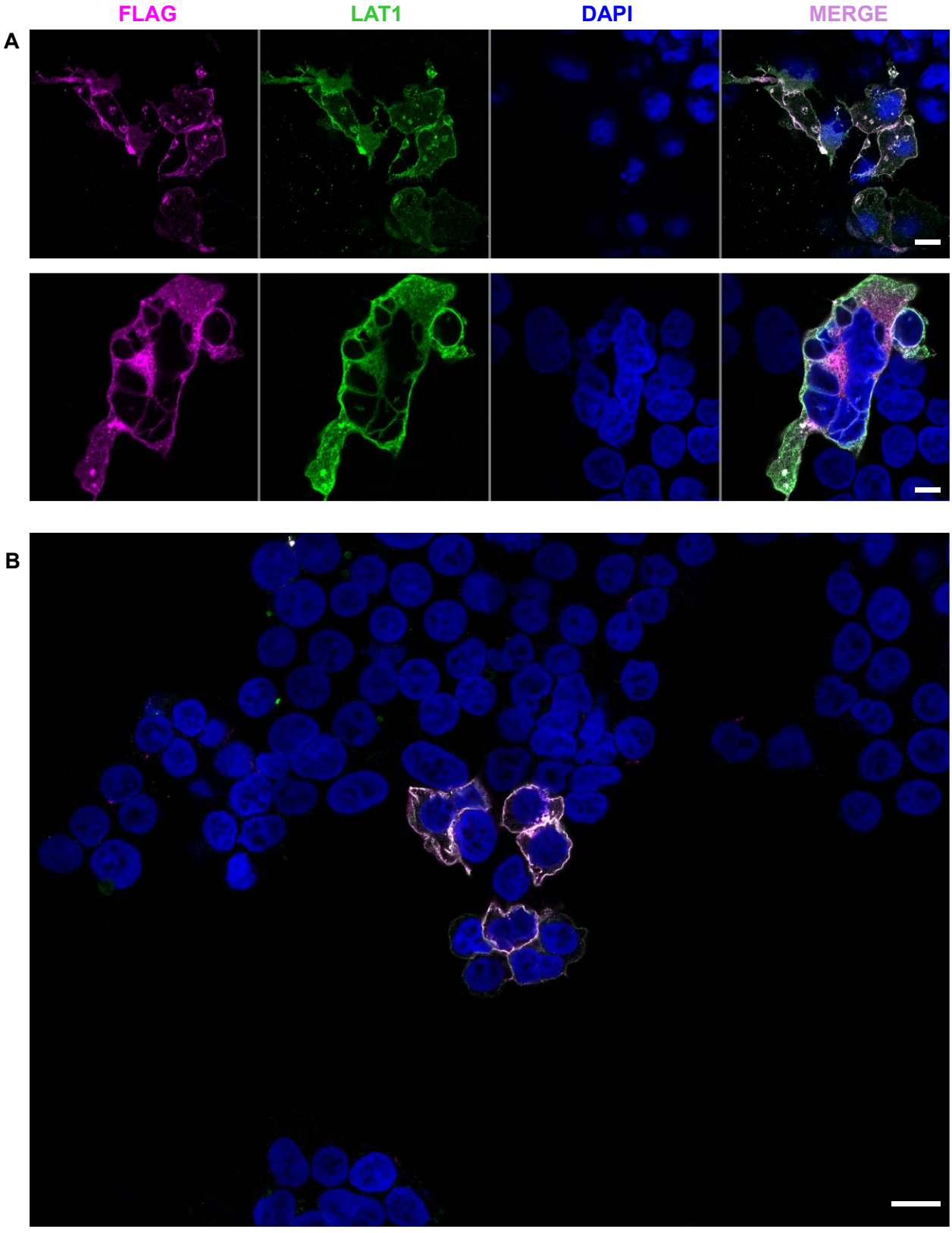

LAT1 single subunit

(Legend on the next page)

Figure 82: Confocal images of LAT1 expressed in HEK293 GnTI$^-$ as single subunit. Single cells and wide field (lower panel) are presented. To avoid the background signal coming from the endogenous expressed LAT1 in HEK cells and to confirm the localization of LAT1, a co-immuno localization was performed. Magenta and green signals correspond respectively to the detection of the FLAG tag, and LAT1. The overlay of FLAG and LAT1 is shown as white/light green signal on the MERGE squares of the single cell images. Images were collected on the microscope LSM980 (Zeiss) at Mag. ×63 with immersion oil objective.

This was unexpected especially that depletion of the extracellular loop 2 (ΔEL2) of the GABA transporter 1 (monomer modified as "LAT1-like" subunit) could not reach the plasma membrane and stack into the cytoplasm forming aggregates, as its exporting glycosylated signal was absent (Figure 83)

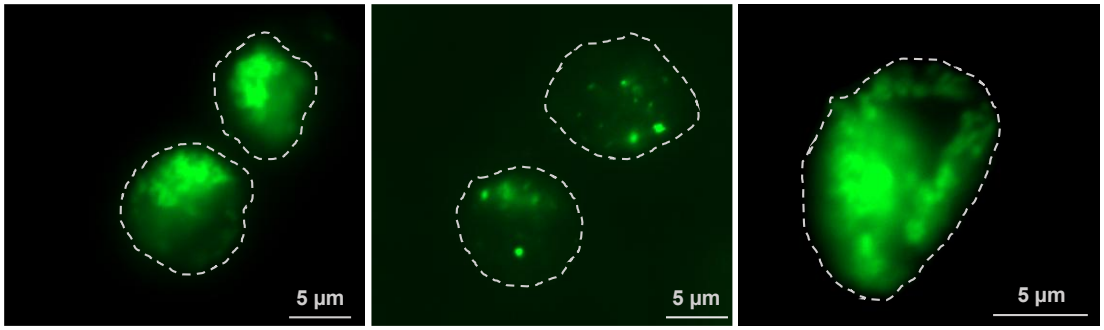

Figure 83: Confocal images of the rat GABA transporter 1 ΔEL2 transfected in HEK293 GnT$^-$ (Mag. ×63, immersion oil objective, LSM 980, Zeiss). Green signal corresponds to the truncated protein expressed with the eYFP expressed at its N-terminal. Cell contours are represented by dotted white lines.

All together, these results showed that contrastingly to other transporters, LAT1 even without glycosylated motif or CD98 can reach the plasma membrane. Therefore, it exists another mechanism proper to LAT1 and absence in other transporter families, compensating the exporting signal making possible for the protein to be localized in the plasma membrane.

5. LAT1/CD98 heterodimer purification

i. Establishing of initial protocol

After membrane solubilization LAT1/CD98 complex in micelle were purified only on FLAG resin instead of a double purification on anti-FLAG and StrepTactin resins as usually described. This was established to increase the protein yield before size exclusion chromatography (Klinger 2024).

All the purification steps on anti-FLAG resin were analyzed by SDS PAGE and western blot (Figure 84A and B). After solubilization, the membrane fraction showed a low signal for both subunits, meaning that most of the complex was extracted (Figure 84A and B). Although the elution fraction F1 and F3 showed bands at 40 and 100 kDa respectively corresponding to LAT1 and CD98 on western blot, their concentration remains low because hardly visible on the Coomassie blue stained SDS PAGE (Figure 84A). Therefore, only fraction F2 is used further for concentration and gel filtration.

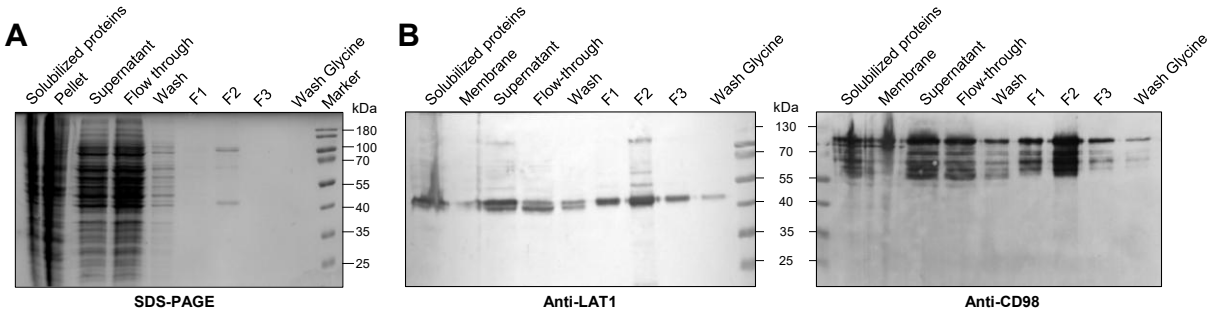

Figure 84: FLAG affinity chromatography steps analyzed by a) SDS PAGE and b) Western blot.

As LAT1/CD98 is a highly glycosylated complex, protein concentration was analyzed stepwise by SDS PAGE, BCA assay and nanodrop to determine the concentration before SEC. 2 ml from F2 fraction was concentrated with 100 kDa molecular cut-off concentrator and each centrifugation cycle lasted 2 min at 2000×*g*, 4°C (Figure 85).

	BCA assay	A_{280} (nanodrop)	Associated concentration
F2	0.269 mg/ml	0.33	0.246 mg/ml
First cycle (to 500 µl)	0.347 mg/ml	0.60	0.446 mg/ml
Second cycle (to 110 µl)	0.734 mg/ml	1.32	0.985 mg/ml

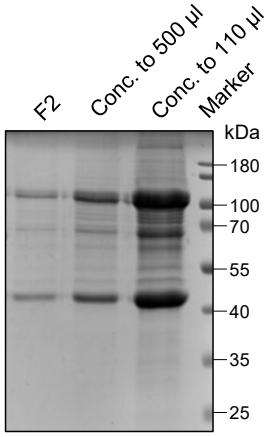

Figure 85: Analysis of fraction F2 during concentration before SEC. The concentration associated with each cycle was determined either by BCA assay or absorbance at 280 nm by nanodrop technology. The extinction coefficient of the heterodimer (164750 $M^{-1}.cm^{-1}$, see Table 22 in ***Material and methods***) was used to convert the absorbance value in mg/ml.

Approximately, the final concentration of the sample reached slightly less than 1 mg/ml before SEC (Figure 85). After passage on Superose Increase 6 (Cytiva), shoulders and peaks analysis showed that B3/B2 and B1/C1/C2 contain the same protein species (Figure 86A, B and C). The concentration of the pooled fraction under the main peak (B1/C1/C2) was determined by BCA assay at 0.054 mg/ml. Chromatogram fractions were analyzed in reductive (Figure 86B and C) non-reductives and native conditions (Figure 86D, E, F). On silver and Coomassie stained SDS PAGE, 3 bands showed the different complex isoforms. The same pattern was observed on the native PAGE (Figure 86E) therefore the purified sample did not form super-dimers as previously described (Wu et al. 2024).

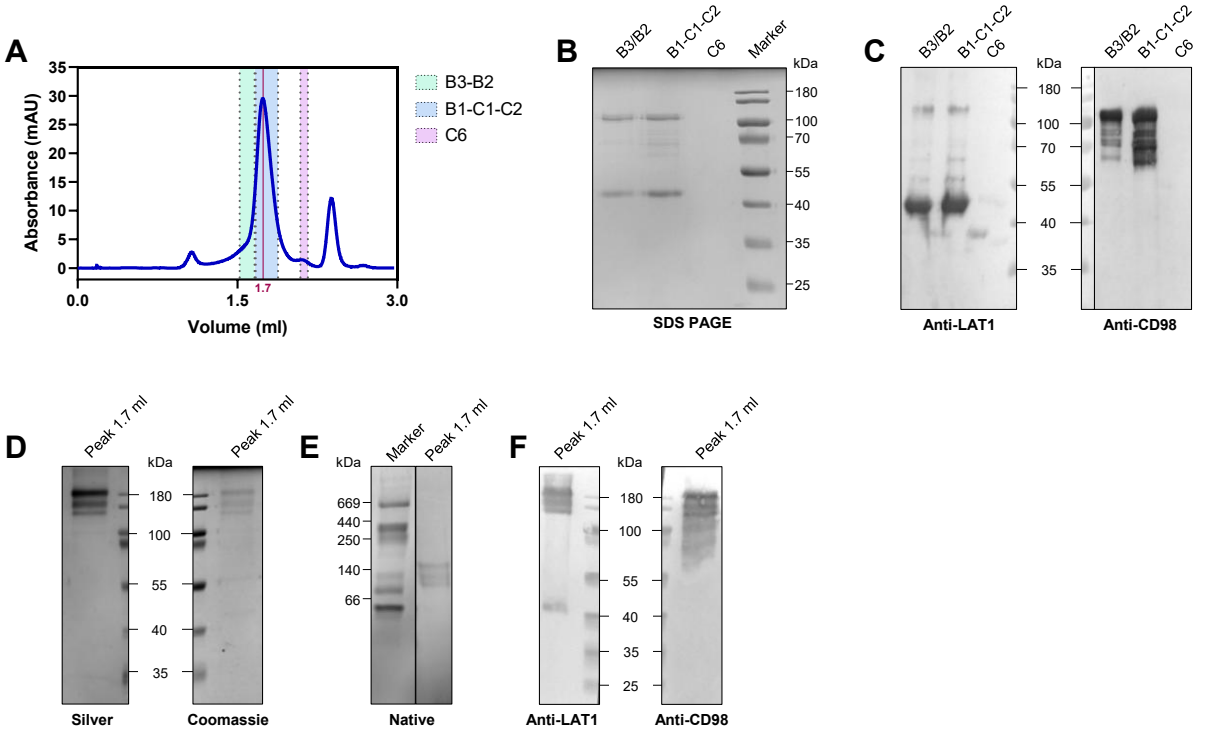

Figure 86: Analysis of LAT1/CD98 purification post SEC. a) Chromatogram representing the elution profil followed at 280 nm. The colored areas represent the diverse fraction analyzed by SDS PAGE and western blot. b) SDS PAGE stained with Coomassie blue in reductive conditions (10 % (v/v) β-Mercaptoethanol). c) Western blot with anti-LAT1 or CD98 antibodies to detect the respective subunits in reductive conditions. d) SDS PAGE stained with silver coloration and Coomassie blue in non-reductive conditions. e) Native

PAGE. f) Western blot with anti-LAT1 or CD98 antibodies to detect the respective subunits in non-reductive conditions.

Although the complex is clearly concentrated on the gel of the Figure 85 (F2 versus concentration up to 110 µl) the concentrating factor is not proportional to the ratio initial:final volumes. Also, the chromatogram peak, the SDS PAGE (Figure 86) attested to a low concentrated protein sample, compromising studies by cryo-EM. Therefore, lost in the concentrator flowthrough and SEC column Superose Increase6 were suspected. They were both analyzed by SDS PAGE and western blot.

ii. Challenges and shortcomings

- *Concentrator flow-through*

The latter showed a signal for both monomers (Figure 87A). With non-reductive conditions, a band at 130 kDa was detected with anti-LAT1 and CD98 antibodies meaning that the concentration does not influence on the heterodimer and the disulfide bond (Figure 87B). However, bands are almost invisible on SDS PAGE (Figure 87C), Therefore, most of the protein lost while concentrating is not present in the flow through. Probably the glycosylation pattern of CD98 favors interaction with the concentrator membrane, reducing greatly the final protein yield.

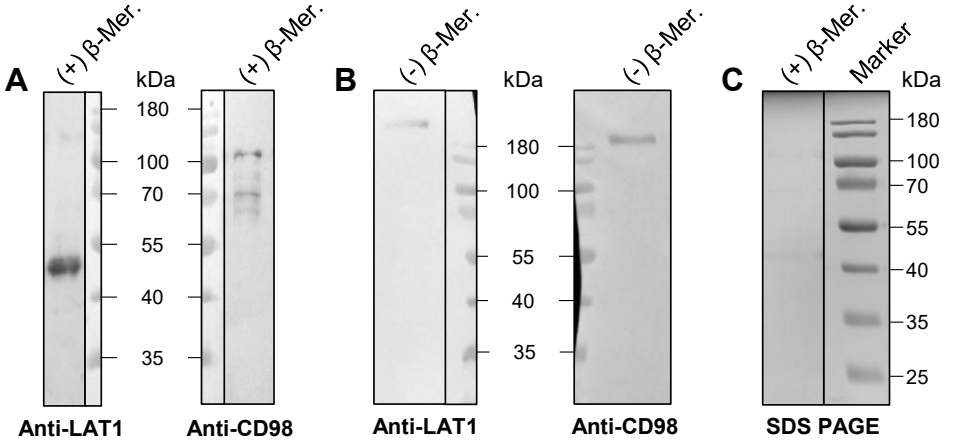

Figure 87: Analysis of the 100 kDa molecular cut-off flow through. Western blot a) with reductive conditions (10 % (v/v) β-Mercaptoethanol) to break the disulfide bond between both monomer and b) without reducing agent. LAT1 and CD98 subunits were detected respectively with anti-LAT1 and anti-CD98 antibodies. c) SDS PAGE with reductive conditions (10 % (v/v) β-Mercaptoethanol).

- *Column washes*

Two SEC columns were used, i.e. Superose Increase 6 and Superdex200 (Cytiva) to optimize protein yield after SEC. Both columns were washed with 500 mM sodium Hydroxide (NaOH) and the fractions collected were analyzed by SDS-PAGE and western blot (Figure 88). No traces of the protein complex was found, therefore the matrix of these columns did not interact with the heterodimer LAT1/CD98.

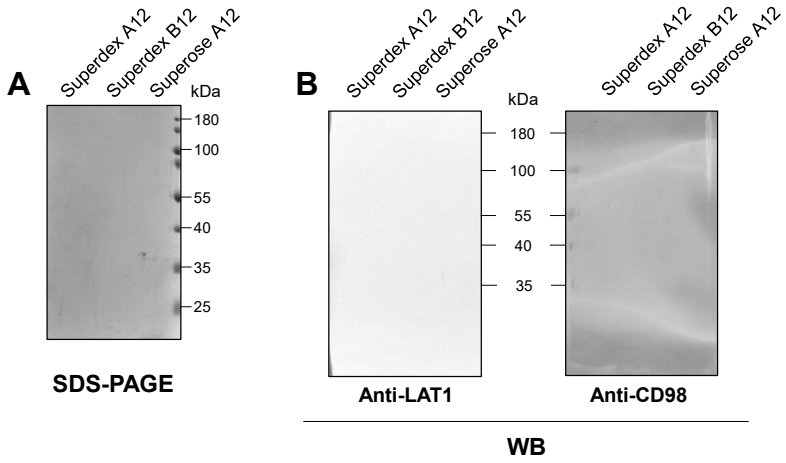

Figure 88: Analysis of SEC columns (Superose Increase 6 and Superdex200) washed with 2 CV of 500 mM NaOH. a) SDS PAGE and b) western blot to detect the presence of LAT1 and/or CD98.

To summarize, although protein loss was observed during sample concentration and SEC, the reason remains unclear. Therefore, the ideal situation would be to avoid these steps to increase the final protein concentration.

iii. Optimized protocol

In this regard, after the purification on anti-FLAG resin, another affinity chromatography was performed using the Streptactin XT Flow material (IBA, Germany), taking advantage of the STREP tag expressed at the N-terminal of CD98. This resin requires a low bed volume (100 µl) to elute the protein in small fraction volumes, avoiding its dilution. The concentration of the fraction F4 (Figure 89B) was determined at 0.138 mg/ml (BCA assay and nanodrop). It is less than the Fraction F2 after anti-FLAG purification (Figure 85, table). However, the sample presents fewer CD98 isoforms than the fraction F2 (Figure 85, gel) and is therefore more concentrated in one

homogenous specie (F2, 3, 4 Figure 89B). Indeed, the second affinity chromatography eliminates overexpressed LAT1 and LAT1 bound to native expressed CD98, increasing the purity of the complex itself. Without concentration, fraction F4 was passed on Superose Increase 6 column for SEC. According to the chromatogram or SDS PAGE (Figure 89A, B) most of the protein is lost, reinforcing that a double affinity chromatography without SEC is the best option for high purity and improved concentration of LAT1/CD98.

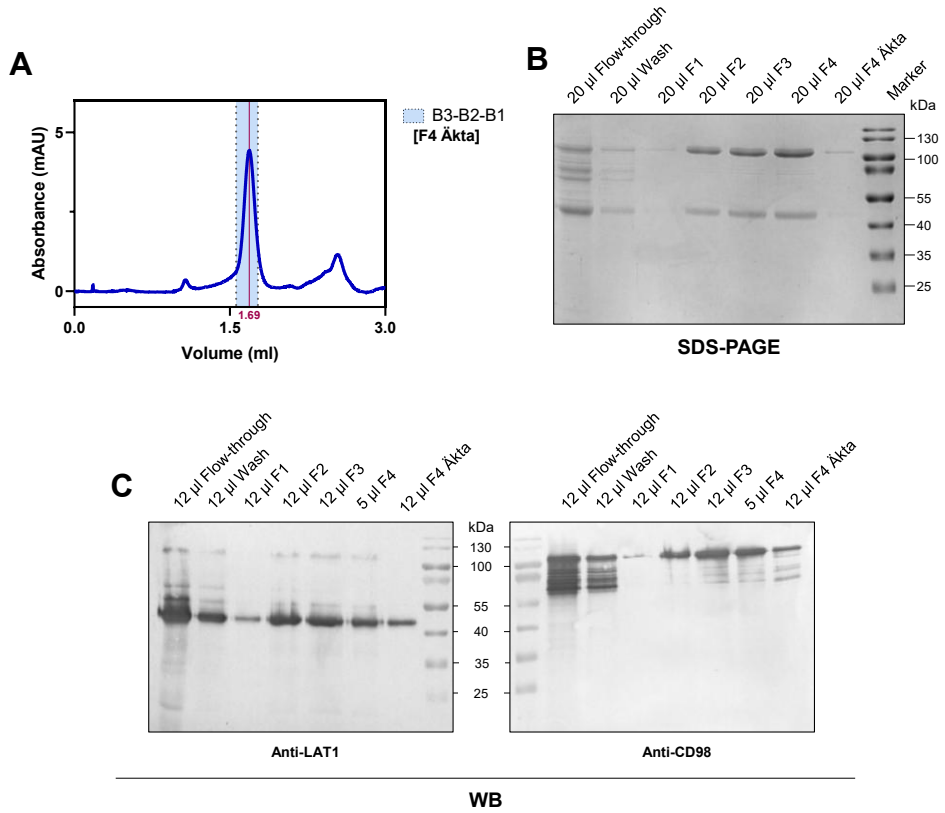

Figure 89: Second affinity chromatography steps on StrepTactin Superflow XT material (IBA). a) SEC profile after passage on the Superose Increase 6, followed by analysis on b) SDS PAGE and c) Western blot where anti-LAT1 and-CD98 antibodies were used. All fractions for SDS PAGE and western blot were in reductive conditions (10 % (v/v) β-Mercaptoethanol).

To conclude, the last optimizations of LAT1/CD98 purification might largely improve the protein yield, necessary for single particle analysis. Incubation and vitrification of the heterodimer in presence of the inhibitor Brasilicardin A will be the next step towards structural insights of the binding mode of the molecule in the protein complex. Indeed, these details are still unknown while

the inhibition potency of BraA is well described (Botas et al. 2021; Usui et al. 2006; Komaki et al. 1999).

IV. Prostatic bone metastasis: cell target validation for BrasilicardinA and LAT1/CD98 heterodimer paradox

The interaction of BraA with LAT1 activates General Non Depressible 2 (GCN2) amino acid sensitive pathway that lately suppresses protein translation, reducing the cell proliferation (Usui et al. 2006). However, BraA was tested on few cancerogenic cell lines although LAT1 is overexpressed in almost every tumorous tissue. Surprisingly, *in vitro* studies on prostatic metastases located in bones (PC-3 cell line) showed that leucine starvation stimulated the same pathway for enhancing LAT1 expression and counterbalancing amino acid supply (Q. Wang et al. 2011). Therefore, long term inhibition of this pathway by BraA might represent a possible treatment of prostatic bone metastases. In this regard, the presence of the heterodimer LAT1/CD98 was studied in subline PC-3M for further cytotoxic experiments for validating these cells as a putative drug target for BraA.

1. Heterodimer is detected on cell lysate western blot

After 10-15 days of culture cells were harvested for protein analysis on western blot. According to the work from Otsuki and co-workers in 2017, they solubilized the protein with a buffer containing 1% Triton. However, the absence of cholesterol mimic like CHS promotes the degradation of LAT1/CD98 (Dickens et al. 2017; Rosell et al. 2014). Therefore, the usual solubilization buffer for LAT1/CD98 is also used in parallel (*Cf:* ***Material and Methods, Table 15***). After solubilization, and centrifugation, the supernatants were analyzed by western blot in oxidative and reductive conditions (Figure 90). PC-3M express both LAT1 (ca. 45 kDa) and CD98 (between 70 and 130 kDa) visible as single subunit in the reductive conditions or as complex (ca. between 100 to 180 kDa) in the oxidative conditions. Moreover, no difference is seen between the solubilization buffers containing CHS or Triton, validating the method already used (Figure 90).

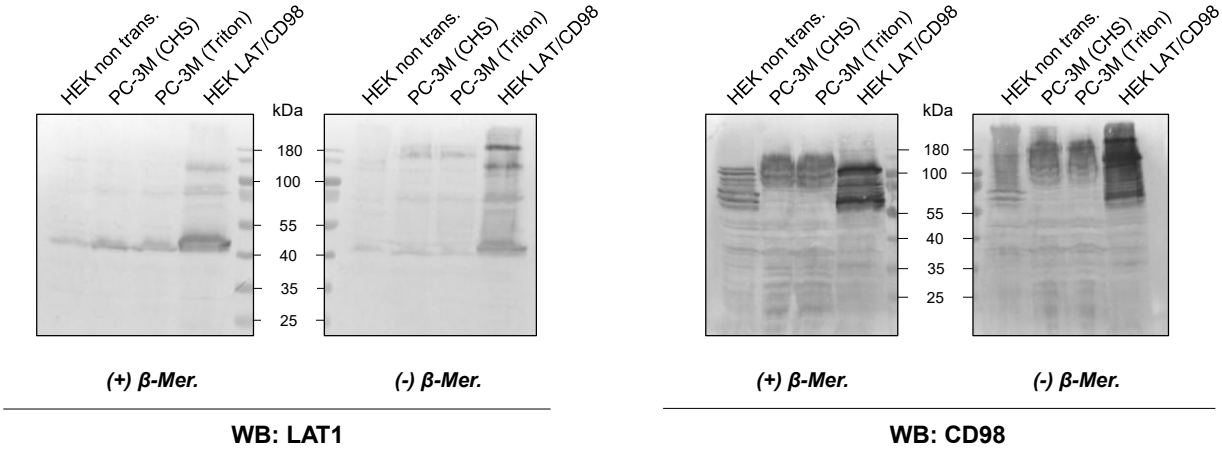

Figure 90: Western blot analysis on PC-3M cells lysate to detect the presence of LAT1/CD98 heterodimer. The anti-LAT1 and anti-CD98 antibodies were used. As control, non-transfected HEK cells (first line) and overexpressed HEK cells with LAT1/CD98 (last line) are also shown. ***(±) β-Mer***. indicates the presence (reductive conditions) or the absence (oxidative conditions) of β-Mercaptoethanol. (CHS) indicates the cells lysed with the standard LAT1/CD98 solubilization buffer, while (Triton) indicates the cells lysed with a buffer previously described (Otsuki et al. 2017).

2. Only LAT1 is present at the surface of PC-3M cells

Thereafter, PC-3M cells were seeded to localize LAT1 and CD98 by immunofluorescence. No antibody against a purification tag can be used; Hence, PC-3M cells were incubated with two primary antibodies against proteins not expressed in this cell line (i.e. anti-GAT1 and BGT1 antibodies) to appreciate the nonspecific interactions of primary and secondary antibodies. Images were taken on single cells and on wide field to see the protein expression heterogeneity according to each cell. Contrastingly to overexpressed HEK cells showing a co-localization of LAT1 and CD98 signals, only LAT1 is present in the plasma membrane and in the characteristic lamellipodia of the PC-3M (Figure 91). CD98 is detected as nonspecific signal comparable to the negative control images (Figure 92). This does not correlate with the western blot showing the presence of the complex. However, like in HEK cells, LAT1 might have another strategy to reach the plasma membrane, also in the PC-3M subline.

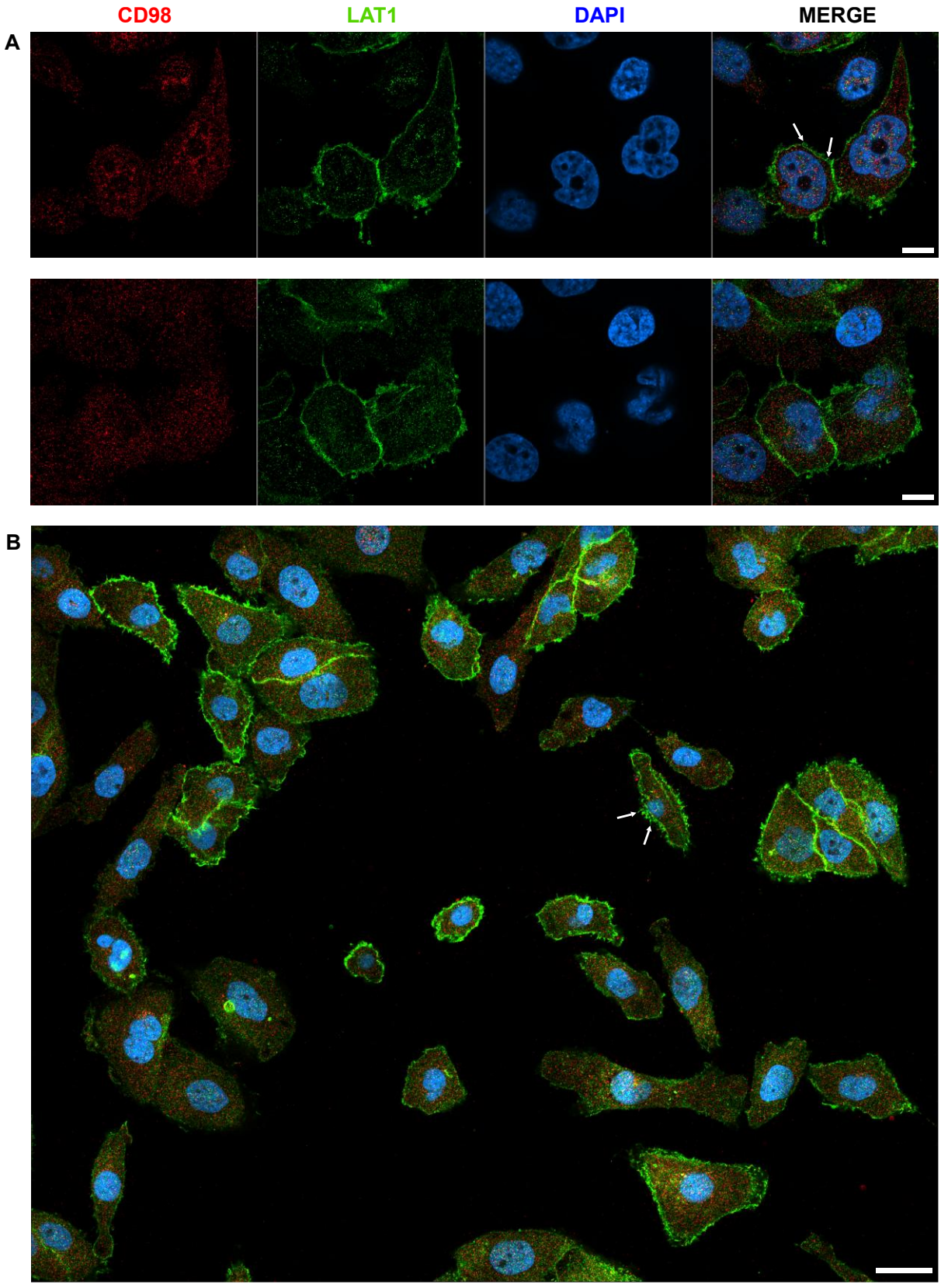

(See Legend next page)

Figure 91: LAT1 and CD98 cellular localization in the bone metastasis PC-3M detected with anti-LAT1 (1:500) and anti-CD98 (1:500) antibodies. a) single cells images (Scale bar:10 µm) and b) wide field image (Scale bar: 25 µm). Red, Green and blue signals correspond respectively to CD98, LAT1 and nucleus stained with DAPI. Images were collected on the microscope LSM 980 (Zeiss) at magnification ×63.

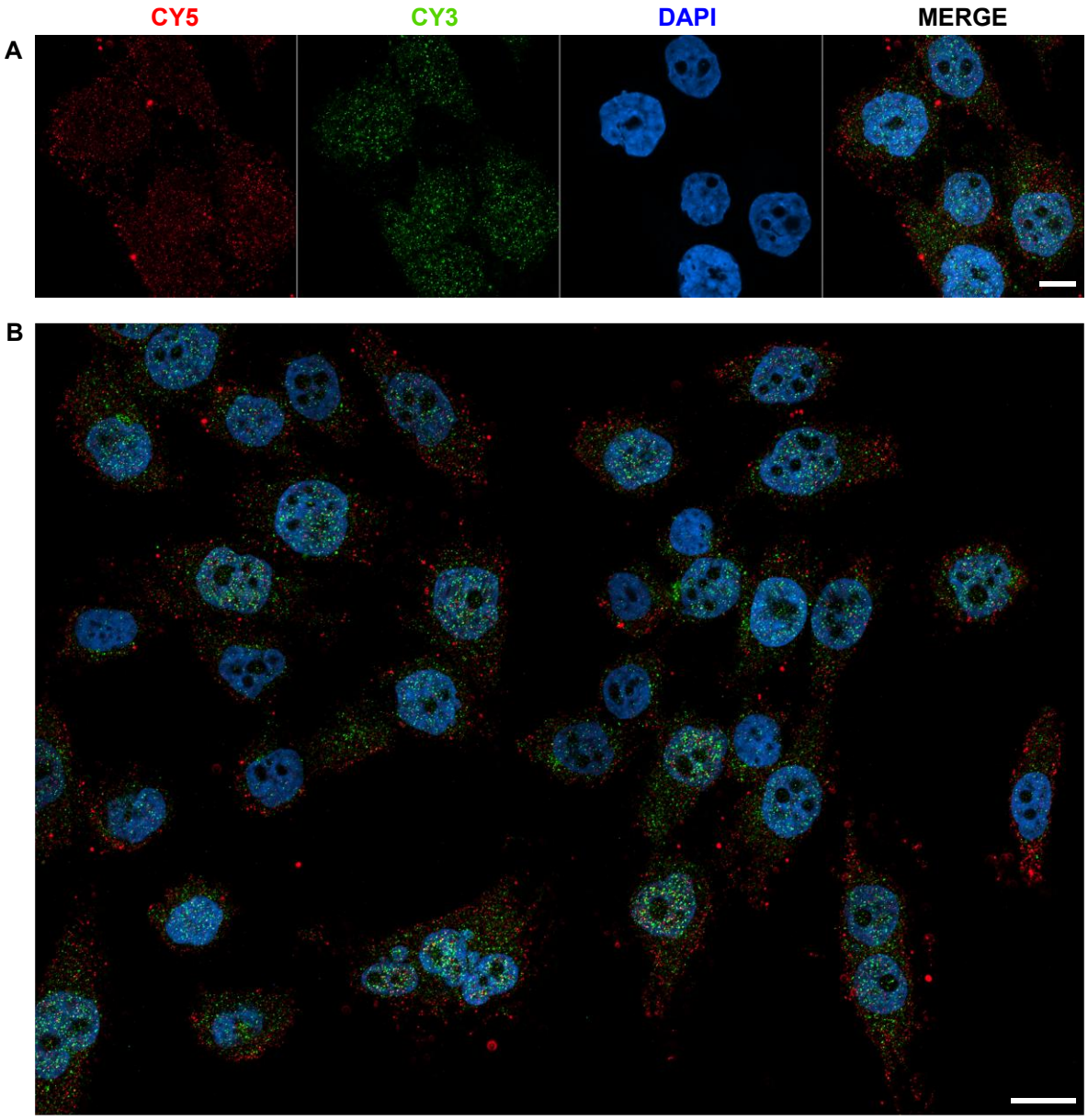

Figure 92: Nonspecific signal associated with the PC-3M cells. Secondary antibodies conjugated with Cy5 and Cy3 are specifically recognizing the anti-BGT1 (1:500) and anti-GAT1 (1:500) antibodies. a) Single cells images (Scale bar:10 µm) and b) wide field image (Scale bar: 25 µm). Images were collected on the microscope LSM 980 (Zeiss) at magnification ×63.

Discussion

I. Probing GAT1 in a lipid environment: Insights from reconstitution studies

We successfully expressed and purified wild-type GABA transporter 1 (rGAT1) and reconstituted it in a brain phospholipid environment. Functional measurements in collaboration with Despoina Kapiki (LMU Munich), confirmed that the protein was both properly folded and functional, allowing us to investigate the critical role of the phospholipid environment on its activity.

Lipids significantly influence transporter function, as demonstrated by prior research on the monoamine neurotransmitter transporter SERT. For instance, phosphatidylinositol bisphosphate (PIP2) is vital for stabilizing specific oligomeric states of SERT, a process essential for the protein's trafficking from the endoplasmic reticulum (ER) to the plasma membrane (Anderluh et al. 2017). This area represents a crucial focus for ongoing research.

On the ER, for many sodium coupled SLC6, transporter oligomerization permits the recruitment of the COPII protein complex to form exporting vesicles (Sitte and Freissmuth 2006). Mutations in the hypothesized interface domains of GAT1 and monoamine transporters retain them in the ER (Scholze, Freissmuth, and Sitte 2002). The consequence of the oligomerization in plasma membrane on SERT transport function was studied in 2005 by Seidel and coworkers in using a GAT-SERT concatemer (Figure 93).

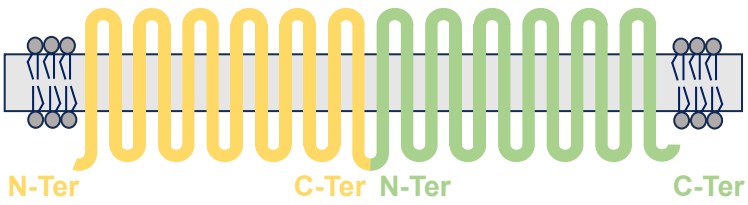

Figure 93: Scheme of GAT-SERT concatemer. GAT1 (in yellow) is at the N-terminal extremity of SERT (green). This chimeric protein is embedded in the plasma membrane (in grey) (from Seidel et al. 2005).

Research showed that GABA transport was inhibited while serotonin efflux was stimulated in the presence of both GABA and amphetamines. Blocking the influx function of one transport unit (GAT, with GABA) activates the other transport unit (SERT, with serotonin), prompting it to

export its substrate. This "counter transport" phenomenon is a direct result of SERT oligomerization, which is, in turn, a consequence of the lipid composition of the plasma membrane, which is enriched in PIP2 compared to other cellular membranes (Jayaraman et al. 2021; Anderluh et al. 2017). For instance, GAT1 can be selectively inhibited by a combination of low concentrations of GABA (3−10 μM) and a very small amount of betaine (0.1 μM) (Bhatt et al., 2024). This observation suggests that the transport modulation of GAT1 by betaine might follow the same "counter transport" model seen in transporters oligomers. However, the specific role of the surrounding lipid environment in this process is currently unknown. It is plausible that, similar to the Serotonin Transporter, the observed mechanism for rGAT1 is a direct consequence of its oligomerization. To explore this, we successfully reconstituted GAT1 into liposomes (Figure 50). This provides a promising platform to study the impact of specific lipids on GAT1's molecular mechanism. A more advanced approach involves using extracellular vesicles (EVs), which offer a "neo-native" phospholipid environment. These EVs also maintain the proper asymmetry between the inner and outer membrane leaflets, making them an excellent choice for studying protein-lipid interactions for both functional and structural analysis. In fact, numerous cryo-EM studies have utilized EVs over the past decade to analyze membrane proteins (Delauzun et al. 2020; Zeev-Ben-Mordehai, Vasishtan, Siebert, and Grünewald 2014; Zeev-Ben-Mordehai, Vasishtan, Siebert, Whittle, et al. 2014). However, achieving atomistic structures (below 4 Å) for small membrane proteins remains a challenge when they are studied within a reconstituted lipid environment. Challenges in classifying and reconstructing 3D maps of transporters arise from preferred orientation and strong amorphous density within the lipid environment, particularly when the transporter lacks an extra-membranous antibody label. Further improvements in labeling techniques and cryo-EM such as collecting tilt series represent a major advancement in overcoming this limitation. This would permit to fully understand the collaborative oligomeric transport versus monomeric transport regulated by multiple substrates of GAT1 *in vivo*. (Yao, Fan, and Yan 2020). Consequently, it represents new therapeutical strategies for imbalanced neurotransmitter transport diseases.

II. The Molecular Basis of GABA Transporter Function and Specificity

1. Molecular mechanism of GABA binding and transport in GAT1 and the mutant L300Q

In 2023, four structures of GAT1 WT were published, two in the inward-occluded state and two in the inward-open state (Zhu et al. 2023). One inward-occluded state (PDB 7Y7W) was solved in complex with GABA and sodium (two) and chloride (one) ions.

Interestingly, the two observed inward-open states are not structurally identical, particularly regarding the conformations of TM5 and TM1 (Figure 94A). This distinction not addressed in the published data, aligns with the successive transitions of TM5 previously detailed by Malinauskaitė (2014) concerning sodium release at the Na2 site. The process begins with the inward-occluded state (7Y7W, in blue, Figure 94A), where the folded TM5 unwinds (7Y7Z, in purple, Figure 94A). This creates an intermediate loop that effectively subdivides the helix into two sections, TM5i and TM5e. Concurrently, a rotamer change in Ser396 facilitates the hydration of the Na2 site, which in turn causes the sodium ion to be released. This action breaks the interaction between Tyr60 and the GABA substrate, thereby unlocking and shifting TM1 away from the binding site (7Y7Z, in purple, Figure 94B). This collective movement creates a large cavity, allowing for the release of both the substrate and the sodium ion into the cytoplasm. The transporter does not remain unwound. Subsequently, the TM5 helix refolds to a conformation similar to the initial inward-occluded state (7Y7V, in green, Figure 94A, B). This refolding causes a corresponding shift in TM1a and the Tyr60 residue. This change, combined with Leu64 occupying the empty substrate site, helps the transporter return to its outward-open conformation, ready for a new transport cycle (Malinauskaite et al. 2016).

This sequence of events leading to substrate release for the WT GAT1 are important notions to understand functional changes in the L300Q mutant or for the WT in presence of betaine obtained in this thesis. Our electrophysiology data suggest that there are limiting steps in the alternating access model because of an alteration in substrate and sodium binding, associated with their respective sequential binding events.

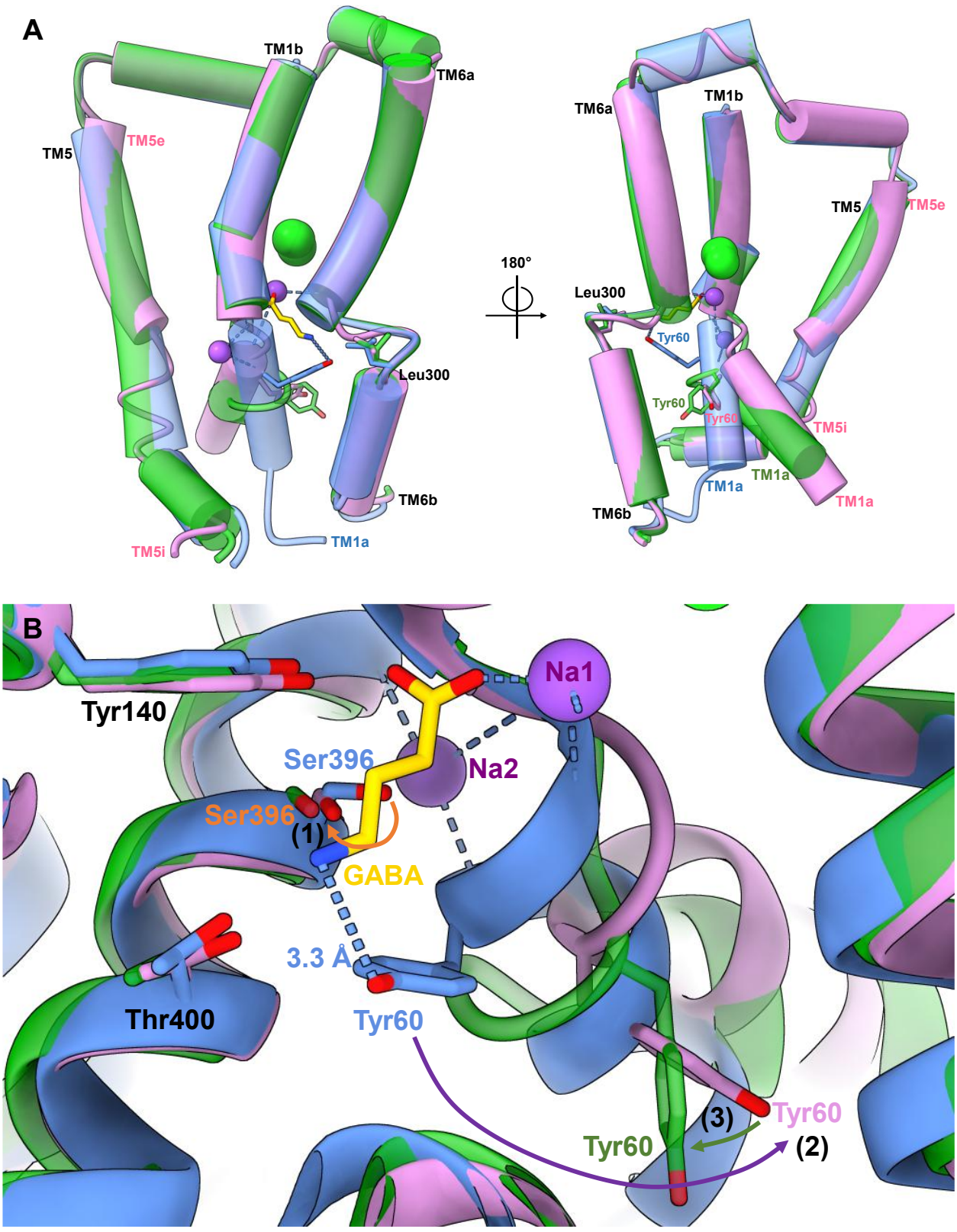

(See legend next page)

Figure 94: Superposition of rGAT1 WT in its two inward-open conformations (Apo 7Y7V, in Green and Tiagabine-bound 7Y7Z, in Pink) and in its inward-occluded conformation, coordinating GABA (7Y7W, blue). The residues written in the corresponding color of the structure reveal a different position, while residues in black show an identical position from one conformation to another. a) Tube helix representation of TM1, 5 and 6 to show the unwinding of TM5 in the first inward-open state. b) Focus on the molecular mechanism for sodium and GABA release. Unwinding of TM5 and rotation of Ser396 facilitate the Na2 site hydration while Tyr60 stops its interaction with GABA inducing the shift of TM1a for substrate and co-substrate release.

GAT1 L300Q mimicking the BGT1 transporter exhibits altered sodium affinity and cooperativity, indicating a different coordination of sodium that impacts coupling. Our structural data enables us to interpret our functional results in the context of structural changes occurring during sodium coupling. While Na2 is conserved, Na1 site is dilated due to the shift of TM7 and 6 (*Cf:* ***Results, Figure 74***) where Asn327 and Ser295 moved out of coordination range (3.6 Å). Due to Gln300, the (G/A/C)ΦG loop points now towards GABA and creates an additional coordination via a 2.5 Å hydrogen bond (*Cf:* ***Results, Figure 74*** and Figure 95A) compensating for the weakened GABA-Na^+ coupling and consequently increases the affinity for GABA in the mutant. Its transition to an inward-open conformation is caused by the rotation of Ser396 and the disruption of the GABA-Tyr60 interaction (Figure 95B). Although this causes TM1a to shift away in a manner similar to the wild-type protein, Gln300 continues to coordinate the amino group of GABA (Figure 95C).

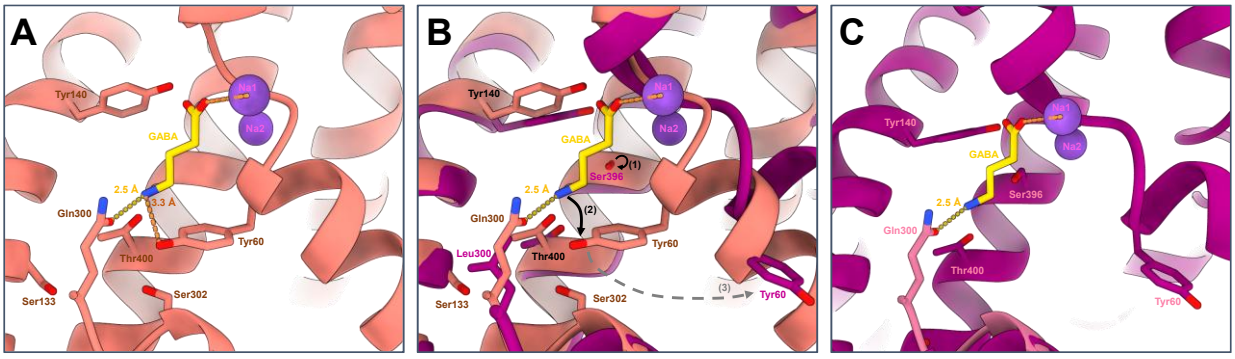

Figure 95: Successive events in GAT1 L300Q from GABA binding to retention in the binding site. a) Double coordination of GABA with Gln300 and Tyr60. b) Intermediate state between inward-occluded to inward-open where Ser396 is rotating to stop interacting with Na2 and Tyr60 associated with the movement of TM1 is creating a cavity for intracellular accessibility. c) Gln300 keeps interacting with the amino group of GABA, retaining GABA in the binding site and the protein in a state between inward-occluded and

inward-open (Superposition of GAT1 L300Q generated by AlphaFold 3 in coral and GAT1 WT inward-open 7Y7Z in purple).

Consequently, the transporter is in a transient state between inward-occluded and inward-open state. This intermediate conformation is a quasi-stable transient state and therefore a rate limiting step in the alternating access cycle, before a third sodium ion binding (*Cf:* ***Results, Figure 66 and Table 37***). It is unlikely that Ser302 coordinates sodium at the Na1' site because it undergoes a significant conformational rearrangement during the intermediate state (purple structure Figure 96A). Given its high affinity for sodium, Gln300, which is in the vicinity of the Na1' site, would likely coordinate a sodium ion rather than the amino group of GABA. This action would disrupt the Gln300-GABA interaction and promote the movement of the (G/A/C)ΦG motif, leading to the simultaneous release of both ions and GABA (Figure 96B).

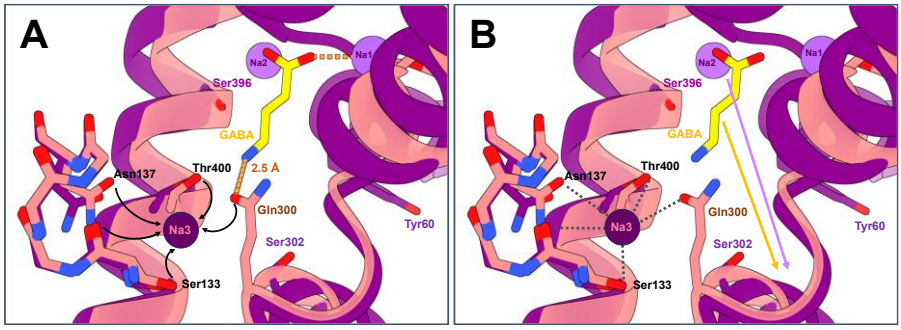

Figure 96: GABA and sodium release in GAT1 L300Q. a) a third sodium ion coordinated by Ser133, Asn137, Gln300, and Thr400 permitting b) to break the interaction Gln300-Na3 that will liberate GABA allowing the transporter to accomplish its transport cycle. (Superposition of GAT1 L300Q generated by Alphafold3 in coral and GAT1 WT inward-open 7Y7Z, in purple).

While the overall sodium affinity of the mutant is slightly lower than the wild-type, suggesting that the Na1' site is a weaker binding site than the Na1 and Na2 sites, Intensity/Voltage analysis presents a more complex picture. These experiments showed that a sodium concentration corresponding to $K_{0.5}$ is sufficient to facilitate robust GABA transport. This finding suggests that while sodium binding is a prerequisite for transporter activity, it is not a rate-limiting step. Instead, the binding of a sodium ion to any of the three sites appears to be what rescues and enables the transporter's function. The heightened transport rate observed in GAT1 L300Q, in contrast to BGT1, can be attributed to the synergistic impact of the Gln300-Na3 interaction and the conformational alterations in Tyr60/TM1

2. Betaine binding and transport: WT versus L300Q mutant

Structure superposition of GAT1 WT and BetP (*Cf:* ***Introduction,*** **Figure 13**) suggests that betaine is coordinated by the backbones of Ile62 and Ala61 in GAT1 WT, representing a different site from the GABA binding site. Betaine exhibits a lower affinity compared to GABA because, like the betaine methylammonium group, sodium is positively charged, leading to less stable coordination. Interestingly, Ile62 in GAT1 L300Q is in a loop conformation while in GAT1 WT it is still part of the TM1a helix (Figure 97A and B). Also, Gln300 within the (G/A/C)ΦG motif provides greater flexibility to the unwound helix. This allows it to push TM6a forward, thereby increasing the distance between the Na1 site and betaine. As suggested by Focht and coworkers in 2021, this structural arrangement also serves to protect the initial empty GABA binding site from unwanted hydration from the intracellular space (Figure 97B). This unique and stable conformation in the mutant, which is absent in the WT, ensures that betaine binding is not a rate-limiting step and explains why its affinity is 15-fold higher than the WT.

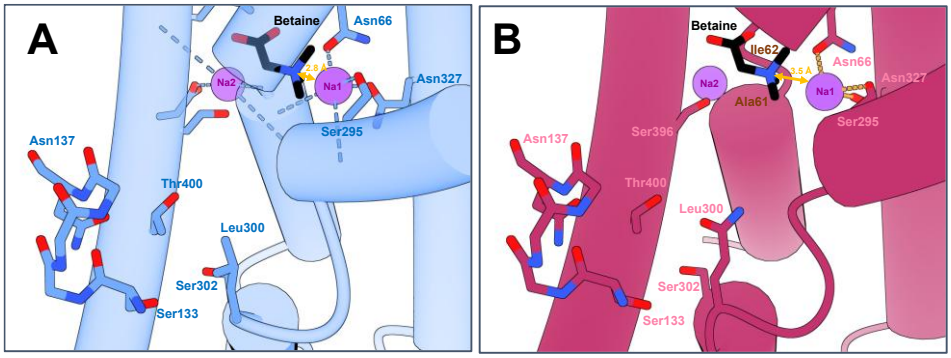

Figure 97: Putative betaine binding site a) GAT1 WT an b) GAT1 L300Q. Structure used for the figure: GAT1 WT inward-occluded pdb 7Y7W (blue), from Zhu et al., 2023 and AlphaFold3 model of GAT1 L300Q inward-occluded state (dark red).

While the GAT1 L300Q mutant shows improved betaine binding properties, the WT remains a more effective transporter for betaine when sodium concentrations vary. Under these conditions, the mutant's betaine transport efficiency is five times lower than the WT's, which is a direct result of its decreased affinity for sodium (*Cf:* ***Results,*** **Table 37**). This leads to high cooperativity and requires saturating sodium concentrations to drive transport (*Cf:* ***Results,*** **Figure 67**). Consequently, these data suggest that betaine impairs sodium binding, a step that is highly rate-limiting for both transporters in their respective cycles.

The presence of Leu300 in GAT1 WT requires a prior movement of the (G/A/C)ΦG motif in the unwound TM6 to protect the empty GABA binding site. Betaine and sodium in the Na1 are competing with each other (Figure 98A) forcing the sodium to be coordinated in Na1', which would involve Ser133, the side chain of Asn137, Ser302, and Thr400 (*Cf:* ***Introduction,*** **Figure 13**). The interaction of sodium in Na1' is rather unstable because Ser302-Na^+ interaction is missing due to the unwound TM6 loop movement (Figure 98B, and C). This explains why saturating concentrations are necessary for triggering the inward-open state (*Cf:* ***Results,*** **Figure 67**).

This transport mechanism requires a precise, sequential binding of sodium and betaine. If a sodium ion binds to the Na1' site before betaine is in its proper position, the barrier created by the (G/A/C)ΦG loop movement would be compromised.

Therefore, the proposed sequence in the wild-type transporter is as follows:

1. A sodium ion first binds to the Na2 site (Figure 98A).
2. Next, betaine binds (Figure 98A).
3. This induces the (G/A/C)ΦG loop to close the inner cavity (Figure 98B)
4. Finally, a second sodium ion binds to the Na1' site, which triggers the final inward-open conformation (Figure 98B, and C).

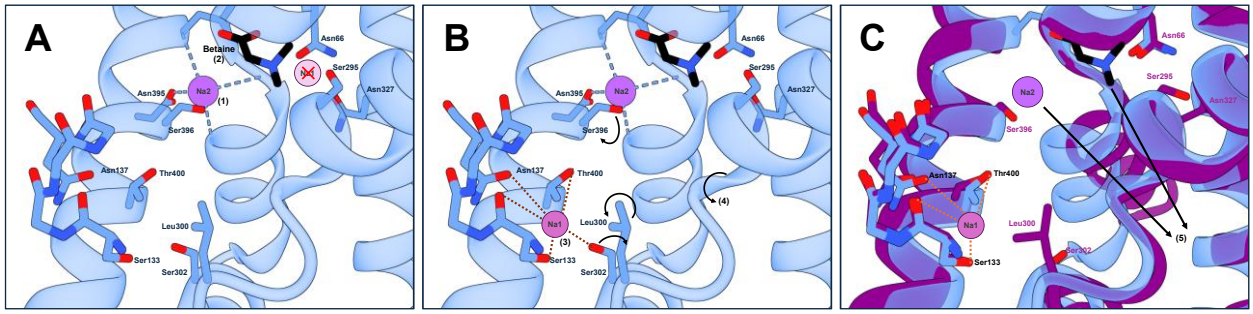

Figure 98: Betaine transport mechanism in GAT1 WT. a) sodium in the Na1 site cannot happen and the (G/A/C)ΦG motif must move towards the free GABA binding site. b) Na1 site is re-localized to Na1' but the interaction is transient because of c) rotation of Ser302 and Leu300 for sodium in Na2 and substrate release (Structure used for mechanism model: GAT1 WT inward-open structure pdb 7Y7Z in purple, inward-occluded pdb 7Y7W in blue, from Zhu et al., 2023)

In L300Q mutant the charge repulsions between methylammonium group of betaine and sodium in the Na1 can only be resolved by a three-sodium ion stoichiometry, based on the Hill factor values (*Cf:* ***Results,*** **Table 37**). This finding supports the idea that a third sodium ion binds at the Na1' site. Furthermore, the low apparent sodium affinity of the mutant in the presence of betaine (~86 mM, *Cf:* ***Results,*** **Table 37**) indicates that the Na1 site's interaction is also compromised, shifting to a new position. The constant repulsion between the sodium ion and betaine at this site, leading to repeated binding and unbinding, is consistent with the observed low transport efficiency for betaine. Therefore, sodium binding in the distant Na1'' is the limiting step in presence of betaine. Amino acids involved in Na1'' are probably the same than in Na1 (Ser295 and Asn327) but they adopt different rotamers (Figure 99B) to allow sodium binding without competing with betaine (Figure 99C(I) and (II)). This pre-conformational change of the protein would be driven most likely by high ionic forces brought by sodium and explaining why high saturated concentration are required for betaine transport in the mutant (*Cf:* ***Results,*** **Figure 67**). Finally, Na1'' could have a negatively cooperative role. Indeed, when betaine is bound, sodium in the Na1 cannot bind anymore. Consequently, high concentrations of sodium are needed to constrict TM1, 6, and 7 movements and sodium binding in the Na1'' created by the rotation of Ser295 and Asn327 (Figure 99B, C(I) and (II)). The transport cycle is limited by this energetically demanding process that, in turn, enables a third sodium ion to access the Na1' site (Figure 99D). Once bound, the ion is coordinated by a cluster of residues including Ser133, Asn137, Gln300, and Thr400. This binding event is crucial as it unlocks the (G/A/C)ΦG motif and the entire unwound TM6 helix, thereby triggering the full inward-open conformation necessary for the release of the substrate and all sodium ions into the cytoplasm.

This transport mode, which requires a high concentration of sodium, offers a potential explanation for betaine uptake during osmotic stress. In this context, the binding of sodium at the Na1" site could function as a sensor for external osmotic conditions, initiating the high-capacity transport of betaine.

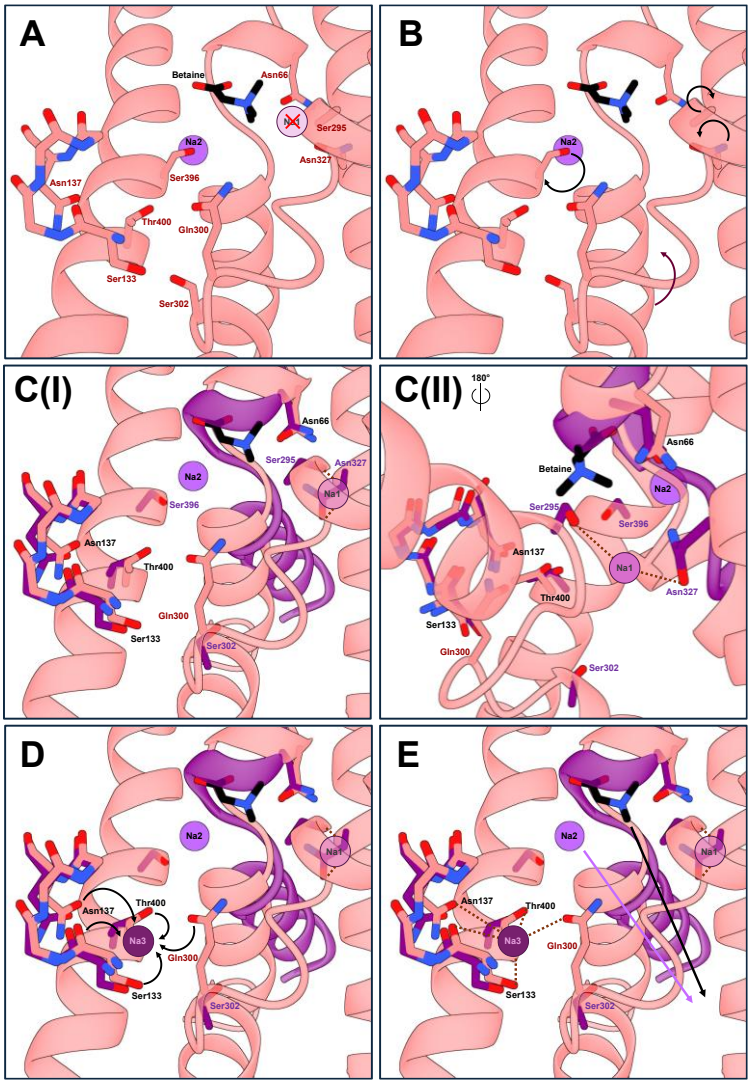

Figure 99: Betaine transport mechanism in GAT1 L300Q. a) Gln300 protects the free GABA site, and sodium in the Na1 site cannot bind. b) high ionic strength promotes a pre-conformational change of the protein, with backward movement of TM1 (maroon arrow) and rotation of some residues like Ser295, Asn327, Ser396. c) sodium in Na1'' site formed by the rotation of Ser295 and Asn327 (180° view) permits d) sodium access to the Na1' site for e) moving the unwound TM6 (1) and liberating substrate and sodium (2). (Structure used for mechanism model: AlphaFold 3 model of GAT1 L300Q in coral and inward-open structure of GAT1 WT pdb 7Y7Z, in purple from Zhu et al., 2023)

To conclude, based on their unique amino acid sequences, GAT1 WT and the L300Q mutant each employ a distinct molecular mechanism to transport substrates and respond to external conditions. These individual mechanisms can be broken down into two key elements. First, the (G/A/C)ΦG loop, which plays a crucial role in substrate interaction, recognition, and release. Differences in

this region dictate how the transporters bind and release their specific substrates. Secondly, the intricate interaction of sodium ions at three distinct sites: Na1, Na1', and Na1". The binding of these ions not only couples the transport process but also orchestrates the precise movements of the transmembrane helices that drive the transport cycle.

3. From GAT1 WT and GAT1 L300Q to BGT1 mechanisms

Tyr60 and Leu300 in GAT1 WT correspond respectively to Glu52 and Gln299 in BGT1. In GAT1, GABA is coordinated by different residues (Table 38). However, Tyr60 is the most critical one for conformational changes (Zhu et al. 2023).

	Residues or structural elements in GAT1 WT
GABA carboxylate group	N-terminus of TM1b, Gly65, Tyr140, **Na1**
GABA amino group	Tyr60, and **2 water molecules**
GABA carbons atoms	Tyr60, Tyr140, Phe294, Gly297, Ser396

Table 38: Residues or element in GAT1 WT coordinating the molecule of GABA (Zhu et al. 2023).

While GABA amino group is coordinated by Tyr60 and Gln300 in the GAT L300Q mutant (Figure 95A), it is coordinated only by Tyr60 in GAT1 (Figure 94B), and most probably, only by Gln299 in BGT1. This would explain that the affinities of GAT1 WT and BGT1 are equivalent. The transition to the inward-open conformation in GAT1 WT and the L300Q mutant is facilitated by the movement of TM1 in association with the Tyr60 residue. This mechanism is absent in BGT1, where the equivalent position is occupied by Glu52. Therefore, the inward-open conformation in BGT1 might depend only on the binding of a third sodium in the Na1' to rotate the Gln299. This interaction Gln-Na^+ in Na1', found also in GAT1 L300Q is coherent with the respective identical I_{max} of GAT mutant and BGT1.

For transporting betaine, the residues involved in Na1' of GAT1 are Ser133, Asn137, Ser302, and Thr400. In contrast, in GAT1 L300Q, Ser302 is not involved in the Na1'(Figure 96A). This confirms that there is no support from this residue in BGT1 corresponding to Cys301, residue anyway poorly interacting with sodium (P. Wang et al. 2007; Kish, Ohanessian, and Wesdemiotis 2003; Bojesen, Breindahl, and Andersen 1993). Therefore, the residues contributing to Na1' in

BGT1 would be most likely Glu126, Asn130, Gln299 and the amide groups on the backbone of these respective residues to provide octahedral sodium coordination.
For transporting betaine by GAT1 L300Q, it was shown that the drastic limiting step is re-positioning the sodium ion of the Na1 to avoid repulsion by betaine methylammonium group. Indeed, GAT1 L300Q, like BGT1, they both stick to a 3 sodium ions stoichiometry in presence of betaine meaning that in any case, sodium binds to Na1. The results from GAT1 mutant suggest that high ionic strength would promote a "pre-conformational change" in BGT1 inducing the movement of TM1, 6, and 7 resulting in the rotation of Ser294 and Asn326 (Na1 residues in BGT1) and allow a weak sodium binding facilitating the access the third sodium binding to Na1' site. This mechanism requests a high cooperativity of BGT1 with sodium, that is also supported by the data obtained for GAT1 mutant.

According to Zafra and Gimenez (2008), sodium ions are more than just co-substrates; they function as secondary structural elements that actively drive conformational changes. Indeed, when the amino acid sequence cannot allow the transport activity with only two sodium ions (like it is the case for BGT1, without Tyr60 present in GAT1), an alternative mechanism with a third sodium ion permits also to accumulate substrate. According to each single sequence polymorphism in the GABA family, the Na1' site residues were more or less conserved from BetP. For example, Cys301 is compensated by Gln299 in BGT1, while Leu300 is compensated by Ser302 in GAT1. Point mutations that occurred during evolution helped to define each transporter family and subfamily, granting them the ability to specialize in transporting specific substrates using unique molecular mechanisms.

4. Unraveling GAT1 and BGT1 Specificity: Linking Molecular Mechanism to Cellular Function

GABA transporters inherited of a standard fold and a rudimentary symporter mechanism with sodium ions from LeuT/BCCTs families. Gene duplication and single point mutations induced the differentiation between the four members GAT1, 2, 3 and BGT1. According to the present data, GAT1 and BGT1 were able to transport GABA and betaine. They also showed that within a

subfamily, transport of an identical substrate is different from one protein to another (e.g. GABA transport in GAT1 or BGT1) and transport of another substrate induces a different molecular mechanism in the same protein (e.g. betaine VS GABA transport in GAT1) due to their respective amino acid sequence polymorphism.

During preliminary cellular differentiation process, GAT1 and BGT1 were expressed identically on the cell surfaces. According to the extracellular environments (high electrolytes, counteracting solutes or compatible solutes concentrations), it promotes the activity of a specific GABA transporter, with the best adapted molecular mechanism to efficiently maintain the homeostasis required by the cells, and in a lesser extent, the organ functions.

In the CNS, GABA has a transient concentration of 1.5-3 mM when synaptically released (Hou, Strand-Amundsen, and Martinsen 2023). Thus, there is a need to regulate quickly its external concentration to avoid E/I imbalances. In GAT1, GABA and sodium binding are not rate limiting steps and explain why it is the main responsible for GABA reuptake in the neuronal intracellular space. These fast GABA reuptake characteristics, explain why GAT1 is expressed on pre-synaptic neurons. In contrast, BGT1 could support this activity, but its amino acid sequence makes the whole GABA transport mechanism highly sodium dependent. Moreover, osmotic stress associated with electrolyte fluctuations are rare in the CNS and happen only in pathological cases (Pasantes-Morales and Cruz-Rangel 2010). Therefore, the transport mechanism of BGT1 is not adapted for fast neurotransmitter reuptake in the synaptic cleft. The low presence of BGT1 on astrocytes might be a remaining expression from the evolving selection of GAT1/BGT1 in the CNS along time. On the other hand, BGT1 (according to the data obtained for GAT1 L300Q), is adapted to appreciate high concentrations of sodium and to uptake consequently betaine for protecting cells exposed to osmotic stress, explaining its high expression level on medulla cells in the kidney or hepatocytes (Figure 100).

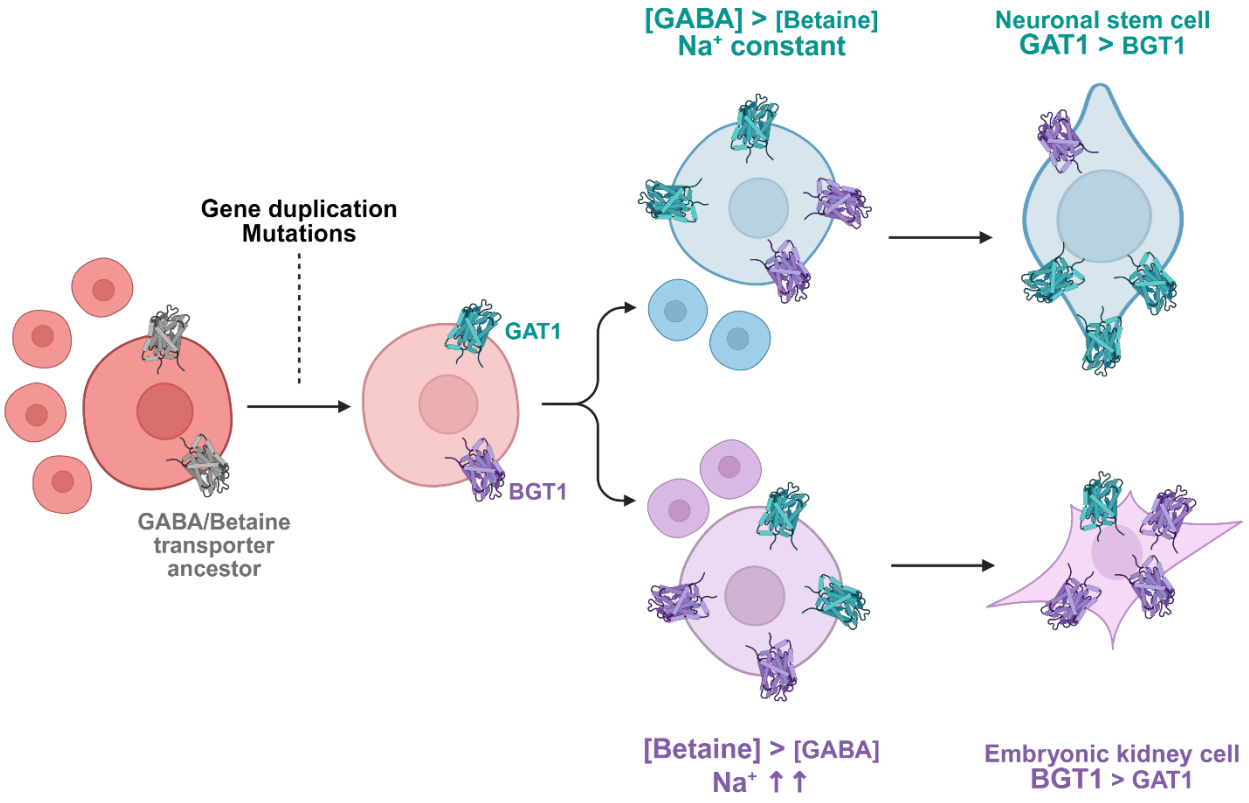

Figure 100: Selection and specification of GAT1 and BGT1 along evolution according to the extracellular environment (figure made on Biorender.com).

5. Limitations and outlooks to the mechanisms suggested

Currently, the precise mechanism driving the movement of the (G/A/C)ΦG motif remains unclear. However, a comparison between rGAT1WT and L300Q, along with data published by Focht in 2021, suggests that this movement occurs. To definitively confirm this hypothesis, clear structural data of GAT1 WT in the inward occluded state with both betaine and sodium would be necessary. Betaine might be oriented differently, with its carboxylate group potentially facing Na1 to improve coupling. However, in the WT, the affinity for betaine would be higher and the transporting data with variation of sodium should be equivalent than in presence of GABA, because sodium would not be re-localized to Na1' anymore. For the mutant, the value observed in presence of betaine would also be the same as in presence of GABA. It is unlikely that betaine has the same binding site as GABA. Mutation of the residue Met150 in BetP (corresponding to Glu52 in BGT1 and

Tyr60 in GAT1) to a glutamic acid (BGT1-like BetP mutant) showed by solid supported membrane electrophysiology that the affinity of BetP mutant for betaine decreases. Therefore, Glu52 in BGT1 (and Tyr60 in GAT1) are probably not involved in betaine binding (Klinger 2024). The mechanism release of sodium in Na1' is unknown. As it is a low affinity site, it might be that sodium biding is transient and released after the substrate and other sodium ions. This means that the (G/A/C)ΦG motif shifting must be fast, but this is coherent with its localization in the unwound flexible loop of TM6.

Na1'' created by the residue rotation of the original Na1 is a coherent hypothesis for GAT1 L300Q/BGT1 according to the charge repulsions and low sodium affinity in presence of betaine. Even if Na1 site should be conserved in all NSS family, the data suggested that interaction with sodium is substrate and proteo-dependent. Indeed, amino acid polymorphisms of proteins from a same sub-family induce single adjustments and adaptation for substrate transport according to extracellular environment.

III. Prostatic bone metastases: invasion mechanism and new pharmacological target of Brasilicardin A

A sub-line of bone metastasis from prostate cancer (PC-3M) was cultivated and analyzed by western blot and confocal microscopy to localize the presence of the heterodimer LAT1/CD98 and validate the PC-3M as further target for Brasilicardin A cytotoxicity experiments.

In prostatic bone metastasis, CD98 is detected by western blot (Figure 90) but could not be localized in any subcellular compartment by confocal microscopy (Figure 91) for different reasons. Similar to findings in transfected HEK cells, Western blot analysis of the PC-3M cell lysate likely overestimated the effective expression of CD98, suggesting that the protein is, in fact, only expressed at very low levels. Alternatively CD98 could be present in the plasma membrane, but the epitope of the antibody anti-CD98 might not recognize its ectodomain because of a "shedding" effect, commonly found for type II single-span transmembrane proteins (Lichtenthaler, Lemberg, and Fluhrer 2018). Glycosylation is a crucial step for the folding and plasma membrane trafficking of CD98 (Console et al. 2022). Also, enzymes and cellular processes related to protein glycosylation might be mis-regulated in these cells, although an increase of glycosylation branching and sialylation is observed in prostate cancers (M. He, Zhou, and Wang 2024).

LAT1 was unambiguously detected in the membrane of PC-3M (Figure 91) suggesting that the transporter unit relies on different trafficking processes than CD98 (Figure 82). A study on breast cancer cell line showed that LAT1 was transported to the plasma membrane by the scaffolding protein LLGL2, regulating basal/apical cell polarity (Saito et al. 2019). Thus, LAT1 has additional binding partners beyond CD98, which assist to shuttle the protein to the plasma membrane. Vice versa, CD98 is involved in other molecular interactions and cellular roles, like endocytosis (C. Zhang et al. 2023), cell adhesion and fusion (M. He, Zhou, and Wang 2024; Läubli and Borsig 2019; Nguyen and Merlin 2012; Dalton et al. 2007; S. Cai et al. 2005; Colin Hughes 2001; Ohkame et al. 2001).

It is known that CD98 interacts with Galectin-3 (Fort, Nicolàs-Aragó, and Palacín 2021; Dalton et al. 2007). Moreover, it was proposed that Gal-3 is an endogenous crosslinker of CD98 as less Gal-3 molecules were detected than CD98 (Dalton et al. 2007), promoting its dimerization; CD98 dimers interact then with integrins. The latter are a large family of heterodimeric α/β receptors,

that bind to extra cellular matrix biomolecules (M. He, Zhou, and Wang 2024; Läubli and Borsig 2019; Nguyen and Merlin 2012). Specifically, the cytoplasmic and transmembrane domains of CD98 bind to β1 and β3 integrins cytoplasmic tails (Nguyen and Merlin 2012; S. Cai et al. 2005). Such interaction activates the phosphorylation of phosphoinositol 3-OH kinase (PI3-K) and focal adhesion kinase (FAK), that respectively promote integrin-mediated adhesion to fibronectin and laminin (Figure 101), and focal adhesion formation (S. Cai et al. 2005; Colin Hughes 2001). Instead, when the interaction Gal-3/CD98 is interrupted, cells tend to disrupt from each other, resulting in cell death induced by detachment (Nguyen and Merlin 2012; Dalton et al. 2007).
To conclude, the crucial role of Gal-3 in dimerizing CD98 resulting to its interaction with integrin β1, induces cell fusion and adhesion.

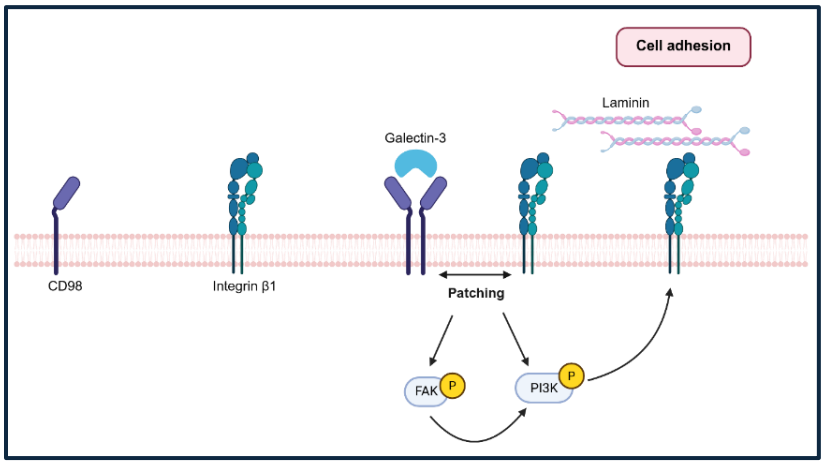

Figure 101: Molecular cascade for cellular adhesion. Galectin-3 crosslinks CD98 molecules that dimerize. The consequent interaction with integrins β1 promotes the phosphorylation of phosphoinositol 3-OH kinase (PI3K) in a dependent or independent Focal Adhesion Kinase (FAK) manner. PI3K phosphorylated activates the integrins, i.e. induces the interaction with laminin (illustration created on BioRender.com).

Galectins are either silenced or up regulated in neoplastic tissues (Sundblad, Croci, and Rabinovich 2010). Interestingly prostate refractory hormone cancer cells have the lowest histochemical staining index for Gal-3 compared to hormone dependent PC cells, and benign prostate lesions, meaning that Gal-3 is almost absent in these tissues (Merseburger et al. 2008). Prostate metastatic sites were also analyzed, and low expression of Gal-3 was also found (Ellerhorst et al. 1999). Therefore, Gal-3 misexpression appears as a phenotypic evolution of PC associated with a poor

prognosis (Merseburger et al. 2008; Ellerhorst et al. 1999). Also, recent work on PC-3 cells showed that expression of the integrins β1 favors tumoral invasion and nodules formation in other organs (Cerutti et al. 2024).

Taking together, neuroendocrine cells, characterized by a certain proteomic burden like an absence of Gal-3, low expression of CD98 full length/ectodomain, presence of integrins β1 and bony markers, tend to slowly detach from the original tumor in the prostate and start forming metastasis sites in the bones (Figure 102).

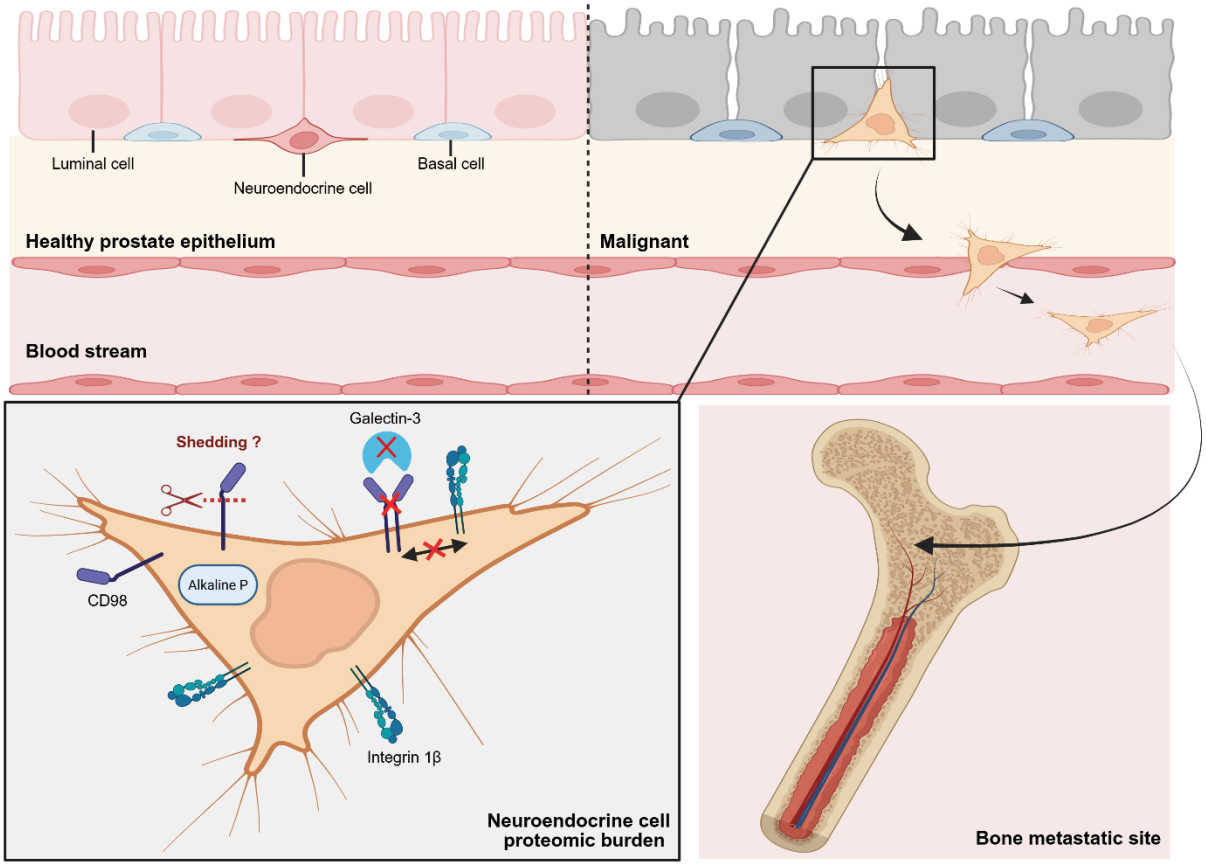

Figure 102: Model of bone colonization by malignant prostatic cancer cells after proteomic burden accumulated in neuroendocrine cells in the prostate epithelium. Low presence of CD98, hypothetic shedding on its ectodomain, absence of galectin-3 avoiding CD98 dimerization and further interactions with integrin β1, promotes cell detachment from the original tumor site. Expression of bony markers like alkaline phosphatase (Alkaline P.) favors bone invasion (illustration created on Biorender.com).

LAT1 in PC-3M specifically imports leucine in the intracellular space (Kantipudi et al. 2020) that supplies the mTOR pathway (Kahlhofer and Teis 2023; Häfliger and Charles 2019; Napolitano et al. 2017) promoting an enhanced aggressiveness of cancer cells in the bones. Although the cellular

expression of LAT1 in PC-3M cells is not homogenous (Figure 91), LAT1 enriched cells might represent an advance stage of metastatic proliferation even harder to treat in patients.

The cytotoxic effect of Brasilicardin A (BraA), a well-known LAT1 inhibitor, provides a unique advantage for developing LAT1-directed therapies. Unlike previous *in vitro* studies (Botas et al. 2021; Jung et al. 2015; Usui et al. 2006; Komaki et al. 1999), our research is the first to characterize the specific molecular species of LAT1 (as either a monomer or the LAT1/CD98 heterodimer) present in the cell population. This is a crucial finding because it may explain why the efficacy and affinity of the same LAT1 inhibitor can differ across various cell lines, depending on the specific LAT1 species they express.

IV. SLC6 and SLC7 families: an evolutionary convergence?

Heteromeric amino acid transporters (HATs) and cationic amino acid transporters (CATs) are both part of the SLC7 family. However, certain characteristics of the CATs are shared with the SLC6 family as shown on the Table 39 below.

SLC7		**SLC6**
HATs	*CATs*	
Light chain transporting unit and glycosylated heavy chain	Monomeric “light chain” with Glycosylated extracellular loop	
Sodium independent Antiporters		Sodium dependent Symporters

Table 39: Differences and similarities between SLC6 and 7 families

Indeed, SLC6 and CATs have glycosylated asparagine residues on extracellular loop as plasma membrane target signals (Jungnickel, Parker, and Newstead 2018). We hypothesized that the SLC6 and HAT transporter families share a common ancestor, leading us to investigate whether SLC6 members, similar to HATs, interact with other proteins for proper trafficking when their own trafficking signal is absent. To test this, we used genetic engineering to create a GAT1 mutant, named GAT1 ΔEL2, in which the native extracellular glycosylated loop was replaced with a 12-amino acid Glycine-Serine linker. This enables us to understand the influence of the loop structure (as Gly-Ser linkers are non-folding sequences) and glycosylation. The length was chosen so to keep the flexibility of the connected transmembrane helices although being shorter linker than the

original loop. The Figure 83 showed that GAT1 ΔEL2 aggregated before reaching the plasma membrane. Therefore, trafficking of SLC6 proteins depends exclusively on the glycosylation and length of the extracellular loops and is not counterbalanced by an interaction with a globular or glycoprotein like for LAT1. Consequently, the putative interactions between SLC6 members, specifically within the GATs family, and other proteins are more likely to regulate their transport activity at the plasma membrane rather than influencing their trafficking pathway to the cell surface. This distinction is vital for understanding the comprehensive regulatory landscape of these transporters. Indeed, compelling evidence supports this notion: syntaxin-1A, has been shown to interact with the N-terminal tail of GAT1. This interaction leads to the inhibition of substrate translocation after binding, thereby modulating the functional activity of GAT1 at the plasma membrane (D. Wang et al. 2003). This highlights a sophisticated layer of regulation where protein-protein interactions fine-tune the transport function rather than dictating the initial delivery of the transporter to its functional location (D. Wang et al. 2003).

Conclusions and outlooks

- *GABA Transporters family*

A Histidine-FLAG tag was engineered at the N-terminal of the GABA transporter 1 (GAT1) to facilitate its expression and purification. Using GnTI- cells, recombinant GAT1 (rGAT1) was successfully purified and reconstituted it into proteoliposomes. In collaboration with Despoina Kapiki (LMU, Munich), we confirmed that this reconstituted rGAT1 is both properly folded and functional, capable of binding and transporting GABA using a newly developed FRET based transport assay. This method provides a powerful platform for future studies to test lipid interactions by reconstituting WT and mutant GAT1 in liposomes with varying lipid compositions. Furthermore, we collaborated with the startup CytobodX to successfully purify rGAT1 in its neo-native environment from extracellular vesicles. Subsequent structural analysis by Cryo-EM and transport assays on these samples will provide crucial insights into the protein's behavior within a more physiological context.

In collaboration with the University of Insubria (Italy) we established seven mutants (single, double and triple) involving the residue Ser133, Leu300 and Gly403 in GAT1. They were substituted respectively by the residues of Glu, Gln, and Cys from BGT1 to understand their impact for recognition and binding of sodium ions and substrate in the GAT family

GAT1 L300Q mutant is a valuable model for characterizing BGT1 kinetics, as their transport parameters are similar in the presence of betaine. We found that the sodium affinity of both – GAT1 WT and L300Q – changes depending on the substrate (betaine or GABA) and that betaine transport requires a high external sodium concentration (>100 mM).

In GAT1 WT or L300Q, betaine constricts sodium to move into a lower-affinity site corresponding to the putative Na1' site of BetP, bacterial betaine transport structurally related to the GAT family. In WT and mutant, we interpreted the low I_{max} in presence of betaine as an extend outward open state due to the delay of sodium binding. In both cases, sodium binding in the Na1’ triggers the inward-open state.

Similar to BGT1, we demonstrated that GAT1 L300Q mutant has a 3-sodium stoichiometry for GABA and Betaine transport. With GABA, two sodium ions bind to the canonical Na1 and Na2

sites, while a third binds to the Na1' site. With betaine, a more complex mechanism is at play. We suggest that two sodium ions compete for the same Na1' site, leading to the creation of a secondary sodium site that initiates protein occlusion. Subsequently, a sodium ion binding to the Na1' site triggers the inward-open state. This mechanism is only valid at high sodium concentrations and is a structural and transport modulation that allows for betaine accumulation in response to external conditions. This transport mechanism, observed in the GAT1 WT and L300Q mutant, demonstrates how cell homeostasis is preserved during osmotic stress, where high environmental electrolyte concentrations lead to the influx of counteracting osmolytes like betaine. The conservation of this mechanism in both transporters suggests an evolutionary link. Our findings highlight the evolutionary link between GAT1 and BGT1, suggesting that gene duplication and cell differentiation led to their specialized transport specificities, with GAT1 promoting neurotransmitter uptake to prevent excitation/inhibition imbalances and BGT1 maintaining cell volume under hyperosmotic conditions.

To build on our current findings, future research should focus on a few key areas. First, we can strengthen our conclusions by performing additional current/voltage experiments on the L300Q mutant. Testing the transporter's activity in the presence of higher sodium concentrations (>150 mM) could demonstrate a faster transport cycle for betaine. This would provide crucial evidence for our hypothesis that high sodium concentrations are the key to efficient betaine transport.

Additionally, we should determine the betaine affinity of the L300Q mutant at high sodium concentrations (e.g., >100 mM). A higher affinity under these conditions would strongly support the idea that a BGT1-like mutant—and by extension, BGT1 itself—is optimized for betaine transport specifically during osmotic stress. Moreover, the transporting activity observed for the double mutants S133E/L300Q and L300Q/G403C attest that performing experiments at high sodium concentration plays a crucial role in the recognition and influx of the substrate that still need to be fully understood.

Molecular dynamics and computational studies would be necessary to screen if any other residue could be involved in a potential Na1'' binding site, combined later with mutagenesis for experimental data (by structural biology/electrophysiology) to rationalize the predictions.

In addition, these findings suggest expanding the experiments to a broader scope of the entire SLC6 Family. To understand the broader evolutionary context of this mechanism, we can perform preliminary betaine transport experiments on other members of the SLC6 family, such as dopamine

transporters (DATs), glycine transporters (GlyTs), and serotonin transporters (SerTs). These experiments would help us determine whether the ability to transport betaine during osmotic stress is a unique characteristic shared only by GABA transporters or if it is a general, conserved mechanism throughout the entire SLC6 family. Taking together, these studies would provide a more complete picture of the molecular and physiological basis of osmolyte transport and its role in cellular homeostasis**.**

- *LAT Transporter family*

The expression/purification conditions for LAT1/CD98 heterodimer found in the literature were tested and lately optimized to increase the sample yield and purity. The succession of affinity purifications on anti-FLAG/StrepTactin™ materials resulted in an improved quality of the protein sample, which now has to be up-scaled for a future structural study by cryo-EM.

For this, the transfection conditions need to be optimized to increase the quantity of cells expressing the complex. Once optimal vitrification conditions are established for the LAT1/CD98 heterodimer, the protein will be incubated with the well-described inhibitors JPH203 and BCH and vitrified. This critical step will serve to validate our vitrification methodology and confirm that we can successfully capture the transporter's structure in the presence of a known inhibitor.
Following this validation, the main experiment will proceed by incubating the protein with Brasilicardin A (BraA) and vitrifying the sample. The high potency of BraA (IC_{50} of 130 nM) is a significant advantage, as only a small amount will be needed to achieve full inhibition, making the experiment feasible even if our compound stocks are limited.
It can be speculated that, similar to JPH203, the inhibitory mechanism of BraA involves trapping the LAT1 structure in its outward-open conformational state, revealed by single-particle analysis of the vitrified sample. Determining this molecular mechanism would be a breakthrough, as it would provide a structural explanation for the drug's cellular effects. By blocking the outward-open state, BraA prevents the influx of essential amino acids like leucine. The resulting intracellular leucine deprivation is known to activate the GCN2 pathway, which, in turn, reduces metastatic cell proliferation.

We showed that LAT1 can be exported to the plasma membrane of HEK and PC-3M cells via LLGL2, instead of the canonical CD98. Therefore, LAT1 is an obligatory heterodimer for its trafficking, however its binding partners can be diverse. SLC6 transporter family has a glycosylated extracellular loop (EL2) to get to the plasma membrane. GAT1 (SLC6A1) ΔEL2 mutant was studied to see if a molecular interaction would compensate for their standard exporting signal as for the HATs (i.e. LAT1). To our knowledge, such a loop has never been engineered for studying the trafficking of SLC6 proteins. We demonstrated that this GAT1 variant aggregated in the cytoplasm. Therefore, the absence of glycosylation and standard loop is not counterbalanced with a molecular interaction in the SLC6 family, and we also hypothesized that the same mechanism operates for the cationic amino acid transporters (CATs), the monomeric counterpart of the SLC7.

We concluded by saying that GAT1 interacting partners modulate rather its transport activity, as is the case for the syntaxi-1A. Deeper structural information on the interacting complex Syntaxin-1A/GAT1 WT or variants could help in the understanding of GAT1-related diseases like epilepsy.

We validated a subline of prostatic bone metastasis cells, PC-3M, as an ideal model for our cytotoxic experiments with the inhibitor Brasilicardin A (BraA). These cells are particularly well-suited for this research because they are enriched with the amino acid transporter LAT1 on their plasma membranes. We found that the accessory protein CD98 does not co-localize with LAT1 in this cell line, likely due to its low expression. Instead, LAT1's trafficking to the plasma membrane appears to be managed by the LLGL2 protein. Furthermore, we observed that Galectin-3, a protein linked to cell adhesion, is absent in these hormone-independent prostate cancer cells and their associated metastases. We propose that the unique mis-expression of certain proteins accumulated in neuroendocrine cells could be the underlying cause of bone metastasis in the advanced stages of prostate cancer.

Recent advancements in structural biology, such as cryo-EM tomography and native mass spectrometry, would allow to solve the structures of protein complexes in their native environments and investigate metabolic processes on a cellular level. We believe that the LAT1-CD98-Galectin3-integrin β1 complex is an excellent candidate for these studies, as it could help us unravel the still-unclear mechanism behind the metastatic process.

We were able to firstly characterize the specific molecular population of a cancer subline, revealing whether it consists of LAT1 monomers or LAT1/CD98 heterodimers. This is a critical distinction because it could explain why a single inhibitor can have vastly different efficacies across various cancer cell types. Therefore, the PC-3M cells are a perfect model for determining if BraA is more effective against the LAT1 monomer or its heterodimer form. After determining the IC_{50} of BraA for the PC-3M cells, we can proceed with more detailed pharmacological experiments to test this hypothesis. Previous research has shown that transfecting cancer cells with a vector expressing Galectin-3 can decrease their proliferation rate (Merseburger et al. 2008). We hypothesize that a two-pronged therapeutic approach could be highly effective. We can treat the PC-3M cells with BraA to inhibit their leucine metabolism while transfecting them with a Galectin-3 expressing vector to limit their motility and ability to invade bone. This combination could be a promising strategy for eradicating bone metastasis *in vitro* by simultaneously targeting both metabolism and cell motility.

Bibliography

Abbott, N. Joan, Lars Rönnbäck, and Elisabeth Hansson. 2006. “Astrocyte–Endothelial Interactions at the Blood–Brain Barrier.” *Nature Reviews Neuroscience* 7(1): 41–53. doi:10.1038/nrn1824.

Ahmed, H. Shafeeq. 2025. “The Multifaceted Role of L-Type Amino Acid Transporter 1 at the Blood–Brain Barrier: Structural Implications and Therapeutic Potential.” *Molecular Neurobiology* 62(3): 3813–32. doi:10.1007/s12035-024-04506-9.

Almasi, Shekoufeh, and Yassine El Hiani. 2020. “Exploring the Therapeutic Potential of Membrane Transport Proteins: Focus on Cancer and Chemoresistance.” *Cancers* 12(6): 1624. doi:10.3390/cancers12061624.

Anderluh, Andreas, Tina Hofmaier, Enrico Klotzsch, Oliver Kudlacek, Thomas Stockner, Harald H. Sitte, and Gerhard J. Schütz. 2017. “Direct PIP2 Binding Mediates Stable Oligomer Formation of the Serotonin Transporter.” *Nature Communications* 8(1): 14089. doi:10.1038/ncomms14089.

Ängehagen, Mikael, Elinor Ben-Menachem, Lars Rönnbäck, and Elisabeth Hansson. 2003. “Novel Mechanisms of Action of Three Antiepileptic Drugs, Vigabatrin, Tiagabine, and Topiramate.” *Neurochemical Research* 28(2): 333–40. doi:10.1023/A:1022393604014.

Baumgartner, W., L. Islas, and F.J. Sigworth. 1999. “Two-Microelectrode Voltage Clamp of Xenopus Oocytes: Voltage Errors and Compensation for Local Current Flow.” *Biophysical Journal* 77(4): 1980–91. doi:10.1016/S0006-3495(99)77039-6.

Bennett, Estelle R., and Baruch I. Kanner. 1997. “The Membrane Topology of GAT-1, a (Na++ Cl−)-Coupled γ-Aminobutyric Acid Transporter from Rat Brain.” *Journal of Biological Chemistry* 272(2): 1203–10. doi:10.1074/jbc.272.2.1203.

Bennett, Estelle R., Hailing Su, and Baruch I. Kanner. 2000. “Mutation of Arginine 44 of GAT-1, a (Na+ + Cl−)-Coupled γ-Aminobutyric Acid Transporter from Rat Brain, Impairs Net Flux

but Not Exchange." *Journal of Biological Chemistry* 275(44): 34106–13. doi:10.1074/jbc.M004229200.

Bennett, Wuilliam M. 1996. "The Nephrotoxicity of Immunosuppressive Drugs." *Nephrology Dialysis Transplantation* 11(9): 1899–1901.

Ben-Yona, Assaf, Annie Bendahan, and Baruch I. Kanner. 2011. "A Glutamine Residue Conserved in the Neurotransmitter:Sodium:Symporters Is Essential for the Interaction of Chloride with the GABA Transporter GAT-1." *Journal of Biological Chemistry* 286(4): 2826–33. doi:10.1074/jbc.M110.149732.

Ben-Yona, Assaf, and Baruch I. Kanner. 2009. "Transmembrane Domain 8 of the γ-Aminobutyric Acid Transporter GAT-1 Lines a Cytoplasmic Accessibility Pathway into Its Binding Pocket." *Journal of Biological Chemistry* 284(15): 9727–32. doi:10.1074/jbc.M809423200.

Bhatt, Manan, Angela Di Iacovo, Tiziana Romanazzi, Cristina Roseti, Raffaella Cinquetti, and Elena Bossi. 2022. "The 'Www' of Xenopus Laevis Oocytes: The Why, When, What of Xenopus Laevis Oocytes in Membrane Transporters Research." *Membranes* 12(10): 927. doi:10.3390/membranes12100927.

Bhatt, Manan, Laure Gauthier-Manuel, Erika Lazzarin, Rocco Zerlotti, Christine Ziegler, Andre Bazzone, Thomas Stockner, and Elena Bossi. 2023. "A Comparative Review on the Well-Studied GAT1 and the Understudied BGT-1 in the Brain." *Frontiers in Physiology* 14: 1145973. doi:10.3389/fphys.2023.1145973.

Bhatt, Manan, Erika Lazzarin, Ana Sofia Alberto-Silva, Guido Domingo, Rocco Zerlotti, Ralph Gradisch, Andre Bazzone, et al. 2024. "Unveiling the Crucial Role of Betaine: Modulation of GABA Homeostasis via SLC6A1 Transporter (GAT1)." *Cellular and Molecular Life Sciences* 81(1): 269. doi:10.1007/s00018-024-05309-w.

Bismuth, Yona, Michael P. Kavanaugh, and Baruch I. Kanner. 1997. "Tyrosine 140 of the γ-Aminobutyric Acid Transporter GAT-1 Plays a Critical Role in Neurotransmitter

Recognition." *Journal of Biological Chemistry* 272(26): 16096–102. doi:10.1074/jbc.272.26.16096.

Bodoor, Khaldon, Rowida Almomani, Mohammad Alqudah, Yazan Haddad, and Walaa Samouri. 2020. "LAT1 (SLC7A5) Overexpression in Negative Her2 Group of Breast Cancer: A Potential Therapy Target." *Asian Pacific Journal of Cancer Prevention* 21(5): 1453–58. doi:10.31557/APJCP.2020.21.5.1453.

Bojesen, Gustav, Torben Breindahl, and Ulla N. Andersen. 1993. "On the Sodium and Lithium Ion Affinities of Some A-amino Acids." *Organic Mass Spectrometry* 28(12): 1448–52. doi:10.1002/oms.1210281215.

Bossi, Elena, Maria Serena Fabbrini, and Aldo Ceriotti. 2007. "Exogenous Protein Expression in Xenopus Oocytes." In *In Vitro Transcription and Translation Protocols*, Methods in Molecular Biology™, Humana Press, 278.

Bossi, Elena, Stefano Giovannardi, Francesca Binda, Greta Forlani, and Antonio Peres. 2002. "Role of Anion-cation Interactions on the Pre-steady-state Currents of the Rat Na^+ -Cl^- -dependent GABA Cotransporter rGAT1." *The Journal of Physiology* 541(2): 343–50. doi:10.1113/jphysiol.2001.013457.

Botas, Alma, Michael Eitel, Paul N. Schwarz, Anina Buchmann, Paula Costales, Luz Elena Núñez, Jesús Cortés, et al. 2021. "Genetic Engineering in Combination with Semi-Synthesis Leads to a New Route for Gram-Scale Production of the Immunosuppressive Natural Product Brasilicardin A." *Angewandte Chemie International Edition* 60(24): 13536–41. doi:10.1002/anie.202015852.

Breyton, Cécile, Waqas Javed, Annelise Vermot, Charles-Adrien Arnaud, Christine Hajjar, Jérôme Dupuy, Isabelle Petit-Hartlein, et al. 2019. "Assemblies of Lauryl Maltose Neopentyl Glycol (LMNG) and LMNG-Solubilized Membrane Proteins." *Biochimica et Biophysica Acta (BBA) - Biomembranes* 1861(5): 939–57. doi:10.1016/j.bbamem.2019.02.003.

Brunelle, Julie L., and Rachel Green. 2014. "Coomassie Blue Staining." In *Methods in Enzymology*, Elsevier, 161–67. doi:10.1016/B978-0-12-420119-4.00013-6.

Brunocilla, Chiara, Lara Console, Filomena Rovella, and Cesare Indiveri. 2023. “Insights into the Transport Cycle of LAT1 and Interaction with the Inhibitor JPH203.” *International Journal of Molecular Sciences* 24(4): 4042. doi:10.3390/ijms24044042.

Burg, MB, ED Kwon, and EM Peters. 1996. “Glycerophosphocholine and Betaine Counteract the Effect of Urea on Pyruvate Kinase.” *Kidney Int Suppl.* (57).

Cai, Guoqiang, Petrus S. Salonikidis, Jian Fei, Wolfgang Schwarz, Ralf Schülein, Werner Reutter, and Hua Fan. 2005. “The Role of N-glycosylation in the Stability, Trafficking and GABA-uptake of GABA-transporter 1: Terminal N-glycans Facilitate Efficient GABA-uptake Activity of the GABA Transporter.” *The FEBS Journal* 272(7): 1625–38. doi:10.1111/j.1742-4658.2005.04595.x.

Cai, Songmin, Nada Bulus, Priscila M. Fonseca-Siesser, Dong Chen, Steven K. Hanks, Ambra Pozzi, and Roy Zent. 2005. “CD98 Modulates Integrin B1 Function in Polarized Epithelial Cells.” *Journal of Cell Science* 118(5): 889–99. doi:10.1242/jcs.01674.

Carrol, A G, H J Voeller, L Sugars, and E P Gelmann. 1993. “P53 Oncogene Mutations in Three Human Prostate Cancer Cell Lines.” *Prostate* 23(2): 123–34. doi:10.1002/pros.2990230206.

Cerutti, Camilla, Serena Lucotti, Sofia T. Menendez, Nicolas Reymond, Ritu Garg, Ignacio A. Romero, Ruth Muschel, and Anne J. Ridley. 2024. “IQGAP1 and NWASP Promote Human Cancer Cell Dissemination and Metastasis by Regulating B1-Integrin via FAK and MRTF/SRF.” *Cell Reports* 43(4): 113989. doi:10.1016/j.celrep.2024.113989.

Chaiswing, Luksana, and Terry D’Oberley. 2010. “Extracellular/Microenvironmental Redox State.” *Antioxid Redox Signal.* 13(4): 449–65. doi:10.1089/ars.2009.3020.

Cherubino, Francesca, Andreea Miszner, Maria Daniela Renna, Rachele Sangaletti, Stefano Giovannardi, and Elena Bossi. 2009. “GABA Transporter Lysine 448: A Key Residue for Tricyclic Antidepressants Interaction.” *Cellular and Molecular Life Sciences* 66(23): 3797–3808. doi:10.1007/s00018-009-0153-9.

Chiduza, George N., Rachel M. Johnson, Gareth S. A. Wright, Svetlana V. Antonyuk, Stephen P. Muench, and S. Samar Hasnain. 2019. “LAT1 (SLC7A5) and CD98hc (SLC3A2) Complex Dynamics Revealed by Single-Particle Cryo-EM.” *Acta Crystallographica Section D Structural Biology* 75(7): 660–69. doi:10.1107/S2059798319009094.

Choi, Jaewoo, Tai Yin, Koichiro Shinozaki, Joshua W. Lampe, Jan F. Stevens, Lance B. Becker, and Junhwan Kim. 2018. “Comprehensive Analysis of Phospholipids in the Brain, Heart, Kidney, and Liver: Brain Phospholipids Are Least Enriched with Polyunsaturated Fatty Acids.” *Molecular and Cellular Biochemistry* 442(1–2): 187–201. doi:10.1007/s11010-017-3203-x.

Clark, Janet A. 1997. “Analysis of the Transmembrane Topology and Membrane Assembly of the GAT-1 γ-Aminobutyric Acid Transporter.” *Journal of Biological Chemistry* 272(23): 14695–704. doi:10.1074/jbc.272.23.14695.

Colin Hughes, R. 2001. “Galectins as Modulators of Cell Adhesion.” *Biochimie* 83(7): 667–76. doi:10.1016/S0300-9084(01)01289-5.

Console, Lara, Mariafrancesca Scalise, Simona Salerno, Raffaella Scanga, Deborah Giudice, Loredana De Bartolo, Annamaria Tonazzi, and Cesare Indiveri. 2022. “N-Glycosylation Is Crucial for Trafficking and Stability of SLC3A2 (CD98).” *Scientific Reports* 12(1): 14570. doi:10.1038/s41598-022-18779-4.

Copp, Brent R. 2003. “Antimycobacterial Natural Products.” *Natural Product Reports* 20(6): 535. doi:10.1039/b212154a.

Curse, Julius M, Robert E Lewis, and Huan Wang. 2004. “Immunology Guidebook.” In *Immunology Guidebook*, Elsevier Acadamic Press, 4–124.

Dalton, Paola, Helen C. Christian, Christopher W. G. Redman, Ian L. Sargent, and C. A. R. Boyd. 2007. “Membrane Trafficking of CD98 and Its Ligand Galectin 3 in BeWo Cells − Implication for Placental Cell Fusion.” *The FEBS Journal* 274(11): 2715–27. doi:10.1111/j.1742-4658.2007.05806.x.

Dash, Prakruti. 2015. “Reconnoitring the Status of Prostate Specific Antigen and Its Role in Women.” *Indian Journal of Clinical Biochemistry* 30(2): 124–33. doi:10.1007/s12291-014-0451-3.

Dayan-Alon, Oshrat, and Baruch I. Kanner. 2019. “Internal Gate Mutants of the GABA Transporter GAT1 Are Capable of Substrate Exchange.” *Neuropharmacology* 161: 107534. doi:10.1016/j.neuropharm.2019.02.016.

De Biase, D., D. Barra, F. Bossa, P. Pucci, and R.A. John. 1991. “Chemistry of the Inactivation of 4-Aminobutyrate Aminotransferase by the Antiepileptic Drug Vigabatrin.” *Journal of Biological Chemistry* 266(30): 20056–61. doi:10.1016/S0021-9258(18)54890-0.

Delauzun, Vincent, Beatrice Amigues, Anais Gaubert, Philippe Leone, Magali Grange, Laurent Gauthier, and Alain Roussel. 2020. “Extracellular Vesicles as a Platform to Study Cell-Surface Membrane Proteins.” *Methods* 180: 35–44. doi:10.1016/j.ymeth.2020.03.004.

Dickens, David, George N. Chiduza, Gareth S. A. Wright, Munir Pirmohamed, Svetlana V. Antonyuk, and S. Samar Hasnain. 2017. “Modulation of LAT1 (SLC7A5) Transporter Activity and Stability by Membrane Cholesterol.” *Scientific Reports* 7(1): 43580. doi:10.1038/srep43580.

Dodd, Joanna R., and David L. Christie. 2007. “Selective Amino Acid Substitutions Convert the Creatine Transporter to a γ-Aminobutyric Acid Transporter.” *Journal of Biological Chemistry* 282(21): 15528–33. doi:10.1074/jbc.m611705200.

Don, R.H., P. T. Cox, B.J. Wainwright, K. Baker, and J. S. Mattick. 1991. “‘Touchdown’ PCR to Circumvent Spurious Priming during Gene Amplification.” *Nucleic Acids Research* 19(14): 4008–4008. doi:10.1093/nar/19.14.4008.

Dubochet, J., J.-J. Chang, R. Freeman, J. Lepault, and A.W. McDowall. 1982. “Frozen Aqueous Suspensions.” *Ultramicroscopy* 10(1–2): 55–61. doi:10.1016/0304-3991(82)90187-5.

Einhauer, A, and A Jungbauer. 2001. “The FLAGe Peptide, a Versatile Fusion Tag for the Purification of Recombinant Proteins.” *J. Biochem. Biophys. Methods* 49: 455–65.

Ellerhorst, J, T Nguyen, D N Cooper, D Lotan, and R Lotan. 1999. “Differential Expression of Endogenous Galectin-1 and Galectin-3 in Human Prostate Cancer Cell Lines and Effects of Overexpressing Galectin-1 on Cell Phenotype.” *International Journal of Oncology* 14(2): 217–41. doi:doi.org/10.3892/ijo.14.2.217.

Endou, Hitoshi, Yoshikatsu Kanai, Kenji Tsujihara, and Kunio Saito. 2008. “Aromatic Amino Acid Derivatives and Medicinal Composition.” *US Patent 7,345,068 B2,*: 1–46.

Engler, Carola, Romy Kandzia, and Sylvestre Marillonnet. 2008. “A One Pot, One Step, Precision Cloning Method with High Throughput Capability” ed. Hany A. El-Shemy. *PLoS ONE* 3(11): e3647. doi:10.1371/journal.pone.0003647.

Fan, Hongcheng, and Fei Sun. 2022. “Developing Graphene Grids for Cryoelectron Microscopy.” *Frontiers in Molecular Biosciences* 9: 937253. doi:10.3389/fmolb.2022.937253.

Farooqui, Akhlaq A, Lloyd A Horrocks, and Tahira Farooqui. 2000. “Glycerophospholipids in Brain: Their Metabolism, Incorporation into Membranes, Functions, and Involvement in Neurological Disorders.” *Chemistry and Physics of Lipids* 106(1): 1–29. doi:10.1016/S0009-3084(00)00128-6.

Ferrada, Evandro, and Giulio Superti-Furga. 2022. “A Structure and Evolutionary-Based Classification of Solute Carriers.” *iScience* 25(10): 105096. doi:10.1016/j.isci.2022.105096.

Focht, Dorota, Caroline Neumann, Joseph Lyons, Ander Eguskiza Bilbao, Rickard Blunck, Lina Malinauskaite, Ilona O Schwarz, et al. 2021. “A Non-helical Region in Transmembrane Helix 6 of Hydrophobic Amino Acid Transporter MhsT Mediates Substrate Recognition.” *The EMBO Journal* 40(1): e105164. doi:10.15252/embj.2020105164.

Fort, Joana, Laura R. De La Ballina, Hans E. Burghardt, Carles Ferrer-Costa, Javier Turnay, Cristina Ferrer-Orta, Isabel Usón, et al. 2007. “The Structure of Human 4F2hc Ectodomain Provides a Model for Homodimerization and Electrostatic Interaction with Plasma Membrane.” *Journal of Biological Chemistry* 282(43): 31444–52. doi:10.1074/jbc.M704524200.

Fort, Joana, Adrià Nicolàs-Aragó, and Manuel Palacín. 2021. “The Ectodomains of rBAT and 4F2hc Are Fake or Orphan α-Glucosidases.” *Molecules* 26(20): 6231. doi:10.3390/molecules26206231.

Furuse, Junji, Masafumi Ikeda, Makoto Ueno, Masayuki Furukawa, Chigusa Morizane, Tetsuo Takehara, Tomohiro Nishina, et al. 2023. “Nanvuranlat, an L-Type Amino Acid Transporter (LAT1) Inhibitor for Patients with Pretreated Advanced Refractory Biliary Tract Cancer (BTC): Primary Endpoint Results of a Randomized, Double-Blind, Placebo-Controlled Phase 2 Study.” *Journal of Clinical Oncology* 41(4_suppl): 494–494. doi:10.1200/JCO.2023.41.4_suppl.494.

Gawhale, Sharadchandra, Yogita Thakare, Dipalee Malkhede, and Gajanan Chaudhari. 2014. “Study on Complex Formation of Fluorescein-p-Sulfonatocalix[4]Arene by Spectroscopic Methods.” *Optics and Photonics Journal* 04(09): 237–45. doi:10.4236/opj.2014.49024.

Giskeødegård, Guro F, Ailin Falkmo Hansen, Helena Bertilsson, Susana Villa Gonzalez, Kåre Andre Kristiansen, Per Bruheim, Svein A Mjøs, et al. 2015. “Metabolic Markers in Blood Can Separate Prostate Cancer from Benign Prostatic Hyperplasia.” *British Journal of Cancer* 113(12): 1712–19. doi:10.1038/bjc.2015.411.

Godoy-Hernandez, Albert, Amer H. Asseri, Aiden J. Purugganan, Chimari Jiko, Carol De Ram, Holger Lill, Martin Pabst, et al. 2023. “Rapid and Highly Stable Membrane Reconstitution by LAiR Enables the Study of Physiological Integral Membrane Protein Functions.” *ACS Central Science* 9(3): 494–507. doi:10.1021/acscentsci.2c01170.

Goode, Emily Archer, Ning Wang, and Jennifer Munkley. 2023. “Prostate Cancer Bone Metastases Biology and Clinical Management (Review).” *Oncology Letters* 25(4): 163. doi:10.3892/ol.2023.13749.

Goodspeed, Kimberly, Eduardo Pérez-Palma, Sumaiya Iqbal, Dominique Cooper, Annalisa Scimemi, Katrine M Johannesen, Arthur Stefanski, et al. 2020. “Current Knowledge of SLC6A1-Related Neurodevelopmental Disorders.” *Brain Communications* 2(2): fcaa170. doi:10.1093/braincomms/fcaa170.

Grossman, Tamar R, and Nathan Nelson. 2002. “Differential Effect of pH on Sodium Binding by the Various GABA Transporters Expressed in *Xenopus* Oocytes.” *FEBS Letters* 527(1–3): 125–32. doi:10.1016/S0014-5793(02)03194-0.

Guan, Bingcai, Xingjuan Chen, and Hailin Zhang. 2013. “Two Electrode Voltage Clamp.” In *Ion Channels: Methods and Protocols*, Methods in Molecular Biology, Springer Protocols.

Guastella, John, Nathan Nelson, Hannah Nelson, Linda Czyzyk, Shoshi Keynan, May C. Miedel, Norman Davidson, Henry A. Lester, and Baruch I. Kanner. 1990. “Cloning and Expression of a Rat Brain GABA Transporter.” *Science* 249(4974): 1303–6. doi:10.1126/science.1975955.

Guo, Dong-Sheng, and Yu Liu. 2014. “Supramolecular Chemistry of P-Sulfonatocalix[4]Arenes and Its Biological Applications.” *Accounts of Chemical Research* 47(7): 1925–34. doi:10.1021/ar500009g.

Gupta, Raghav, Chandan K. Das, Sujit S. Nair, Adriana Marcela Pedraza-Bermeo, Ali H. Zahalka, Natasha Kyprianou, Nina Bhardwaj, and Ashutosh K. Tewari. 2024. “From Foes to Friends: Rethinking the Role of Lymph Nodes in Prostate Cancer.” *Nature Reviews Urology* 21(11): 687–700. doi:10.1038/s41585-024-00912-9.

Häfliger, Pascal, and Roch-Philippe Charles. 2019. “The L-Type Amino Acid Transporter LAT1—An Emerging Target in Cancer.” *International Journal of Molecular Sciences* 20(10): 2428. doi:10.3390/ijms20102428.

Haining, Zhen, Nobuyuki Kawai, Keisuke Miyake, Masaki Okada, Shuichi Okubo, Xiang Zhang, Zhou Fei, and Takashi Tamiya. 2012. “Relation of LAT1/4F2hc Expression with Pathological Grade, Proliferation and Angiogenesis in Human Gliomas.” *BMC Clinical Pathology* 12(1): 4. doi:10.1186/1472-6890-12-4.

Harayama, Takeshi, and Howard Riezman. 2018. “Understanding the Diversity of Membrane Lipid Composition.” *Nature Reviews Molecular Cell Biology* 19(5): 281–96. doi:10.1038/nrm.2017.138.

Harvey, P. 2002. “Wide-Rim and Outer-Face Functionalizations of Calix[4]Arene.” *Coordination Chemistry Reviews* 233–234: 289–309. doi:10.1016/S0010-8545(02)00199-6.

Hayashi, Yutaka, Nobuyasu Matsuura, Hiroaki Toshima, Nobuya Itoh, Jun Ishikawa, Yuzuru Mikami, and Tohru Dairi. 2008. “Cloning of the Gene Cluster Responsible for the Biosynthesis of Brasilicardin A, a Unique Diterpenoid.” *The Journal of Antibiotics* 61(3): 164–74. doi:10.1038/ja.2008.126.

He, Lei, Konstandinos Vasiliou, and Daniel W Nebert. 2009. “Analysis and Update of the Human Solute Carrier (SLC) Gene Superfamily.” *Human Genomics* 3(2): 195. doi:10.1186/1479-7364-3-2-195.

He, Mengyuan, Xiangxiang Zhou, and Xin Wang. 2024. “Glycosylation: Mechanisms, Biological Functions and Clinical Implications.” *Signal Transduction and Targeted Therapy* 9(1): 194. doi:10.1038/s41392-024-01886-1.

Hou, Jie, Runar Strand-Amundsen, and Ørjan G. Martinsen. 2023. “Detection of Physiological Concentrations of GABA Using Dielectric Spectroscopy - A Pilot Study.” *Journal of Electrical Bioimpedance* 14(1): 47–52. doi:10.2478/joeb-2023-0006.

Hu, J., J. Fei, W. Reutter, and H. Fan. 2011. “Involvement of Sialic Acid in the Regulation of -Aminobutyric Acid Uptake Activity of -Aminobutyric Acid Transporter 1.” *Glycobiology* 21(3): 329–39. doi:10.1093/glycob/cwq166.

Hu, Ziwei, and Renhong Yan. 2024. “Structural Basis for the Inhibition Mechanism of LAT1-4F2hc Complex by JPH203.” *Cell Discovery* 10(1): 73. doi:10.1038/s41421-024-00697-6.

Ibrahim, George M., James T. Rutka, and O. Carter Snead. 2014. “Epilepsy Surgery in Childhood: No Longer the Treatment of Last Resort.” *Canadian Medical Association Journal* 186(13): 973–74. doi:10.1503/cmaj.140427.

Ilgü, Hüseyin, Jean-Marc Jeckelmann, David Kalbermatter, Zöhre Ucurum, Thomas Lemmin, and Dimitrios Fotiadis. 2021. “High-Resolution Structure of the Amino Acid Transporter AdiC

Reveals Insights into the Role of Water Molecules and Networks in Oligomerization and Substrate Binding." *BMC Biology* 19(1): 179. doi:10.1186/s12915-021-01102-4.

Ingólfsson, Helgi I., Timothy S. Carpenter, Harsh Bhatia, Peer-Timo Bremer, Siewert J. Marrink, and Felice C. Lightstone. 2017. "Computational Lipidomics of the Neuronal Plasma Membrane." *Biophysical Journal* 113(10): 2271–80. doi:10.1016/j.bpj.2017.10.017.

Jaremek, Adam, Mariyan J. Jeyarajah, Gargi Jaju Bhattad, and Stephen J. Renaud. 2021. "Omics Approaches to Study Formation and Function of Human Placental Syncytiotrophoblast." *Frontiers in Cell and Developmental Biology* 9: 674162. doi:10.3389/fcell.2021.674162.

Jayaraman, Kumaresan, Anand K. Das, Dino Luethi, Dániel Szöllősi, Gerhard J. Schütz, Maarten E. A. Reith, Harald H. Sitte, and Thomas Stockner. 2021. "SLC6 Transporter Oligomerization." *Journal of Neurochemistry* 157(4): 919–29. doi:10.1111/jnc.15145.

Jin, Chunhuan, Xinyu Zhou, Minhui Xu, Hiroki Okanishi, Ryuichi Ohgaki, and Yoshikatsu Kanai. 2025. "Pharmacological and Structural Insights into Nanvuranlat, a Selective LAT1 (SLC7A5) Inhibitor, and Its N-Acetyl Metabolite with Implications for Cancer Therapy." *Scientific Reports* 15(1): 2903. doi:10.1038/s41598-025-87522-6.

Jung, Michael E., Brian T. Chamberlain, Pierre Koch, and Kayvan R. Niazi. 2015. "Synthesis and Bioactivity of a Brasilicardin A Analogue Featuring a Simplified Core." *Organic Letters* 17(14): 3608–11. doi:10.1021/acs.orglett.5b01712.

Jung, Michael E., and Pierre Koch. 2011. "An Efficient Synthesis of the Protected Carbohydrate Moiety of Brasilicardin A." *Organic Letters* 13(14): 3710–13. doi:10.1021/ol2013704.

Jungnickel, Katharina E. J., Joanne L. Parker, and Simon Newstead. 2018. "Structural Basis for Amino Acid Transport by the CAT Family of SLC7 Transporters." *Nature Communications* 9(1): 550. doi:10.1038/s41467-018-03066-6.

Kahlhofer, Jennifer, and David Teis. 2023. "The Human LAT1–4F2hc (SLC7A5–SLC3A2) Transporter Complex: Physiological and Pathophysiological Implications." *Basic & Clinical Pharmacology & Toxicology* 133(5): 459–72. doi:10.1111/bcpt.13821.

Kaira. 2010. “CD98 Expression Is Associated with the Grade of Malignancy in Thymic Epithelial Tumors.” *Oncology Reports*. doi:10.3892/or_00000931.

Kanner, Baruch I., Annie Bendahan, Shifrah Pantanowitz, and Hailing Su. 1994. “The Number of Amino Acid Residues in Hydrophilic Loops Connecting Transmembrane Domains of the GABA Transporter GAT-1 Is Critical for Its Function.” *FEBS Letters* 356(2–3): 191–94. doi:10.1016/0014-5793(94)01255-5.

Kantipudi, Satish, Jean-Marc Jeckelmann, Zöhre Ucurum, Patrick D. Bosshart, and Dimitrios Fotiadis. 2020. “The Heavy Chain 4F2hc Modulates the Substrate Affinity and Specificity of the Light Chains LAT1 and LAT2.” *International Journal of Molecular Sciences* 21(20): 7573. doi:10.3390/ijms21207573.

Kempson, Stephen A., Yun Zhou, and Niels C. Danbolt. 2014. “The Betaine/GABA Transporter and Betaine: Roles in Brain, Kidney, and Liver.” *Frontiers in Physiology* 5. doi:10.3389/fphys.2014.00159.

Keshet, Gilmor I., Annie Bendahan, Hailing Su, Sela Mager, Henry A. Lester, and Baruch I. Kanner. 1995. “Glutamate-101 Is Critical for the Function of the Sodium and Chloride-coupled GABA Transporter GAT-1.” *FEBS Letters* 371(1): 39–42. doi:10.1016/0014-5793(95)00859-8.

Khafizov, Kamil, Camilo Perez, Caroline Koshy, Matthias Quick, Klaus Fendler, Christine Ziegler, and Lucy R. Forrest. 2012. “Investigation of the Sodium-Binding Sites in the Sodium-Coupled Betaine Transporter BetP.” *Proceedings of the National Academy of Sciences* 109(44). doi:10.1073/pnas.1209039109.

Kickinger, Stefanie, Eva Hellsberg, Bente Frølund, Arne Schousboe, Gerhard F. Ecker, and Petrine Wellendorph. 2019. “Structural and Molecular Aspects of Betaine-GABA Transporter 1 (BGT1) and Its Relation to Brain Function.” *Neuropharmacology* 161: 107644. doi:10.1016/j.neuropharm.2019.05.021.

Kish, Michelle M., Gilles Ohanessian, and Chrys Wesdemiotis. 2003. “The Na+ Affinities of α-Amino Acids: Side-Chain Substituent Effects.” *International Journal of Mass Spectrometry* 227(3): 509–24. doi:10.1016/S1387-3806(03)00082-4.

Klinger, Sebastian. 2024. “Investigation of Sodium/Substrate Interactions in BetP Mutant M150E and Expression/Purification of the Human Amino Acid Transporter LAT1 for Rational Drug Design Studies.” University of Regensburg.

Komaki, Hisayuki, Akira Nemoto, Yasushi Tanaka, Hiroaki Takagi, Katsukiyo Yazawa, Yuzuru Mikami, Hideyuki Shigemori, et al. 1999. “Brasilicardin A, a New Terpenoid Antibiotic from Pathogenic Nocardia Brasiliensis: Fermentation, Isolation and Biological Activity.” *The Journal of Antibiotics* 52(1): 13–19. doi:10.7164/antibiotics.52.13.

Krämer, Reinhard. 2009. “Osmosensing and Osmosignaling in Corynebacterium Glutamicum.” *Amino Acids* 37(3): 487–97. doi:10.1007/s00726-009-0271-6.

Krämer, Reinhard, and Christine Ziegler. 2009. “Regulative Interactions of the Osmosensing C-Terminal Domain in the Trimeric Glycine Betaine Transporter BetP from Corynebacterium Glutamicum.” *Biol Chem* 8(390): 685–91. doi:doi:%2010.1515/BC.2009.068.

La Verde, Valentina, Paola Dominici, and Alessandra Astegno. 2017. “Determination of Hydrodynamic Radius of Proteins by Size Exclusion Chromatography.” *BIO-PROTOCOL* 7(8). doi:10.21769/BioProtoc.2230.

Läubli, Heinz, and Lubor Borsig. 2019. “Altered Cell Adhesion and Glycosylation Promote Cancer Immune Suppression and Metastasis.” *Frontiers in Immunology* 10: 2120. doi:10.3389/fimmu.2019.02120.

Lee, Yongchan, Chunhuan Jin, Ryuichi Ohgaki, Minhui Xu, Satoshi Ogasawara, Rangana Warshamanage, Keitaro Yamashita, et al. 2023. “Structural Basis of Anticancer Drug Recognition and Amino Acid Transport by LAT1.” doi:10.1101/2023.12.03.567112.

Lee, Yongchan, Pattama Wiriyasermkul, Chunhuan Jin, Lili Quan, Ryuichi Ohgaki, Suguru Okuda, Tsukasa Kusakizako, et al. 2019. “Cryo-EM Structure of the Human L-Type Amino Acid

Transporter 1 in Complex with Glycoprotein CD98hc." *Nature Structural & Molecular Biology* 26(6): 510–17. doi:10.1038/s41594-019-0237-7.

Lehre, A.C., N.M. Rowley, Y. Zhou, S. Holmseth, C. Guo, T. Holen, R. Hua, et al. 2011. "Deletion of the Betaine–GABA Transporter (BGT1; Slc6a12) Gene Does Not Affect Seizure Thresholds of Adult Mice." *Epilepsy Research* 95(1–2): 70–81. doi:10.1016/j.eplepsyres.2011.02.014.

Lei, Zi-Ning, Qin Tian, Qiu-Xu Teng, John N. D. Wurpel, Leli Zeng, Yihang Pan, and Zhe-Sheng Chen. 2023. "Understanding and Targeting Resistance Mechanisms in Cancer." *MedComm* 4(3): e265. doi:10.1002/mco2.265.

LeVine, Michael V., Daniel S. Terry, George Khelashvili, Zarek S. Siegel, Matthias Quick, Jonathan A. Javitch, Scott C. Blanchard, and Harel Weinstein. 2019. "The Allosteric Mechanism of Substrate-Specific Transport in SLC6 Is Mediated by a Volumetric Sensor." *Proceedings of the National Academy of Sciences* 116(32): 15947–56. doi:10.1073/pnas.1903020116.

Lichtenthaler, Stefan F, Marius K Lemberg, and Regina Fluhrer. 2018. "Proteolytic Ectodomain Shedding of Membrane Proteins in Mammals—Hardware, Concepts, and Recent Developments." *The EMBO Journal* 37(15): e99456. doi:10.15252/embj.201899456.

Lilja, Hans, Jörgen Oldbring, Gunnar Rannevik, and Carl-Bertil Laurell. 1987. "Seminal Vesicle-Secreted Proteins and Their Reactions during Gelation and Liquefaction of Human Semen." *Journal of Clinical Investigation* 80: 281–85.

Liu, Q.R., B. López-Corcuera, S. Mandiyan, H. Nelson, and N. Nelson. 1993. "Molecular Characterization of Four Pharmacologically Distinct Gamma-Aminobutyric Acid Transporters in Mouse Brain [Corrected]." *Journal of Biological Chemistry* 268(3): 2106–12. doi:10.1016/S0021-9258(18)53968-5.

Liu, Xiaodong. 2019. "ABC Family Transporters." In *Drug Transporters in Drug Disposition, Effects and Toxicity*, Advances in Experimental Medicine and Biology, eds. Xiaodong Liu

and Guoyu Pan. Singapore: Springer Singapore, 13–100. doi:10.1007/978-981-13-7647-4_2.

Liu, Yanhong, Ursula Eckstein-Ludwig, Jian Fei, and Wolfgang Schwarz. 1998. “Effect of Mutation of Glycosylation Sites on the Na+ Dependence of Steady-State and Transient Currents Generated by the Neuronal GABA Transporter.” *Biochimica et Biophysica Acta (BBA) - Biomembranes* 1415(1): 246–54. doi:10.1016.

Longo, Patti A., Jennifer M. Kavran, Min-Sung Kim, and Daniel J. Leahy. 2013. “Transient Mammalian Cell Transfection with Polyethylenimine (PEI).” In *Methods in Enzymology*, Elsevier, 227–40. doi:10.1016/B978-0-12-418687-3.00018-5.

MacAulay, Nanna, Annie Bendahan, Claus Juul Loland, Thomas Zeuthen, Baruch I. Kanner, and Ulrik Gether. 2001. “Engineered Zn2+ Switches in the γ-Aminobutyric Acid (GABA) Transporter-1.” *Journal of Biological Chemistry* 276(44): 40476–85. doi:10.1074/jbc.M105578200.

Malinauskaite, Lina, Matthias Quick, Linda Reinhard, Joseph A Lyons, Hideaki Yano, Jonathan A Javitch, and Poul Nissen. 2014. “A Mechanism for Intracellular Release of Na+ by Neurotransmitter/Sodium Symporters.” *Nature Structural & Molecular Biology* 21(11): 1006–12. doi:10.1038/nsmb.2894.

Malinauskaite, Lina, Saida Said, Caglanur Sahin, Julie Grouleff, Azadeh Shahsavar, Henriette Bjerregaard, Pernille Noer, et al. 2016. “A Conserved Leucine Occupies the Empty Substrate Site of LeuT in the Na+-Free Return State.” *Nature Communications* 7(1): 11673. doi:10.1038/ncomms11673.

Mari, S. A., A. Soragna, M. Castagna, M. Santacroce, C. Perego, E. Bossi, A. Peres, and V. F. Sacchi. 2006. “Role of the Conserved Glutamine 291 in the Rat γ-Aminobutyric Acid Transporter rGAT-1.” *Cellular and Molecular Life Sciences* 63(1): 100. doi:10.1007/s00018-005-5512-6.

Marillonnet, Sylvestre, and Ramona Grützner. 2020. “Synthetic DNA Assembly Using Golden Gate Cloning and the Hierarchical Modular Cloning Pipeline.” *Current Protocols in Molecular Biology* 130(1): e115. doi:10.1002/cpmb.115.

Martinac, Boris. 2022. “2021 Nobel Prize for Mechanosensory Transduction.” *Biophysical Reviews* 14(1): 15–20. doi:10.1007/s12551-022-00935-9.

Matskevitch, Ioulia, Carsten A. Wagner, Carola Stegen, Stefan Bröer, Birgitta Noll, Teut Risler, H. Moo Kwon, et al. 1999. “Functional Characterization of the Betaine/γ-Aminobutyric Acid Transporter BGT-1 Expressed in Xenopus Oocytes.” *Journal of Biological Chemistry* 274(24): 16709–16. doi:10.1074/jbc.274.24.16709.

Meinild, Anne-Kristine, and Ian C. Forster. 2012. “Using Lithium to Probe Sequential Cation Interactions with GAT1.” *American Journal of Physiology-Cell Physiology* 302(11): C1661–75. doi:10.1152/ajpcell.00446.2011.

Merseburger, Axel S., Mario W. Kramer, Jörg Hennenlotter, Perikles Simon, Judith Knapp, Jörg T. Hartmann, Arnulf Stenzl, Jürgen Serth, and Markus A. Kuczyk. 2008. “Involvement of Decreased Galectin-3 Expression in the Pathogenesis and Progression of Prostate Cancer.” *The Prostate* 68(1): 72–77. doi:10.1002/pros.20688.

Meury, Marcel, Meritxell Costa, Daniel Harder, Mirko Stauffer, Jean-Marc Jeckelmann, Béla Brühlmann, Albert Rosell, et al. 2014. “Detergent-Induced Stabilization and Improved 3D Map of the Human Heteromeric Amino Acid Transporter 4F2hc-LAT2” ed. Dmitri Boudko. *PLoS ONE* 9(10): e109882. doi:10.1371/journal.pone.0109882.

Monod, Jacques. 1970. *Le Hasard et La Necessité*.

Motiwala, Zenia, Nanda Gowtham Aduri, Hamidreza Shaye, Gye Won Han, Jordy Homing Lam, Vsevolod Katritch, Vadim Cherezov, and Cornelius Gati. 2022. “Structural Basis of GABA Reuptake Inhibition.” *Nature* 606(7915): 820–26. doi:10.1038/s41586-022-04814-x.

Munn, David H., Madhav D. Sharma, Babak Baban, Heather P. Harding, Yuhong Zhang, David Ron, and Andrew L. Mellor. 2005. “GCN2 Kinase in T Cells Mediates Proliferative Arrest

and Anergy Induction in Response to Indoleamine 2,3-Dioxygenase." *Immunity* 22(5): 633–42. doi:10.1016/j.immuni.2005.03.013.

Mycielska, Maria E., Ameet Patel, Nahit Rizaner, Maciej P. Mazurek, Hector Keun, Anup Patel, Vadivel Ganapathy, and Mustafa B. A. Djamgoz. 2009. "Citrate Transport and Metabolism in Mammalian Cells: Prostate Epithelial Cells and Prostate Cancer." *BioEssays* 31(1): 10–20. doi:10.1002/bies.080137.

Napolitano, Lara, Michele Galluccio, Mariafrancesca Scalise, Chiara Parravicini, Luca Palazzolo, Ivano Eberini, and Cesare Indiveri. 2017. "Novel Insights into the Transport Mechanism of the Human Amino Acid Transporter LAT1 (SLC7A5). Probing Critical Residues for Substrate Translocation." *Biochimica et Biophysica Acta (BBA) - General Subjects* 1861(4): 727–36. doi:10.1016/j.bbagen.2017.01.013.

Napolitano, Lara, Mariafrancesca Scalise, Michele Galluccio, Lorena Pochini, Leticia Maria Albanese, and Cesare Indiveri. 2015. "LAT1 Is the Transport Competent Unit of the LAT1/CD98 Heterodimeric Amino Acid Transporter." *The International Journal of Biochemistry & Cell Biology* 67: 25–33. doi:10.1016/j.biocel.2015.08.004.

Nevitt, Sarah J, Anthony G Marson, and Catrin Tudur Smith. 2018. "Carbamazepine versus Phenobarbitone Monotherapy for Epilepsy: An Individual Participant Data Review" ed. Cochrane Epilepsy Group. *Cochrane Database of Systematic Reviews* 2018(10). doi:10.1002/14651858.CD001904.pub4.

Nguyen, Hang Thi Thu, and Didier Merlin. 2012. "Homeostatic and Innate Immune Responses: Role of the Transmembrane Glycoprotein CD98." *Cellular and Molecular Life Sciences* 69(18): 3015–26. doi:10.1007/s00018-012-0963-z.

Niman, Scott W., Roberta Buono, David A. Fruman, and Christopher D. Vanderwal. 2023. "Synthesis of a Complex Brasilicardin Analogue Utilizing a Cobalt-Catalyzed MHAT-Induced Radical Bicyclization Reaction." *Organic Letters* 25(19): 3451–55. doi:10.1021/acs.orglett.3c01019.

Nishikubo, Kou, Ryuichi Ohgaki, Xingming Liu, Hiroki Okanishi, Minhui Xu, Hitoshi Endou, and Yoshikatsu Kanai. 2023. “Combination Effects of Amino Acid Transporter LAT1 Inhibitor Nanvuranlat and Cytotoxic Anticancer Drug Gemcitabine on Pancreatic and Biliary Tract Cancer Cells.” *Cancer Cell International* 23(1): 116. doi:10.1186/s12935-023-02957-z.

Norrsell, Ragnar, Monika Bauden, Roland Andersson, and Daniel Ansari. 2024. “L-Type Amino Acid Transporter 1 as a Therapeutic Target in Pancreatic Cancer.” *Cancer Control* 31: 10732748241251583. doi:10.1177/10732748241251583.

Noskov, Sergei Y., and Benoît Roux. 2008. “Control of Ion Selectivity in LeuT: Two Na+ Binding Sites with Two Different Mechanisms.” *Journal of Molecular Biology* 377(3): 804–18. doi:10.1016/j.jmb.2008.01.015.

Ochoa-de La Paz, Lenin D., Rosario Gulias-Cañizo, Estela D´Abril Ruíz-Leyja, Hugo Sánchez-Castillo, and Jorge Parodí. 2021. “The Role of GABA Neurotransmitter in the Human Central Nervous System, Physiology, and Pathophysiology.” *Revista Mexicana de Neurociencia* 22(2): 5355. doi:10.24875/RMN.20000050.

Ohkame, Hirohisa, Hideki Masuda, Yukimoto Ishii, and Yoshikatsu Kanai. 2001. “Expression of L-type Amino Acid Transporter 1 (LAT1) and 4F2 Heavy Chain (4F2hc) in Liver Tumor Lesions of Rat Models.” *Journal of Surgical Oncology* 78(4): 265–72. doi:10.1002/jso.1165.

Okano, Naohiro, Fumio Nagashima, Mariko Nishioka, Haruki Kusaka, Kouji Yamamoto, and Junji Furuse. 2024. “Treatment Outcomes by Stratifying the N-Acetyl Transferase 2 Phenotype in Pre-Treated Patients with Advanced Refractory Biliary Tract Cancer Treated with Nanvuranlat, an L-Type Amino Acid Transporter Inhibitor: An Ad-Hoc Analysis of a Randomized, Double-Blind, Placebo-Controlled Phase 2 Study.” *Journal of Clinical Oncology* 42(3_suppl): 483–483. doi:10.1200/JCO.2024.42.3_suppl.483.

Okano, Naohiro, Daisuke Naruge, Kirio Kawai, Takaaki Kobayashi, Fumio Nagashima, Hitoshi Endou, and Junji Furuse. 2020. “First-in-Human Phase I Study of JPH203, an L-Type

Amino Acid Transporter 1 Inhibitor, in Patients with Advanced Solid Tumors." *Investigational New Drugs* 38(5): 1495–1506. doi:10.1007/s10637-020-00924-3.

Ortega, Arturo, and Arne Schousboe, eds. 2017. 16 *Glial Amino Acid Transporters*. Cham: Springer International Publishing. doi:10.1007/978-3-319-55769-4.

Otsuki, Hideo, Toru Kimura, Takashi Yamaga, Takeo Kosaka, Jun-ichi Suehiro, and Hiroyuki Sakurai. 2017. "Prostate Cancer Cells in Different Androgen Receptor Status Employ Different Leucine Transporters." *The Prostate* 77(2): 222–33. doi:10.1002/pros.23263.

Pantelic, Radosav S., Jannik C. Meyer, Ute Kaiser, and Henning Stahlberg. 2012. "The Application of Graphene as a Sample Support in Transmission Electron Microscopy." *Solid State Communications* 152(15): 1375–82. doi:10.1016/j.ssc.2012.04.038.

Pasantes-Morales, H., and S. Cruz-Rangel. 2010. "Brain Volume Regulation: Osmolytes and Aquaporin Perspectives." *Neuroscience* 168(4): 871–84. doi:10.1016/j.neuroscience.2009.11.074.

Patel, Avinash, Daniel Toso, Audrey Litvak, and Eva Nogales. 2021. "Efficient Graphene Oxide Coating Improves Cryo-EM Sample Preparation and Data Collection from Tilted Grids." doi:10.1101/2021.03.08.434344.

Perez, Camilo, Kamil Khafizov, Lucy R Forrest, Reinhard Krämer, and Christine Ziegler. 2011. "The Role of Trimerization in the Osmoregulated Betaine Transporter BetP." *EMBO reports* 12(8): 804–10. doi:10.1038/embor.2011.102.

Perez, Camilo, Caroline Koshy, Susanne Ressl, Sascha Nicklisch, Reinhard Krämer, and Christine Ziegler. 2011. "Substrate Specificity and Ion Coupling in the Na^+ /Betaine Symporter BetP: Structure and Function of BetP-G153D." *The EMBO Journal* 30(7): 1221–29. doi:10.1038/emboj.2011.46.

Perez, Camilo, Caroline Koshy, Özkan Yildiz, and Christine Ziegler. 2012. "Alternating-Access Mechanism in Conformationally Asymmetric Trimers of the Betaine Transporter BetP." *Nature* 490(7418): 126–30. doi:10.1038/nature11403.

Ponzoni, Luca, She Zhang, Mary Hongying Cheng, and Ivet Bahar. 2018. “Shared Dynamics of LeuT Superfamily Members and Allosteric Differentiation by Structural Irregularities and Multimerization.” *Philosophical Transactions of the Royal Society B: Biological Sciences* 373(1749): 20170177. doi:10.1098/rstb.2017.0177.

Puris, Elena, Mikko Gynther, Seppo Auriola, and Kristiina M. Huttunen. 2020. “L-Type Amino Acid Transporter 1 as a Target for Drug Delivery.” *Pharmaceutical Research* 37(5): 88. doi:10.1007/s11095-020-02826-8.

Rebello, Richard J., Christoph Oing, Karen E. Knudsen, Stacy Loeb, David C. Johnson, Robert E. Reiter, Silke Gillessen, Theodorus Van Der Kwast, and Robert G. Bristow. 2021. “Prostate Cancer.” *Nature Reviews Disease Primers* 7(1): 9. doi:10.1038/s41572-020-00243-0.

Rii, Junryo, Shinichi Sakamoto, Atsushi Mizokami, Minhui Xu, Ayumi Fujimoto, Shinpei Saito, Hidekazu Koike, et al. 2024. “L-type Amino Acid Transporter 1 Inhibitor JPH203 Prevents the Growth of Cabazitaxel-resistant Prostate Cancer by Inhibiting Cyclin-dependent Kinase Activity.” *Cancer Science* 115(3): 937–53. doi:10.1111/cas.16062.

Rodriguez, Carlos F., Paloma Escudero-Bravo, Lucía Díaz, Paola Bartoccioni, Carmen García-Martín, Joan G. Gilabert, Jasminka Boskovic, et al. 2021. “Structural Basis for Substrate Specificity of Heteromeric Transporters of Neutral Amino Acids.” *Proceedings of the National Academy of Sciences* 118(49): e2113573118. doi:10.1073/pnas.2113573118.

Rosell, Albert, Marcel Meury, Elena Álvarez-Marimon, Meritxell Costa, Laura Pérez-Cano, Antonio Zorzano, Juan Fernández-Recio, Manuel Palacín, and Dimitrios Fotiadis. 2014. “Structural Bases for the Interaction and Stabilization of the Human Amino Acid Transporter LAT2 with Its Ancillary Protein 4F2hc.” *Proceedings of the National Academy of Sciences* 111(8): 2966–71. doi:10.1073/pnas.1323779111.

Rosenberg, Alex, and Baruch I. Kanner. 2008. “The Substrates of the γ-Aminobutyric Acid Transporter GAT-1 Induce Structural Rearrangements around the Interface of Transmembrane Domains 1 and 6.” *Journal of Biological Chemistry* 283(21): 14376–83. doi:10.1074/jbc.M801093200.

Russell, Pamela J., Paul Jackson, and Elizabeth A. Kingsley. 2003. *Prostate Cancer Methods and Protocols*. Totowa, NJ: Springer New York. doi:10.1385/1592593720.

Saito, Yasuhiro, Lewyn Li, Etienne Coyaud, Augustin Luna, Chris Sander, Brian Raught, John M. Asara, Myles Brown, and Senthil K. Muthuswamy. 2019. "LLGL2 Rescues Nutrient Stress by Promoting Leucine Uptake in ER+ Breast Cancer." *Nature* 569(7755): 275–79. doi:10.1038/s41586-019-1126-2.

Sakata, Takeshi, Golam Ferdous, Tomoko Tsuruta, Takefumi Satoh, Shiro Baba, Tomoko Muto, Akinori Ueno, et al. 2009. "L-type Amino-acid Transporter 1 as a Novel Biomarker for High-grade Malignancy in Prostate Cancer." *Pathology International* 59(1): 7–18. doi:10.1111/j.1440-1827.2008.02319.x.

Scalise, Mariafrancesca, Michele Galluccio, Lara Console, Lorena Pochini, and Cesare Indiveri. 2018. "The Human SLC7A5 (LAT1): The Intriguing Histidine/Large Neutral Amino Acid Transporter and Its Relevance to Human Health." *Frontiers in Chemistry* 6: 243. doi:10.3389/fchem.2018.00243.

Schmidt, Dieter, and Wolfgang Löscher. 2005. "Drug Resistance in Epilepsy: Putative Neurobiologic and Clinical Mechanisms." *Epilepsia* 46(6): 858–77. doi:10.1111/j.1528-1167.2005.54904.x.

Scholze, Petra, Michael Freissmuth, and Harald H. Sitte. 2002. "Mutations within an Intramembrane Leucine Heptad Repeat Disrupt Oligomer Formation of the Rat GABA Transporter 1." *Journal of Biological Chemistry* 277(46): 43682–90. doi:10.1074/jbc.M205602200.

Schousboe, Arne, Orla M. Larsson, Alan Sarup, and H. Steve White. 2004. "Role of the Betaine/GABA Transporter (BGT-1/GAT2) for the Control of Epilepsy." *European Journal of Pharmacology* 500(1–3): 281–87. doi:10.1016/j.ejphar.2004.07.032.

Schweikhard, Eva S., Stephen A. Kempson, Christine Ziegler, and Birgitta C. Burckhardt. 2014. "Mutation of a Single Threonine in the Cytoplasmic NH_2 Terminus Disrupts Trafficking of

Renal Betaine-GABA Transporter 1 during Hypertonic Stress." *American Journal of Physiology-Renal Physiology* 307(1): F107–15. doi:10.1152/ajprenal.00085.2014.

Schweikhard, Eva S., Birgitta C. Burckhardt, Friedericke Joos, Cristina Fenollar-Ferrer, Lucy R. Forrest, Stephen A. Kempson, and Christine Ziegler. 2015. "Role of N-Glycosylation in Renal Betaine Transport." *Biochemical Journal* 470(2): 169–79. doi:10.1042/BJ20131031.

SEC Principles and Methods, Handbook. 2020. Cytiva.

Seidel, Stefan, Ernst A. Singer, Herwig Just, Hesso Farhan, Petra Scholze, Oliver Kudlacek, Marion Holy, et al. 2005. "Amphetamines Take Two to Tango: An Oligomer-Based Counter-Transport Model of Neurotransmitter Transport Explores the Amphetamine Action." *Molecular Pharmacology* 67(1): 140–51. doi:10.1124/mol.67.1.140.

Sente, Andrija, Rooma Desai, Katerina Naydenova, Tomas Malinauskas, Youssef Jounaidi, Jonas Miehling, Xiaojuan Zhou, et al. 2022. "Differential Assembly Diversifies GABAA Receptor Structures and Signalling." *Nature* 604(7904): 190–94. doi:10.1038/s41586-022-04517-3.

Sheng, Qi, Xiao-Yu Wu, Xinyi Xu, Xiaoming Tan, Zhimin Li, and Bin Zhang. 2021. "Production of L-Glutamate Family Amino Acids in Corynebacterium Glutamicum: Physiological Mechanism, Genetic Modulation, and Prospects." *Synthetic and systems biotechnology* 6(4): 302–25. doi:DOI:%2010.1016/j.synbio.2021.09.005.

Shouffani, A, and B I Kanner. 1990. "Cholesterol Is Required for the Reconstruction of the Sodium- and Chloride-Coupled, Gamma-Aminobutyric Acid Transporter from Rat Brain." *Journal of Biological Chemistry* 265(11): 6002–8. doi:10.1016/S0021-9258(19)39282-8.

Sigel, Erwin, and Michael E. Steinmann. 2012. "Structure, Function, and Modulation of GABAA Receptors." *Journal of Biological Chemistry* 287(48): 40224–31. doi:10.1074/jbc.R112.386664.

Singh, Natesh, and Gerhard F. Ecker. 2018. “Insights into the Structure, Function, and Ligand Discovery of the Large Neutral Amino Acid Transporter 1, LAT1.” *International Journal of Molecular Sciences* 19(5): 1278. doi:10.3390/ijms19051278.

Sitte, Harald H., and Michael Freissmuth, eds. 2006. *Neurotransmitter Transporters*. Berlin, Heidelberg: Springer-Verlag Berlin Heidelberg. doi:10.1007/3-540-29784-7.

Stolzenberg, Sebastian, Zheng Li, Matthias Quick, Lina Malinauskaite, Poul Nissen, Harel Weinstein, Jonathan A. Javitch, and Lei Shi. 2017. “The Role of Transmembrane Segment 5 (TM5) in Na2 Release and the Conformational Transition of Neurotransmitter:Sodium Symporters toward the Inward-Open State.” *Journal of Biological Chemistry* 292(18): 7372–84. doi:10.1074/jbc.M116.757153.

Storici, Paola, Guido Capitani, Daniela De Biase, Markus Moser, Robert A. John, Johan N. Jansonius, and Tilman Schirmer. 1999. “Crystal Structure of GABA-Aminotransferase, a Target for Antiepileptic Drug Therapy.” *Biochemistry* 38(27): 8628–34. doi:10.1021/bi990478j.

Subramanian, Nandhitha, Amanda J Scopelitti, Jane E Carland, Renae M Ryan, Megan L O’Mara, and Robert J Vandenberg. 2016. “Identification of a 3rd Na+ Binding Site of the Glycine Transporter, GlyT2.” *PLOS ONE*. doi:10.1371/journal.pone.0157583.

Sundblad, Victoria, Diego O Croci, and Gabriel A Rabinovich. 2010. “Regulated Expression of Galectin-3, a Multifunctional Glycan-Binding Protein, in Haematopoietic and Non-Haematopoietic Tissues.” *Histology and Histopathology* (26): 247–65. doi:10.14670/HH-26.247.

Tai, Sheng, Yin Sun, Jill M. Squires, Hong Zhang, William K. Oh, Chao-Zhao Liang, and Jiaoti Huang. 2011. “PC3 Is a Cell Line Characteristic of Prostatic Small Cell Carcinoma.” *The Prostate* 71(15): 1668–79. doi:10.1002/pros.21383.

Tamura, Shigehiko, Hannah Nelson, Akiko Tamura, and Nathan Nelson. 1995. “Short External Loops as Potential Substrate Binding Site of γ-Aminobutyric Acid Transporters.” *Journal of Biological Chemistry* 270(48): 28712–15. doi:10.1074/jbc.270.48.28712.

Tan, Mh Eileen, Jun Li, H Eric Xu, Karsten Melcher, and Eu-leong Yong. 2015. “Androgen Receptor: Structure, Role in Prostate Cancer and Drug Discovery.” *Acta Pharmacologica Sinica* 36(1): 3–23. doi:10.1038/aps.2014.18.

Taylor, Kenneth A., and Robert M. Glaeser. 1974. “Electron Diffraction of Frozen, Hydrated Protein Crystals.” *Science* 186(4168): 1036–37. doi:10.1126/science.186.4168.1036.

Terunuma, Miho. 2018. “Diversity of Structure and Function of $GABA_B$ Receptors: A Complexity of $GABA_B$-Mediated Signaling.” *Proceedings of the Japan Academy, Series B* 94(10): 390–411. doi:10.2183/pjab.94.026.

Usui, Takeo, Yoko Nagumo, Ai Watanabe, Takaaki Kubota, Kazusei Komatsu, Jun’ichi Kobayashi, and Hiroyuki Osada. 2006. “Brasilicardin A, a Natural Immunosuppressant, Targets Amino Acid Transport System L.” *Chemistry & Biology* 13(11): 1153–60. doi:10.1016/j.chembiol.2006.09.006.

Van Meer, Gerrit, Dennis R. Voelker, and Gerald W. Feigenson. 2008. “Membrane Lipids: Where They Are and How They Behave.” *Nature Reviews Molecular Cell Biology* 9(2): 112–24. doi:10.1038/nrm2330.

Van Rosmalen, Martijn, Mike Krom, and Maarten Merkx. 2017. “Tuning the Flexibility of Glycine-Serine Linkers To Allow Rational Design of Multidomain Proteins.” *Biochemistry* 56(50): 6565–74. doi:10.1021/acs.biochem.7b00902.

Västermark, Åke, and Milton H. Saier. 2014. “Evolutionary Relationship between 5+5 and 7+7 Inverted Repeat Folds within the Amino Acid-Polyamine-Organocation Superfamily: Evolutionary Relationship of Inverted Repeat Folds.” *Proteins: Structure, Function, and Bioinformatics* 82(2): 336–46. doi:10.1002/prot.24401.

Wagner, Carsten A., Florian Lang, and Stefan Bröer. 2001. “Function and Structure of Heterodimeric Amino Acid Transporters.” *American Journal of Physiology-Cell Physiology* 281(4): C1077–93. doi:10.1152/ajpcell.2001.281.4.C1077.

Wang, Dan, Scott L. Deken, Terri L. Whitworth, and Michael W. Quick. 2003. “Syntaxin 1A Inhibits GABA Flux, Efflux, and Exchange Mediated by the Rat Brain GABA Transporter GAT1.” *Molecular Pharmacology* 64(4): 905–13. doi:10.1124/mol.64.4.905.

Wang, Ping, Chrys Wesdemiotis, Catherine Kapota, and Gilles Ohanessian. 2007. “The Sodium Ion Affinities of Simple Di-, Tri-, and Tetrapeptides.” *Journal of the American Society for Mass Spectrometry* 18(3): 541–52. doi:10.1016/j.jasms.2006.10.024.

Wang, Qian, Charles G. Bailey, Cynthia Ng, Jessamy Tiffen, Annora Thoeng, Vineet Minhas, Melanie L. Lehman, et al. 2011. “Androgen Receptor and Nutrient Signaling Pathways Coordinate the Demand for Increased Amino Acid Transport during Prostate Cancer Progression.” *Cancer Research* 71(24): 7525–36. doi:10.1158/0008-5472.CAN-11-1821.

Weissenberger, Giulia, Rene J. M. Henderikx, and Peter J. Peters. 2021. “Understanding the Invisible Hands of Sample Preparation for Cryo-EM.” *Nature Methods* 18(5): 463–71. doi:10.1038/s41592-021-01130-6.

Wempe, Michael F., Peter J. Rice, Janet W. Lightner, Promsuk Jutabha, Michinari Hayashi, Naohiko Anzai, Shin Wakui, et al. 2012. “Metabolism and Pharmacokinetic Studies of JPH203, an L-Amino Acid Transporter 1 (LAT1) Selective Compound.” *Drug Metabolism and Pharmacokinetics* 27(1): 155–61. doi:10.2133/dmpk.DMPK-11-RG-091.

Weyand, Simone, Tatsuro Shimamura, Oliver Beckstein, Mark S. P. Sansom, So Iwata, Peter J. F. Henderson, and Alexander D. Cameron. 2011. “The Alternating Access Mechanism of Transport as Observed in the Sodium-Hydantoin Transporter Mhp1.” *Journal of Synchrotron Radiation* 18(1): 20–23. doi:10.1107/S0909049510032449.

Williams, Simon A., Christine A. Jelinek, Ivan Litvinov, Robert J. Cotter, John T. Isaacs, and Samuel R. Denmeade. 2011. “Enzymatically Active Prostate-specific Antigen Promotes Growth of Human Prostate Cancers.” *The Prostate* 71(15): 1595–1607. doi:10.1002/pros.21375.

Wolański, Marcin, Michał Krawiec, Kay Nieselt, Tobias Schwarz, Dilek Dere, Bernhard Krismer, Carolina Cano-Prieto, Harald Gross, and Jolanta Zakrzewska-Czerwińska. 2024. “Multiple

Regulators Control the Biosynthesis of Brasilicardin in Nocardia Terpenica." doi:10.1101/2024.06.11.594307.

Wu, Di, Renhong Yan, Siyuan Song, Andrew K. Swansiger, Yaning Li, James S. Prell, Qiang Zhou, and Carol V. Robinson. 2024. "The Complete Assembly of Human LAT1-4F2hc Complex Provides Insights into Its Regulation, Function and Localisation." *Nature Communications* 15(1): 3711. doi:10.1038/s41467-024-47948-4.

Xie, Tengyu, Ximin Chi, Bangdong Huang, Fangfei Ye, Qiang Zhou, and Jing Huang. 2022. "Rational Exploration of Fold Atlas for Human Solute Carrier Proteins." *Structure* 30(9): 1321-1330.e5. doi:10.1016/j.str.2022.05.015.

Xinjie, Lu. 2019. "The Role of Large Neutral Amino Acid Transporter (LAT1) in Cancer." *Current Cancer Drug Targets* 19(11): 863–76. doi:10.2174/1568009619666190802135714.

Yamashita, Atsuko, Satinder K. Singh, Toshimitsu Kawate, Yan Jin, and Eric Gouaux. 2005. "Crystal Structure of a Bacterial Homologue of Na+/Cl--Dependent Neurotransmitter Transporters." *Nature* 437(7056): 215–23. doi:10.1038/nature03978.

Yan, Renhong, Yaning Li, Jennifer Müller, Yuanyuan Zhang, Simon Singer, Lu Xia, Xinyue Zhong, et al. 2021. "Mechanism of Substrate Transport and Inhibition of the Human LAT1-4F2hc Amino Acid Transporter." *Cell Discovery* 7(1): 16. doi:10.1038/s41421-021-00247-4.

Yan, Renhong, Xin Zhao, Jianlin Lei, and Qiang Zhou. 2019. "Structure of the Human LAT1–4F2hc Heteromeric Amino Acid Transporter Complex." *Nature* 568(7750): 127–30. doi:10.1038/s41586-019-1011-z.

Yancey, Paul H., and George N. Somero. 1979. "Counteraction of Urea Destabilization of Protein Structure by Methylamine Osmoregulatory Compounds of Elasmobranch Fishes." *Biochemical Journal* 183(2): 317–23. doi:10.1042/bj1830317.

Yang, Dehua, Qingtong Zhou, Viktorija Labroska, Shanshan Qin, Sanaz Darbalaei, Yiran Wu, Elita Yuliantie, et al. 2021. "G Protein-Coupled Receptors: Structure- and Function-Based Drug

Discovery." *Signal Transduction and Targeted Therapy* 6(1): 7. doi:10.1038/s41392-020-00435-w.

Yao, Xia, Xiao Fan, and Nieng Yan. 2020. "Cryo-EM Analysis of a Membrane Protein Embedded in the Liposome." *Proceedings of the National Academy of Sciences* 117(31): 18497–503. doi:10.1073/pnas.2009385117.

Yip, Ka Man, Niels Fischer, Elham Paknia, Ashwin Chari, and Holger Stark. 2020. "Atomic-Resolution Protein Structure Determination by Cryo-EM." *Nature* 587(7832): 157–61. doi:10.1038/s41586-020-2833-4.

Yoshimura, Fumihiko, Ryusei Itoh, Makoto Torizuka, Genki Mori, and Keiji Tanino. 2018. "Asymmetric Total Synthesis of Brasilicardins." *Angewandte Chemie International Edition* 57(52): 17161–67. doi:10.1002/anie.201811403.

Zacharias, Niki Marie, Christopher McCullough, Sriram Shanmugavelandy, Jaehyuk Lee, Youngbok Lee, Prasanta Dutta, James McHenry, et al. 2017. "Metabolic Differences in Glutamine Utilization Lead to Metabolic Vulnerabilities in Prostate Cancer." *Scientific Reports* 7(1): 16159. doi:10.1038/s41598-017-16327-z.

Zafra, Francisco, and Cecilio Gimenez. 2008. "Glycine Transporters and Synaptic Function." *IUBMB Life* 60(12): 810–17.

Zeev-Ben-Mordehai, Tzviya, Daven Vasishtan, C. Alistair Siebert, and Kay Grünewald. 2014. "The Full-Length Cell–Cell Fusogen EFF-1 Is Monomeric and Upright on the Membrane." *Nature Communications* 5(1): 3912. doi:10.1038/ncomms4912.

Zeev-Ben-Mordehai, Tzviya, Daven Vasishtan, C. Alistair Siebert, Cathy Whittle, and Kay Grünewald. 2014. "Extracellular Vesicles: A Platform for the Structure Determination of Membrane Proteins by Cryo-EM." *Structure* 22(11): 1687–92. doi:10.1016/j.str.2014.09.005.

Zhang, Cunjie, Massiullah Shafaq-Zadah, Judy Pawling, Geoffrey G. Hesketh, Estelle Dransart, Karina Pacholczyk, Joseph Longo, et al. 2023. "SLC3A2 N-Glycosylation and Golgi

Remodeling Regulate SLC7A Amino Acid Exchangers and Stress Mitigation." *Journal of Biological Chemistry* 299(12): 105416. doi:10.1016/j.jbc.2023.105416.

Zhang, Jingshun, Ying Xu, Dandan Li, Lulu Fu, Xueying Zhang, Yigang Bao, and Lianwen Zheng. 2020. "Review of the Correlation of LAT1 With Diseases: Mechanism and Treatment." *Frontiers in Chemistry* 8: 564809. doi:10.3389/fchem.2020.564809.

Zhang, Jun-He, Fang Wang, and Tian-Yun Wang. 2011. "A Simple and Effective SuperBuffer for DNA Agarose Electrophoresis." *Gene* 487(1): 72–74. doi:10.1016/j.gene.2011.05.018.

Zhou, Y., S. Holmseth, R. Hua, A. C. Lehre, A. M. Olofsson, I. Poblete-Naredo, S. A. Kempson, and N. C. Danbolt. 2012. "The Betaine-GABA Transporter (BGT1, Slc6a12) Is Predominantly Expressed in the Liver and at Lower Levels in the Kidneys and at the Brain Surface." *American Journal of Physiology-Renal Physiology* 302(3): F316–28. doi:10.1152/ajprenal.00464.2011.

Zhou, Yonggang, Elia Zomot, and Baruch I. Kanner. 2006. "Identification of a Lithium Interaction Site in the γ-Aminobutyric Acid (GABA) Transporter GAT-1." *Journal of Biological Chemistry* 281(31): 22092–99. doi:10.1074/jbc.M602319200.

Zhu, Angqi, Junhao Huang, Fang Kong, Jiaxin Tan, Jianlin Lei, Yafei Yuan, and Chuangye Yan. 2023. "Molecular Basis for Substrate Recognition and Transport of Human GABA Transporter GAT1." *Nature Structural & Molecular Biology* 30(7): 1012–22. doi:10.1038/s41594-023-00983-z.

Ziegler, Christine, Erhard Bremer, and Reinhard Krämer. 2010. "The BCCT Family of Carriers: From Physiology to Crystal Structure." *Molecular Microbiology* 78(1): 13–34. doi:10.1111/j.1365-2958.2010.07332.x.

Zomot, Elia, Annie Bendahan, Matthias Quick, Yongfang Zhao, Jonathan A. Javitch, and Baruch I. Kanner. 2007. "Mechanism of Chloride Interaction with Neurotransmitter:Sodium Symporters." *Nature* 449(7163): 726–30. doi:10.1038/nature06133.

Zomot, Elia, Mert Gur, and Ivet Bahar. 2015. “Microseconds Simulations Reveal a New Sodium-Binding Site and the Mechanism of Sodium-Coupled Substrate Uptake by LeuT.” *Journal of Biological Chemistry* 290(1): 544–55. doi:10.1074/jbc.M114.617555.

Zomot, Elia, and Baruch I. Kanner. 2003. “The Interaction of the γ-Aminobutyric Acid Transporter GAT-1 with the Neurotransmitter Is Selectively Impaired by Sulfhydryl Modification of a Conformationally Sensitive Cysteine Residue Engineered into Extracellular Loop IV.” *Journal of Biological Chemistry* 278(44): 42950–58. doi:10.1074/jbc.M209307200.